NEURODEGENERATIVE AND METABOLOMIC IMPACT OF GENETIC ELIMINATION OF THE ORPHAN METALLO β-LACTAMASE, SWIP-10/MBLAC1

By

Chelsea Lynn Gibson

Dissertation

Submitted to the Faculty of the

Graduate School of Vanderbilt University

in partial fulfillment of the requirements

for the degree of

DOCTOR OF PHILOSOPHY

in

Neuroscience

May 11, 2018

Nashville, Tennessee

Approved:

Randy D. Blakely, Ph.D.

Eric J. Delpire, Ph.D.

David M. Miller Ph.D.

Bruce D. Carter, Ph.D.

John A. McLean, Ph.D.

DEDICATION

For my supportive husband, family, and friends.

ACKNOWLEDGEMENTS

I would like to thank Vanderbilt University's Neuroscience Graduate Program for the opportunity to conduct research and receive premier training. The administrative staff within the Brain Institute, especially Beth Sims and Roz Johnson, provided great institutional support during my time in the Neuroscience Graduate Program, especially assisting in administrative matters after relocating to FAU. Additionally, I would like to acknowledge the excellent research support within the Blakely Lab at Vanderbilt by Sarah Sturgeon, Tracy Moore-Jarrett, Chris Svitek, Angela Steele, Qiao Han, and Jane Wright; and the research support at FAU provided by Matt Gross, Samara Vilca and Peter Rodriguez. For my exploration of mass-spectrometry and metabolomics, I am very grateful for the unwavering support and expertise provided by Alex Schrimpe-Rutledge, Simona Codreanu, and Stacy Sherrod within Vanderbilt's Center for Innovative Technology. The mentorship and scientific input from my dissertation committee has been extremely beneficial to my development as scientist, and I'd like to thank Dr. Delpire, Dr. Carter, Dr. Miller, and Dr. McLean for their continued support and encouragement.

Lastly, and certainly not least, I would like to acknowledge and thank Dr. Randy Blakely for his mentorship, support, and training throughout my graduate career. Dr. Blakely's boundless enthusiasm and dedication to excellence in neuroscience research provided an exceptional environment for training and becoming a neuroscientist. This work was supported by grants from the National Institute of Health (NIH).

TABLE OF CONTENTS

LIST OF TABLES

Table Page

LIST OF FIGURES

Figure Page

LIST OF ABBREVIATIONS

5-HT	5-hydroxytryptamine/ Serotonin
5-HTP	5-hydroxytryptophane
6-OHDA	6-hydroxydopamine
AADC	Aromatic Amino Acid Decarboxylase
AAT	Amino Acid Transporter
AD	Alzheimer's Disease
ADE	Anterior Deirid
ADEsh	Anterior Deirid sheath
ADEso	Anterior Deirid socket
ALS	Amyotrophic Lateral Sclerosis
AMPA	α-amino-3-hydroxy-5-methy-4-isoxazole
ATP	Adenosine Triphosphate
BSR	Basal Slowing Response
CEF	Ceftriaxone
CEP	Cephalic Neuron
CEPsh	Cephalic sheath
CEPso	Cephalic socket
CGC	Caenorhabditis Genetics Center
CNS	Central Nervous System
COMT	Catechol-*o*-methyltransferase
CRISPR	Clustered Regularly Interspaced Short Palindromic Repeats

DA	Dopamine
DAT	Dopamine Transporter
DDA	Data Dependent Acquisition
DEG/ENaC	Na^{2+}/Ca^{2+}-permeable Degenerin/ Epithelial sodium channels
DOPA	3,4-dihydroxyphenylalanine
DOPAC	3,4-dihydroxyphenylacetic acid
DRD	Dopamine-related dystonia
EM	Electron Microscopy
EMS	Ethylmethanesulfonate
FSCV	Fast-Scan Cyclic Voltammetry
FIF	Formaldehyde-Induced-Fluorescence
GFP	Green Fluorescent Protein
Glu	Glutamic Acid (Glutamate)
GluR	Glutamate Receptor
GLT	Glutamate Transporter
GS	Glutamine Synthetase
GSH	Glutathione
GST	Glutathione S-transferase
HD	Huntington's disease
HILIC	Hydrophilic Interaction Chromatography
HMDB	Human Metabolome Database
HPLC	High Performance Liquid Chromatography
HSP	Heat Shock Protein

iGluR	Ionotropic Glutamate Receptor
ISI	inter-stimulus interval
KO	Knockout
L-DOPA	L-dihydroxyphenylalanine
LC	Liquid Chromatography
LOESS	Locally Weighted Scatterplot Smoothing
MAO	Monoamine Oxidase
MBL	Metallo-β–Lactamase
MBLAC	Metallo-β–Lactamase domain containing protein
mGluR	Metabotropic Glutamate Receptor
MGO	Methylglyoxal
MPTP	1-methyl-4-phenyl-1,2,3,6-tetrahydroxypyridine
MS	Mass Spectrometry
myrRFP	Myrisolated Red Fluorescent Protein
m/z	Mass to Charge ratio
NE	Norepinephrine
NET	Norepinephrine transporter
NEG	Negative ion mode
NGM	Nematode Growth Medium
NMDA	N-methyl-D-aspartate
OLL	Outer Labial Lateral
ORF	Open Reading Frame
PAM	Protospacer Adjacent Motif

PCA	Principal Component Analysis
PCR	Polymerase Chain Reaction
PD	Parkinson's Disease
PDE	Posterior Deirid
PDEsh	Posterior Deirid sheath
PDEso	Posterior Deirid socket
POS	Positive ion mode
RPLC	Reverse Phase Liquid Chromatography
SCZ	Schizophrenia
Swip	Swimming Induced Paralysis
TAM	Tubule-Associated Material
TEM	Transmitting Electron Microscopy
TH	Tyrosine Hydroxylase
UPLC	Ultra-Performance Liquid Chromatography
VGLUT	Vesicular Glutamate Transporter
VMAT	Vesicular Monoamine Transporter
WT	Wildtype
xCT	Cystine/Glutamate Exchanger

Chapter I

THE *C. elegans* DOPAMINERGIC NERVOUS SYSTEM

Dopamine Neurotransmission in the Mammalian Central Nervous System

Dopamine (DA), also known as 3-hydroxytyramine or 3,4-dihydroxyphenylethylamine, was first described as a chemical present in the mammalian brain in the late 1950s by Carlsson and colleagues [1]. Through the use of ion-exchange chromatography and fluorometric assays, Carlsson distinguished DA from other catecholamines (norepinephrine and epinephrine) and identified DA as a neurochemical with brain levels of DA enhanced by pretreatment of 3,4-dihydroxyphenylalanine (DOPA) and reduced by pretreatment with reserpine [2]. To be classified as a neurotransmitter, DA needed to be shown as a) present in presynaptic neurons, b) released from the presynaptic neuron upon electrical stimulation, c) acting on receptors for DA-specific signaling and d) having a mechanism for DA signaling termination.

DA biosynthesis and vesicular packaging

DA is an amino acid derivative, synthesized from its precursor, tyrosine in the cytosol. The first, and rate limiting, step of DA synthesis is the hydroxylation of tyrosine at the 3rd carbon by tyrosine hydroxylase (TH) enzyme forming L-dihydroxyphenylalanine, L-DOPA (Fig. 1) [3, 4]. Successively, the enzyme, aromatic acid decarboxylase (AADC or DDC) removes a carboxyl group from L-DOPA to form 3,4-dihydroxyphenylethylamine or DA (Fig. 1) [5].

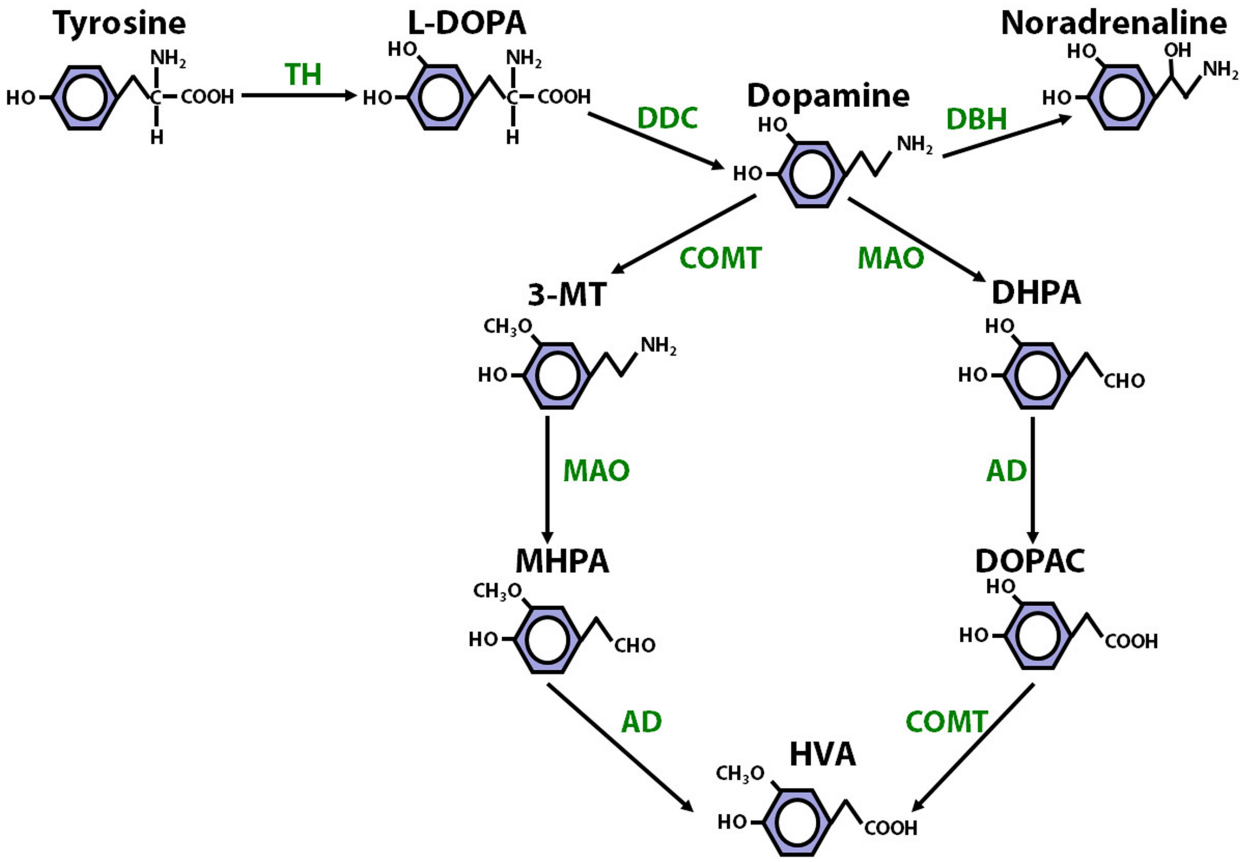

Fig. 1. DA biosynthesis and metabolism. Image from Laatikainen et al. 2013.

In order to be released into the synaptic cleft from the presynaptic nerve terminal following electrical stimulation, DA is packaged into synaptic vesicles. Initial studies showed that DA and other catecholamines were transported into chromaffin granules and this transport was enhanced by ATP and inhibited by the drug reserpine [6]. Later, molecular cloning studies identified two cDNAs that encode proteins with the ability to transport biogenic amines, encoding proteins with twelve transmembrane domains and cytosolic N and C termini, the vesicular monoamine transporter 1 and 2 (vMAT1 and vMAT2) [7]. Further studies revealed that vMAT2 is the primary and high affinity vesicular transporter for biogenic amines in the midbrain, including DA, serotonin (5HT) and norepinephrine (NE) packaging [8]. vMAT2 is expressed in DA neurons on synaptic vesicles as determined by immuno-electron microscopy studies [9] and is responsible for ATP-dependent vesicular packaging of DA.

Mammalian distribution of DA neuron cell bodies and projections

Through the use of DA-labeling techniques such as formaldehyde-induced-fluorescence (FIF), researchers determined that DA was present in mammalian neuronal cell bodies in the midbrain and at presynaptic regions of terminal fibers in the striatum [10, 11]. Later, via the use of immunohistochemical techniques to staining for DA specific proteins, such as TH or the DA transporter (DAT), researchers revealed that DA neuron cell bodies reside predominantly in two midbrain nuclei: the ventral tegmental area (VTA) and the substantia nigra pars compacta (SNc) [12, 13]. A small subset of DA neurons is located within the arcuate nucleus and send their axons to the median eminence (the tuberoinfundibular pathway) [14]. VTA DA neurons send their axons to the forebrain and

innervate several targets, A) the mesocortical pathway, with DA terminals in the prefrontal cortex and the insular cortex or B) the mesolimbic pathway, with DA terminals innervating the limbic cortex, hippocampus, ventral striatum, nucleus accumbens (Acc) and amygdala. The nigro-striatal pathway refers the DA neurons in the SNc that send axonal projections to the dorsal striatum [15]. These pathways are summarized in Fig. 2 (from psychopharmacologyinstitute.com).

Utilizing retrograde labeling techniques, via horseradish peroxidase tracer or the more modern method of pseudo-rabies virus mediated retrograde labeling, researchers have established that midbrain DA neurons receive inputs from areas throughout the brain. Inputs to the SNc originate from brain areas such as the dorsal striatum, dorsal raphe nuclei, amygdala, globus pallidus and neighboring GABAergic interneurons [16, 17]. In summary, the VTA receives inputs from brain regions including the dorsal raphe nuclei, amygdala, hypothalamus, pre-frontal cortex, bed nucleus of stria terminalis (BNST), nucleus accumbens (Acc), superior colliculus, locus coeruleus, the paraventricular nucleus, and neighboring GABAergic interneurons [17, 18].

DA release and signaling through DA receptors

By coupling newly developed brain perfusion techniques, selective brain region electrical stimulation methods, and chromatographic DA detection methods, Portig and colleagues found that electrical stimulation of the SN resulted in DA release in the striatum [19, 20]. Following studies utilized pre-treatment of brain slices with radiolabeled DOPA to visualize subsequently synthesized radiolabeled DA release from presynaptic terminals upon electrical stimulation of DA neuron cell bodies [21]. As detection

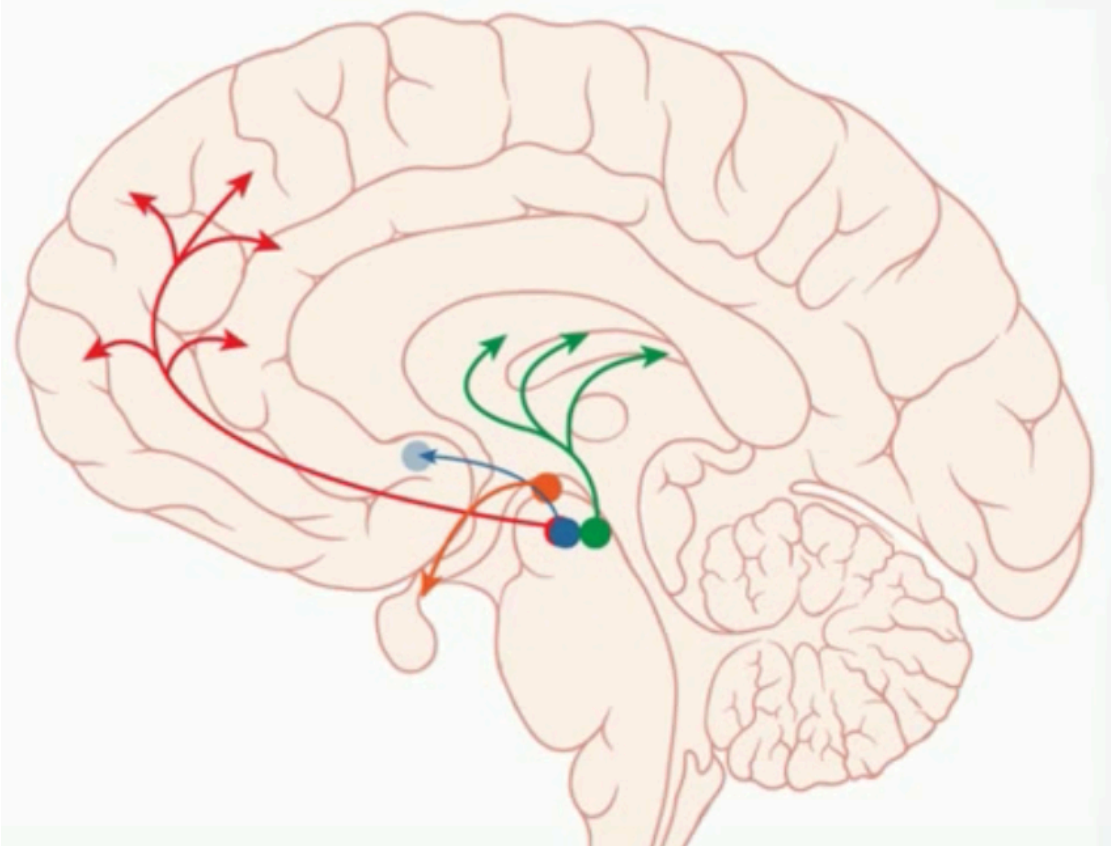

Fig. 2. Mammalian DA projection pathways. ↑**Red**: The mesocortical pathway; DA neurons in the VTA project to the prefrontal cortex. ↑**Blue**: The mesolimbic pathway; VTA DA neurons send their projections to the limbic cortex and nucleus accumbens. ↑**Green**: The nigro-striatal pathway; DA neurons in the substantia nigra send projections to the dorsal striatum. ↑**Orange**: The tuberoinfundibular pathway; DA neurons in the arcuate nucleus send axons to the median eminence. Adapted from www.psychopharmacologyinstitute.com.

techniques advanced, high performance liquid chromatography (HPLC) coupled to micro-dialysate collection allowed more precise and accurate measurements of DA release in the brain [22, 23]. Additionally, electrochemical detection via the unique “signature” or oxidative potential of DA by fast-scan cyclic voltammetry (FSCV) provided researchers with the ability to measure DA *in vivo* with increased sensitivity and greater temporal and spatial precision [24, 25]. In addition to stimulated DA release, work by Deister and colleagues demonstrate that the DA neurons in the midbrain fire in a tonic, burst pattern [26] and further work by Williams and colleagues demonstrate that the burst-firing pattern of DA release is controlled by DA itself through an inhibitory autoreceptor (D2R) feedback mechanism [27, 28].

Solidifying DA’s role as a neurotransmitter, use of radiolabeled compounds allowed researchers to determine that DA specifically bound a putative plasma membrane DA receptor in mammalian brain membrane fractions [29-31]. This work lead to the subsequent molecular cloning of human and rodent DA receptor cDNAs, such that five mammalian DA receptors, D1-D5 were found to be responsible for DA specific modulation of neuronal signaling [32-36]. DA receptors are categorized based on how activation of these receptors impacts cAMP, a second messenger, production. D1-type receptor (D1R and D5R) stimulation increases adenylyl cyclase activity and cAMP production, whereas D2-type receptor (D2R, D3R, and D4R) stimulation reduces cAMP production to modulate neuronal signaling [37].

DA reuptake and metabolism

To function as a neurotransmitter, DA signaling must be terminated precisely and quickly to maintain spatially and temporally specific modulation of neuronal activity. Using molecular cloning techniques, researchers identified mammalian DA transporter (DAT) cDNAs and began studying DAT function. In a study by Kilty and colleagues, rat DAT, heterologously expressed in HeLa cells, displayed high affinity DA uptake into the cells, and this uptake could be antagonized by DA analogs and psychostimulants, including cocaine [38]. Immunohistochemistry studies determined that DAT was expressed in the VTA and SNc [12] and later studies utilized FSCV to determine the endogenous function of DAT in the mouse brain [39]. DA signaling was therefore found to be terminated by selective DA reuptake by the DA transporter (SLC6A3), a member of the Na^+- and Cl^--dependent neurotransmitter transporter family.

Although the majority of DA is cleared from the extracellular space by DAT, recycled, and repackaged into synaptic vesicles, a portion of DA is metabolized, and the abundance of these DA derivatives can be utilized to assess DA turnover. Metabolism of DA occurs by two metabolic pathways, 1) methyl group transfer to the 3' carbon of DA by the cytosolic catechol o-methyltransferase (COMT) to form 3-methoxytyramine (3MT), or 2) DA deamination by the monoamine oxidase (MAO) forms the DA metabolite, 3,4 dihydroxyphenylacetic acid (DOPAC) (Fig. 1). These two metabolic pathways converge, as both 3MT and DOPAC are modified to the final DA-related metabolite, homovanillic acd (HVA).

Brain Disorders, Behaviors, and Phenotypes Associated with Dysregulated DA Signaling

Through action on both DA receptors that activate adenylyl cyclase (D1R, D5R) and inhibit adenylyl cyclase (D2R, D3R, D4R), DA modulates the inherent excitability of many neuronal cells including glutamate (Glu), GABA, and acetylcholine releasing neurons. Via these modulatory actions, DA regulates many mammalian behaviors including cognition, reward behaviors and motor actions. Understanding the molecular components and regulators of DA under normal physiological conditions has been extremely useful in understanding how different brain disorders are associated with altered or dysregulated DA signaling. Though this brief review of brain disorders associated with changes in DA signaling is not comprehensive, I will focus this summary on highlighting well-described disorders predominately associated with altered DA signaling.

Movement related disorders with altered DA signaling

Parkinson's disease (PD) is perhaps the brain disorder most tightly connected with DA signaling dysfunction. The impaired motor function and symptoms classically used to diagnose PD (bradykinesia, tremor, rigidity, shuffling gait, and postural instability) are attributed to loss of DA neurons in the SNc and subsequent loss of DA modulation of neurotransmitter signaling in the basal ganglia [40, 41]. Furthermore, clinical confirmation of a PD diagnosis is dependent on DA related treatments improving the movement related symptomology of patients. More recently, the non-motor symptoms of PD such as depression, autonomic dysfunction, impulse control deficits, and cognitive decline are

also attributed, at least in part, to dysregulated DA signaling prior to the severe (60-70%) SNc DA neuron loss required for the motor symptom manifestation [42]. In PD pathology, Lewy bodies (dense inclusions of abnormal protein aggregates with in nerve cells) and α-synuclein aggregation occurs in SNc DA neurons as well as other non-DArgic nuclei [43, 44]. The exact mechanism leading to Lewy body formation and SNc DA neuron cell death in PD patients has not been determined, however bodies of research indicate that Glu induced excitotoxicity, oxidative stress, mitochondrial dysfunction, mishandling of misfolded proteins/ proteasome dysfunction, and inflammation contribute to PD pathology [45-48], summarized in Fig. 3 [49]. In order to study animal models of PD, many researchers employ neurotoxins that selectively and specifically lesion DA neurons, such as 6-OHDA and MPTP [50-53].

Although less well-characterized in terms of abnormal DA neurotransmission, Huntington's disease (HD) pathology also implicates DA signaling as a contributor to the symptoms of HD. A dominant, inherited, progressive neurodegenerative disease, HD arises due to a mutation that increases the expansion of CAG repeats in the *HTT* gene. Differing from PD, the primary sites of neurodegeneration in the brain are the striatum, cerebral cortex, and to lesser extent in the hippocampus [54, 55]. However post-mortem studies indicate that the motor and cognitive symptoms of HD occur prior to severe neuronal loss, indicating that symptoms are a result of neuronal and synaptic dysfunction [56]. Researchers have used positron emission tomography and autoradiography to determine the DA D1 and D2 receptor densities in HD patients, prior to and after symptom onset, and have observed reduced striatal D1 and D2 receptor densities in both HD patients and non-symptomatic, heterozygous carriers [57, 58]. These alterations in DA

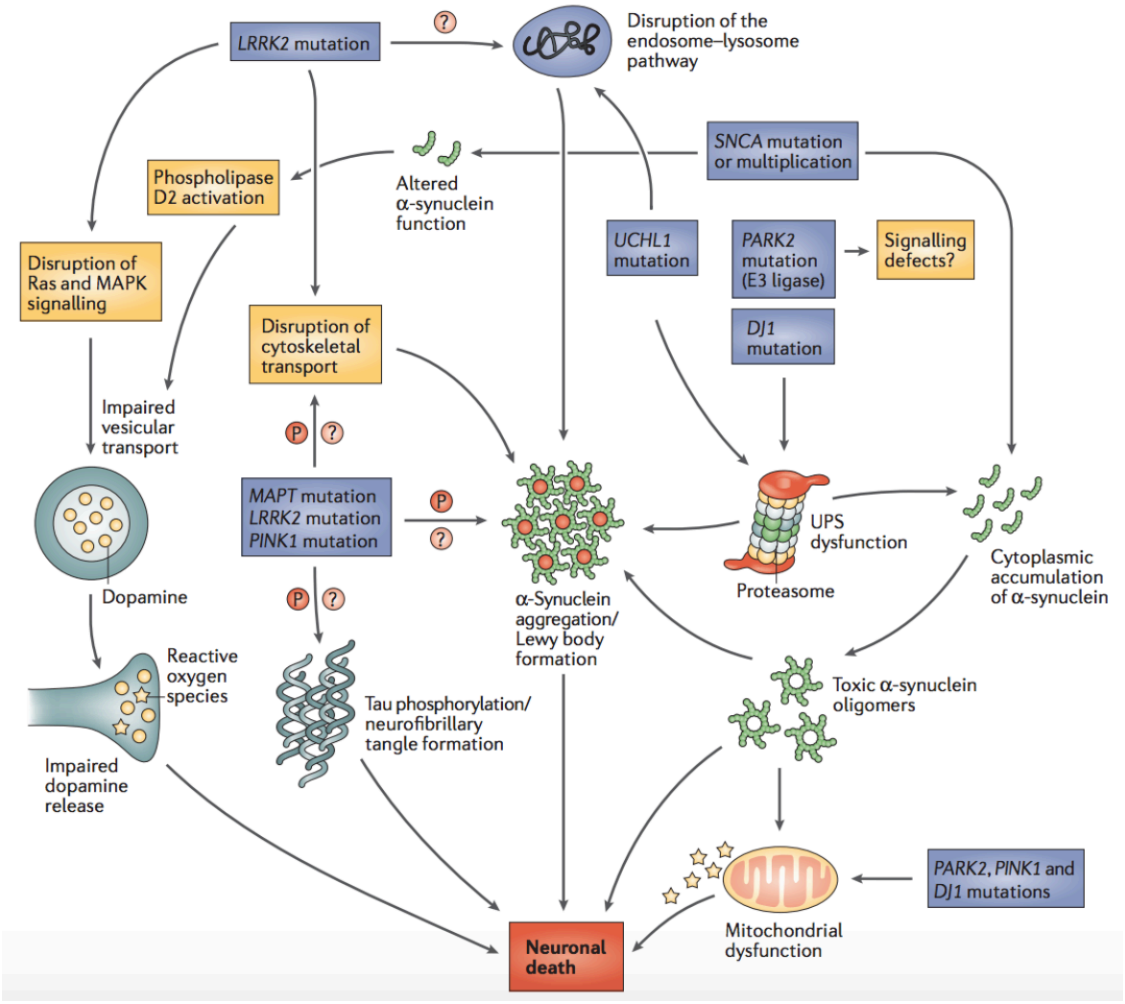

Fig. 3. Diagram of the key pathological and clinical features of Parkinson's Disease. This schematic summarizes the key pathways identified as contributing to the pathology and symptoms associated with Parkinson's disease. Several genetic mutations associated with PD susceptibility are highlighted for their contributions to the physiological pathology of PD (i.e. *LRRK2*, *SNCA, PINK1,* etc.). Additionally, this diagram highlights known mechanistic contributors to DA neuron cell death including mitochondrial dysfunction, reactive oxygen species, protein misfolding and aggregation, etc. (Adapted from Farrer, 2006).

receptor densities in the striatum (observed in HD patients and HD genetic mouse models) have been correlated with cognitive deficits including changes in memory, learning, and attention [59, 60]. Studies support the hypothesis that dysregulated DA signaling follows a biphasic trend, mirroring the biphasic trend of dysregulated Glu signaling in HD. Researchers use electrophysiological methods to demonstrate that cortical Glu signaling is increased, and lead to increased DA neuron firing/ DA tone early in HD [61, 62]. In treating the chorea (jerky, involuntary movements) associated with HD, often, the VMAT2 inhibitor, tetrabenazine, is prescribed to reduce DA signaling within the basal ganglia [63]. Researchers then hypothesize that as the disease progresses, DA neuron modulation of Glu release ultimately results in reduced Glu and DA signaling in late stages of HD [56].

Dystonia, characterized by repetitive or sustained motor contractions, including tremor and abnormal gait or postures, is associated with neurological disorders, including but not exclusive to PD. One distinct form of dystonia that was set apart from sporadic Parkinson's disease is known as infantile-onset parkinsonism-dystonia, named for the hypokinetic parkinsonism that presents in early infancy and develops into a complex movement disorder. Using biochemical detection techniques, researchers determined that patients with infantile parkinsonism-dystonia have abnormal levels dopamine metabolites, such as homovanillic acid, in their cerebral-spinal fluid (CSF) [64]. Kurian and colleagues determined that increased levels of homovanillic acid in the CSF of three unrelated patients with infantile parkinsonism-dystonia was a result of separate loss-of-function mutations in the *dat* gene [65]. This work, as well as subsequent studies identifying additional inherited DAT mutations leading to infantile parkinsonism-dystonia,

suggest that these mutations reduce surface level DAT expression therefore impairing DAT-mediated DA clearance resulting in dysregulated dopaminergic neurotransmission and disease pathology [65-67]. Researchers and clinicians group a subset of dystonia associated neurological disorders as DA-responsive dystonia (DRD), in that treatment with L-DOPA alleviates the abnormal movement symptoms that fluctuate diurnally [68, 69]. Within the group of DA-related dystonias, CTP cyclohydrolase I (GCH1) deficiency and tyrosine hydroxylase (TH) deficiency arising from genetic mutations are the most well characterized types of DRDs [70]. Various mutations in these genes result in a reduced capacity to synthesize DA and patient's and mouse-model symptoms are alleviated by administration of L-DOPA, the DA synthesis precursor, as it increases striatal DA levels [71-74]. Post-synaptic DA signaling on DA receptors, both D1R and D2R, is dysregulated in models of DRD. Cai and colleagues found that agonist activation of both subtypes of DA receptors ameliorated the motor symptoms in the *Th*$^{tm/Ehess}$ mouse model of DRD, a knock-in mouse model that recapitulates a known human TH mutation associated with DRD and reduced TH activity, yet the mice only exhibit increased behavioral sensitivity to D1R activation [70, 74]. By using genetic mouse models with construct, face, and predictive validity, researchers are focusing their efforts to understanding the mechanism by which DA depletion and maladaptive DA receptor changes results in dystonia, and how to best treat human patients with DRDs.

Cognitive disorders associated with disrupted DA signaling

The most commonly diagnosed neuropsychiatric disorder of childhood, Attention-deficit/hyperactivity disorder (ADHD), affects 4-12% of United states school-aged children

[75, 76]. With a wide spectrum of behavioral criteria used for clinical diagnosis, including motor hyperactivity, inattention, and impulsivity, researchers have long been interested in determining the genetic and environmental factors that contribute to this disorder. The behavioral symptomology of ADHD observed by clinicians and researchers implicates dysregulated DA and NE in the pre-frontal cortex, and first-line medications to alleviate the disruptive symptoms of ADHD include the psychostimulants, methylphenidate and amphetamines, that interact with and inhibit DAT and the related NE transporter (NET) [77]. Pairing pharmacological treatment with behavioral therapy helps many adults and children with ADHD, however about 30% of patients are unresponsive to the primary stimulants prescribed. To better understand the etiology of ADHD, many researchers point to disruptions in DA system genes as underlying the symptoms of ADHD, for example, animal models of ADHD utilize DA D1R agonist to phenocopy locomotor hyperactivity [78-80], and polymorphisms in DA receptors [81-83] the DA transporter [84-87], and DA metabolizing enzymes [88, 89] have all been found in patients with ADHD. First identified in a patient diagnosed with bipolar disorder, a coding variant in the human DAT, Val 559 [90, 91], was further characterized as a heritable variant in two brothers with ADHD, and later identified in two unrelated subjects with autism spectrum disorder. Mergy, Davis, and Gowrishankar have respectively developed, characterized behaviorally, and biochemically a murine ADHD model with a human ADHD variant (DAT Val559) [92, 93]. This construct, phenotypic, and predictively valid mouse model for ADHD, has allowed researchers to better understand the contributions of DAT and DA signaling to locomotor hyperactivity (no overt hyperactivity in this mouse model, however the DAT Val559 mice display a robust darting phenotype) and *in vivo* response to

psychostimulants as well identify a role for DA signaling in impulsive behaviors dependent on a reward context [92-94]. In addition to animal models of ADHD, researchers have gained insight to various contributions of the DA system to ADHD through case-control PET and SPECT imaging studies, to assess DA receptor densities and DAT levels in drug exposed and drug naïve individuals [95-98].

Mesolimbic DA signaling has been extensively studied in terms of mediating the enjoyable aspects of biologically salient rewards (food, water, and sex) and also in mediating arousal as animals and humans learn to predict future reward or positive reinforcer [99]. Many drugs of abuse act via the mesolimbic DA signaling pathway to exert their initial rewarding properties [100]. Psychoactive drugs, such as cocaine and amphetamines increase DA signaling above physiological levels in the brain-reward circuit to activate direct striatal D1R pathways and inhibit the indirect striato-cortical pathway by D2Rs [101] (Fig. 4) [99]. Addiction requires the transition from a controlled to a compulsive drug taking behavior despite adverse consequences. This change is likely resultant from long-term compensatory changes in neurotransmitter signaling (including DA, GABA, and Glu) in the brain by exploiting the brain's normal reward circuitry (Fig. 4) (addiction) [102, 103]. Researchers implicate DA signaling in brain regions responsible for habit formation and the rewarding response to drugs (dorsal striatum and Acc respectively) in the development in addiction. Researchers found reduced striatal levels of D2R in self-administration non-human primate and rodent models of addiction [104-106]. Furthermore, human brain-imaging studies similarly show reduced striatal D2R availability in the brains of patients struggling with addiction, for the majority of drugs of abuse [107]. D2R reductions in the striatum reduce inhibition of the indirect pathway and

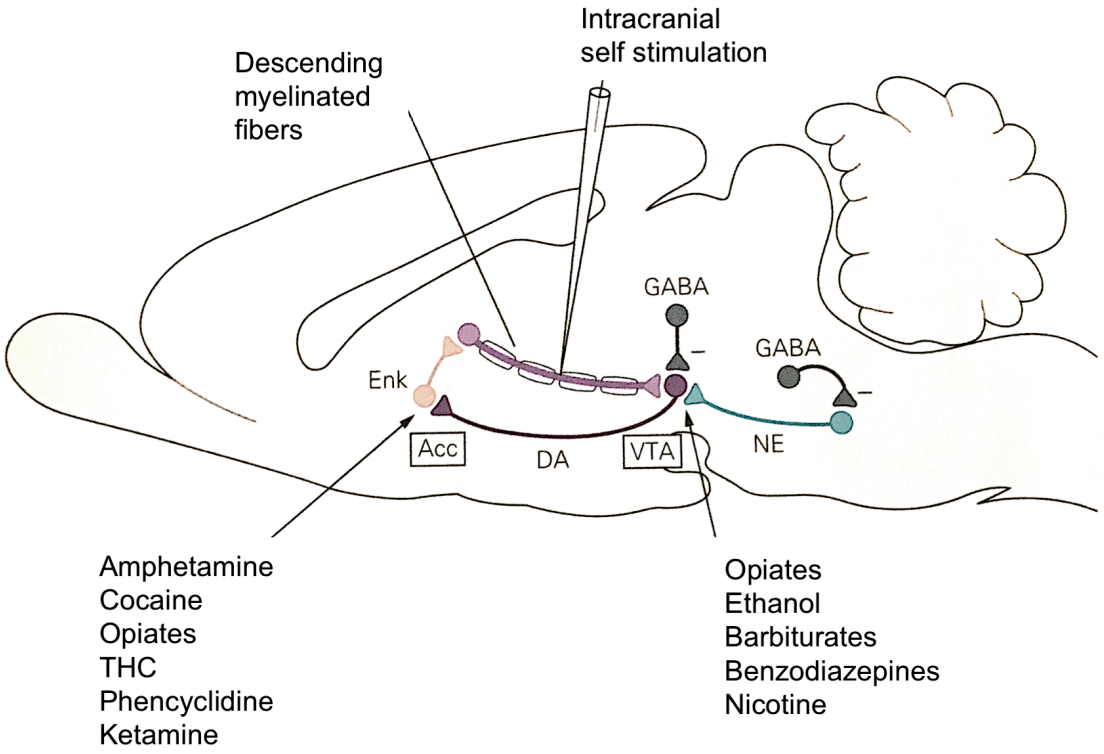

Fig. 4. Brain-reward circuitry in the rat. Proposed sites of drug actions are shown in boxes, Acc= Nucleus Accumbens, VTA=ventral tegmental area, such that drugs of abuse impinge on normal brain reward circuitry and alter neurotransmitter signaling, DA= dopamine, Enk=encephalin, NE= norepinephrine. (Figure adapted from Gardner and Lowinson 1993, and Kandel, Schwartz, and Jessell, Principles of Neural Science, 4th edition, 2000).

reduce activity in the PFC, altering behaviors such as planning, control, flexibility in response, and delayed gratification [107]. Although DA signaling is not the sole mediator of the addiction as a brain disorder, the neurotransmitter plays a critical role in both the initial response to drugs of abuse, and brain adaptations responsible for addiction.

Schizophrenia (SCZ) is a devastating mental disorder, affecting about 1% of the population worldwide [108, 109], with great health care and social care costs. Researchers are actively pursuing studies to better understand the complex genetic contributions, environmental contributions, and symptoms associated with SCZ. The symptoms of this mental disorder fall roughly into two categories, the positive symptoms, typically accompanying a psychotic episode are more strikingly abnormal and include paranoia, hallucinations, delusions, disordered thoughts, whereas the negative symptoms reflect the absence of normal behaviors including social withdrawal, flat affect, lack of motivation and poor attention span [99]. In the 1950-1960s researchers found that a group of drugs, termed “typical antipsychotics” including phenothiazines (chlorpromazine), butyrophenones (haloperidol), and thioxanthenes, successfully treated the positive, psychosis related symptoms of SCZ [110-112]. More recently a second class of drugs termed “atypical antipsychotics” (including the dibenzodiazepine, clozapine) were employed to treat the negative and cognitive symptoms of patients with SCZ [113]. Originally, both classes of antipsychotics were prescribed based on treatment efficacy without truly understanding the mechanism of action by which these drugs alleviated the symptoms of SCZ, however the side effects of these drugs, including Parkinsonian-like movement alterations (Tardive dyskinesia), indicated a role for dysregulated DA signaling in the symptomology of SCZ. Pioneered by Carlsson, researchers determined that many

antipsychotic agents block DA receptors (typical antipsychotics have high affinity for the D2-type receptors, whereas the atypical antipsychotics bind effectively to D3 and D4 receptors) which lead to the DA hypothesis of SCZ, that excess DA neurotransmission underlies, at least in part, the pathology and symptoms of SCZ [31, 114-116]. Post-mortem studies provide additional evidence for pre- and post-synaptic DA changes in SCZ patients. For example, early studies provided evidence for increased levels of striatal DA [117], and more recently, TH levels, determined by TH specific immunostaining, were found to be significantly increased in the SNc of SCZ patients compared to controls [118]. A clear association between the D2R gene (DRD2) and SCZ has been supported by extensive research demonstrating increased D2R densities in post-mortem samples from patients [119, 120], DRD2 gene polymorphisms as a genetic risk factor for SCZ [121, 122], and *in vitro* data showing a significant increase in the expression of D2R homodimers compared to controls [123, 124]. In addition to post-mortem studies, PET and SPECT imaging studies over the past 25 years or so allowed researchers to quantify DA function and signaling in SCZ patients and controls *in vivo.* In summary, neuroimaging studies provide evidence that 1) following radioactive L-DOPA analog intake capacity demonstrates increased DA synthesis in SCZ patients [125-127], 2) there is no significant evidence for altered DA reuptake via DAT in SCZ patients [128-130], and 3) imaging studies using radio-labeled ligands demonstrates increased D2 receptor density in SCZ patients versus controls [131]. Though research studies provide clear evidence that dopaminergic transmission abnormalities contribute to the pathology of SCZ, especially the psychosis associated with the positive symptoms, other neurotransmitters such as Glu are emerging as important contributors to schizophrenia.

Anatomy of DA Neurons in *C. elegans*

Comparable to their mammalian counterparts, the DA neurons of the nematode, *Caenhorhabditis elegans*, are well-described and adopt stereotypical morphology and neuronal connections. As a catecholamine derived from the amino acid tyrosine, DA can be cross-linked with formaldehyde to produce formaldehyde-induced-fluorescence (FIF), that can be detected as a green fluorescent color in areas or cells where catecholamines are present [132]. As *C. elegans* does not contain the other major mammalian catecholaminergic neurotransmitter, NE, the FIF method could be employed to identify the DA neurons of the worm. Pioneering work by Sulston and colleagues utilized the FIF technique to characterize DA neurons in the nematode [133]. This study revealed two bilaterally symmetric pairs of neurons in the nerve ring, with their cell soma residing between the anterior and posterior bulbs of the pharynx and DA dense “dendritic” projections reaching the cephalic sensilla at the tip of the worm proboscis and “axonal” projections terminating at the nerve ring. These morphological features, paired with electron microscopy (EM) reconstruction, identified these DA neurons as the cephalic neurons (CEPs) in the hermaphrodite Fig. 5 [134]. The EM reconstruction studies by Ward and colleagues also describe the glial-like cells that ensheath the CEP neuron dendritic processes and nerve ring (CEPsh), and the glial-like socket cells that form a channel around the CEP dendrites in the lips of the nematode (CEPso) [135]. The CEP neurons have since been show to make synaptic connections at the nerve ring with neurons such as the interneurons RIA and RIB as well as the motor neurons RIV, SIA, SIB, and SMB which are described as important for *C. elegans* navigation [136]. Another

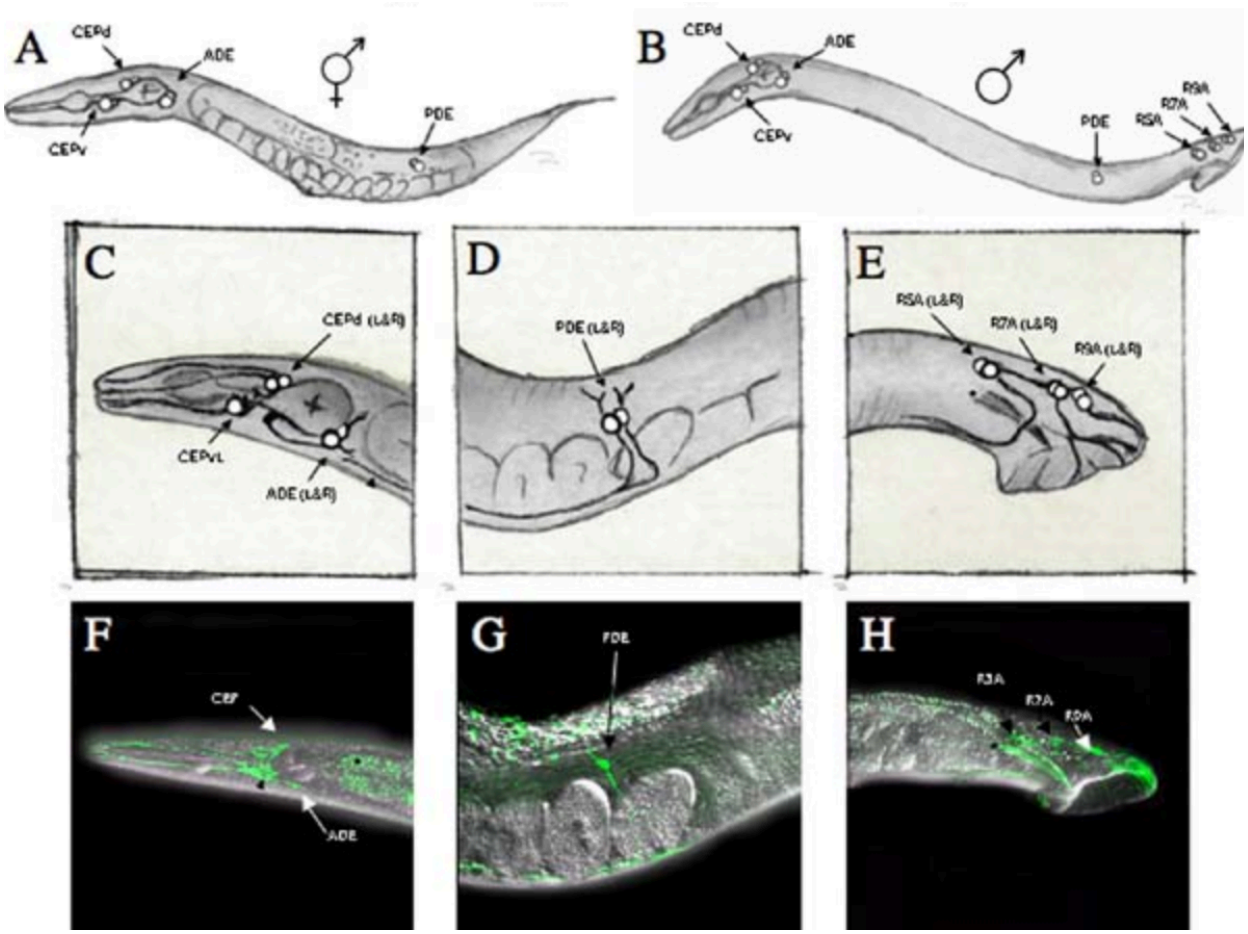

Fig. 5. *C. elegans* DA system. A. A cartoon diagram of an adult *C. elegans* hermaphrodite demonstrating the anatomical location of the DA neurons. B. A cartoon diagram of an adult *C. elegans* male demonstrate the anatomical location of the DA neurons, including the specific male tale DA neurons. C. Enlarged view of the DA neurons located in the head (4 CEP and 2 ADE) of adult hermaphrodites and males. D. Enlarged view of the DA neurons located in the midbody (2 PDE) of adult hermaphrodites and males. E. Enlarged view of the 6 DA neurons (3 pairs, R5A, R7A, R9A) located in the male tail. F-H. Representative confocal images with DIC overlay of adult worms expressing DA neuron specific GFP ($p_{dat\text{-}1}$::GFP), to show the anatomical location of the CEP and ADE neurons (F), the PDE neurons (G), and the male tail DA neurons (H). (Image from McDonald and Blakely, 2006).

pair of DA neurons were identified with ventral “axonal” processes ending just posteriorly to the nerve ring and dorsal “dendritic” processes ending at the deirid pore, denoting these as the anterior deirid neurons (ADE). The ADE neurons make synaptic connections with neurons associated with touch response (ALM, AVA, and AVD) [137]. In the body of the hermaphrodite another pair of neurons were shown to be FIF+, with soma near the vulva and projections in close proximity to the ventral nerve cord, recognized as the posterior deirid neurons (PDE) however little is known about their synaptic connections. The ADE and PDE neurons also form sensillum consisting of a DA neuron, an enseathing glial cell, and a socket glial cell, ADEsh/ADEso cells and PDEsh/PDEso cells respectively [135]. *C. elegans* males were shown to have three FIF+ pairs of neurons in the sensory ray of the mail tail [133]. In total, the *C. elegans* hermaphrodite has eight DA neurons and the male has an additional six DA neurons in the male tail as shown in Fig. 5. Identification of DA neuron specific genes such as the DA transporter, *dat-1,* [138] coupled with the use of promoter fusions with fluorescent proteins (i.e. GFP), confirmed the DA neuron identifications described by Sulston.

The Glia of the *C. elegans* DA Neuron Sensillum

As briefly described above, the DA neurons of *C. elegans* are all associated with ensheathing glial cells (CEPsh, ADEsh, and PDEsh) and socket support glial cells (CEPso, ADEso, PDEso) [135]. Previously, the morphology and anatomy of these and other glial cells were only briefly described in the nematode in terms of their proximity and ensheathment of sensory neuron dendrites (sheath cells) or the presence of socket cell within the sensillum of sensory neurons (Fig. 6) [139][135]. However, over the past

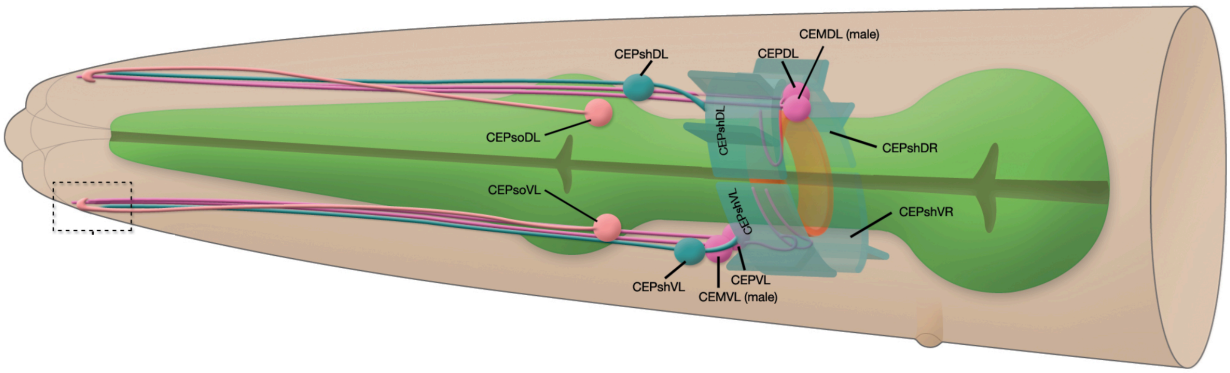

Fig. 6. Cells of the cephalic sensilla. The cartoon rendition above depicts the cells of the left side cephalic sensillar cells. The CEM cells are only found in males. The four CEP DA neurons are located close to the nerve ring, with dendrites sent to the lips of the nematode, and axons projects into the nerve ring to make synaptic connections. CEPsh glial cells reside in close apposition to the CEP neurons, and ensheath the CEP dendrites and send sheet like processes to surround the nerve ring. The CEPso glial cells are just posterior to the anterior bulb and create a pore like structure at the ciliated dendritic ending of the CEP neurons. (Figure adapted from wormatlas.org, Altun and Hall, 2010).

decade, studies indicate that the 50 glial cells associated with sensory organs of the nematode play important functional roles in the *C. elegans* nervous system (reviewed by Shaham [140]). Using laser ablation techniques [141], Yoshimura and colleagues specifically ablated the CEPsh glia of the worm at an early larval stage and determined that ablation of these cells does not cause overt CEP neuronal death making the nematode an excellent model to study, *in vivo,* the effects of perturbed glial support on DA neuron morphology and function (Fig. 6) [142]. The authors determined that loss of these glia resulted in truncated CEP neuronal dendrites, abnormal axon guidance and branching of other sensory neurons leading to defects in the nerve ring [142]. Further studies demonstrate that disruption of CEPsh glial cell specification, via genetic mutation of the CEPsh specific gene, *hlh-17,* encoding a Helix-Loop-Helix transcription factor, results in defects in CEP neuron mediated behaviors including egg-laying, feeding, and impaired gustatory learning [143-145]. More recently, as described below, Hardaway and colleagues characterized a novel glial-expressed gene, *swip-10*, that regulates DA neuron excitability and hyperdopaminergia via a glutamate dependent mechanism [146]. Although not yet described for the glial support of CEP neurons, other nematode glial cells have been shown to support normal neuronal excitability and function via mechanisms including ion buffering, acid sensing, and pH buffering [147-150]. These studies present the nematode as a model organism to study modes of support and communication between glia and DA neurons and the importance of glia for proper neuronal morphology, neuronal function and normal downstream behavioral outcomes.

Molecular Regulation of DA Signaling in the Nematode

In addition to characterizing the CEP, ADE, and PDE neurons as dopaminergic, Sulston and colleagues also initiated the groundwork for identification of DA neuron signaling genes in *C. elegans.* Using a chemical mutagen, Sulston performed a forward genetic screen and identified six mutants with altered FIF, which he named as catecholamine deficient (*cat-1* through *cat-6)* [133].

The first of these mutants, *cat-1,* (shown to have reduced FIF and DA levels), was cloned by Duerr and colleagues and identified as the *C. elegans* vesicular monoamine transporter (VMAT2) homolog [151]. This work determined that *cat-1* was expressed in the DA neurons, localized to synaptic vesicles, and transported biogenic amines (DA and 5-HT) *in vitro.* Mutation to *cat-1* altered nematode behaviors such as locomotion, and these defects were rescued by expression of human VMAT2.

The second of these mutants, *cat-2,* (shown to have reduced FIF and DA levels) was cloned and characterized by Lints *et al.* as the *C. elegans* tyrosine hydroxylase (TH) homolog and was the first *C. elegans* gene identified within the DA biosynthetic pathway [152]. This study was the first to use GFP promotor fusions to show a DA neuron specific gene was expressed selectively in FIF+ cells, and that transgenic expression of wildtype *cat-2* fused to GFP (*cat-2*:GFP) restored FIF in *cat-2* mutants.

cat-4, also initially described in Sulston's original screen, is another gene identified in relation to the DA biosynthetic pathway [133]. Encoding an enzyme, GTP cyclohydrolase, *cat-4* catalyzes the biosynthesis of tetrahydrobiopterin, a critical cofactor in the decarboxylation of the biogenic amine precursors, levadopa (L-DOPA) and 5-hydroxytryptophane (5-HTP). The aromatic amino acid decarboxylase (AADC) that

converts L-DOPA to DA and 5-HTP to 5-HT, was identified as *bas-1* in the nematode [153, 154]. These studies verified the conservation of DA biosynthesis pathways from worm to man. The degradation and catabolism of DA in the worm is also conserved, as demonstrated by the identification of monoamine oxidase (MAO) and catechol-*o*-methyltranferase (COMT) homologs in the *C. elegans* genome and the presence of DA catabolites found in whole worm extracts [155].

As in mammals, DA signaling in the worm is primarily terminated by the clearance of extracellular DA by the DA transporter (DAT), DAT-1*,* in *C. elegans.* Jayanthi and colleagues cloned the nematode DAT homolog using homology-based oligonucleotide plaque hybridization [138]. Using heterologous cell expression methods and pharmacological techniques, they determined that the protein product of the cloned gene, T23G5.5, preferentially transported DA and is highly homologous to the human NE transporter (NET). With no NE in the worm, and the ability of known DAT and NET antagonists to inhibit the transport activity of T23G5.5, the authors named this gene as *dat-1,* encoding the *C. elegans* DA transporter. Further support of *dat-1* as the worm DAT homolog was provided when Nass et al. determined that the *dat-1::*GFP transgene was selectively expressed in DA neurons *in vivo* (Fig. 5) [52]. The strain created by Nass et al, BY200, and the successively created brighter fluorescent transgenic strain, BY250 [156], are now used by multiple labs to visualize the morphology of the *C. elegans* DA neurons [157-159]. Nass and colleagues also demonstrated *in vivo* that DAT-1 was required for 6-hydroxydopamine (6-OHDA) (a known DAT substrate) transport and toxicity, such that following treatment with 6-OHDA the DA neurons in wildtype animals selectively degenerated, whereas *dat-1* mutant animals were protected against toxicity

[52]. The high conservation of presynaptic genes required for DA signaling, such as *cat-1, cat-2,* and *dat-1,* demonstrates the importance of DA signaling across phylogeny (Fig. 7) [160].

As important DA signaling genes were being cloned using traditional techniques, such as those used to identify *dat-1,* the initial publication of the *C. elegans* and human genomes allowed researchers to employ bioinformatics techniques to identify conserved genes that contribute to DA signaling. For example, these methods allowed the identification of four DA receptors in the worm, *dop-1, dop-2, dop-3,* and *dop-4* (Fig. 7). First, Suo and colleagues identified *dop-1 and dop-2,* two *C. elegans* DA receptors [161]. Heterologous expression studies paired with radiolabeled ligand displacement assays, indicated that *dop-1* and is a D_1-type DA receptor. In contrast, heterologous expression studies and ligand binding assays indicated preferential binding of DA to *dop-2* which resulted in inhibition of cAMP production. Together, with the promoter fusion expression of *dop-2* in neurons of the nerve ring as well as presynaptic expression in DA neurons, *dop-2* is likely both a post-synaptic D2-like receptor and the *C. elegans* DA autoreceptor. Chase and colleagues again utilized sequence homology to identify another putative *C. elegans* D_2 receptor, *dop-3*, and soon thereafter *dop-3* was validated as a DA receptor by Suguira et al [162, 163]. In GFP promotor fusion transgene studies, Chase determined the expression patterns for *dop-1 and dop-3.* As predicted, both DA receptors were expressed post-synaptically, with *dop-1* expressed in cholinergic neurons and the mechanosensitive PVD touch neuron, and *dop-3* expressed in the motor circuit including cholinergic and GABAergic neurons and expressed in the body wall muscle in addition to the PVD neuron as well [164]. Sugiura and colleagues also identified another putative

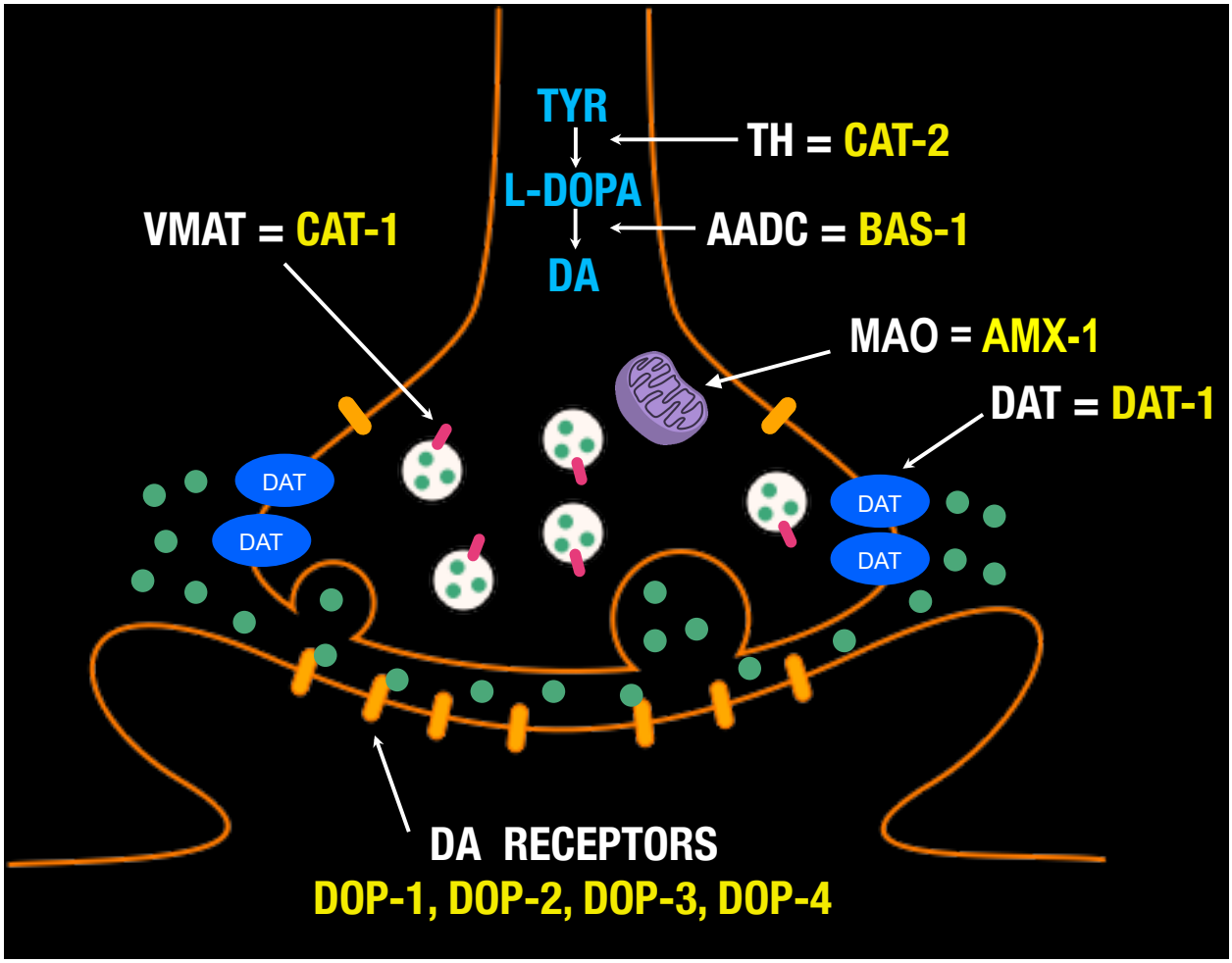

Fig. 7. Conserved DA signaling genes in *C. elegans.* This cartoon depicts the pre- and post-synaptic DA signaling genes conserved from the nematode to man. Although the schematic shows a "typical" tight synapse, DA signaling also occurs distally from synaptic release. DA receptors are expressed on interneurons, and the cholinergic and GABAergic neurons in the ventral nerve cord of the nematode, as well as DOP-2 expressed as an auto-receptor on DA neurons. (Adapted from Nass and Blakely, 2003).

C. elegans DA receptor, *dop-4,* a D_1-type receptor that increased production of cAMP with post-synaptic expression in neurons (ASL, ASG, CAN, and PQR) and non-neuronal cells (rectal epithelial cells, male tail, and vulva) [163].

In summary, molecular determinants and genes involved in DA signaling are highly conserved from worm to man (Fig. 7). Presynaptically, the *C. elegans* genome contains the genes required for the biosynthesis, vesicular packaging, and clearance of DA. Postsynaptically, DA signals in the nematode via conserved D_1- and D_2- type DA receptors (*dop-1/dop-4* and *dop-2/dop-3* respectively).

DA Regulation of Phenotypes and Behaviors in *C. elegans*

The identification of conserved DA signaling-related genes in the worm was critical to understanding the molecular determinates of DA signaling, and these genes have since been manipulated to better understand phenotypes and behaviors dependent on DA signaling. Extensive genetic and pharmacological studies, to either elevate or reduce DA signaling, implicate DA signaling in the modulation of many *C. elegans* behaviors, including locomotion, defecation, touch-habituation, egg-laying, and foraging [134, 165]. While DA plays an important role in all of these behaviors, I will focus selectively on DA regulation of *C. elegans* locomotion-related behaviors.

Early studies established that neurotransmitters, including 5-HT and octopamine, could inhibit nematode locomotion [166], and work by Schafer and Kenyon first described that exogenous DA could inhibit worm locomotion [167]. Subsequent work by Sawin and colleagues examined the role of DA in the context of a normal endogenous behavior. This study demonstrated that the observed behavior of healthy, fed worms slowing their rate

of locomotion as they enter a lawn of bacteria (termed a basal slowing response, BSR) is dependent on DA signaling as loss of *cat-2* results in defective BSR [154]. The authors further corroborate this findings by showing that exogenous DA treatment can restore normal BSR to *cat-2* mutant animals, and they used partial or complete laser ablation of the DA neurons to demonstrate that the DA neurons act redundantly to mediate BSR, with the CEP neurons most strongly associated with a strong BSR response. Sawin et al. suggests that mechanosensation, as the worms come into contact with the bacteria, might trigger stimulation of the DA neuron dendrites as mechanical stimulation alone via a matrix of glass beads also produced BSR.

As the important regulators of DA signaling in the nematode were being characterized, such as the cloning of the DA receptors, these DA dependent behaviors, locomotion inhibition/paralysis and BSR, became important to understanding the mechanism of DA's role in controlling locomotion. Chase and colleagues found that loss of the D2-like receptor, *dop-3*, abolished BSR, and transgenic restoration of *dop-3* restored this behavior, whereas genetic loss of the D1-like receptor, *dop-1,* restored normal BSR to *dop-3* mutant animals [162]. This study used DA sensitivity to determine that these receptors function antagonistically to promote a paralysis response to exogenous DA and normal BSR. *dop-1*, in GABAergic motor neurons, acts through the G-protein *egl-30* and downstream effector phospholipase Cβ, *egl-8*, while *dop-3* acts through the G-protein *goa-1* and downstream effector *dgk-1.* More recently, researchers utilized the DA-dependent BSR behavior to identify other genes that regulate DA signaling. For example, it was determined loss of nematode neuroligin (*nlg-1*), a postsynaptic cell adhesion protein critical for synaptic formation and function, resulted in

impaired BSR and increased expression of *comt-4,* the worm ortholog of COMT, and one of the known enzymes responsible for DA degradation [168, 169]. These studies showed that RNAi knockdown of *comt-4* restored normal BSR in *nlg-1* mutants, suggesting that neuroligin in the worm regulates DA related behavior.

As in mammalian systems, complex behaviors in the nematode, such as a locomotor response to various stimuli, are not controlled by one neurotransmitter in isolation, rather require the precise coordination of many neurotransmitters and neuropeptides. A study by Hills, Brockie, and Maricq described the DA and glutamate (Glu) regulated locomotor behavior, area restricted search (ARS) such that *C. elegans* (and other animals) will turn more frequently after finding food to restrict their search area to that location and after food depletion, animals turn with less frequency, moving more linearly, to explore new areas [170]. They show that DA plays a role in ARS as loss of *cat-2,* DA neuron ablation, or treatment with the DA receptor antagonist raclopride inhibits ARS, and exogenous DA restores normal ARS behavior. Further characterizing this phenotype, they show that genetic disruption of the ionotropic Glu receptors, *glr-1* and *glr-2,* results in failure to show ARS. The authors suggest that DA may directly modulate downstream glutamatergic signaling or that DA and Glu may act in parallel to control this behavior.

Locomotor habituation to a tap stimulus, ranging from short-term to long-term memory, requires the precise coordination of DA, Glu and other neuro-signaling molecules in the worm, emphasizing the importance of dynamic neural signaling molecules to allow flexible signaling potential. Researchers found that DA signaling modulates short-term tap-habituation. Kindt and colleagues demonstrated that loss of

dop-1 caused animals to habituate more rapidly in the presence of food in a paradigm of short term habituation with a short inter-stimulus interval (ISI) [171]. To further establish a role for DA in habituation, the authors also showed that animals with genetic loss of *cat-2* and mutation to the downstream effectors of *dop*-1, such as *elg-8,* display a more rapid habituation than wildtype animals. In keeping with a role for DA modulation of short term habituation, Kindt et al. revealed that genetic loss of *dat-1* slowed the time it took for animals to habituate to a tap stimulus presented with a short ISI. Glu signaling was also hypothesized to play a role in the molecular mechanism of habituation, and studies conducted by Rankin and Wicks confirmed that mutation to the vesicular Glu transporter, *eat-4,* results in animals that significantly habituate more rapidly than wildtype counterparts and *eat-4* mutant animals did not experience dishabituation like wildtype animals [172]. In contrast, other studies indicated that Glu signaling contributes to the long-term memory component of tap-habituation. Rose and colleagues first determined that *eat-4* mutants did not show capacity for long-term tap habituation, and subsequently corroborated a role for Glu signaling in *C. elegans* long-term habituation as genetic loss of the AMPA-type, ionotropic Glu receptor (iGluR), *glr-1*, and pharmacological blockade of iGluRs prevented animals from showing long-term memory [173, 174]. The described work shows that *C. elegans* are able to alter their locomotor response to a stimulus in a simple learning related behavior, and these studies uncovered that DA and GLU are required for overlapping and distinct aspects of this behavior. Though researchers identified the foundational molecular mechanisms driving tap-habituation, reviewed by Giles and Rankin [175], it is clear that this behavior is actually quite complex, and involves many neuro-signaling molecules in the worm.

Chapter II

IDENTIFICATION AND CHARACTERIZATION OF NOVEL REGULATORS OF DA SIGNALING IN *C. elegans*

Identification of Swimming Induced Paralysis Phenotype

The previous work describing DA signaling in the worm relied heavily on the use of genetic mutation of DA-related genes and the response of mutant animal locomotion to exogenous DA, supporting an extrasynaptic role for DA signaling in the worm. Despite the demonstrated role of *C. elegans dat-1,* in DA re-uptake and the neurotoxic action of 6-OHDA, loss of *dat-1* had no major effect on nematode locomotion on plates. Tangentially to investigations of an endogenous behavioral role for *dat-1,* we found that mutation of the presynaptic choline transporter, *cho-1,* resulted in animals displaying deficits in sustaining normal swimming behavior [176]. Our lab therefore hypothesized, given the critical role DA in nematode locomotion, that *dat-1* contributes to *C. elegans* locomotor behavior in different behavioral context. McDonald and colleagues described that loss of *dat-1* resulted in a rapid, complete paralysis of swimming locomotion in water, whereas wildtype counterparts sustained normal swimming or thrashing behavior for 10 minutes [177]. The paralysis behavior of *dat-1* animals was aptly termed, Swimming induced paralysis, or Swip. The authors further verified that the *dat-1* Swip was dependent on DA signaling as genetic disruption of DA synthesis, by loss of *cat-2,* completely restored normal swimming behavior in *dat-1* mutants. Furthermore, *dat-1* Swip is dependent on DA signaling solely via DOP-3 as loss of *dop-3* restores normal swimming behavior completely, despite evidence that the transition from swimming to crawling

requires DOP-1 and DOP-4 [178]. Additionally, McDonald and colleagues determined that the Swip phenotype of *dat-1* mutants was suppressed by pharmacological disruption of DA signaling utilizing the *cat-1* (vMAT2 in mammals) inhibitor, reserpine. Critically, the authors utilized transgenic animals to demonstrate that restoring *dat-1* expression in the DA neurons of mutant animals rescued the Swip phenotype, therefore supporting the role of DA clearance via *dat-1* in normal *C. elegans* swimming behavior.

Forward Genetic Screen for Novel Regulators of DA Signaling in *C. elegans*

The Swip phenotype represented a behavior mediated by endogenous DA well suited to further elucidation of the pre- and post-synaptic regulators of DA signaling in *C. elegans.* Forward genetic mutagenesis screens following a particular behavior or phenotype have been extensively utilized in the worm to identify novel, conserved genes [179]. Hardaway and colleagues implemented the fast, highly reproducible Swip phenotype in a forward genetic screen to identify novel regulators of DA signaling in the worm. As described in Fig. 8A [180], L4 staged BY200 (P_{dat-1}:GFP) animals (serving as wildtype) were chemically mutagenized by ethyl methanesulfonate (EMS) to generate random mutations across the genome of their progeny. Second generation (F2) progeny were tested for the Swip behavior, and those at least showing 80% paralysis were cloned to determine the persistence and the penetrance of Swip in the F3 progeny. Mutants that displayed abnormal locomotion on solid substrate were discarded to reduce the probability that the recovered mutants shared control of molecular signaling with other neurotransmitters, such as GABA or ACh. In order to isolate mutants that displayed DA-

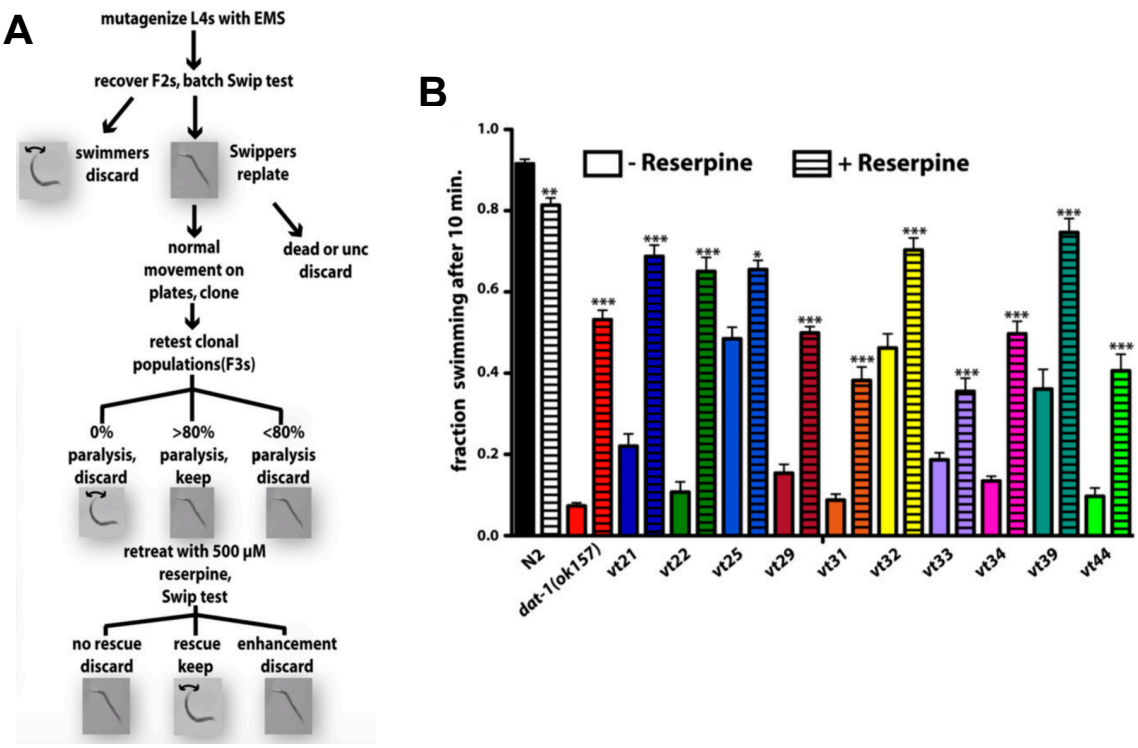

Fig. 8. Implementing a forward genetic screen to identify novel *C. elegans* mutants displaying reserpine-sensitive Swimming induced paralysis, Swip. A. Schematic depicting the forward genetic mutagenesis screen using the hyperdopaminergic, reserpine-sensitive phenotype, Swip, to identify novel regulators of DA signaling in *C. elegans*. Animals that did not reproduce, displayed gross morphological differences from N2, or uncoordinated movement on plates were discarded. B. After three rounds of outcrossing, the forward genetic screen yielded 10 novel mutants (*vt)* that retained reserpine sensitive Swip. (Adapted from Hardaway, 2012).

dependent Swip, a tertiary screen tested for Swip reversal after reserpine incubation [177]. Ten mutant lines with penetrant, reserpine-sensitive Swip after 3X outcrossings were discovered in this initial forward genetic screen (Fig. 8B) [180]. Genetic validation of the Swip DA-dependence observed in the novel mutant alleles was determined by Swip reversal after crossing to *cat-2* and/or *dop-3* mutant animals.

This screen revealed two novel point mutation alleles in the DAT-1 gene that cause robust DA dependent Swip similar to the canonical *dat-1* loss of function allele, *ok157.* These findings attest to the validity of the designed forward genetic screen based on the Swip phenotype to identify critical regulators of DA signaling in the worm. One of these *dat-1* alleles, *vt21,* contains a non-conservative missense mutation while the other allele, *vt22,* harbors a nonsense mutation resulting in a truncated DAT-1 protein. Hardaway and colleagues further characterized two mutant lines, *vt25* and *vt29,* (of the original ten identified in the screen) that possess mutations in genetic loci independent of one another and independent of other known regulators of DA signaling. Like *dat-1* mutants, the Swip phenotype of both *vt25* and *vt29* is reserpine sensitive and *cat-2* and/or *dop-3* mutation restores normal swimming behavior [180]. The authors utilized automated thrashing analysis to determine that the Swip of these two mutant alleles does differ from *dat-1*, in measures of latency to paralysis and paralysis reversal events. Further characterization of *vt29* revealed that the mechanism of Swip arises via a parallel pathway to *dat-1* as *vt29* demonstrates normal sensitivity to the DA neuron specific toxin 6-OHDA, and *dat-1;vt29* mutant animals display an additive Swip phenotype at various solution osmolarities. Both of these novel regulators of DA signaling, as well as the other uncharacterized mutant lines discovered in the forward genetic screen conducted by Hardaway et al. can be

targeted in future studies to further elucidate conserved regulators of DA signaling and reveal insight into brain disorders associated with altered DA signaling.

Characterization of the Novel, Glial-Expressed Regulator of DA Signaling in the Nematode, *swip-10*

After identifying novel mutant lines that demonstrate DA-dependent Swip, Hardaway and colleagues sought to further characterize the molecular basis by which the disrupted genes regulate DA signaling. In these efforts, we determined that two non-complementing alleles, *vt29* and *vt33*, harbored a nonsense and missense mutation respectively in the same gene, *F53B1.6*, which we termed *swip-10* [146]. Genetic disruption of DA signaling via either *cat-2* or *dop-3* mutation restores all available *swip-10* mutation alleles, *vt29, vt33,* and the deletion allele *tm5915,* to wildtype swimming behavior, indicating that genetic disruption to *swip-10* results in DA-dependent Swip. Interestingly, *swip-10* exerts its control of DA signaling in a cell non-autonomous mechanism; through transgenic promotor fusions, we showed that *swip-10* is expressed in the epidermis and uterine muscle cells in early developmental stages (L1 and L2), and in later development (L4) and adult stages *swip-10* is predominately expressed in the glial-like support cells of the worm (Fig. 9) [146]. Glial-specific rescue experiments also determined that *swip-10* paralysis is rescued via wildtype *swip-10* expression under a pan-glial promoter, P_{ptr-10}.

As *swip-10* was previously shown to act in a parallel pathway to *dat-1* by Hardaway and colleagues (Hardaway, 2012), we hypothesized that *swip-10* acts in glia to regulate DA neuron excitability and thus modulates DA release and downstream signaling. Using

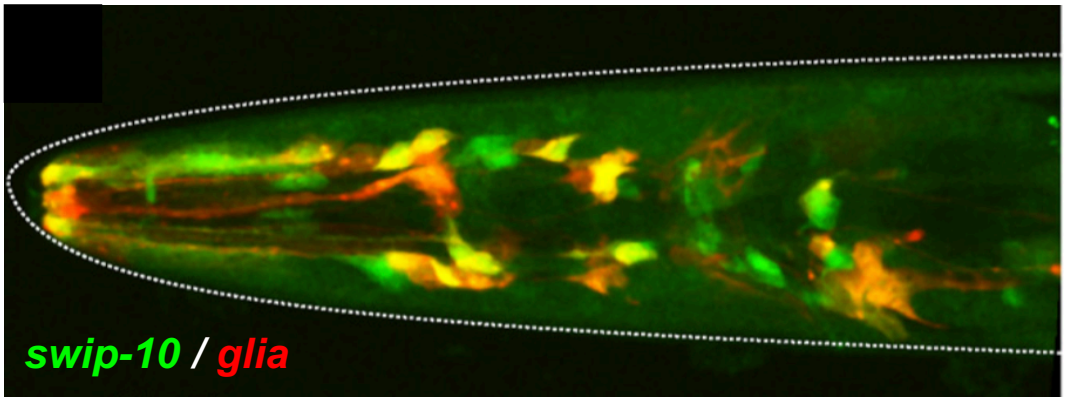

Fig. 9. *swip-10* is expressed in the glial cells of the nematode. The *swip-10* transcriptional reporter, $p_{swip-10}$::GFP, co-localized in multiple cells labeled by the pan-glial transcriptional reporter, p_{ptr-10}*::myrRFP.* (Adapted from Hardaway, 2015).

a fluorescence recovery after photo-bleaching (FRAP) approach, we assessed the rates synaptic vesicle fusion with the plasma membrane specifically in the nematode DA neurons and determined that *swip-10* mutants display increased DA vesicular fusion rates or hyper-DA secretion than N2 counterparts (Fig. 10A-B) [146]. To further support our hypothesis, *in vivo* DA neuron specific Ca^{2+} imaging revealed that the DA neurons of *swip-10* mutants are hyper-excitable by the presence of food, and that glial expression of *swip-10* is sufficient to restore normal DA neuron excitability (Fig. 10C-D) [146]. Knowing the importance of mammalian glia in the tight regulation of extracellular and synaptic Glu levels and Glu being the primary excitatory neurotransmitter in worms and man, we hypothesized that *swip-10* acts in glia to control neuronal excitation by maintaining normal extracellular Glu homeostasis in the worm. In support of this hypothesis, we demonstrated that genetic disruption of Glu signaling via loss of the well characterized Glu vesicular transporter, *eat-4,* or loss of the Glu receptors, *glr-4, glr-6* and *mgl-1,* suppress the Swip phenotype of *swip-10* mutant animals (Fig. 11A and 11B) [146]. Additionally, we showed that loss of select plasma membrane Glu transporters was sufficient to drive DA-dependent Swip (Fig. 11C) [146]. In our study, we provided a model for the mechanism of *swip-10* hyperdopaminergia dependent on extra-synaptic Glu signaling such that the Swip phenotype of *swip-10* mutants arises due to excess extracellular Glu signaling that results in increased DA neuron excitability and hyper-secretion of DA beyond the clearance capacity of *dat-1,* allowing hyperdopaminergic signaling on *dop-3* to result in Swip (Fig. 12) [146].

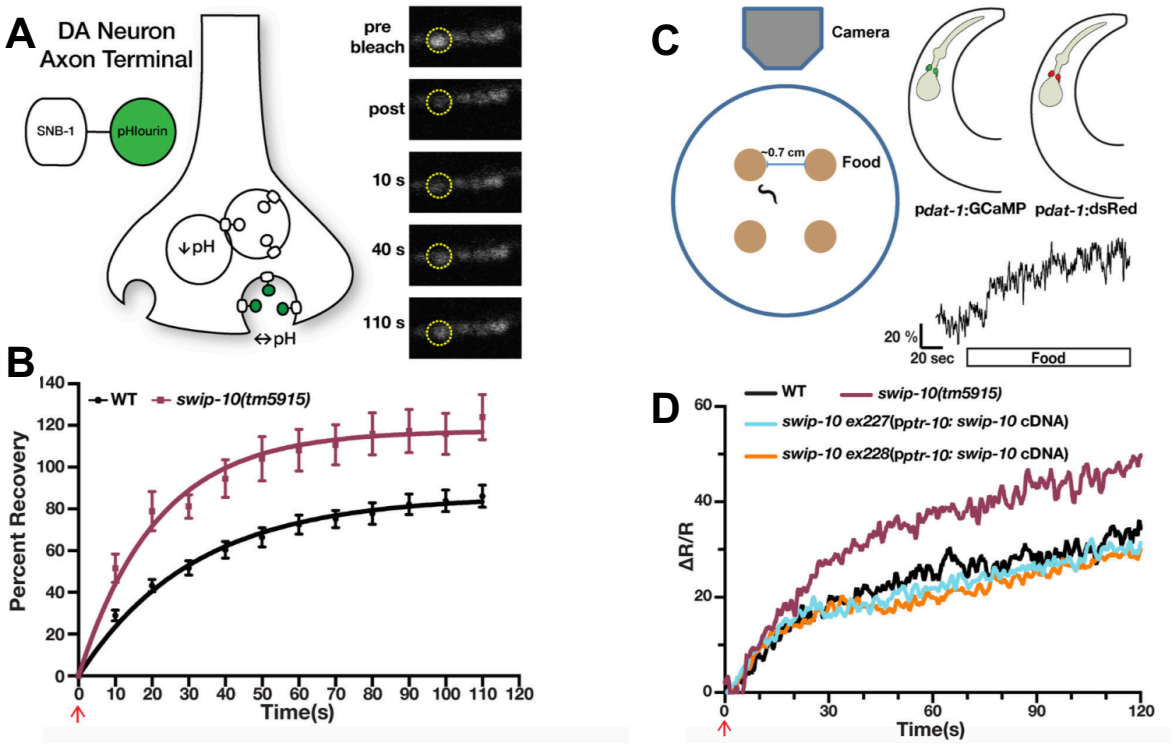

Fig. 10. Loss of *swip-10* results in increased rates of DA vesicular release and elevated DA neuron excitability. A. Schematic describing the fluorescence recovery after photo-bleaching (FRAP) experiment designed to examine DA vesicular fusion rates. B. Loss of *swip-10* results in significantly elevated rate of fluorescence, indicating a more rapid rate of DA vesicular release. C. Schematic describes the *in vivo* Ca^{2+} imaging experiment design used to determine DA neuron specific activity in the context of response to a food stimulus using radiometric value, comparing Ca^{2+}-sensitive GFP to a stable non-Ca^{2+}-sensitive RFP. D. Food triggers an increase in DA neuron activity, and this response is significantly elevated in *swip-10* mutants, and glial-specific expression of *swip-10* (blue and orange) restores *swip-10* mutant DA excitability to N2 levels. (Adapted from Hardaway, 2015).

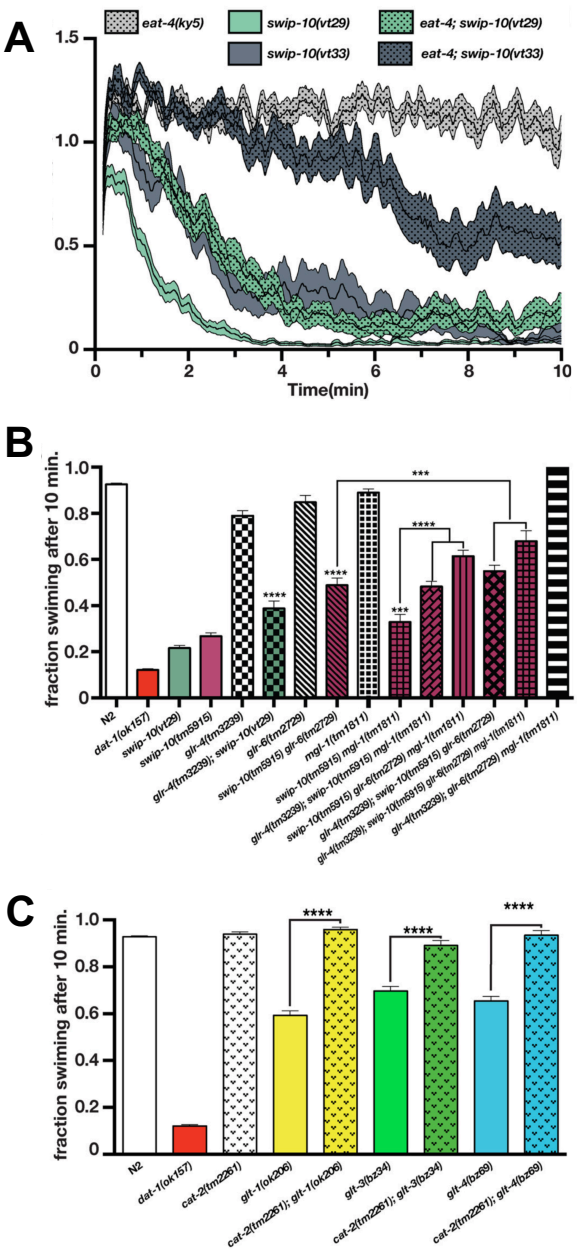

Fig. 11. *swip-10* paralysis is dependent on glutamate signaling and loss of glutamate clearance results in DA-dependent Swip. A. *swip-10* mutant animal Swip behavior is suppressed by loss of the vesicular Glu transporter, *eat-4*, as determined by automated thrashing analysis. B. Manual Swip assays determined that loss of the Glu receptors, *glr-4, glr-6,* and *mgl-1*, significantly (and additively) suppress *swip-10* paralysis. C. Manual Swip assays determined that loss of the plasma membrane Glu transporters, *glt-1, glt-3,* and *glt-4* result in significant DA-dependent Swip as loss of *cat-2* restores normal wildtype swimming behavior in these mutants. (Adapted from Hardaway, 2015).

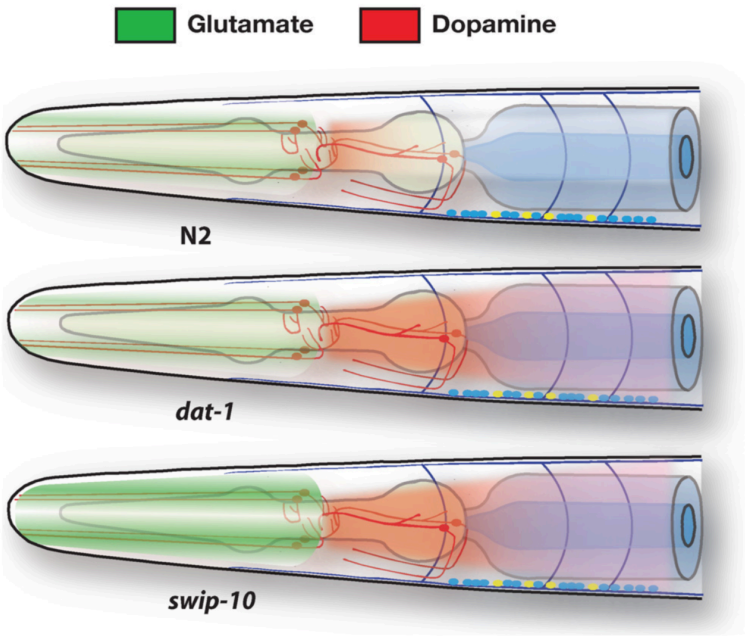

Fig. 12. Model for *swip-10* mutant, Glu-signaling dependent hyperdopaminergia. Cartoon illustration depicting the hypothesis that *swip-10* hyperdopaminergia induced Swip arises due to a glial dependent increase in extrasynaptic Glu driving increased DA neuron excitability and increased DA secretion, overwhelming normal DA clearance via DAT-1 to result in excessive activation of DA receptors (DOP-3) expressed on cholinergic motor neurons resulting in DA-dependent Swip. (Adapted from Hardaway, 2015).

Conservation of SWIP-10 as the Mammalian Metallo-β-Lactamase Domain Containing Protein, MBLAC1.

In our efforts to characterize the *C. elegans* SWIP-10 protein, we employed an *in silico* protein database search approach and discerned that SWIP-10 contains a metallo-β-lactamase domain (MBD) in the protein's C-terminus. We found this domain to be highly conserved across phylogeny and identified the mammalian ortholog, MBLAC1. Furthermore, the two *swip-10* point mutation alleles (*vt29* and *vt33)* from the aforementioned screen are conserved within the MBD domain (Fig. 8 and Fig. 13) [146]. The MBD derives its name from the prokaryotic enzymes containing conserved amino acid residues that form the active site required for the coordination of metal ions (such as Zn^{2+}) and water molecules to aid in the hydrolysis of β-lactam antibiotics such as penicillin [181]. Though we hypothesize that SWIP-10 and MBLAC1 function enzymatically to hydrolyze a substrate, the specific target of these enzymes is currently unknown. However, we recently determined that MBLAC1 is a specific, high-affinity target for the neuroprotective β-lactam antibiotic, ceftriaxone (Cef) [182]. Retzlaff and colleagues utilized an MBLAC1-specific polyclonal antibody to determine that MBLAC1 is expressed throughout the mammalian brain and using fractionated mouse fibroblasts, further show that MBLAC1 is localized within the cytosol [182]. Using two independent techniques, affinity capture with cyanogen bromide immobilized Cef and backscattering interferometry with freely-mobile, unmodified Cef, Retzlaff and colleagues demonstrate that MBLAC1 is a high affinity binding partner of Cef in the CNS (K_D=2.2 μM) [182]. Retzlaff provides further evidence that MBLAC1 is potentially an exclusive binding partner for Cef as binding activity in mouse brain lysates was totally eliminated by MBLAC1

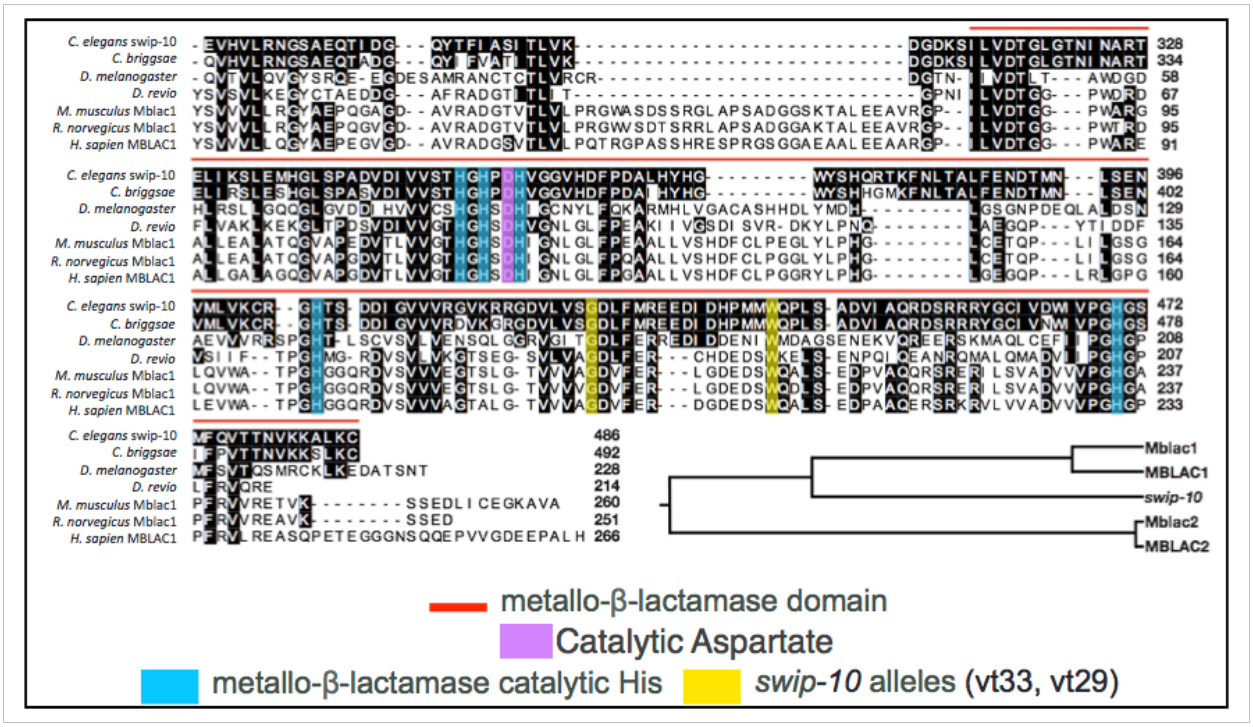

Fig. 13. SWIP-10 is conserved across phylogeny as the mammalian protein, MBLAC1. The SWIP-10 C-terminus contains a metallo β-lactamase domain (red bar) highly conserved across phylogeny especially within the canonical β-lactamase family HxHxDH motif required for metal/water coordination for substrate hydrolysis (His in blue, Asp in purple). Additionally, the mutant *swip-10* alleles, *vt33* and *vt29,* respectively resulting in a missense mutation of a conserved glycine to glutamic acid, and a nonsense mutation of a conserved tryptophan to a stop codon. (Adapted from Hardaway, 2015).

immunodepletion [182]. The neuroprotective actions of Cef arise from its known regulation of glial Glu transporter expression, further described in the subsequent chapter. The identified specific Mblac1/Cef interaction, as well as the established role for glial-expressed *swip-10* in the regulation of Glu dependent DA neuron function and excitability in the nematode, points to the importance of further investigation of SWIP-10/MBLAC1 related mechanisms supporting normal Glu signaling and brain health.

Chapter III

GLUTAMATE INDUCED EXCITOTOXICITY AND CELL DEATH

Molecular Mechanisms of Glu-Induced Excitotoxicity

Across phylogeny, the amino acid Glu plays multiple, important roles including contributions to protein synthesis, intermediary metabolism, and chemical neurotransmission [183-186]. Very early studies by Krebs identified the important metabolic role of Glu in the brain [187], however, years later, Glu was determined to be the major neurotransmitter responsible for excitatory neuronal signaling, and therefore Glu neurotransmission is involved in most aspects of normal brain function. Maintenance of Glu homeostasis within the brain is critical to allow Glu signaling to occur with exact temporal and local accuracy. At neuronal synapses, Glu signals through both metabotropic receptors that initiate G-protein coupled signaling [188-190] as well as ionotropic receptors that flux ions such as Na^+ and Ca^{2+}, altering membrane excitability and facilitating induction of normal intracellular Ca^{2+} signaling cascades associated with neuronal synaptic plasticity (Fig. 14) [188, 191-193]. Researchers further classified ionotropic Glu receptors based on the agonist that binds or activates the iGluR, N-methyl-D-aspartate (NMDA) receptors [194, 195], α-amino-3-hydroxy-5-methyl-4-isoxazole (AMPA) receptors [196], and kainate receptors [197, 198]. Excitotoxicity, a term first coined by Olney [199], refers to neuronal cell death arising from excess Glu activation of Glu receptors. Excessive ionotropic Glu signaling in the mammalian brain has been implicated in a variety of brain disorders including addiction, schizophrenia, amyotrophic

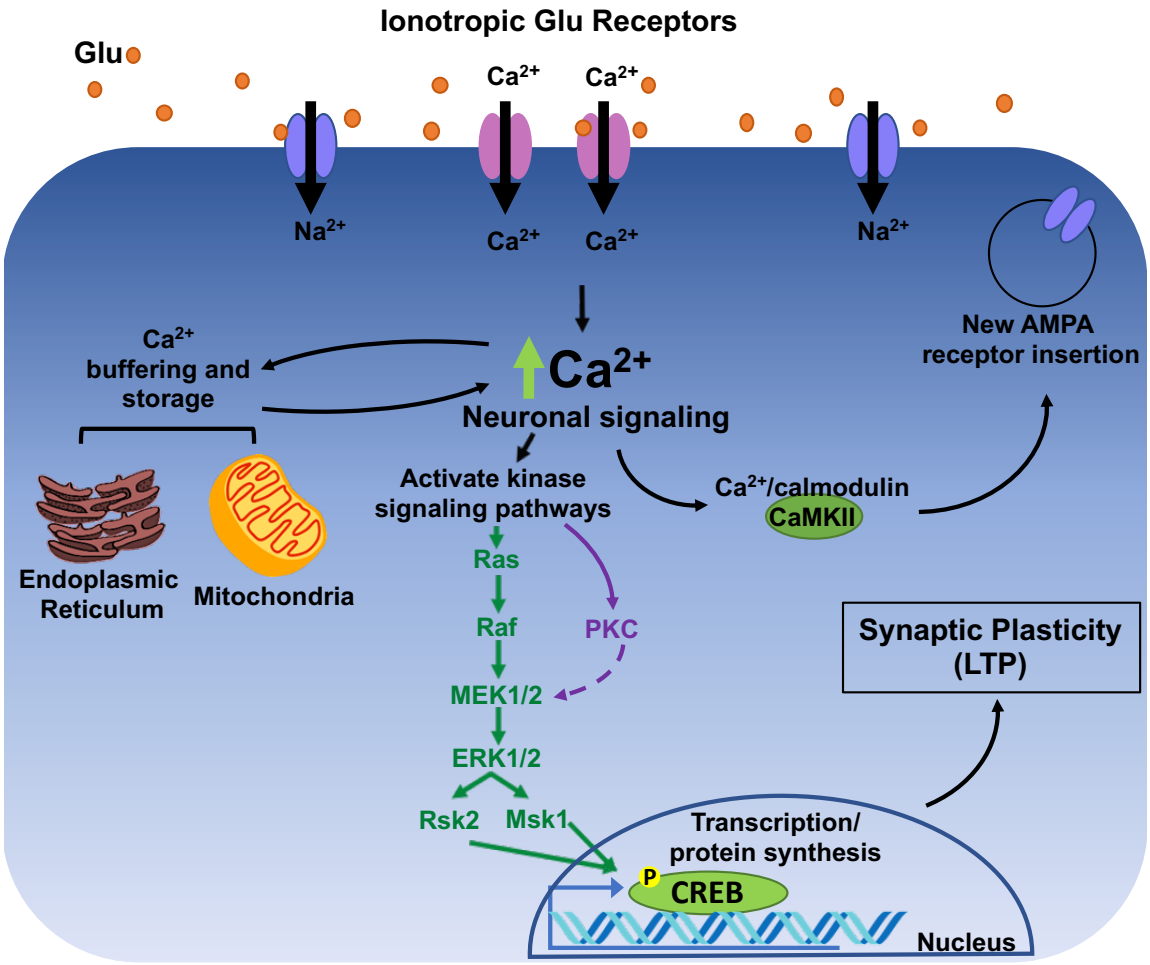

Fig. 14. Cartoon depicting normal post-synaptic Glu neurotransmission induced intracellular Ca^{2+} signaling. Glu stimulated influx of Ca^{2+} through ionotropic NMDA Glu receptors results in Ca^{2+} storage in the endoplasmic reticulum and mitochondria. Intracellular Ca^{2+} signaling results in insertion of new AMPA-type ionotropic Glu receptors in the post-synaptic density, as well as activates kinase signaling pathways to activate translation and *de novo* protein synthesis, both which contribute to synaptic plasticity.

lateral sclerosis (ALS), and Parkinson's disease (PD) [200-203], as well as the neuronal death that arises in the context of stroke and glioblastoma [204, 205] (Fig. 15).

Mammalian models of excitotoxicity

Much of what the neuroscience community knows about the molecular mechanism of Glu-induced excitotoxicity is through work utilizing mammalian cell culture models, and *in vivo* rodent and non-human primate models [199, 206], summarized in Fig. 16. Acute treatment of neurons in culture with high, non-physiological, levels of Glu can induce signs of cell death within minutes, characterized by intense vacuolization and cell swelling characteristic of necrosis [207-210]. In contrast, chronic hyper-activation of neurons by Glu, within physiological limits, can drive apoptotic mediated neural degeneration, particularly if other genetic or environmental risk pathways are engaged [211-213]. Chronic Glu activation of Glu receptors can lead to prolonged alterations in intracellular Ca^{2+} homeostasis, driving Ca^{2+}-dependent proteolysis and activation of apoptotic programs [214] (Fig. 16). Determining the cell autonomous mechanisms underlying Glu excitotoxic neurodegeneration is complicated due to this heterogeneity of cell death observed. Bonfoco and colleagues observed this using a cortical neuronal cell culture model of excitotoxicity where the initial severity and duration of NMDA insult dictated necrotic (short, high concentration NMDA treatment) or apoptotic (longer, less severe NMDA treatment) neurotoxicity [215]. *In vivo* murine studies by Portera-Cailliau, Price, and Martin utilized NMDA or non-NMDA agonists to stimulate neuronal excitotoxicity and demonstrated that the cell death mechanism driving neurodegeneration is influenced by neuronal maturity and neuronal GluR subunit composition [216]. More recently, Anilkumar

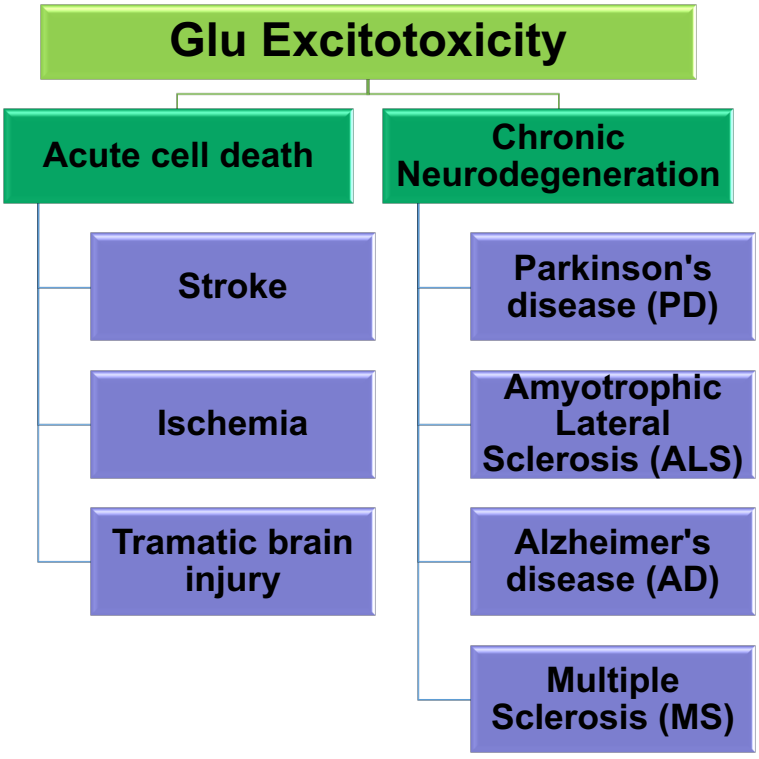

Fig. 15. Schematic illustrating the variety of human brain disorders and neurodegenerative diseases associated with acute versus chronic Glu induced excitotoxicity.

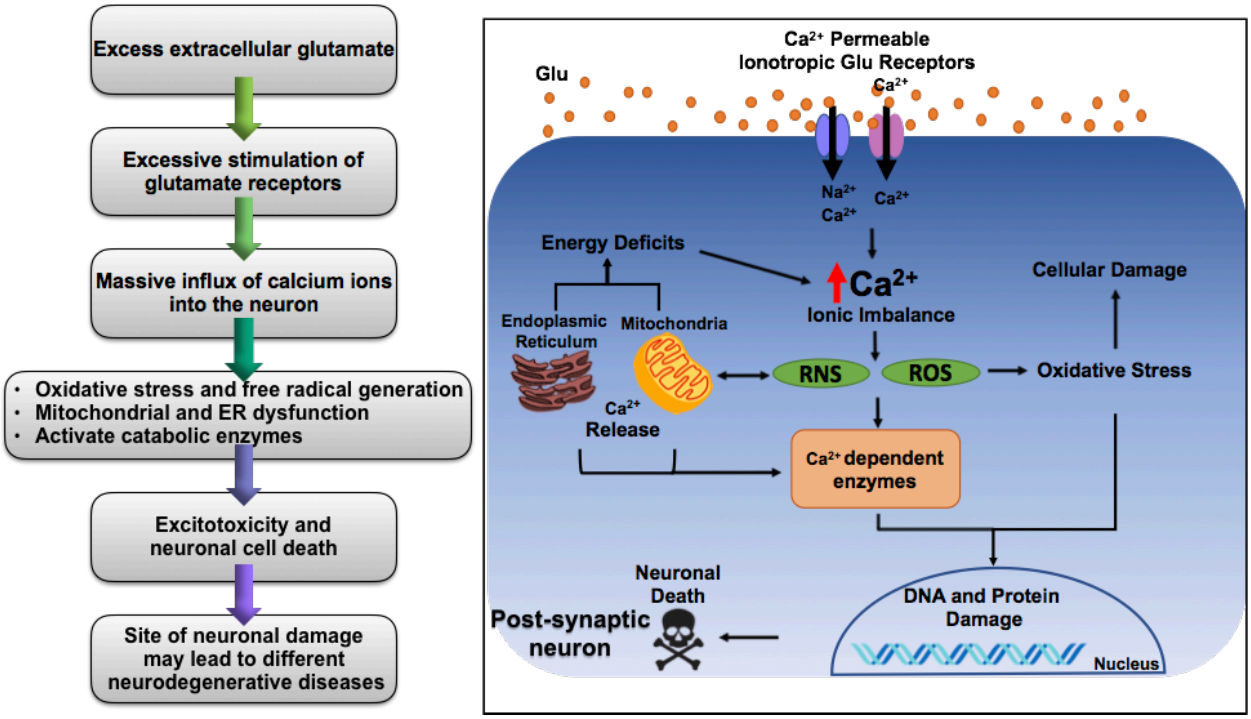

Fig. 16. Schematic of Glu-induced excitotoxicity arising due to aberrant intracellular Ca^{2+} signaling and subsequent induction of cell death mechanisms. (Figure adapted from Lo et al. 2003).

and colleagues used a mammalian cell culture model to find that extrinsic factors, such as glucose or nutrient availability, influence the mode of neural degeneration despite similar levels of Glu stimulation [217]. Glu excitotoxicity studies, such as those highlighted here, suggest that the induced mode of cell death occurs along a spectrum, ranging from necrosis to apoptosis with both shared and distinct molecular mechanisms driving neural degeneration [218].

One shared molecular feature of Glu stimulated necrosis or apoptosis, is the dysregulation of intracellular Ca^{2+} regulation and signaling [219]. Choi first described the involvement of Ca^{2+} influx in Glu excitotoxicity using neuronal cultures, where Glu-induced neurodegeneration was markedly decreased in neurons cultured in Ca^{2+}-free solution, and further implicated NMDA receptors as responsible for Ca^{2+} influx in Glu excitotoxicity [220, 221]. Further research suggests that excessively stimulated iGluRs lead to post-synaptic membrane depolarization and aberrant Ca^{2+} influx either through the iGluRs or through secondary Ca^{2+}-permeable channels such as DEG/ENaCs (Na^{+}/Ca^{2+}-permeable degenerin/ epithelial sodium channels) [148, 222, 223]. After entering the cell, Ca^{2+} activates many Ca^{2+}-dependent enzymes including proteases, phosphatases, lipases, and DNAses, and excessive activation of these proteins has deleterious effects on neuronal viability. Along these lines, Wang and colleagues used a hippocampal cell culture model of Glu-induced excitotoxicity to demonstrate that Glu-stimulated Ca^{2+} influx activated the Ca^{2+}-dependent phosphatase, calcineurin, which subsequently dephosphorylated BAD, a pro-apoptotic effector, leading to apoptosis induction and degeneration [224]. Multiple studies implicate calpain, a Ca^{2+}-dependent protease, as a mediator of Glu induced cell stress that can ultimately culminate in

neurodegeneration through apoptotic or necrotic cell death pathways [225, 226]. Recently, Gold and colleagues demonstrated that pharmacological inhibition of calpain reduced Glu-induced excitotoxicity in murine primary neurons [227]. In addition to dysregulated activation of Ca^{2+}-dependent proteins, excitotoxic Ca^{2+} influx leads to deficiencies in mitochondrial and ER Ca^{2+} buffering which increases cellular stress to the point of activating cell death mechanisms [228-230]. Dykens was able to show that brain mitochondria exposed to increased levels of cytosolic Ca^{2+} produced significantly more free radicals, and led to increased measures of mitochondrial dysfunction [231]. Mitochondrial dysfunction has been associated with both necrotic and apoptotic cell death pathways in the context of Glu-induced neurodegeneration [232, 233].

Although cell autonomous mechanisms remain a focal point for many investigations seeking insights into determinants of neurodegeneration, increasing attention has been given to astrocytic mechanisms that can sustain neuronal viability [234], in the context of constant Glu stimulation that could otherwise lead to cell death. These mechanisms include the shuttling of metabolic intermediates such as lactate to neurons that can help sustain ATP synthesis [235-237], the buffering of extracellular ions such as K^+, since excess extracellular K^+ due to chronic ion channel activation and Na^+/K^+ ATPase dysregulation can contribute to excess neuronal activation [236, 238, 239], and more recently, Grant and colleagues determined that *C. elegans* glia support neuronal health via pH buffering by transport of bicarbonate [150]. Important for neuronal viability, glia are critical for the efficient clearance of extracellular Glu that both limits the amplitude of synaptic and extrasynaptic Glu signaling but also limits Glu-driven neuronal degeneration [236, 240, 241].

Glutamate transporter regulation of glutamate signaling

Maintaining Glu homeostasis, and regulating extracellular Glu concentrations prior to, during, and after pre-synaptic Glu release is crucial to normal neurotransmission, neuronal heath, and normal brain function. Extracellular Glu uptake is mediated by multiple Na^+-dependent Glu-transporters of the SLC1 family that terminate Glu signaling via binding and uptake of Glu in proximity to synaptic release sites [202, 241, 242]. Of these plasma membrane Glu transporters, GLT1 (rodents) / EAAT2 (humans) is responsible for the majority of synaptic Glu clearance. By solubilizing rat brain membranes and employing chromatographic methods, Danbolt and colleagues first identified GLT-1 as a specific Glu transporter in the brain, and later generated a specific antibody to this protein and by immunoreactivity methods determined that GLT-1 expression is localized to glial cells in the brain [243-245]. With the identification of the GLT-1 protein, several research groups independently used various molecular cloning techniques to identify the cDNA for GLT-1 and two other Na^+-dependent Glu-transporter cDNAs now known as GLAST (rodents)/ EAAT-1 (humans), and EAAC1 (rodents)/ EAAT-3 (humans) [246-248]. Brain localization of these Glu transporters varies, with GLT-1 expressed in glial cells in the forebrain, GLAST immunostaining reveals localization to both neurons and glial cells primarily in the cerebellum, and EAAC-1 expressed in neurons throughout the brain, but at much lower levels [249-251]. Later, two additional glutamate transporters were identified as EAAT-4 and EAAT-5 (with expression restricted to the cerebellum and retina respectively [252-254]. While all of these plasma membrane Glu transporters transport extracellular Glu, the astrocytic glial Glu transporter, GLT-

1/EAAT-2, is responsible for tightly regulating synaptic Glu, and 90% of Glu uptake (Fig. 17) [255]. With excessive synaptic Glu signaling leading to excitotoxicity in both acute and chronic neurological disorders, normal GLT-1/EAAT-2 function is critical to normal brain health and elevating the expression or activity this protein has become a pharmacological strategy explored for protecting neurons against excessive Glu signaling. In this regard, pharmacological inhibition or genetic disruption to GLT-1 is sufficient to generate Glu induced excitotoxicity [211, 240] and GLT-1 dysfunction has been implicated in a number of brain disorders associated with excitotoxicity, including but not limited to stroke, addiction, ALS, PD, etc. [256-259].

A second astrocytic Glu transporter that participates in extracellular Glu homeostasis is xCT (SLC7A11), the transporter subunit of a dimer that supports intracellular Glu exchange for extracellular cystine. First identified as a Na^+-independent Glu transporter [260], the Glu/cystine exchange was first characterized by Bannai using human fibroblast cells, and subsequent molecular cloning by Sato and colleagues identified xCT as the subunit responsible for Glu/cystine transport [261, 262]. Several groups have used xCT specific antibodies coupled to immunoreactivity staining techniques to show that within the CNS, xCT is expressed in astrocytes as well as neurons, and highly expressed in glioma cell lines [263, 264]. xCT is generally thought to provide basal extrasynaptic Glu tone to modulate Glu neurotransmission as well as providing the precursor (cystine) for astrocytic glutathione synthesis (Fig. 17) [255, 265-267]. Work conducted by Baker and colleagues to monitor radiolabeled cystine uptake *in vivo,* demonstrated that Glu export by xCT exerted modulatory Glu tone on metabotropic GluRs (mGluR2/3) thus regulating Glu neurotransmission [268]. Additional studies

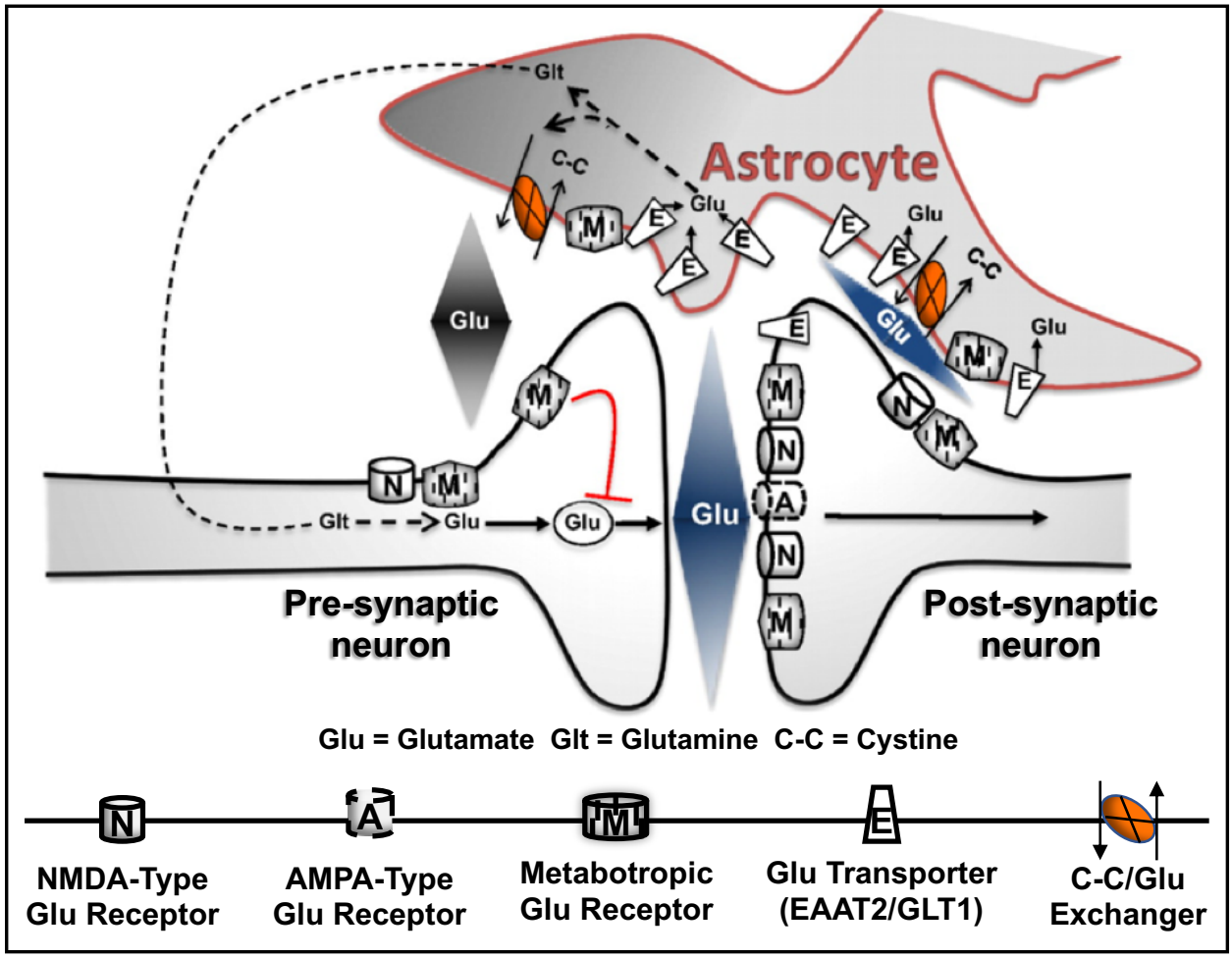

Fig. 17. Cartoon depicting a glutamatergic synapse ensheathed by an astrocytic process and the glial control of extracellular glutamate via glutamate transporters and the cystine/glutamate exchanger. Glu released from the presynaptic terminal acts on post-synaptic AMPA (A) and NMDA (N) ionotropic Glu receptors. Glu within the synaptic cleft is rapidly cleared by the glial Glu transporters (E), where within the astrocyte Glu is incorporated into the Glu/Glutamine cycle. Extrasynaptic glutamatergic tone is, where Glu modulates neuronal activity by acting on metabotropic Glu receptors (M), is regulated by the cystine/Glu exchanger (Orange). (Figure from Bridges and Baker, 2012).

revealed evidence that the extrasynaptic Glu released by xCT is cleared as it diffuses toward synaptic areas by EAATs [268, 269]. These findings support the hypothesis that xCT acts oppositely to SLC1 transporters, thereby maintaining Glu homeostasis via compartmentalization of extracellular Glu into different domains (Fig. 17) [255]. Excessive Glu efflux via xCT has been shown to result in pathological excitation of iGluRs, and result in Glu-induced excitotoxicity [270]. Therefore, similar to GLT-1, xCT dysregulation has been associated in the pathology of brain disorders linked to excitotoxicity including addiction, Alzheimer's disease, and multiple sclerosis [257, 271, 272].

Due to their significant impact on synaptic and extrasynaptic Glu homeostasis, Glu transporters and exchangers have been widely studied to determine their contribution to Glu-induced neural degeneration as well as in efforts to manipulate their activity and expression for therapeutic ends [257, 267, 273]. In a landmark study, Rothstein and coworkers screened a library of FDA-approved compounds for their ability to increase GLT-1 mRNA and protein levels [202]. They identified β-lactam antibiotics, typified by the cephalosporin-type antibiotic ceftriaxone (Cef), as capable of elevating GLT1 expression *in vitro* and *in vivo*, protecting neurons from Glu toxicity, and enhancing longevity in an ALS mouse model [202]. Subsequently, many investigators have demonstrated the neuroprotective activity of Cef administration in a variety of rodent models of brain disorders including stroke, addiction, PD [274-276]. Researchers, such as Rothstein, provide evidence that Cef imparts neuroprotection by modulation of both GLT1 and xCT expression [202, 267, 277]. Lee and colleagues use immunoreactivity techniques (western blots and immunofluorescence) and electrophoretic mobility shift assays to provide evidence that Cef increases expression of GLT-1 in primary human fetal

astrocytes through increased activation the nuclear factor-κB (NF-κB) signaling pathway [278]. Likewise, studies conducted by Lewerenz and colleagues provide support that Cef induces xCT protein expression in a hippocampal neuron derived cell line by increasing transcription of the exchanger via the nuclear factor erythroid 2-related factor (Nrf2) signaling pathway [277]. While the studies by Lee and Lewerenz both suggest transcriptional regulation of Glu transporters by Cef, the candidate(s) or substrate(s) targeted by the antibiotic in glia have, until recently, been unidentified. As described in the previous chapter, Retzlaff and colleagues determined that the metallo β-lactamase domain containing protein 1, MBLAC1 (SWIP-10 in *C. elegans*), interacts specifically and selectively with Cef [182]. Studies are underway in the Blakely lab to evaluate the expression of MBLAC1 as essential to the neuroprotective actions of Cef.

C. elegans Elucidation of Cell Death Mechanisms

Mammalian models of Glu induced excitotoxicity demonstrate that the duration, time, and extent of Glu signaling elicits neuronal cell death via two major forms of cellular demise, apoptosis or necrosis (Fig. 18). The utilization of *C. elegans* as a model organism was instrumental in the genetic, molecular, and cellular characterization of both programmed cell death (apoptotic) and necrotic cell death pathways. Well-described developmental stages, transparency, and a known cell lineage map made the nematode an excellent model for studying normal and aberrant cell death. I will concentrate the following review on foundational studies that used the worm as a powerful genetic model to uncover the cellular and molecular mechanisms that mediate either apoptotic or necrotic cell death.

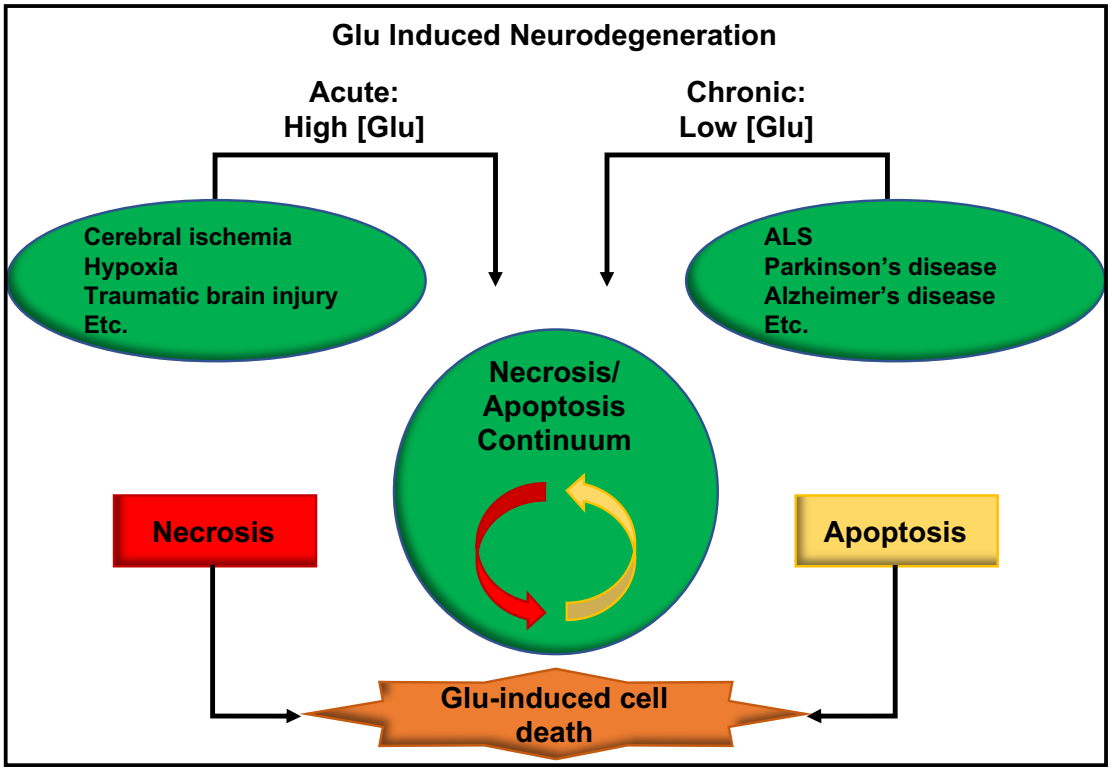

Fig. 18. Diagram depicting the cell death mechanisms by which various paradigms of Glu-induced neurodegeneration occurs. High, acute levels of Glu exposure, such as that observed in models of stroke, ischemia, and traumatic brain injury, result in necrotic mediated cell death. Chronic, low levels of excess Glu are implicated in neurodegeneration over a longer period of time in models of neurodegenerative diseases such as PD, ALS, etc. Models of chronic neurodegeneration implicate apoptosis in mediating neuronal cell death. (Figure adapted from Lea and Faden. 2003).

Programmed cell death – apoptosis

In the mid-1960's, pioneering researchers, such as Kerr, were first beginning to characterize "controlled cell deletion", now known as programmed cell death. Originally called "shrinking necrosis" based on morphological description [279, 280], apoptosis has become the term used in the scientific community to describe cell-autonomous programmed cell death, although we now know that apoptosis can also be triggered by extrinsic factors such as excessive Glu signaling. Apoptosis was characterized as morphologically distinct from other types of cell death by Kerr, Wyllie, and Currie [281]. Using electron microscopy techniques these researchers described the morphological cues still used to determine apoptotic cell death; cells first become rounded and separated in appearance, and electron density increases as the chromatin condenses within the nucleus, and eventually apoptotic cells undergo nuclear fragmentation, plasma membrane blebbing, and vacuole shedding [281, 282].

Outstanding work by Sydney Brenner, John Sulston, and Robert Horvitz, for which they were jointly awarded the 2002 Nobel Prize in Physiology or Medicine, informed the scientific community of the conserved, genetic regulation of programmed cell death. In the 1970's, Brenner developed and refined *C. elegans* research and genetic techniques, including the methods for mutagenesis-based genetic screens, gene isolation, genetic complementation and gene mapping. These methods allowed subsequent research to link genetic analyses with studies ranging from cell development and cell death to animal behavior [179, 283]. Taking advantage of the transparency and stereotyped development of *C. elegans,* Sulston used Nomarski differential interference contrast (DIC) microscopy, *in vivo,* to follow cell lineage maps from fertilized egg to the 959-cell adult hermaphrodite

[284-286]. These studies revealed that every time a fertilized egg develops into an adult, 131 somatic cells die during normal, developmental, programmed cell death with apoptotic like morphology, including chromatin condensation, cell shrinkage, and a "button-like" appearance due to increased cytosol refractility (Fig. 19) [287]. Strikingly, 105 of the cells that undergo programmed cell death during *C. elegans* development are neurons, resembling the neuronal overpopulation and subsequent neuronal pruning that occurs during vertebrate nervous system development.

After the elucidation the *C. elegans* cell lineage maps, Sulston and Horvitz employed Brenner's genetic techniques to isolate and characterize gene mutations resulting in altered nematode cell lineage [288, 289]. Hedgecock and colleagues identified two genes, *ced*-1 and *ced*-2, that when mutated prevent the engulfment of dying cells during development, such that cells undergoing apoptosis do not disappear and remain identifiable via their increased refractility and "button-like" appearance [290]. Via chemical mutagenesis, Horvitz and Ellis conducted a forward genetic screen on a *ced-1* mutant background to discover mutations that result in a cell death abnormal (*ced)* phenotype such that cells that normally become "button-like" retained normal refractility, survived, and even differentiated [291]. Subsequent genetic mapping and complementation tests revealed the first genes, *ced-3* and *ced-4,* identified within the genetic pathway controlling programmed cell death in the worm [291]. Additional screening by Ellis and Horvitz revealed a dominant mutation in a novel gene that resulted in visible loss of apoptotic cells [292]. A follow-up study by Hengartner named this new gene as *ced-9,* and further determined that loss of function mutations result in embryonic lethality, presenting *ced-9* as a negative regulator of genes required for programmed cell death [293]. Originally

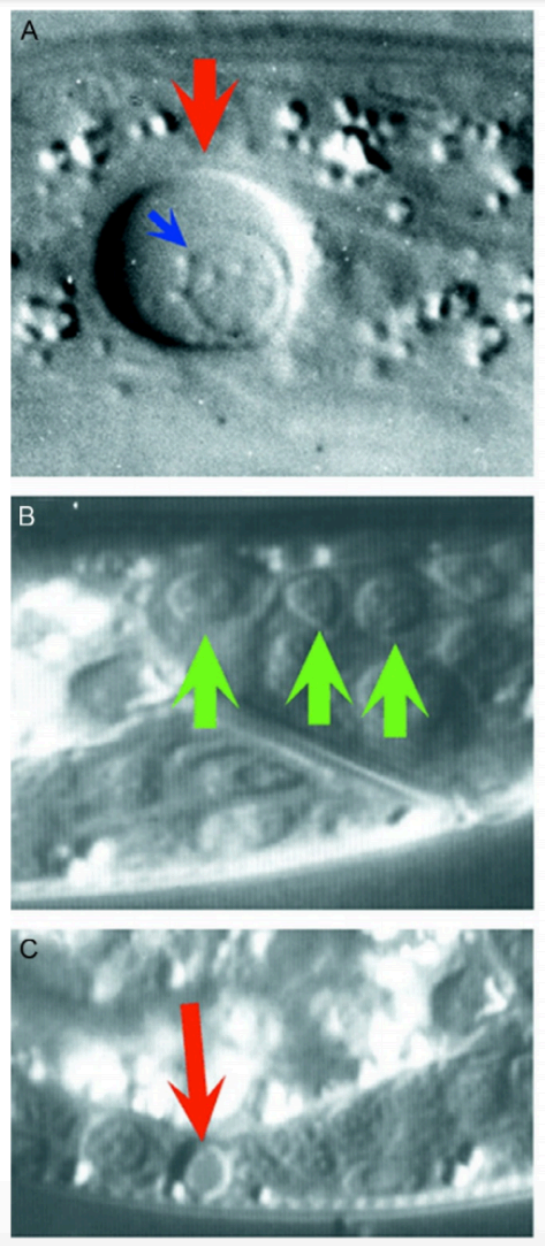

Fig. 19. Representative DIC images of necrotic, healthy, and apoptotic neurons in the nematode. A. The PVM touch receptor neuron (red arrow) of a *mec-4(d)* mutant animal displays the typical morphology, vacuole like- cell swelling and nucleus expansion (blue arrow), of necrotic cell death. B. Healthy cells are indicated by green arrows. C. An example of an apoptosis generated retractile cell corpse (red arrow), compact and button-like, with dark electron dense formations. Figure from Syntichaki and Tavernarakis, 2002.

identified as a gene regulating egg-laying behavior, *egl-1* was first described by Horvitz and colleagues as they determined that gain of function mutation to *egl-1* results in ectopic programmed cell death in the HSN neuron in the nematode. Later work by Conradt and Horvitz determined that loss of function mutation to *egl-1* prevents normal programmed cell death [294, 295]. Following the elucidation of the genes required for normal developmental programmed cell death, researchers utilized genetic epistasis experiments to determine the interactions between *egl-1, ced-9, ced-4,* and *ced-3.* These studies often involved overexpression of one of these genes to kill cells in the context of different genetic backgrounds. These epistasis experiments revealed *egl-1* to be a negative regulator of *ced-9*, which in turn negatively regulates *ced-4,* and finally *ced-4* activates *ced-3* to execute programmed cell death (Fig. 20) [296][297].

In parallel to the discovery of the genes within the genetic pathway controlling programmed cell death in *C. elegans*, researchers also sought to characterize the conservation and function of the proteins for which these genes encoded. Fig. 21 also depicts the nematode apoptotic pathway, including portraying the functional role attributed to each gene of the genetic pathway. *ced-3,* the final gene effector in the programmed cell death pathway is known as the “executioner”, and Yuan and colleagues found that the CED-3 protein sequence has homology to the human and rodent interleukin-1β-converting (ICE) enzyme therefore determining that CED-3 is a member of the caspase family (cysteine aspartate-specific protease), and suggesting that CED-3 activation results in cell death via its proteolytic cleavage of protein substrates [298, 299]. Further evidence of a conserved mammalian genetic apoptosis pathway was provided by Zou and colleagues in their studies to isolate and purify the cDNA for Apaf-1 from HeLa

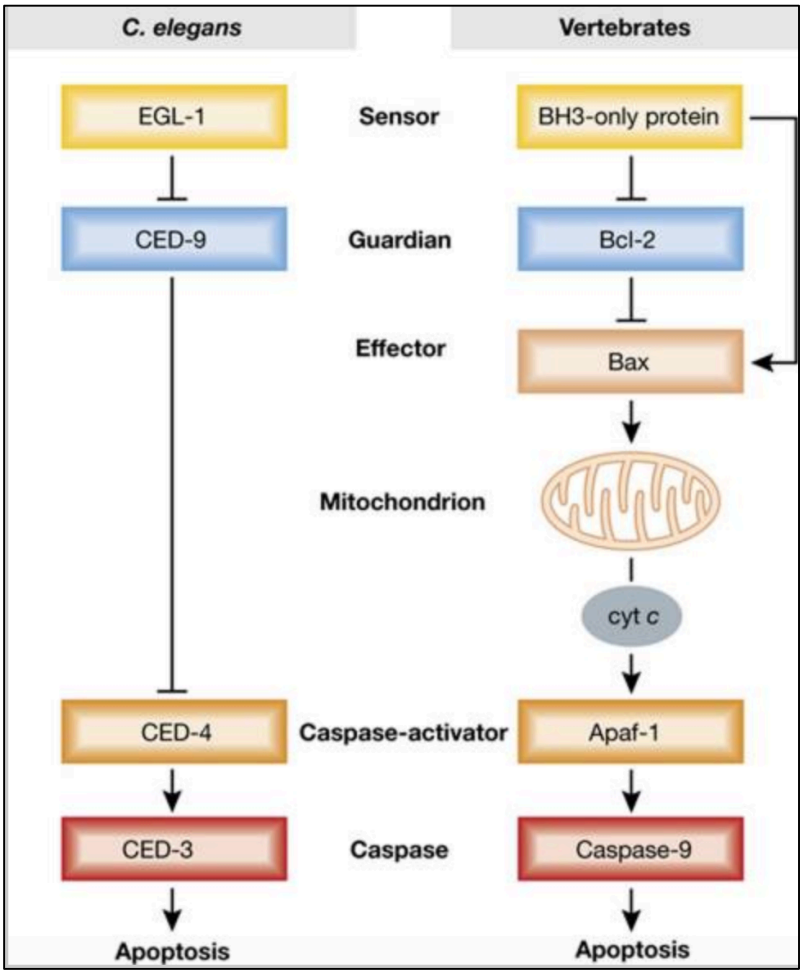

Fig. 20. Apoptotic – Programmed cell death pathway. The basic genetic pathway (dogma) of apoptosis is conserved from worm to man. (Figure from Strasser, Cory, and Adams, 2011).

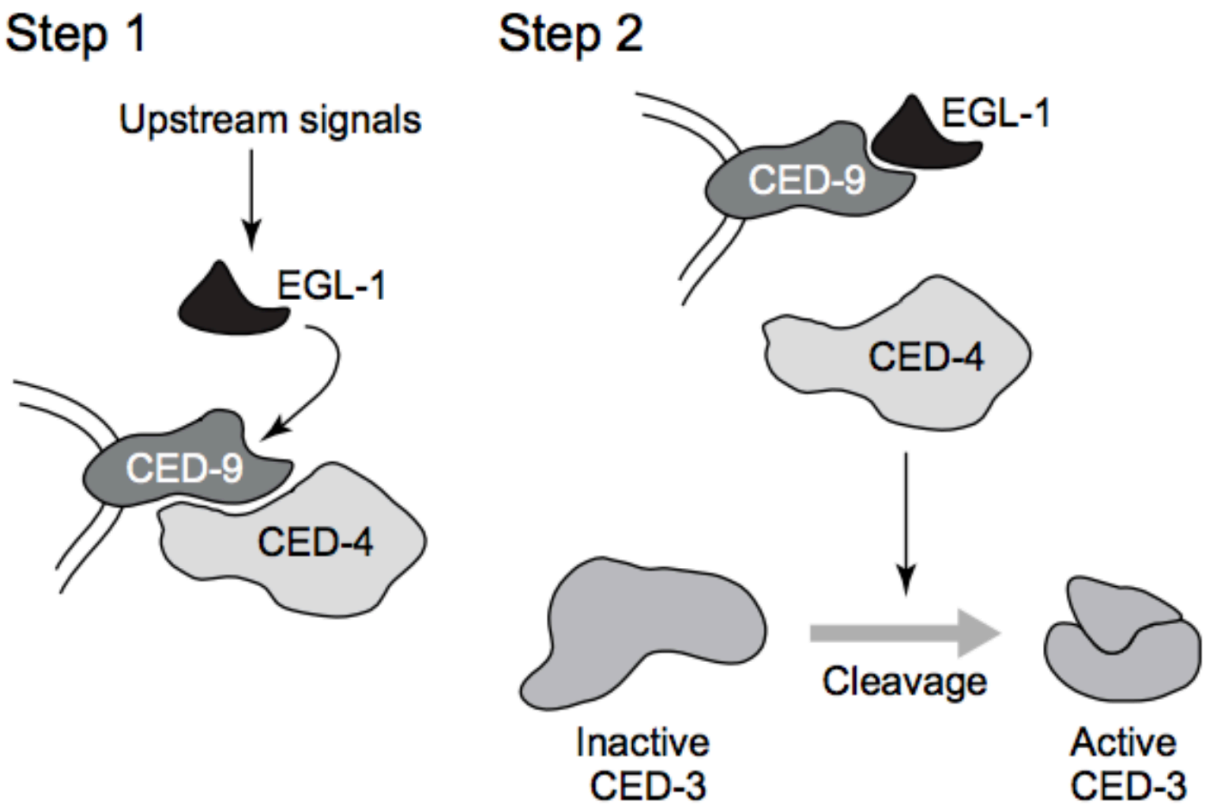

Fig. 21. *C. elegans* programmed cell death pathway function. Upstream apoptotic signaling triggers EGL-1 to interact with CED-9, displacing the inhibitory CED-9 interaction from CED-4. CED-4 is then able to cleave the inactive CED-3 precursor to the generate active CED-3. Active CED-3 will then cleave its substrate(s) to complete the apoptotic cell death pathway. (Adapted from Metzstein, Stanfield, and Horvitz, 1998)

cells, by which they demonstrated protein homology between APAF-1 and *C. elegans* CED-4 [300]. APAF-1 and CED-4 both contain multiple WD repeats, previously shown to mediate protein-protein interactions, and Zou and colleagues used immunoprecipitation experiments to show that APAF-1 interacts with cytochrome c and subsequently activates a downstream caspase (i.e. caspase-3) as shown in immunoblots by the appearance of the cleavage products from the caspase-3 precursor (Fig. 21) [300][296]. As the gain of function mutant allele of *ced-9* prevented normal programmed cell death [293], it was hypothesized that *ced-9* acted as a negative regulator of apoptosis and Hengartner and Horvitz determined that the mammalian ortholog of *ced-9* is the proto-oncogene *bcl-2,* previously shown to protect lymphoma-derived cells from apoptosis [301, 302]. Using a yeast expression model system without intrinsic cell death machinery, *S. pombe,* James and collaborators expressed *C. elegans* apoptotic genes in yeast demonstrating that expression of *ced-4* resulted in chromatin condensation and lethality that could be attenuated by co-expression of wildtype *ced-9* [303]. The researchers confirmed a direct interaction between CED-4 and CED-9 via yeast two-hybrid analysis (Fig. 17) [303][296]. In the phenotypic characterization of *egl-1* as a regulator of programmed cell death, Conradt and Horvitz cloned *egl-1* cDNA and describe an amino acid region of EGL-1 with homology to the Bcl-2 homology region 3 (BH3) domain found in the family of mammalian cell death activators including Bik (human) and Bid/Bad (mouse) [295]. After using genetic epistasis experiments to support that *egl-1* functions through *ced-9,* Conradt and Horvitz utilized a yeast two-hybrid approach to demonstrate that EGL-1 interacts directly with CED-9, supporting the hypothesis that BH-3-domain containing regulators of cell death (EGL-1, Bid, Bax, etc) activate cell death by binding to and blocking Bcl-2-like cell death

inhibitors (i.e. CED-9) [295] (Fig. 21) [296]. By using *C. elegans* to identify the genes in the programmed cell death pathway, and further characterize their mammalian orthologs and protein product functions, researchers such as Brenner, Sulston, and Horvitz provided an extensive framework for future scientists studying apoptotic cell death mechanisms in a wide variety of contexts including cancer, excitotoxicity, and neurodegeneration.

Genetic and environmental regulation of necrotic cell death

The early studies describing the morphology of dying cells characterized two primary modes of cell death based on visual assessment, necrosis and apoptosis. Necrosis-like cell death was distinguished from programmed cell death by Wyllie, Kerr and Currie as being an accidental or deranged form of cell death occurring due to extrinsic factors causing irreversible injury [304]. Morphologically distinct from apoptotic dying cells, Hall and colleagues used light and electron microscopy techniques to describe the morphological cues used to determine necrosis-like cell death in *C. elegans*; the first signs of necrotic cell death are the appearance of membrane infoldings and whorls, followed by cell swelling resulting in the cytoplasm becoming less electron-dense and vacuoles emerge and enlarge, eventually cellular organelles disappear and the swollen cell ruptures (Fig. 19) [287, 305].

In *C. elegans* normal developmental cell death typically follows the canonical apoptotic genetic program described above (Fig. 20) however, there are a few exceptions. For example, Sulston and collaborators describe the “in-between” necrosis-like programmed cell death that occurs in the male nematode linker cell. The linker cell dies

by the L4 stage of the animal, and this cell death persists even with genetic loss of the apoptotic executioner, *ced-3* [306]. This example highlights the potential for overlapping mechanisms in cell death pathways originally thought to be distinct, and mammalian cell death studies provide even more support for the hypothesis of cell death being a spectrum, ranging from apoptosis to necrosis.

Necrotic cell death in the worm has been extensively studied in the context of non-developmental cell death in the adult animal that can be triggered by extrinsic and intrinsic signals [307]. Dramatic environmental changes result in cellular toxicity and pathologies in mammals as well as in the worm (Fig. 22) [308]. Widespread necrotic cell death was observed in nematodes briefly exposed to hyperthermic conditions, modeling the pathologies of heat stroke in humans [309]. Oxygen deprivation, or hypoxia, has been shown to induce cell death in human disorders such as stroke and heart attack. Similarly, Scott, Aviden and Croweder demonstrate that hypoxic environmental exposure induces muscle and neuronal necrotic cell death in *c. elegans*, and further demonstrate that hypoxia resistance is modulated by the insulin/IGF receptor tyrosine kinase, DAF-2 [310]. Work by Yuan and colleagues demonstrated that nematodes with mutation to *slo-2*, a conserved Na^+-activated K^+ ion channel, are hypersensitive to hypoxic death, suggesting that SLO-2, normally protects against hypoxia induced necrosis by hyperpolarizing the neuronal resting potential to limit electrical activity [311].

As in mammalian nervous systems, ionic imbalances can lead to neuronal injury and trigger necrotic cell death in the nematode. Genetic mutations that alter ion channel permeability in the plasma membrane, leading to toxic intracellular ionic imbalancesand necrosis, are extensively studied in the worm. Chalfie and Wolinsky utilized Nomarski DIC

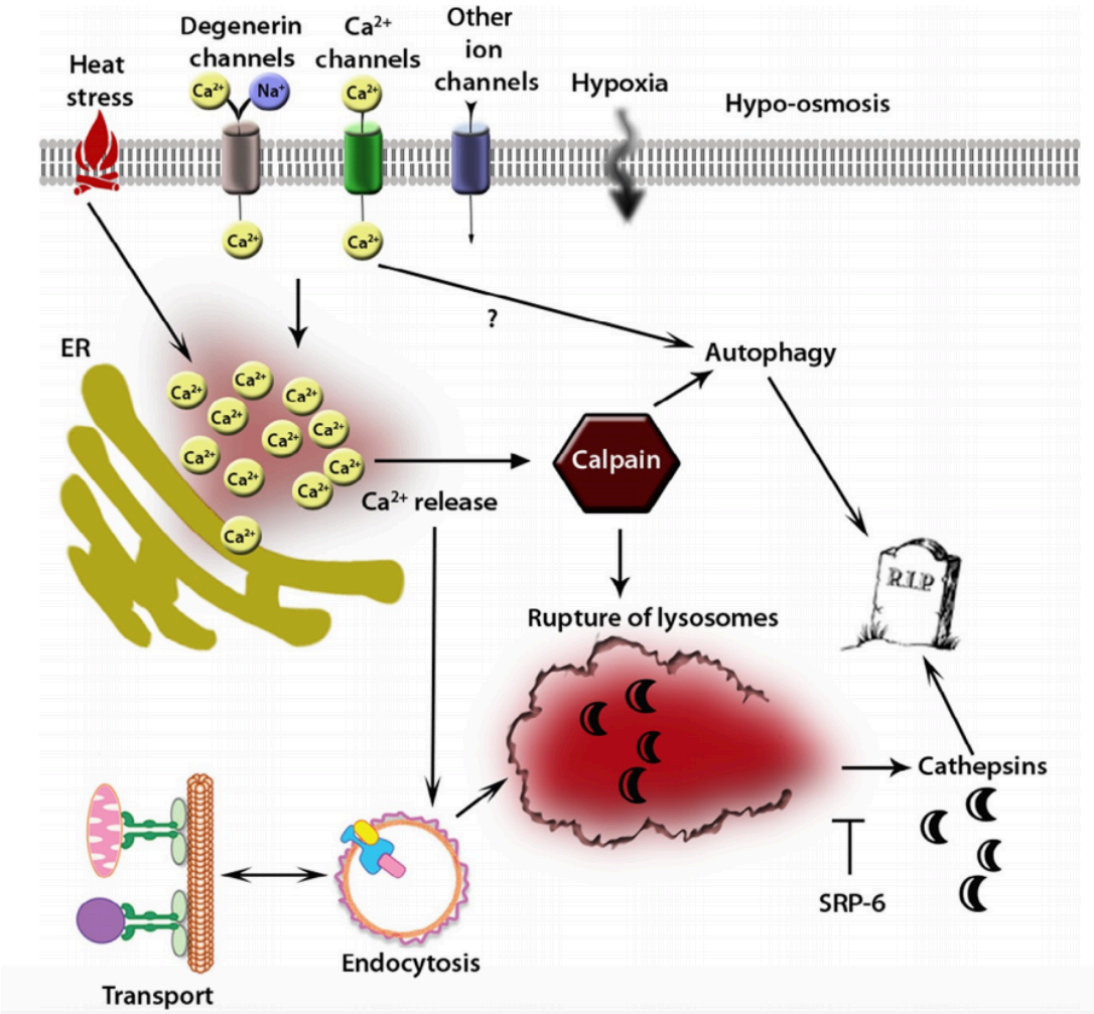

Fig. 22. Necrotic cell death mechanisms. Various extrinsic (i.e. heat shock and hypoxic conditions) and intrinsic (i.e. genetically-induced increase in membrane Ca^{2+}-permeability) factors converge on ionic imbalances and aberrant intracellular Ca^{2+} signaling to result in necrotic cell death. Figure from Nikoletopoulou and Tavernarakis, 2014.

imaging to determine that a dominant mutation to *deg-1,* first identified in a genetic screen for regulators of touch receptor neuron differentiation [312], resulted in non-apoptotic degeneration of the posterior touch neuron of the nematode after embryogenesis [313]. In parallel, Driscoll and Chalfie, determined that three dominant mutations in the gene *mec-4,* previously described for its role mechanosensation, resulted in cell-swelling and late onset degeneration of the 6 soft-touch receptor neurons of the worm, assessed via light microscopy [314]. *deg-1* and *mec-4* were found to be homologous using a DNA cross-hybridization technique [314], and both belong to a larger nematode family of genes named degenerins (DEG) for the cell degeneration phenotype observed in dominant mutant alleles of these genes. These genes are homologous to mammalian epithelial sodium channels, (ENaCs) [308, 315]. Other *C. elegans* neuronal DEG/ENaC genes include, *mec-10* and *unc-8,* and dominant mutations in these genes also results in osmotic imbalance and necrotic neuronal cell death in the gentle touch receptor neurons and cholinergic neurons of the ventral nerve cord, respectively [223, 316]. The neuronal toxicity resulting from hyperactive DEG/ENaC channels was demonstrated, in part, to arise due to increased Ca^{2+} permeability and aberrant intracellular Ca^{2+} signaling including a role for calreticulin and Ca^{2+} release from the ER as well as activation of Ca^{2+} dependent proteases, such as calpain [226, 317]. Research conducted by Bianchi, Matthewman, and others used a heterologous expression system and chimeric channels to study the ion conductance and toxicity of the dominant mutations of *mec-4* and *unc-8* and thereby provided evidence that the cellular toxicity arising from hyperactive DEG/ENaC can be attributed increased Ca^{2+} permeability (MEC-4) [318] and as well as increased Na^{+} conductance (UNC-8) [222]. Dominant mutations in other classes of ion

channels, such as *deg-3,* an acetylcholine receptor ion channel permeant to Ca^{2+}, or *trp-4,* a DA neuron expressed transient receptor potential (TRP) channel, have been shown to cause Ca^{2+}-dependent neuronal degeneration, separate from apoptosis [319, 320]. Using *C. elegans* as a model for necrotic neurodegeneration provides convincing evidence that tight regulation of ions is critical for maintaining neuron viability, a concept further supported by mammalian excitotoxicity studies.

C. elegans Models of Glutamate Induced Excitotoxicity

The molecular consequence of ionic imbalance in *C. elegans* is strikingly similar to the molecular mechanisms driving neuronal cell death in mammalian models of Glu-induced excitotoxicity. Nematode models of Glu-induced neuronal degeneration are still in their infancy, with the primary paradigm developed by the groups of Driscoll and Mano. Using Nomarski DIC imaging, Mano and Driscoll provided evidence of Glu induced excitotoxic necrotic cell death in the worm, arising from a combined loss of Glu clearance (via the plasma membrane Glu transporter, *glt-3*) and a hyperactive, constitutively active form of the alpha subunit of the G-protein, G_s, elevating cAMP signaling via adenylyl cyclase, *acy-1,* activity (Fig. 23) [321]. Unlike mammalian models of Glu-induced excitotoxicity, single or combinatory loss of multiple Glu transporters was not sufficient to induce cell death, likely due to the genetic redundancy of Glu transporters in the worm. However, Mano and Driscoll further describe the contributions of Ca^{2+}-permeable AMPA type Glu receptors to the excitotoxicity observed their model, such that genetic loss of *glr-1* and *glr-2* attenuated the observed necrotic cell death (Fig. 23) [321]. In keeping with mammalian models of Glu-excitotoxicity, the authors provide evidence that disrupted ER

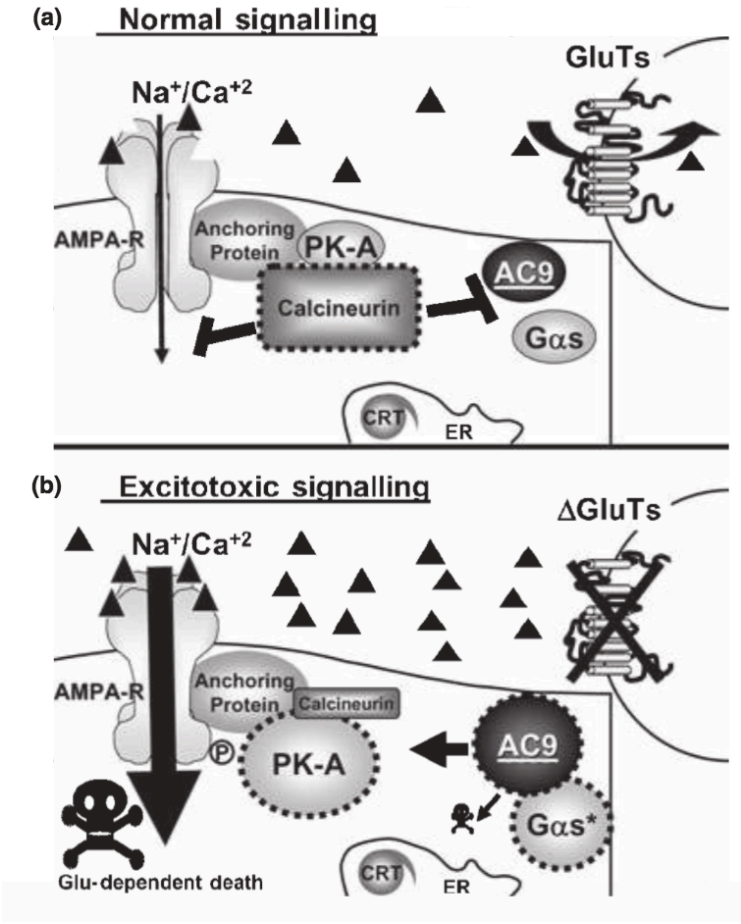

Fig. 23. Model for excitotoxic neurodegeneration in *C. elegans*. This schematic depicts the suggested mechanism for Glu induced excitotoxic signaling leading to necrotic cell death in the nematode. In this paradigm, excitotoxicity occurs in the context of disrupted Glu clearance by loss of *glt-3,* combined with constitutively active $G_{\alpha s}$ protein. Excitotoxic signaling in this model is reliant on Glu signaling via AMPA receptors, disruption to intracellular Ca^{2+} signaling. (Figure from Mano and Driscoll, 2009).

Ca^{2+} storage and release contributes to excitotoxic neural degeneration as genetic loss of calreticulin, *crt-1,* suppresses necrotic cell death (Fig. 23) [321]. The Mano group continued to use this *C. elegans* paradigm of Glu-induced necrotic degeneration to implicate the involvement of additional molecular regulators of excitotoxicity. Despite contrary findings for a role of the insulin/IGF signaling (IIS) cascade in mammalian models of excitotoxic neurodegeneration, Tehrani and colleagues provide evidence that genetic hyperactivation of the IIS cascade exacerbates excitotoxic necrosis, and pharmacological disruption of the IIS cascade, through PI3K inhibition, can protect against the neurodegeneration observed in the *C. elegans* excitotoxicity induced necrosis paradigm [322]. Del Rosario and collaborators continued to use this paradigm to characterize a role for the autophagy-associated, cell death protein kinase, *dapk-1,* and it is known interaction partner, *pin-1*, as conserved regulators of excitotoxicity, whereby they act in parallel to autophagy induction of neurodegeneration and do not act to regulate neurotoxicity via modulation of synaptic strength [323]. This *C. elegans* model of Glu-induced excitotoxicity provides insight to conserved molecular mechanisms of necrotic neurodegeneration. However, there is a need for additional nematode paradigms of Glu-induced excitotoxicity, particularly those with a variety of cell death phenotypes ranging from apoptosis to necrosis, to further identify and characterize novel genetic regulators of Glu-induced neuronal degeneration.

Specific Aims

Aim #1 – Determine and characterize the DA neuron morphology/ degeneration of *swip-10* mutant animals.

Aim #2 – Elucidate the molecular mechanism of the Glu-excitotoxicity induced DA neurodegeneration and cell death of *swip-10* mutants.

Aim #3 – Utilize a global, untargeted metabolomic approach to identify the metabolic pathway(s) reliant on expression the metallo-β-lactamase domain containing protein, Mblac1.

Chapter IV

DA NEURON DEGENERATION IS INDUCED BY LOSS OF THE METALLO-β-LACTAMASE DOMAIN CONTAINING PROTEIN, SWIP-10[1]

Introduction

Our previous studies identified a glial-expressed gene, *swip-10*, whose mutation induces hyper-excitability of DA neurons and elevates rates of vesicular DA release, culminating in the hyperdopaminergic phenotype, Swimming induced paralysis (Swip) and demonstrated a critical role for Glu signaling in establishing the paralytic phenotype of *swip-10* mutants [146]. *swip-10* is conserved across phylogeny as a metallo β-lactamase domain containing protein, with the unstudied gene, *Mblac1,* as the putative mammalian ortholog. Additional studies in the lab established that MBLAC1 is a specific, high-affinity target for the neuroprotective β-lactam antibiotic Cef [182]. Together, these findings suggest that further study of SWIP-10/MBLAC1 may reveal mechanisms normally engaged to protect neurons from chronically elevated extracellular Glu and a path to the identification of novel neuroprotective agents. A key piece of data lacking in this hypothesis, however, is evidence that loss of SWIP-10/MBLAC1 either induces Glu-dependent neural degeneration or eliminates the neuroprotective actions of Cef.

Here, we capitalize on the ease of monitoring the morphology and degeneration of *C. elegans* DA neurons engineered to stably express green fluorescent protein (GFP)

[1] Adapted from Gibson CL, Balbona JT, Niedzwiecki A, Rodriguez P, Nguyen KCQ, Hall DH, *et al.* Glial loss of the metallo β-lactamase domain containing protein, SWIP-10, induces age- and glutamate-signaling dependent, dopamine neuron degeneration. PLOSGenet. In press. 2018.

to examine a requirement for *swip-10* expression regulating DA neuron morphology. Using light and electron microscopy methods, we find that *swip-10* mutants demonstrate a striking, progressive degeneration of the DA neurons that can be suppressed by glial expression of wild type *swip-10* therefore providing evidence for a cell non-autonomous action of SWIP-10 to sustain DA neuron viability and suggest that this may not be solely limited to DA neurons but extend to other neurons tightly associated with glia.

Materials and Methods

C. elegans strains and husbandry

Strains were maintained as described previously [179]. We thank J. Rand (Oklahoma Medical Research Foundation); the *Caenhorhabditis* Genetics Center (funded by the National Institutes of Health's Office of Research Infrastructure Programs by Grant P40 OD010440); Shohei Mitani of the National Bioresource Project at Tokyo Women's Medical University; and Shai Shaham, Niels Ringstad, and Oliver Hobert for providing the strains used in this work. N2 (Bristol) served as our wild-type strain, and unless specified otherwise, we utilized the proposed null allele, TM5915, of *swip-10* [146]. Strains used in the studies described in this chapter are enumerated in order of appearance in Table 1.

Plasmid construction and transgenic manipulations

In all cases, insertion of the DNA fragment of interest and the fidelity of the vector was confirmed by sequencing and all PCRs were performed using KAPA HiFi HotStart ReadyMix (Kapa Biosystems). All constructs resulted in C-terminal cDNA fusion to an

Strain no.	Background strain/alleles	Transgene no.	Transgene
BY250		*vtIs7*	p*dat-1*:GFP
BY1175	*vtIs7;swip-10(tm5915)*	*vtIs7*	p*dat-1*:GFP
BY956	*vtIs7;swip-10(vt29)*	*vtIs7*	p*dat-1*:GFP
BY1174	*vtIs7;swip-10(vt29)*	*vtIs7*	p*dat-1*:GFP
BY1224-BY1225	*vtIs7*	*vtIs7; vtEx272-273*	p*dat-1*:GFP; p*dat-1*:myrRFP
BY1209-BY1210	*vtIs7;swip-10(tm5915)*	*vtIs7; vtEx272-273*	p*dat-1*:GFP; p*dat-1*:myrRFP
nsIs105		*nsIs105*	*phlh-17::GFP*
BY1310	*nsIs105;swip-10(tm5915)*	*nsIs105*	*phlh-17::GFP*
nsIs108		*nsIs108*	*pptr-10:*myrRFP
BY1204	*nsIs108;swip-10(tm5915)*	*nsIs108*	*pptr-10:*myrRFP
N2			
TM5915	*swip-10(tm5915)*		
BY1177	*vtIs7;cat-2(tm2261);swip-10(tm5915)*	*vtIs7*	p*dat-1*:GFP
BY1206	*vtIs7;dat-1(ok157)*	*vtIs7*	p*dat-1*:GFP
BY1257-BY1258, BY1262	*vtIs7;swip-10(tm5915)*	*vtIs7; vtEx188-190*	pdat-1:GFP, [SWIP10 genomic PCR, pelt-2:GFP, punc-122:RFP, pdat-1:mCherry]
BY1199-BY1201	*vtIs7;swip-10(tm5915)*	*vtIs7; vtEx269-271*	p*dat-1*:GFP, [*pptr-10:swip-10* cDNA, punc122:RFP]
BY1233-BY1235	*vtIs7;swip-10(tm5915)*	*vtIs7; vtEx283-285*	p*dat-1*:GFP; [*phlh-17:swip-10* cDNA, punc122:RFP]
BY1241-1243	*vtIs7;swip-10(tm5915)*	*vtIs7; vtEx159-161*	p*dat-1*:GFP; [*pdat-1:swip-10* cDNA, pdat-1:mcherry, punc122:RFP]
MT17370		*nsIs242*	*pgcy-33:*GFP
BY1193	*nsIs242;swip-10(tm5915)*	*nsIs242*	*pgcy-33:*GFP
TV12498		*wgIs328*	*pser2prom3:*myrGFP
BY1207	*wgIs328; swip-10(tm5915)*	*wgIs328*	*pser2prom3:*myrGFP
OH1422		*otIs138*	*pser2prom3:*GFP
BY1208	*otIs138; swip-10(5915)*	*otIs138*	*pser2prom3:*GFP

Table 1. *C. elegans* strains utilized for data collection and figures described in Chapter IV.

unc-54 3' UTR. For the membrane bound transcriptional reporter, we used overlap PCR [324] and Gibson Assembly (New England Biolabs) to subclone the 700 bp *dat*-1 promotor into the myrRFP containing backbone from p_{ptr-10}:myrRFP (gift from Shai Shaham) to create pRB1349 (p_{dat-1}:myrRFP). For transgenic *swip-10cDNA::GFP* rescue experiments, DA neuron, pan-glial, and CEPsh glial expression was achieved using the previously described plasmids, pRB1157, pRB1158, and pRB1159, respectively [146]. Genomic full-length *swip-10* rescue experiments were conducted as previously described [146].

Genetic crosses

Crosses were performed using publicly available, integrated fluorescent reporter strains to mark chromosomes *in trans*. Single worm PCR was performed to confirm the presence of the indicated mutation. For all deletions, we used a three primer multiplex strategy that produces PCR amplicons with a 100–200 bp difference between N2 and mutant. This method was highly effective in eliminating preferential amplification of a lower-molecular-weight species. In all cases, a synthetic heterozygous control was used to ensure that heterozygous clones could be identified. We identified recombinant lines by PCR genotyping of single worm genomic DNA lysates. All genotyping PCRs were performed with the KAPA Genotyping Kit (KAPA Biosystems). In some cases, alleles were sequenced with sequence-specific primers to verify mutation homozygosity (GeneHunter and EtonBioscience).

Confocal imaging

Confocal microscopy of mutants on the BY250 strain background was performed using a Nikon A1R confocal microscope in the FAU Brain Institute Cell Imaging Core using a 20x or 60x oil-immersion objective and Nikon Elements capture software. Worms were immobilized using 30 mM levamisole in M9 on a fresh 2% agarose pad and cover-slipped with a 1 mm cover glass before sealing with paraffin wax [164].

Neurodegeneration assay

The neurodegeneration assay was adapted from a previously described method [159]. In our case, we transferred 20 worms to normal NGM/OP50 plates as L4s and incubated these plates for 48 hrs at 19°C until animals reached the gravid adult stage, unless otherwise noted. We then picked 15 worms into 20 µL of 30 mM levamisole in M9 on slides prepared with a 2% agarose pad. For imaging, we utilized a Zeiss Discovery V12 inverted fluorescent microscope outfitted with a Xenon UV light source and GFP/YFP/RFP filter sets. We used a Zeiss mono FWD 16 mm objective lens to visualize Green Fluorescent Protein (GFP) containing integrated transgenes, *vtIs7[*$P_{dat\text{-}1}$::GFP], *nsIs242*[$P_{gcy\text{-}33}$::GFP], *wgIs328*[$P_{ser2prom3}$::GFP] selectively expressed in DA, BAG, and OLL neurons respectively, allowing us to examine neurodegeneration in a cell-specific manner. For the DA neurons, analysis was primarily limited to CEP neurons, because out of the 8 DA neurons in *C. elegans*, the 4 CEP neurons display the clearest and most distinct dendritic projections and can be readily identified via both light and electron microscopy (see below). Neurons were examined for the presence of 1) breaks in the CEP dendrites 2) shrunken or 3) missing somas. Worms were counted as displaying

degeneration if one or more of these features were present. Normal N2 CEP, BAG, and OLL neurons lacked any of these abnormalities at the gravid adult stage. Total animals with degeneration, shrunken and missing somas, or neurite breaks were calculated for each trial. The percentage of animals exhibiting each morphological trait was determined for graphical analysis. Animals were tested 15 animals/day on 7-9 separate days (n = 90-135 animals assayed per genotype) blinded to genotype.

Lifespan assay

Lifespan analyses were conducted on OP50/NGM plates at 20°C as previously described [325]. Age refers to days following adulthood, and animals were transferred to fresh plates every 48hrs after the L4 stage to prevent *E. coli* depletion and confusion with subsequent generations. Animals were determined as dead if they did not respond with any movement to 3 head touches. 200-250 animals were assayed per genotype and animals were excluded from analysis if they crawled off the plate.

Electron microscopy

N2 and *swip-10* mutant animals were raised and maintained at 20ºC on *E. coli* OP50/NGM plates and 2-day adult animals (fixed 2 days after the L4 stage) were fixed and embedded for transmission electron microscopy (TEM) following a chemical immersion protocol [305, 326]. Briefly, animals were first cut open in a cacodylate-buffered osmium tetroxide fixative, then *en bloc* stained in uranyl acetate, and dehydrated and embedded in Spurr resin. Thin sections were collected onto Formvar-coated slot grids and examined on a Philips CM10 electron microscope. Digital images were

collected with an Olympus Morada camera on the TEM, and figures were created using Photoshop.

Statistical analyses

All statistical tests were performed and graphs generated using Prism version 7.0. Data were analyzed by Student's t-tests, one-way ANOVAs followed by Sudak or Dunnet's post-hoc tests, two-way ANOVAs, and Log Rank (Mantel-Cox) where appropriate. A $P<0.05$ was taken as evidence of statistical significance in all cases.

Results

DA neuron degeneration in *swip-10* mutants

Given the Glu signaling-dependent, Swimming-induced paralysis (Swip) phenotype present in *swip-10* mutants [146], and evidence from the latter study that *swip-10* DA neurons are hyper-excitable, as assessed by a cytoplasmic Ca^{2+} reporter (GCamp), we sought to determine whether these animals might display signs of excitotoxic neural degeneration. We examined the DA neurons of multiple mutant *swip-10* alleles crossed to BY250, a strain that stably expresses the integrated transcriptional fusion $p_{dat\text{-}1}$*::GFP* (*vtIs7)* (Fig. 24) [156]. We primarily focused our evaluations on CEP DA neurons, and quantitatively evaluated degeneration by three distinct morphological assessments: 1) neurite truncations and breaks in GFP-labeled dendrites (Fig. 24B,C, F), 2) shrunken cell soma (Fig. 24D, G) and 3) missing cell soma (Fig. 24E, H), as previously described [159, 327]. From these categories, we also calculated an overall degeneration

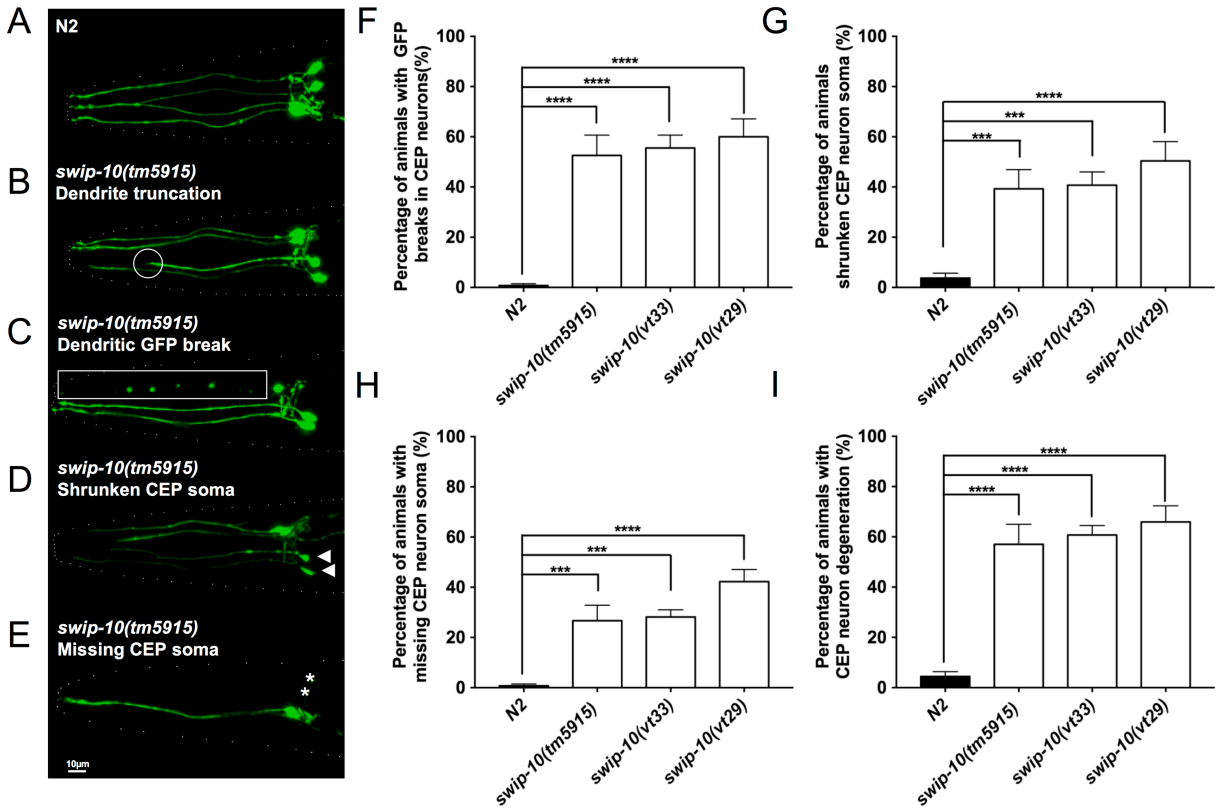

Fig. 24. CEP DA neuron degeneration observed in loss of function *swip-10* alleles. A. N2 DA neurons labeled with GFP demonstrating evenly expressed fluorescence throughout the neuronal processes. B-D. Representative images of *swip-10(tm5915)* mutant degeneration depicting (B) truncated CEP DA neuron dendrites indicated by a white circle, (C) breaks in GFP along CEP dendrites (white rectangle), (C) shrunken CEP cell soma (white arrowheads) and (D) missing CEP cell soma (white asterisks), scale bar is 10µm. F-I. Quantification of the components of CEP DA neuron degeneration for (F) truncations/breaks in GFP, (G) shrunken CEP soma, (H) missing CEP soma, and (I) total degeneration phenotype, inclusive of all three degeneration measures. Data were analyzed by one-way ANOVA with Sidak's post-test to N2; *, **, *** indicate $P<0.05$, <0.01 and <0.001 respectively. Error bars represent ± SEM, with n=105-150 animals per strain.

score where the appearance of any of the components qualifies an animal as displaying CEP degeneration [159]. We found that all three available *swip-10* alleles (*vt29* and *vt33* from our forward genetic screen, and the larger deletion allele, *tm5915*) exhibited elevations in the degeneration index, relative to wildtype animals (Fig. 24I). To further support that mutation of *swip-10* induces morphological changes in CEP DA neurons, versus a sequestration or inactivation of cytoplasmic GFP, we corroborated our findings using a DA neuron-targeted, membrane-bound reporter ($p_{dat\text{-}1}$*::myrRFP*) which also yielded evidence of *tm5915* CEP DA neurodegeneration (Fig. 25). While we did not assign quantitative measures to the examination of the ADE or PDE DA neurons, we report that qualitatively, there are subtle morphological differences between *swip-10*(*tm5915)* mutants and N2 animals (Fig. 26). Our preliminary assessment of the ADE DA neurons in *swip-10* animals reveals that at least 50% of the animals display normal ADE neuron morphology (Fig. 26A), however other *swip-10* animals display dim GFP expression in the ADE neurons compared to consistently bright N2 GFP expression, and some *swip-10* animals display abnormally shaped or missing ADE projections (Fig. 26A). Surprisingly we observe fewer qualitative differences between *swip-10* and N2 PDE DA neuron morphology, although likely this is a reflection on the reduced GPF fluorescence of *vtIs7* in N2 PDE neurons making qualitative and quantitative morphological assessment more challenging (Fig. 26B). Interestingly, evaluation of *swip-10* impact on *C. elegans* glia broadly (marked by the *ptr-10* promoter driven myrRFP) or on CEPsh glia that ensheath CEP DA neurons specifically (marked by $p_{hlh\text{-}17}$*::*GFP) failed to reveal evidence for gross morphological changes (Fig. 27). These findings suggest that *swip-10*

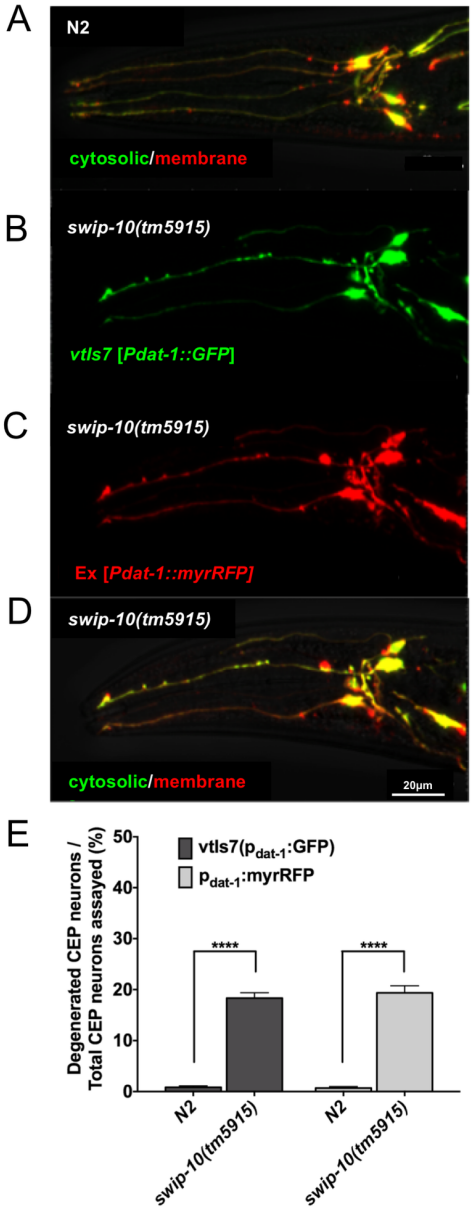

Fig. 25. Membrane-bound fluorescent reporter corroborates *swip-10* mutant DA neuron degeneration. Integrated vtIs7 [p_{dat-1}:GFP] reporter in green and extrachromosomal p_{dat-1}:myrRFP reporter in red show equal levels of degeneration in *swip-10* mutants. Representative images show normal A. N2 DA neuron morphology, merged, and a representative image of a *swip-10* mutant animal B. integrated marker, C. extrachromosomal array marker and D. merged, scale bar is 20µm. E. DA neuron degeneration was quantified in animals expressing both DA neuron fluorescent reporters, and both demonstrate *swip-10* mutant animals have significantly increased DA neuron degeneration. Analyzed by Student's *t* test, **** indicates a *P*<0.0001, error bars represent ± SEM, with n=105-150 animals per strain.

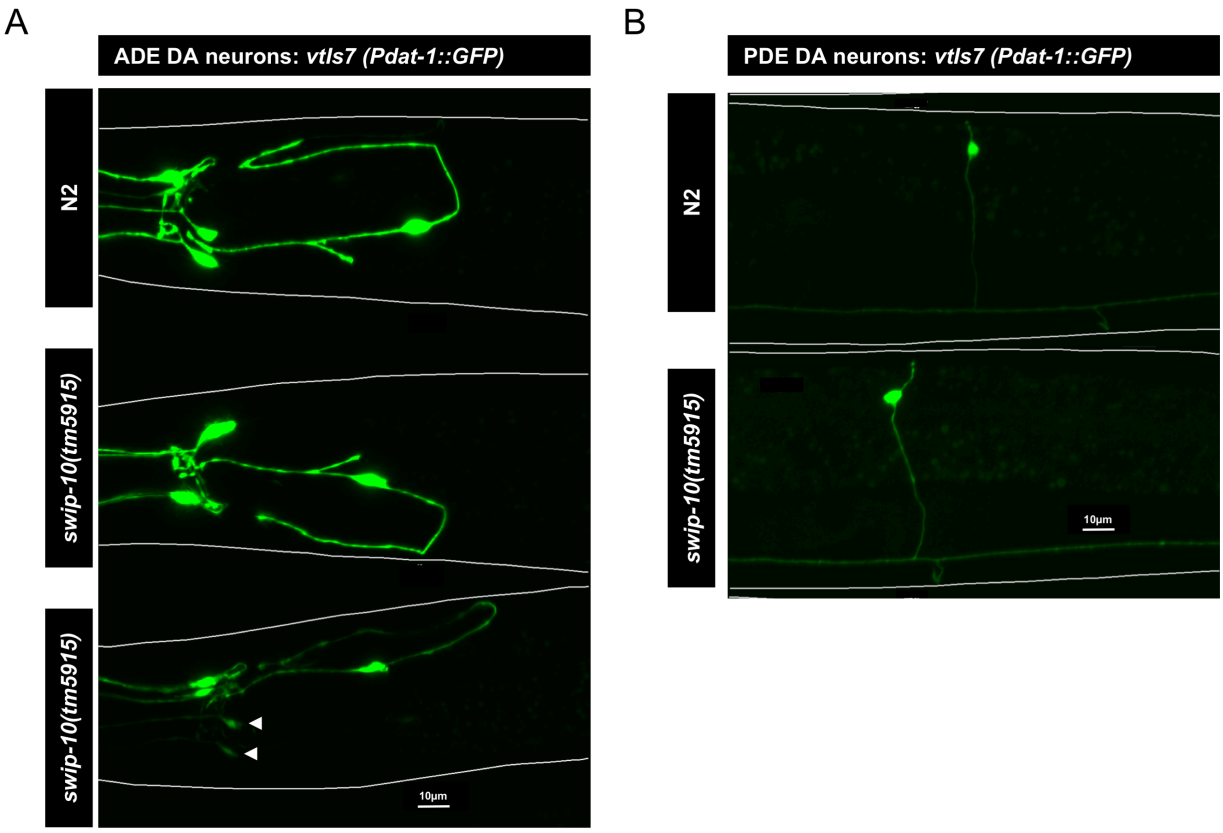

Fig. 26. ADE and PDE DA neuron morphology of *swip-10* mutants. A. Top: N2 ADE DA neurons labeled with GFP demonstrating even expressed fluorescence throughout the neuron cell body and processes. Middle: Representative image of *swip-10(tm5915)* ADE DA neurons with normal, N2-like morphology and GFP expression. Bottom: Representative image of *swip-10(tm5915)* mutant with altered ADE DA neuron morphology, dim GFP expression and altered neuronal processes location. Arrowheads denote shrunken CEP soma. B. Top: N2 PDE DA neurons labeled with GFP demonstrating even expressed fluorescence throughout the neuron cell body and processes. Bottom: Representative image of *swip-10(tm5915)* mutant with normal N2-like PDE neuron morphology and GFP expression. Anterior is left in all images shown,), scale bar is 10µm.

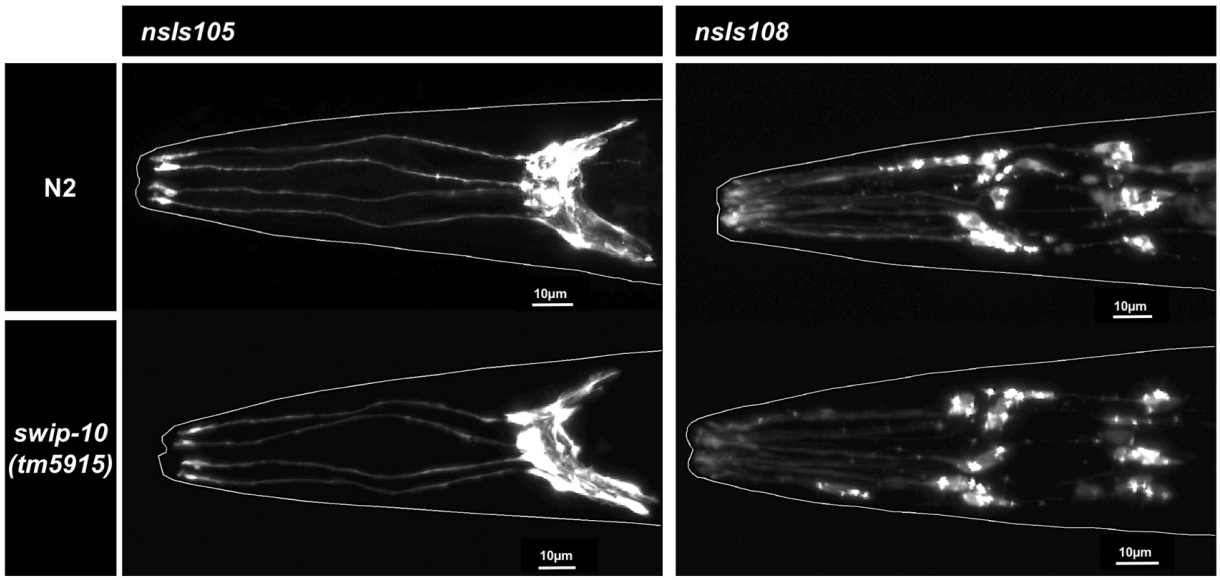

Fig. 27. *swip-10* mutants display normal glial morphology. Representative images of the CEPsh glia of N2 and *swip-10* mutant animals, crossed onto a strain bearing an integrated p_{hlh-17}:GFP transgene (DCR1337, *nsIs105*). Representative images of the glia of N2 and *swip-10* mutant animals, crossed onto a strain bearing an integrated p_{ptr-10}::myrRFP transgene (*nsIs108*). Scale bars are 10µm.

mutation induces a localized, cell non-autonomous effect on the integrity of neighboring DA neurons.

Electron microscopy of *swip-10* DA neurons

To be sure that our fluorescent reporters of DA neuron morphology were faithfully reporting structural changes in DA neurons, we assessed CEP cilia of *swip-10* via electron microscopy (EM). Previously, we used this approach to document damage to CEP dendrites in the context of 6-OHDA induced DA neuron degeneration [52]. The *tm5915* deletion allele was selected for EM studies of *swip-10* induced neural degeneration, though as noted above, all mutants demonstrated comparable degeneration. The morphology of CEP neuronal processes is well characterized at the ultrastructural level [328] especially the specialized cilium at the tip of the CEP dendrite, which can be visualized in transverse thin sections through the lips of adult *C. elegans* (Fig. 28A) [329, 330]. Using relative position and the defined morphological characteristics of CEP DA neurons, such as the electron dense cuticular branch or nubbin associated with their cilia to anchor the dendrite to the cuticle [330] and the presence of the electron dense clumps of tubule-associated material (TAM) previously shown to be characteristic of CEP cilium [329], we were able to identify multiple anomalies in *tm5915* CEP structure. These defects include changes in the size and appearance of the nubbin (Fig. 28B-D), loss or misplacement of TAM and microtubules (Fig. 28C-F), and the presence of large or small vacuoles in several locations either below or above the axoneme (Fig. 28C-F). A summary of the *swip-10* mutant CEP cilium defects is depicted in Fig. 28G. In addition to the defects described above, half of the CEP dendrites of

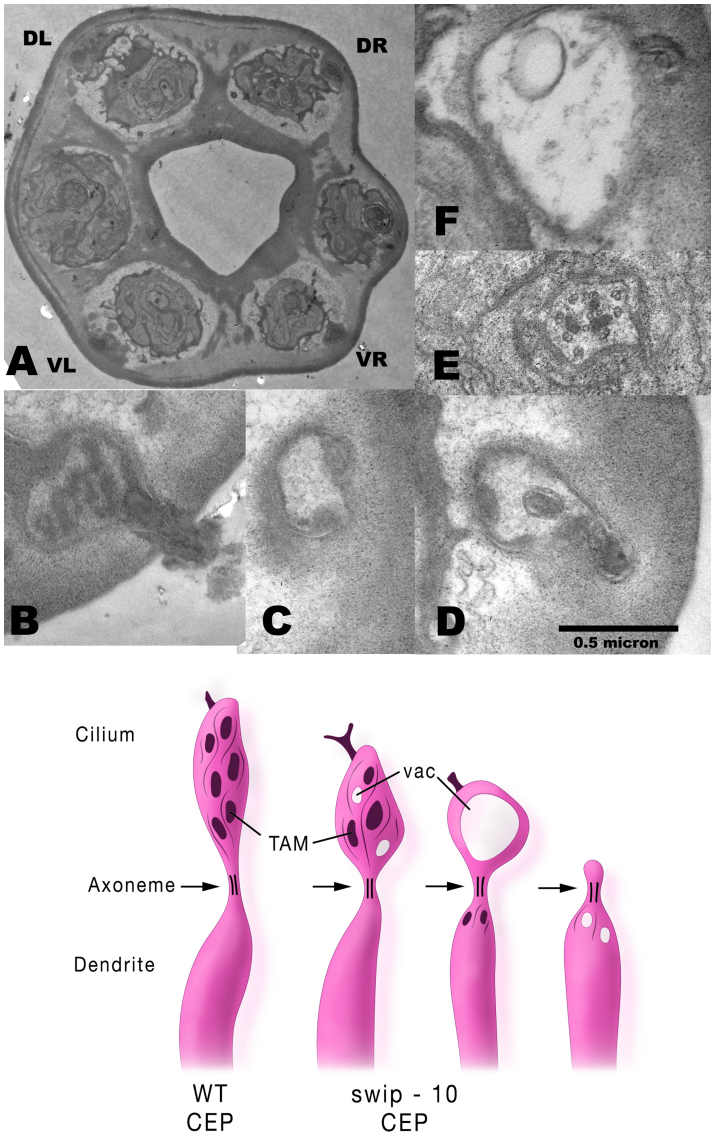

Fig. 28. Electron microscopy confirms missing and deformed cilia of the CEP DA neuron dendrites in *swip-10* mutants. A. Thin section through the lips of a *swip-10* mutant adult all four CEP cilia are formed almost normally in positions DL, DR, VL, VR, forming specialized endings embedded in the lip cuticle. B. High power TEM image of *swip-10* mutant CEPVR cilium, somewhat reduced in overall size, containing normal-looking microtubules and dark staining tubule-associated material (TAM). The nubbin is abnormally enlarged and emerges out of the cuticle in an enlarged tree-like structure, not seen in N2. C. Midway and more D. distal through another the defective CEPVR cilium in a different animal, lacking normal TAM or distal microtubules. E-F. show thin sections from a CEPDR cilium where small bits of TAM have abnormally become stuck inside the well-formed axoneme, while beyond the axoneme F. the malformed cilium consists of large vacuole-filled swelling with no TAM or microtubules, and only a minimal nubbin. Scale bar (0.5 micron) applies to panels B-F. G. Summary illustration of the variety of distal defects found in the CEP cilium, comparing a wildtype cilium to the left, and three progressively more defective mutant cilia on the right. EM analyses performed by David H. Hall and Ken C. Q. Nguyen.

swip-10 mutants were missing any cilium that extended beyond the axoneme. These TEM studies confirm that *swip-10* mutation results in striking DA neuron morphological changes.

DA neuron degeneration increases with age

In order to determine whether the DA neuron degeneration observed in *swip-10* animals represents a late onset phenomenon and/or might arise from a progressive perturbation across development, we assayed DA neuron degeneration in *swip-10* mutants across various post-embryonic ages. We observed that *tm5915* animals display time-dependent indications of DA neuron degeneration that are distinct from the changes seen with wildtype animals (Fig. 29). In wildtype animals, signs of DA neuron degeneration are evident only in older, adult animals whereas signs of degeneration are already evident in *tm5915* animals by day 1 (L1 stage) of larval development (Fig. 29 and Fig. 30A). A breakdown of the components that comprise the overall degeneration score of *tm5915* mutants is revealing, where non-uniform patterns are evident across measures. Although we were unable to follow individual DA neuron morphological changes over time, our population findings are suggestive of a progressive form of degeneration at the single neuron level, with dendritic breaks and truncations as earliest signs of degeneration (Fig. 29A and Fig. 30), followed by the appearance of shrunken soma (Fig. 29B), and then by missing soma (Fig. 29C). Overall similar patterns are evident with wildtype animals, just appearing much later in life. Together our findings indicate that *swip-10* mutation begins to disrupt the health of DA neurons early in development with the appearance of indices of morphological perturbations arising in distal processes that progress to neuronal death.

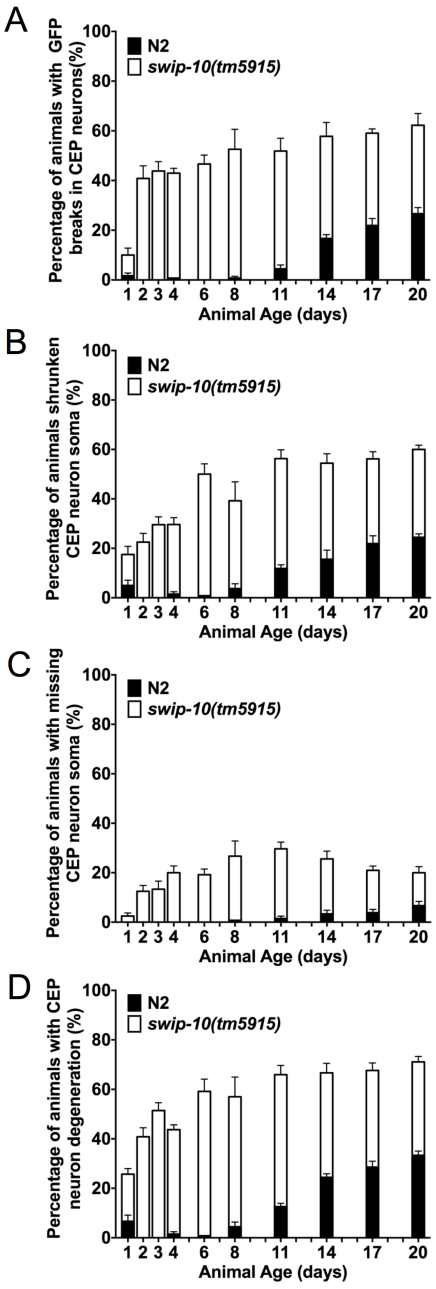

Fig. 29. DA neuron degeneration increases with age, and *swip-10* mutant animals display earlier and more progressive levels of DA neuron degeneration. A. *swip-10(tm5915)* mutants display dendritic breaks/truncations early in development, increasing in frequency with age. B. *swip-10(tm5915)* mutants display shrunken soma earlier in development, increasing in frequency with age compared to N2. C. *swip-10(tm5915)* mutants are missing soma earlier in development, increasing in frequency with age compared to N2. D. As assessed by the combined degeneration index, both N2 and *swip-10* DA neuron degeneration increases with age, though the *swip-10* mutant DA neurons display degeneration at earlier ages than N2. Analyzed by two-way ANOVA with significant differences by age (**** $P<0.0001$) and by genotype (**** $P<0.0001$) and significantly different age by genotype interaction (**** $P<0.0001$). Error bars represent ± SEM, with n=105-150 animals per strain per stage.

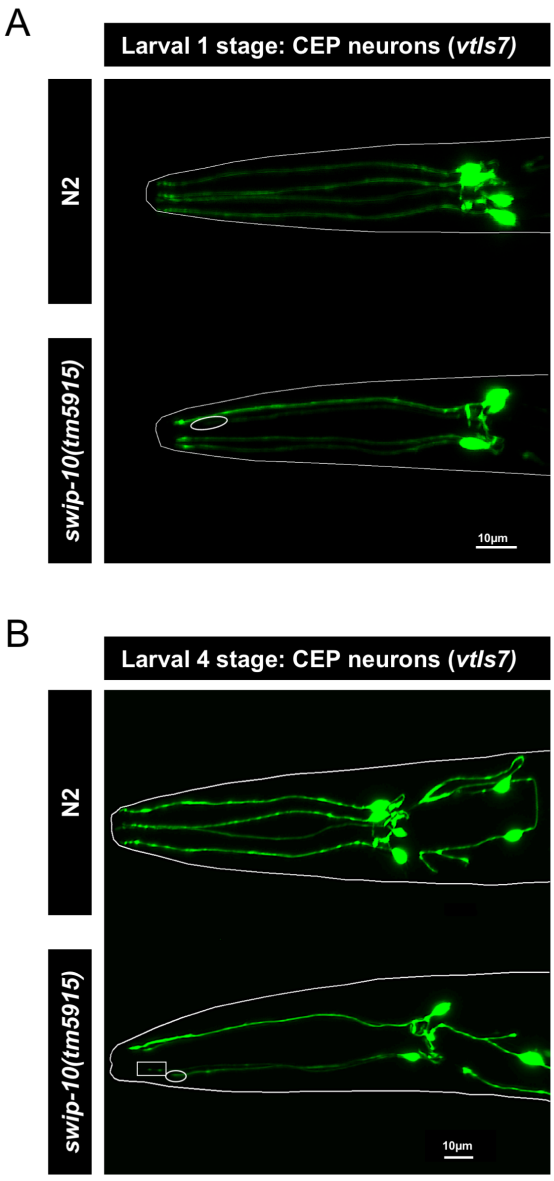

Fig. 30. *swip-10* mutant animals display early and more progressive levels of CEP DA neuron degeneration. A. Representative images of larval stage (L1, day 1)) N2 (top) and *swip-10(tm5915)* (bottom) animals. N2 DA neurons labeled with GFP demonstrating evenly expressed fluorescence throughout the neuronal processes. At the L1 stage, *swip-10* mutant CEP DA neuron display truncated CEP DA neuron dendrites indicated by a white circle. B. Representative images of larval stage (L4, day 4) N2 (top) and *swip-10(tm5915)* (bottom) animals. N2 DA neurons labeled with GFP demonstrating evenly expressed fluorescence throughout the neuronal processes. At the L4 stage, *swip-10* mutant CEP DA neuron display truncated CEP DA neuron dendrites (indicated by a white circle) and breaks in GFP along CEP dendrites (white rectangle). Anterior is left in all images shown, scale bars are 10µm.

While complete loss of *C. elegans* DA neurons, by laser ablation, does not result in obvious changes in the viability of the nematode [154], we sought to determine if loss of *swip-10* resulted in alterations in the lifespan of the nematode. Despite the observed progressive, age-dependent neurodegeneration observed in the CEP DA neurons, *tm5915* animals display a modestly significant increase in median survivability, but have a wildtype-like lifespan (Fig. 31).

No role for DA signaling in *swip-10* neurodegeneration

Mechanisms proposed to support DA neuron degeneration include mishandling of intracellular DA that can form cytotoxic quinones [331, 332]. Thus, elevations in cytosolic DA that arise with pharmacological blockade of the vesicular monoamine transporter (VMAT, *cat-1* in *C. elegans)* by reserpine results in DA neuron degeneration [159], and a genetic reduction of VMAT2 expression causes progressive DA neuron degeneration in mammals [333]. The degeneration of DA neurons in *swip-10* animals does not appear to arise as a consequence of elevations of intracellular DA as disruption of DA synthesis capacity arising from a loss of function mutation in *cat-2,* the *C. elegans* ortholog of tyrosine hydroxylase, the rate-limiting step in DA synthesis, did not alter *tm5915* DA neuron degeneration (Fig. 32A). Extracellular DA elevations can lead to the formation of toxic adducts with vital cell proteins [334] and our prior studies support excess DA secretion in swip-10 animals [146]. However, loss of extracellular DA clearance capacity achieved via mutation of the presynaptic DA transporter, *dat-1,* which triggers Swip [177], did not induce DA neuron degeneration (Fig. 32B).

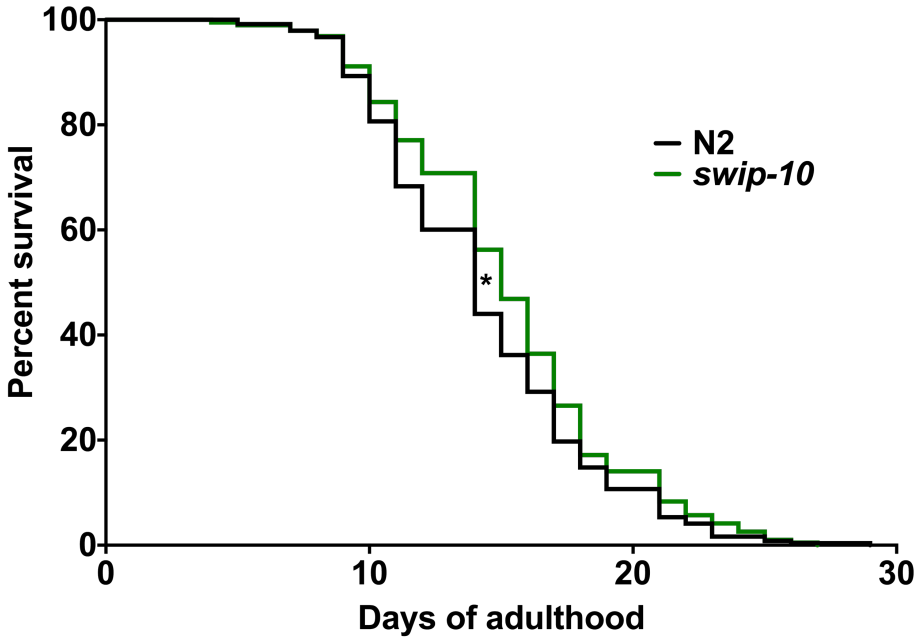

Fig. 31. Loss of *swip-10* does not affect nematode longevity. *swip-10(tm5915)* mutant animals have a significant increase in median survivability compared to N2 (50% of the animals are alive at 15 days versus 14 days respectively), however *swip-10(tm5915)* animals live as long as N2 animals (no significant change in the end of the assay). Analyzed by Mantel-Cox Log Rank, (**P*<0.05) n = 190-240 animals per strain. Experiment performed in collaboration with Peter Rodriguez.

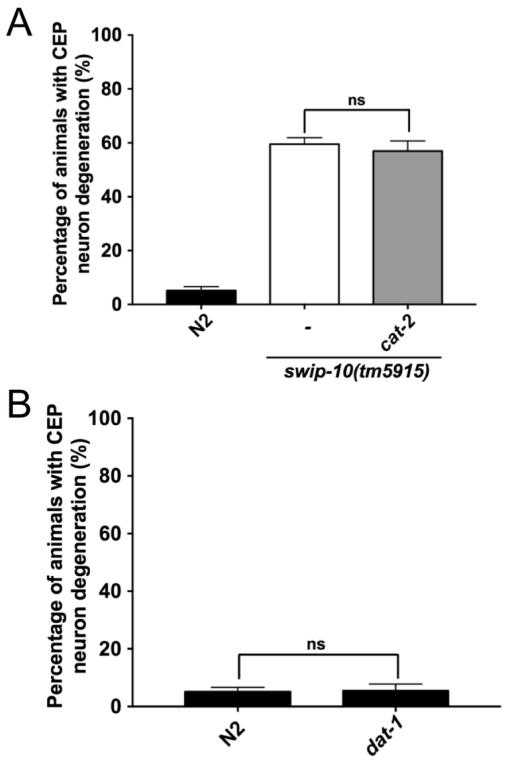

Fig. 32. The DA neuron degeneration of *swip-10* mutants is not a result of aberrant intracellular DA signaling or hyperdopaminergia. A. Disruption of DA synthesis, by loss of the nematode tyrosine hydroxylase ortholog, *cat-2*, does not prevent the DA neuron degeneration of *swip-10* mutant animals. B. Hyperdopaminergia, induced by disrupted DA clearance by loss of the DA transporter, *dat-1,* is not sufficient to induce DA neuron degeneration. Analyzed by Student's *t* test, ns= non-significant (*P*>0.05), error bars represent ± SEM, with n=105-150 animals per strain.

Glial role for *swip-10* in neuron degeneration

Although the Swip behavior of *swip-10* mutants at the L4 stage arises as a consequence of excess DA signaling [180], this paralysis is a cell non-autonomous consequence of glial, and not DA neuron, expression of *swip-10* [146]. To determine whether the degeneration of DA neurons is similarly a consequence of mutation of glial *swip-10*, we expressed a full length wild type *swip-10* cDNA fused to GFP (*swip-10::*GFP*)* under control of glial and DA neuron promotors. Fig. 33A demonstrates that pan-glial *swip-10* expression, as achieved through use of the *ptr-10* promoter (Yoshimura, 2008), robustly rescues DA neuron degeneration of *tm5915* animals, comparable to that achieved with a genomic construct that encodes *swip-10* and the upstream elements needed to achieve full rescue of Swip [146]. Significant rescue of DA neural degeneration was also achieved with the CEP sheath glia-specific promotor *hlh-17* [142]. In contrast, DA neuron specific expression of *swip-10,* driving expression with the *dat-1* promoter, failed to restore normal morphology. Together, these findings support the conclusion that glial expression of *swip-10* is required to maintain the normal viability of DA neurons.

Although not explored extensively, we sought to understand whether neural degeneration in *swip-10* mutant animals is limited to the DA neurons. We chose to evaluate *swip-10* mutant (*tm5915)* animals bearing reporters to demarcate OLL and BAG neurons. Glutamatergic OLL neurons are similar in location and morphology to dopaminergic CEP neurons, are mechanosensitive like CEP neurons, and share an association with glia (OLLsh) that ensheath OLL processes. Carbon-dioxide sensing, glutamatergic BAG neurons are similar in location and morphology to the CEP neurons, although not associated with direct ensheathing or socket glia. We observed

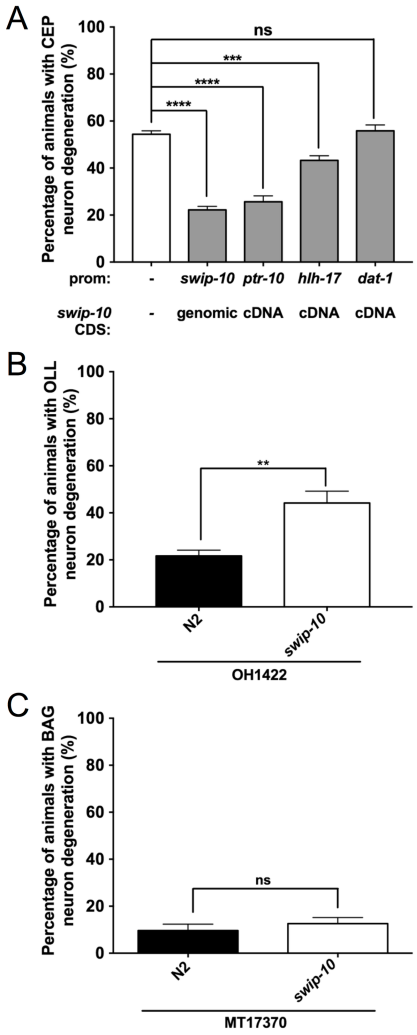

Fig. 33. Glial expressed *swip-10* is required for normal DA neuron morphology, and glial ensheathment may be important for *swip-10* support of neuronal health. A. Expression of *swip-10* genomic fragment significantly restores DA neuron morphology in *swip-10* mutants. Expression of *swip-10* cDNA under the control of a pan glial promoter, *ptr-10*, and not under a DA neuron specific promoter (*dat-1*), significantly reduces *swip-10* DA neurodegeneration, to similar levels as *swip-10* genomic rescue. Additionally, expression of *swip-10* cDNA in the CEPsh glial cell significantly reduces *swip-10* CEP DA neuron degeneration. Data were obtained comparing non-transgenic and transgenic progeny, assayed in parallel. B. The OLL neurons of *swip-10* mutants display morphological characteristics similar to CEP neuron degeneration, including breaks in dendritic GFP, shrunken soma or missing soma (individual components not shown), and quantification of the three components together or "total degeneration" phenotype shows that OLL neurons in *swip-10* mutants are significantly different from N2. C. The BAG neurons of *swip-10* mutants display normal N2 morphology as determined by quantification of total degeneration in gravid adult animals. The horizontal line beneath the genotypes on the x-axis refers to the background strain, B. OH1422, with an integrated OLL neuron transcriptional reporter *(wgIs328*[$P_{ser2prom3}$::GFP]) and C. MT17310, with an integrated BAG neuron transcriptional reporter (*nsIs242*[$_{Pgcy-33}$::GFP]). Data were analyzed using an unpaired Student's *t* test (A-C), with *, **, *** indicating *P*<0.05, <0.01 and <0.001, respectively, ns= non-significant (*P*>0.05), error bars represent ± SEM, with n=105-150 animals per strain.

degeneration of glutamatergic OLL neurons (Fig. 33B) but not of BAG neurons (Fig. 33C). These findings, along with rescue of DA neurodegeneration through glial re-expression of *swip-10*, reinforce a key role for glia in maintaining the viability of *C. elegans* DA neurons.

Discussion

Our findings reveal that loss of glial-expressed *swip-10* results in DA neuron degeneration. By using an integrated DA neuron specific fluorescent reporter, we were able to show and quantify that *swip-10* CEP DA neurons display signs of incipient DA neurodegeneration, dendritic breaks and truncations, and determined that some animals display more severe indices of degeneration, shrunken and/or missing CEP cell soma (Fig. 24). Qualitative, visual inspection of the ADE and PDE DA neurons in gravid adult animals further implicate a role for glial *swip-10* in DA neuron viability not limited to the CEP DA neurons but likely extends to the other *C. elegans* DA neurons, and both the ADE and PDE neurons are tightly associated with glial-like support cells at end of their dendrite-like projections, the ADEsheath/ADEsocket and PDEsheath/PDEsocket respectively (Fig. 26). Interestingly, we note that the PDE DA neurons of *swip-10* mutants do not demonstrate indices of degeneration to the same extent as the CEP DA neurons. We hypothesize that, as the PDE neurons reside in the body of the nematode, distal from the majority of the worm glial cells (including the large sheet-like CEPsh glia that enwrap the nerve ring), that these DA neurons are less vulnerable to the glial disruption due to loss of *swip-10* expression. However, our previous studies, demonstrating the increase in DA vesicular fusion of *swip-10* mutant was assessed in PDE synapses [146],

suggesting that the PDE neurons are sensitive to loss of *swip-10* in the context of generating hyperdopaminergia, and perhaps these DA neurons are responsible for Swip even if the other DA neurons of the worm are degenerating. Future studies to specifically ablate the PDE DA neurons (genetic or laser ablation) could further define the effect of *swip-10* on individual DA neurons. Further analyses are required to quantify the extent to which the ADE and PDE neurons are altered morphologically due to loss of *swip-10*. Although, we predominantly characterized *swip-10* DA neuron viability in gravid (egg-laying) adults, time-dependence studies indicate that early indices of degeneration are evident in larval development, L1 and L4 stages shown in Fig. 30, and all degeneration measures increase across the lifespan (Fig. 29). A predominant display of fragmented or truncated dendrites in young animals versus shrunken or lost soma at later stages (Fig. 29A-B and Fig. 30) suggests that degeneration in individual neurons is progressive, first emerging as altered neurite structure (Fig. 29A), followed by engagement of all compartments and eventually resulting in disappearance of some DA neurons altogether. While technically demanding, following the progressive degeneration of *swip-10* DA neurons over time would provide a clearer picture of the progressive degeneration observed, however as the imaged animals would be exposed frequently to toxic paralytic, we envision the employment of microfluidic devices and 3D confocal imaging capabilities to perform this experiment. This progressive pattern of degeneration is commonly seen with neurons suffering from energy depletion, that can be triggered by excessive stimulation or through metabolic poisoning [335, 336]. While we describe the progressive pattern for *swip-10* mutant induced DA neurodegeneration, as of yet, we have not examined an early developmental role for *swip-10* in regulating DA neuron differentiation

and maturation. CEP DA neurons are observed early in embryogenesis [337] and our transcriptional *swip-10* fluorescent reporter indicates that *swip-10* is highly expressed in several *C. elegans* tissues (including glial and hypodermal expression) during embryonic development. One hypothesis is that glial expressed SWIP-10 has a biphasic role in DA neuron viability, first regulating normal CEP DA neuron development during embryogenesis (i.e. full and correctly placed dendrite extensions) and second plays a critical, supportive role in maintaining DA neuron viability. Future studies aimed at determining a developmental role for *swip-10* may provide valuable insight to normal role for SWIP-10 in *C. elegans* glia.

Most of our observations were obtained with a DA neuron-specific, cytosolic, fluorescent reporter, findings corroborated using a membrane anchored reporter (Figs. 24 and 25). Subsequent studies of *swip-10* mutants using electron microscopy to image DA dendrites and cilia provided clear evidence of physical alterations (Fig. 29) that we believe reflect the declining health of the DA neurons, versus a direct action of *swip-10* or its immediate effectors though further studies are needed. Additional EM studies would also be valuable in investigating the degeneration of *swip-10* mutants at the level of the DA neuron cell bodies, axons, and synapses. While we utilized fluorescent light microscopy to initially describe the effect of *swip-10* loss on ADE and PDE neurons our reporter is more dimly expressed in these neurons, especially the mid-body PDE neurons, and EM studies are better suited to determining detailed morphological changes arising from *swip-10* mutant induced DA neuron degeneration. There are significant greater technical challenges associated with identifying the CEP and ADE DA neurons and their

processes in the densely populated nerve ring, though future studies that make use of correlated light electron microscopy (CLEM) can be envisaged [338].

The discovery that DA neurons degenerate in *swip-10* animals was initially surprising as our identification of *swip-10* derives from a hyperdopaminergic behavioral phenotype [146], though we previously demonstrated reduced DA levels in these animals [180]. Since *swip-10* DA neurons exhibit increased excitability and tonically-elevated DA secretion rates [146], we hypothesize that the degenerative process we have characterized likely contributes to a perturbation of mechanisms that insure a tight control over DA release (e.g. DA autoreceptors), along with a diminished capacity for DA clearance, leading to Swip. Alternatively, a degeneration-induced loss of DA signaling capacity could result in a hypersensitivity of postsynaptic DOP-3 DA receptors, such that DA release arising from water immersion then triggers excessive inhibition of motor neurons and Swip. In support of the latter possibility, movement of *swip-10* animals on plates reveals a heightened sensitivity to exogenous DA [180].

A critical step in defining the mechanism associated with *swip-10* DA neuron degeneration is to determine the site(s) where wildtype *swip-10* expression is required to support normal DA neuron morphology. As with the rescue of DA-dependent Swip behavior [146], we found that glial *swip-10* re-expression, both genomic and cDNA, rescued *swip-10* DA neuron degeneration, whereas DA neuron expression of *swip-10* was without effect (Fig. 33). These findings attest to a cell non-autonomous mode of action and raise the possibility that glial loss of *swip-10* may damage the glial cells themselves, rendering them unable to engage in secretory or contact-mediated support for DA neurons. Although non-quantitative, we detected no obvious morphological

differences between wildtype and *swip-10* glia (Fig. 27), which may indicate that *swip-10* expressing glia are deficient in a capacity to provide specific trophic or metabolic support to DA neurons, versus participating in critical cell autonomous mechanisms. Future studies using higher resolution, EM-based methods should be pursued to refine this analysis. Importantly, we obtained rescue of *swip-10* DA neuron degeneration with a promoter driving wildtype *swip-10* expression in CEP sheath glia. Moreover, degeneration was apparent in OLL neurons that like CEPs are ensheathed by glia but not in BAG neurons, which lack these contacts (Fig. 33B-C). These studies reinforce a contribution of glia to the cell non-autonomous actions of *swip-10* to sustain neuronal viability and suggest that neurons in close apposition to ensheathing glia may preferentially depend on the activity of *swip-10*. While we suggest that loss of *swip-10* affects the viability of neurons requiring close glial support, loss of *swip-10* did not alter the lifespan duration of the nematode (Fig. 31). Despite progressive degeneration and a likely reduction in the health of the animal, *swip-10* animals live as long as N2, and even display an increase in median survivability. As genetic elimination of the capacity to synthesize DA did not reduce *swip-1*0 DA neuron degeneration and aberrant extracellular DA signaling due to hyperdopaminergia via loss of *dat-1* did not induce DA neuron degeneration, we feel it unlikely that *swip-10* induced DA neuron degeneration is resultant from either intracellular or extracellular toxic DA signaling. We suggest a more likely mechanism of neurodegeneration, that excess Glu signaling drives, at least in part, drives the DA neuron degeneration observed in *swip-10* mutant animals.

Our previous studies suggest that the paralysis of *swip-10* arises due to altered extracellular Glu availability and dependent on Glu-signaling [146], a hypothesis

supported by a body of mammalian literature describing the critical role for glia in regulating Glu homeostasis. Additionally, the literature describes the role for glia in regulating extracellular Glu to prevent Glu-induced excitotoxicity and neurodegeneration, therefore we aim to determine if the observed progressive DA neuron degeneration of *swip-10* mutants is reliant on toxic Glu signaling and subsequent activation of cell death mechanisms.

Chapter V

THE METALLO-β-LACTAMSE DOMAIN CONTAINING PROTEIN, SWIP-10, PROTECTS DA NEURONS FROM GLUTAMATE DEPENDENT DEGENERATION AND CELL DEATH[2]

Introduction

Across phylogeny, Glu signaling plays a critical role in regulating neural excitability, thus supporting many complex behaviors. Perturbed synaptic and extrasynaptic Glu homeostasis in the human brain has been implicated in multiple neuropsychiatric and neurodegenerative disorders including Parkinson's disease, where theories suggest that excitotoxic insults may accelerate a naturally occurring process of DA neuron degeneration. We have demonstrated that *swip-10* mutations induce premature and progressive DA neuron degeneration, with light and electron microscopy studies demonstrating the presence of dystrophic dendritic processes, as well as shrunken and/or missing cell soma. We found that the *swip-10*-induced, striking, and progressive degeneration of DA neurons can be suppressed by glial expression of wild type *swip-10*.

Here we provide evidence that a cell non-autonomous action of SWIP-10 sustains DA neuron viability in the context of excess Glu signaling via Ca^{2+} permeable Glu receptors and elevations of cytosolic Ca^{2+} that we hypothesize leads to increased cellular stress and, ultimately, apoptotic cell death. Our findings support SWIP-10 (and by

[2] Adapted from Gibson CL, Balbona JT, Niedzwiecki A, Rodriguez P, Nguyen KCQ, Hall DH, *et al.* Glial loss of the metallo β-lactamase domain containing protein, SWIP-10, induces age- and glutamate-signaling dependent, dopamine neuron degeneration. PLOSGenet. In press. 2018.

extension MBLAC1) as a key protective agent whose further study may yield important insights into risk factors for progressive neurodegenerative disorders and their treatment.

Materials and Methods

C. elegans strains and husbandry

See the Materials and Methods section for Chapter IV for a complete description. Strains used in the studies described in this chapter are enumerated per order of appearance in Table 2.

Plasmid construction and transgenic manipulations

In all cases, insertion of the DNA fragment of interest and the fidelity of the vector was confirmed by sequencing and all PCRs were performed using KAPA HiFi HotStart ReadyMix (Kapa Biosystems). All constructs resulted in C-terminal cDNA fusion to an *unc-54 3'* UTR. For the DA neuron-specific Glu receptor experiments, a PCR product (20ng/μL) was amplified by overlap PCR [324] to include the 700 bp *dat-1* promoter and genomic *glr-1* from the ATG start to 2890 or genomic *nmr-2* from the ATG start to 2974 fused to *unc-54* 3' UTR for injection, along with $p_{unc-122}$:RFP (35ng/μL) and p_{dat-1}:myrRFP (35 ng/μL).

Genetic crosses

See the Materials and Methods section for Chapter IV for a complete description.

Strain no.	Background strain/alleles	Transgene no.	Transgene
BY250		*vtIs7*	p*dat-1*:GFP
BY1175	*vtIs7;swip-10(tm5915)*	*vtIs7*	p*dat-1*:GFP
BY1194	*vtIs7;eat-4(ky5)*	*vtIs7*	p*dat-1*:GFP
BY1184	*vtIs7;vglu-2(ok2356)*	*vtIs7*	p*dat-1*:GFP
BY1190	*vtIs7;vglu-3(tm3990)*	*vtIs7*	p*dat-1*:GFP
BY1195	*vtIs7;eat-4(ky5);swip-10(tm5915)*	*vtIs7*	p*dat-1*:GFP
BY1183	*vtIs7;vglu-2(ok2356);swip-10(tm5915)*	*vtIs7*	p*dat-1*:GFP
BY1185	*vtIs7;vglu-3(tm3990);swip-10(tm5915)*	*vtIs7*	p*dat-1*:GFP
BY1176	*vtIs7;glt-1(ok206)*	*vtIs7*	p*dat-1*:GFP
BY1179	*vtIs7;glt-3(bz34)*	*vtIs7*	p*dat-1*:GFP
BY1180	*vtIs7;glt-4(bz69)*	*vtIs7*	p*dat-1*:GFP
BY1278	*vtIs7;glt-5(bz70)*	*vtIs7*	p*dat-1*:GFP
BY1247	*vtIs7;glt-6(tm1316)*	*vtIs7*	p*dat-1*:GFP
BY1248	*vtIs7;glt-7(tm1641)*	*vtIs7*	p*dat-1*:GFP
BY1292	*vtIs7;aat-1(tm5841)*	*vtIs7*	p*dat-1*:GFP
BY1294	*vtIs7;aat-2(tm5841)*	*vtIs7*	p*dat-1*:GFP
BY1293	*vtIs7;aat-3(tm5203)*	*vtIs7*	p*dat-1*:GFP
BY1327	*vtIs7;aat-5(tm5367)*	*vtIs7*	p*dat-1*:GFP
BY1329	*vtIs7;aat-6(tm2881)*	*vtIs7*	p*dat-1*:GFP
BY1295	*vtIs7;aat-7(tm5480)*	*vtIs7*	p*dat-1*:GFP
BY1307	*vtIs7;aat-9(tm5413)*	*vtIs7*	p*dat-1*:GFP
BY1271	*vtIs7;aat-1(tm5841);swip-10(tm5915)*	*vtIs7*	p*dat-1*:GFP
BY1296	*vtIs7;aat-2(tm5841);swip-10(tm5915)*	*vtIs7*	p*dat-1*:GFP
BY1272	*vtIs7;swip-10(tm5915) aat-3(tm5203)*	*vtIs7*	p*dat-1*:GFP
BY1328	*vtIs7;aat-5(tm5367);swip-10(tm5915)*	*vtIs7*	p*dat-1*:GFP
BY1330	*vtIs7;aat-6(tm2881);swip-10(tm5915)*	*vtIs7*	p*dat-1*:GFP
BY1297	*vtIs7;aat-7(tm5480);swip-10(tm5915)*	*vtIs7*	p*dat-1*:GFP
BY1298	*vtIs7;aat-9(tm5413);swip-10(tm5915)*	*vtIs7*	p*dat-1*:GFP
BY1311	*vtIs7;vglu-3(tm3990);aat-1(tm5841);swip-10(tm5915)*	*vtIs7*	p*dat-1*:GFP
BY1198	*vtIs7;nmr-1(ak4);swip-10(tm5915)*	*vtIs7*	p*dat-1*:GFP
BY1197	*vtIs7;nmr-2(tm3785);swip-10(tm5915)*	*vtIs7*	p*dat-1*:GFP
BY1213	*vtIs7;glr-1(n2461);swip-10(tm5915)*	*vtIs7*	p*dat-1*:GFP
BY1212	*vtIs7;glr-2(ok2342);swip-10(tm5915)*	*vtIs7*	p*dat-1*:GFP
BY1256	*vtIs7;glr-3(tm6403);swip-10(tm5915)*	*vtIs7*	p*dat-1*:GFP
BY1228	*vtIs7;glr-4(ok3239);swip-10(tm5915)*	*vtIs7*	p*dat-1*:GFP
BY1253	*vtIs7;glr-5(tm3506);swip-10(tm5915)*	*vtIs7*	p*dat-1*:GFP
BY1229	*vtIs7;swip-10(tm5915)glr-6(tm2729)*	*vtIs7*	p*dat-1*:GFP
BY1255	*vtIs7;glr-7(tm1824));swip-10(tm5915)*	*vtIs7*	p*dat-1*:GFP
BY1211	*vtIs7;mgl-1(tm1181);swip-10(tm5915)*	*vtIs7*	p*dat-1*:GFP
BY1285	*vtIs7 mgl-2(tm355);swip-10(tm5915)*	*vtIs7*	p*dat-1*:GFP
BY1252	*vtIs7;mgl-3(tm1706);swip-10(tm5915)*	*vtIs7*	p*dat-1*:GFP
BY1227	*vtIs7;glr-1(n2461);nmr-2(tm3785);swip-10(tm5915)*	*vtIs7*	p*dat-1*:GFP

continued from above…

Strain no.	Background strain/alleles	Transgene no.	Transgene
BY1284,BY1286-BY1287	BY250;*nmr-2(tm3785)*	*vtIs7; vtEx293-295*	p*dat-1* :GFP; [p*nmr-2::NMR2 genomic,* p*dat-1::myrRFP,* p*unc122::RFP]*
BY1288-BY1289	BY250;*glr-1(n2561)*	*vtIs7; vtEx290-292*	p*dat-1* :GFP; [pglr-1*::GLR1 genomic, pdat-1::myrRFP, punc122::RFP]*
BY1267-BY1269	BY250;*nmr-2(tm3785);swip-10(tm5915)*	*vtIs7; vtEx293-295*	p*dat-1* :GFP; [p*nmr-2::NMR2 genomic,* p*dat-1::myrRFP,* p*unc122::RFP]*
BY1264-BY1266	BY250;*glr-1(n2561)* ;*swip-10(tm5915)*	*vtIs7; vtEx290-292*	p*dat-1* :GFP; [pglr-1*::GLR1 genomic, pdat-1::myrRFP, punc122::RFP]*
BY1245	*vtIs7;crt-1(ok948)*	*vtIs7*	p*dat-1* :GFP
BY1246	*vtIs7;crt-1(ok948);swip-10(tm5915)*	*vtIs7*	p*dat-1* :GFP
BY1290	*vtIs7;clp-1(ok690)*	*vtIs7*	p*dat-1* :GFP
BY1291	*vtIs7;clp-1(ok690);swip-10(tm5915)*	*vtIs7*	p*dat-1* :GFP
BY1314	*vtIs7;crt-1(ok948);clp-1(690);swip-10(tm5915)*	*vtIs7*	p*dat-1* :GFP
CL2166		*dvIs19*	p*gst-4:* GFP
BY1259	*dvIs19;swip-10(tm5915)*	*dvIs19*	p*gst-4:* GFP
SJ4005		zcIs4	p*hsp-4* :GFP
BY1260	*zcIs4; swip-10(tm5915)*	zcIs4	p*hsp-4* :GFP
TJ356		*zIs356*	p*daf-16* ::DAF-16::GFP + *rol-6(su1006)*
BY1261	*zIs356;swip-10(tm5915)*	*zIs356*	p*daf-16* ::DAF-16::GFP + *rol-6(su1006)*
BY1237	*vtIs7;ced-3(n717)*	*vtIs7*	p*dat-1* :GFP
BY1239	*vtIs7;ced-4(n1162)*	*vtIs7*	p*dat-1* :GFP
BY1308	*vtIs7;ced-9(n1950)*	*vtIs7*	p*dat-1* :GFP
BY1238	*vtIs7;ced-3(n717);swip-10(tm5915)*	*vtIs7*	p*dat-1* :GFP
BY1240	*vtIs7;ced-4(n1162);swip-10(tm5915)*	*vtIs7*	p*dat-1* :GFP
BY1309	*vtIs7;ced-9(n1950);swip-10(tm5915)*	*vtIs7*	p*dat-1* :GFP
BY1312	*vtIs7;ced-1(e1755)*	*vtIs7*	p*dat-1* :GFP
BY1315	*vtIs7;ced-6(n1813)*	*vtIs7*	p*dat-1* :GFP
BY1317	*vtIs7;ced-10(n3246)*	*vtIs7*	p*dat-1* :GFP
BY1313	*vtIs7;ced-1(e1755);swip-10(tm5915)*	*vtIs7*	p*dat-1* :GFP
BY1316	*vtIs7;ced-6(n1813);swip-10(tm5915)*	*vtIs7*	p*dat-1* :GFP
BY1318	*vtIs7;ced-10(n3246);swip-10(tm5915)*	*vtIs7*	p*dat-1* :GFP
BY1186	*vtIs7;acy-1(nu329)swip-10(tm5915)*	*vtIs7*	p*dat-1* :GFP
BY1192	*vtIs7;dapk-1(gk219);swip-10(tm5915)*	*vtIs7*	p*dat-1* :GFP

Table 2. *C. elegans* strains utilized for data collection and figures described in Chapter V.

Confocal imaging

See the Materials and Methods section for Chapter IV for a complete description.

Neurodegeneration assay

See the Materials and Methods section for Chapter IV for a complete description.

Fluorescence microscopy with GFP stress reporters

All fluorescent stress reporter stains were a generous gift from Dr. Matt Gill (Scripps Research Institute, Jupiter, FL). All stress reporter strains were imaged as gravid adult animals grown at 19°C for 48 hrs after transfer to a fresh OP50/NGM plate at the L4 stage. To determine levels of stress we used the transcriptional reporter strains, *dvIs19* [p_{gst-4}:GFP] and *zcIs4* [p_{hsp-4}:GFP] to measure oxidative stress and ER stress respectively. We adapted previously described methods [339, 340]. Briefly, the overall GFP fluorescence intensity/µm per 15-20 3 day adult *swip-10* animals and 15-20 3 day adult N2 animals (with subtracted background fluorescence per animal) was determined, and the fold change GFP intensity compared to N2 signal was calculated for all animals assayed from one population and subsequently averaged over 4 independent days (n=60-75 animals assayed). To determine response to a known inducer of oxidative stress, and serve as positive control, we picked 15-30 L4 N2 and *swip-10* animals to OP50 plates containing 2 mM paraquat (Sigma) mixed with the NGM agar [341]. p_{gst-4}:GFP fluorescence intensity/µm was assayed as described above. To determine susceptibility of *swip-10* mutants to ER stress, we transferred 15-30 L4 N2 and *swip-10* animals to NGM plates containing 10 µg/mL tunicamycin (Sigma) [342]. For the DAF-16

localization experiment, the entire animal was observed, and DAF-16::GFP localization was assessed for each individual animal as 1) cytoplasmic or no nuclear localization 2) partial nuclear localization/ partial cytoplasmic and 3) complete nuclear localization as previously described [343]. Localization percentages were calculated based on total animals assayed per day. For the DAF-16::GFP experiment, imaging slides were prepared individually (blind to genotype) and assayed within 20 min to avoid false DAF-16::GFP nuclear localization due to paralytic exposure or starvation. Individual assays were performed on 8 individual days (50 animals per genotype per day). For each of the fluorescent reporters, images were acquired using identical imaging settings across blinded genotypes and drug treatments, via a Nikon A1R confocal microscope in the FAU Brain Institute Cell Imaging Core using a 4x objective and Nikon Elements capture and analysis software.

Statistical analyses

All statistical tests were performed and graphs generated using Prism version 7.0. Data were analyzed by Student's t-tests, one-way ANOVAs followed by Sudak or Dunnet's post-hoc tests and two-way ANOVAs, where appropriate. A $P<0.05$ was taken as evidence of statistical significance in all cases.

Results

Role of Glu transporters in *swip-10* degeneration

Neural degeneration, more generally, can be triggered by extrinsic or intrinsic activation of cell death genetic programs, first elucidated at a molecular level in *C. elegans*

[291, 344, 345]. Additionally, disruptions of vital cellular processes (e.g. ATP production, membrane permeability, ion gradients or cytoskeletal organization) by genetically encoded neurotoxins or following exposure to reactive chemical species [221, 346, 347], have been shown to lead to the death of neurons. Lastly, excitotoxicity, a form of neurodegeneration with features of both apoptotic and necrotic cell death, is well known in mammalian brain preparations and typically observed in the context of over stimulation of Glu-responsive, ionotropic receptors [193, 215, 347]. Our prior findings that DA neurons in *swip-10* animals display elevated excitability that is dependent on Glu signaling [146] encouraged our consideration of the latter mechanism of DA neuron degeneration. We therefore quantified DA morphological changes in *swip-10* animals bearing loss of function mutations in genes supporting synaptic Glu packaging and Glu signaling, as well as mutations in genes encoding transporters thought to modulate extracellular Glu levels. First, we examined contributions of vesicular Glu transporters (vGLUTs). These proteins are responsible for packaging Glu into synaptic vesicles prior to release [348, 349]. There are three genes that encode proteins homologous to VGLUTs in *C. elegans* (*eat-4, vglu-2,* and *vglu-3)* [350-352] with *eat-4* being the only one functionally characterized to date [349, 353]. Loss of individual vGLUTs (Fig. 34A) had no effect on DA neuron morphology. Interestingly, whereas *eat-4* mutation significantly reduced the Swip behavior of *swip-10* mutants [146], the same *eat-4* allele failed to blunt the degeneration of DA neurons in *tm5915* animals. The *vglu-2* mutation was also unable to reduce DA neuron degeneration. In contrast, loss of *vglu-3* significantly, suppressed DA neuron degeneration (Fig. 34A), suggesting a contribution of vesicular Glu signaling, directly or indirectly, to *swip-10* DA neuron degeneration.

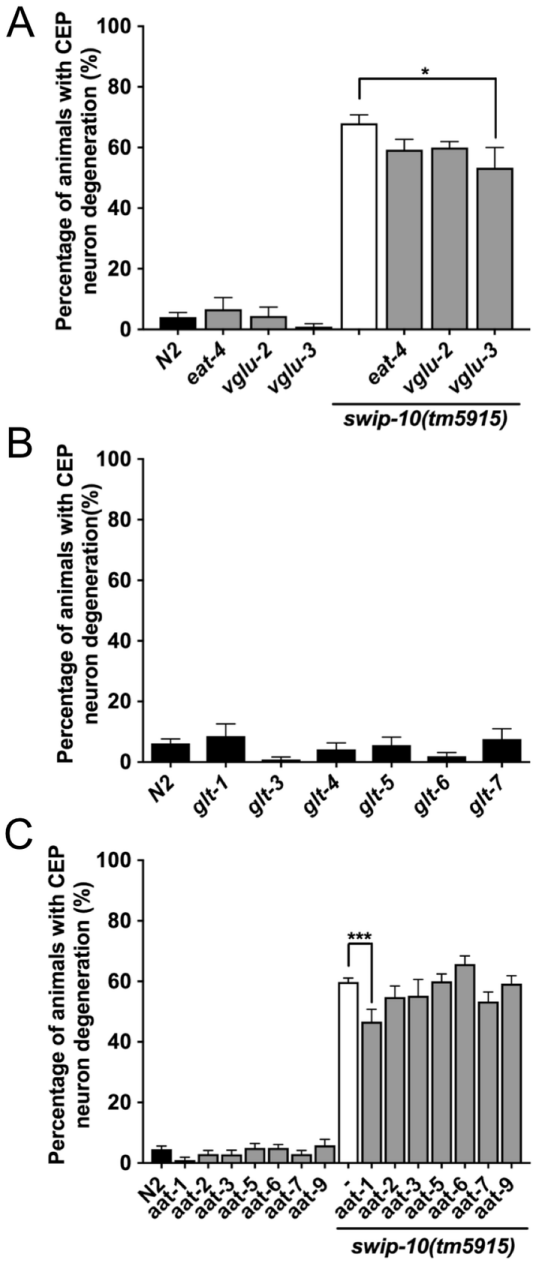

Fig. 34. Disruption of Glu signaling attenuates the DA neuron degeneration of *swip-10* mutants. A. Loss of the vesicular Glu transporter, *vglu-3*, suppresses *swip-10* DA neuron degeneration, whereas loss of *eat-4* or *vglu-2* does not significantly alter the levels of *swip-10* neurodegeneration. B. Disrupting Glu clearance by loss of individual Glu transporters is not sufficient to induced DA neurodegeneration. C. Loss of the amino acid transporter, *aat-1,* but not *aat-2, aat-3, aat-5, aat-6, aat-7 or aat-9*, significantly attenuates the DA neuron degeneration of *swip-10* mutants. Data were analyzed by a one-way ANOVA with Sidak's post-tests, with * and ** indicating $P<0.05$ and <0.01 respectively, error bars represent ± SEM, with n=105-150 animals per strain.

Mammalian glia express multiple Na^+-dependent Glu transporters (GLTs) of the SLC1 family that support efficient clearance of Glu after release at synapses and their dysfunction figures prominently in investigations of Glu-dependent neuronal injury and death [241]. Additionally, our previous studies [146] demonstrated that mutation of several GLTs (*glt1*, *glt3* and *glt4*) conferred DA-dependent Swip. However, we found that mutation of individual *glt* genes failed to induce DA neuron degeneration (Fig. 34B).

A second, glial Glu transport system, xCT, regulates extra-synaptic Glu levels, acting as a cystine/Glu exchanger [255]. xCT imports extracellular cystine in exchange for intracellular Glu, and thus altering the expression or activity of this transporter can modulate extracellular Glu levels. xCT is a member of the mammalian heteromeric amino acid transporter (HAT) family, for which there are 9 *C. elegans* homologs, with the highest homology for xCT being to AAT-1 and AAT-3 [354]. To determine whether xCT-like proteins could contribute to DA neuron degeneration, we generated *tm5915* double mutants with all available *aat* mutants. Of the 7 xCT homologs tested, we found that loss of *aat-1* uniquely attenuated the DA neuron degeneration of *tm5915* (Fig. 34C). These findings implicate non-vesicular Glu release as a contributor to *swip-10* DA neuron degeneration. To determine if both vesicular Glu release supported by VGLU-3 and transporter-mediated Glu release supported by AAT-1 act in parallel or via a shared pathway to support DA neuron degeneration, we examined DA neuron morphology in an *aat-1*;*vglu-3* double mutant. We found no enhancement of the suppression of the *tm5915* degeneration beyond that of the individual mutants (Fig. 35). These findings are consistent with common mechanisms, downstream of extracellular Glu availability

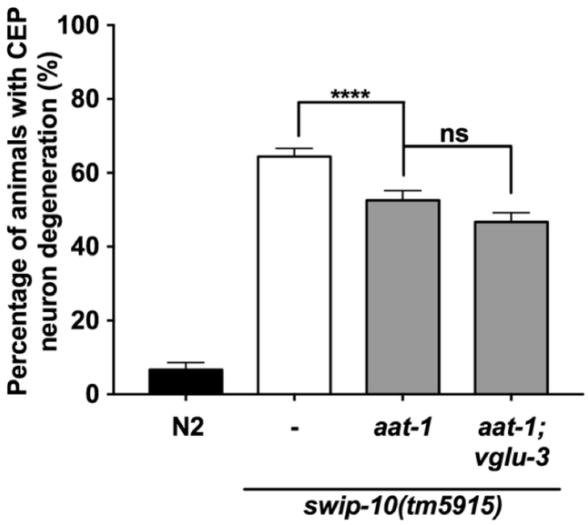

Fig. 35. Combinatorial loss of both *aat-1* and *vglu-3* suppresses *swip-10* neurodegeneration similarly to levels of suppression by individual *aat-1* loss. Data were analyzed by a one-way ANOVA with Sidak's post-tests, ns= non-significant (P>0.05), error bars represent ± SEM, with n=105-150 animals per strain.

through either vesicular or non-vesicular Glu secretion mechanisms, as determinant of the quantitative extent of *swip-10* DA neuron degeneration.

Role of Glu receptors in *swip-10* degeneration

Post-synaptically in both vertebrates and nematodes, Glu binds and activates ionotropic and metabotropic receptors (iGluRs and mGluRs, respectively) [355, 356]. To further pursue the hypothesis that mutation of *swip-10* triggers DA neuron degeneration via excess Glu signaling, we examined DA neuron morphology in *tm5915* lines bearing available mutant alleles for the iGluRs and mGluRs. Among the twelve GluR mutants tested, we found that loss of either the NMDA-type iGluR, *nmr-2,* or loss of the AMPA-type iGluR, *glr-1* [357], significantly suppressed *swip-10* DA neuron degeneration (Fig. 36A). Interestingly, these GluRs are distinct from the GluRs previously shown to suppress the paralysis phenotype of *swip-10* mutants (*glr-4, glr-6* and *mgl-1)* [146]. A double mutant of *glr-1* and *nmr-2* did not further suppress *tm5915* degeneration beyond that seen with either mutant alone, suggesting that these receptors support neurodegeneration through a common pathway (Fig. 36B). To further substantiate that excess GluR signaling via NMR-2 and GLR-1 could support our *swip-10* observations, we selectively overexpressed these receptors in N2 DA neurons and examined CEP neuron morphology. As hypothesized, we detected statistically significant DA neuron degeneration, as compared to non-transgenic lines, similar to that observed in *swip-10* mutants (Fig. 36C). Additionally, we determined that DA neuron selective overexpression of NMR-2 or GLR-1 significantly enhances the DA neuron degeneration of *swip-10* mutant animals (Fig. 37)

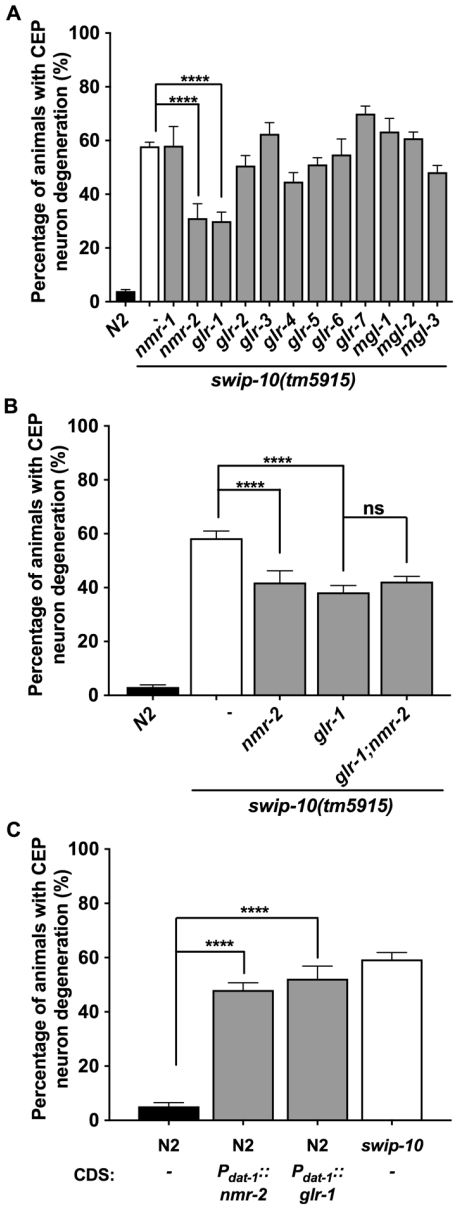

Fig. 36. Support of DA neuron degeneration of *swip-10* mutants by ionotropic Glu receptor signaling and induction of DA neuron degeneration by DA neuron-specific *nmr-2* and *glr-1* overexpression. A. Loss of the Ca^{2+}-permeable ionotropic Glu receptors, *nmr-2* and *glr-1*, suppress *swip-10* mutant DA neuron degeneration. B. Combinatorial loss of both *nmr-2* and *glr-1* does not suppress *swip-10* neurodegeneration beyond the suppression achieved by individual iGluR loss. C. DA neuron-specific overexpression of either *nmr-2* or *glr-1* induces DA neuron degeneration in N2 animals. Analyzed by one-way ANOVA with Sidak's post-tests (A, B) or unpaired Student's *t* test comparing non-transgenic and transgenic progeny, assayed in parallel (C). **** indicates $P<0.0001$ and ns= non-significant ($P>0.05$), error bars represent ± SEM, with n=105-150 animals per strain.

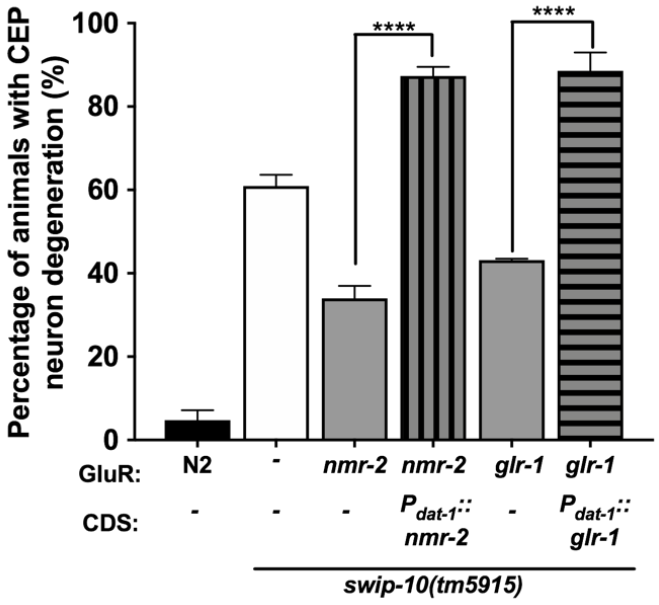

Fig. 37. DA neuron-specific *nmr-2* and *glr-1* overexpression enhances DA neuron degeneration on a *swip-10* mutant background. DA neuron-specific overexpression of either *nmr-2* or *glr-1*, on respective GluR KO, *swip-10(tm5915)* background significantly enhances *swip-10(tm5915)* induced CEP DA neuron degeneration. Analyzed by one-way ANOVA with Sidak's post-tests, **** indicates $P<0.0001$, error bars represent ± SEM, with n=105-150 animals per strain.

further supporting that excess GluR signaling on DA neurons drives *swip-10* induced neurodegeneration.

Role of intracellular calcium signaling in *swip-10* degeneration

The evidence presented above of a role for Ca^{2+}-permeant iGluRs [358] in DA neuron degeneration, as well as our prior findings that *swip-10* DA neurons demonstrate exaggerated Ca^{2+} elevations in response to food contact [146], suggested to us that DA neuron degeneration in these animals could reflect activation of Ca^{2+}-dependent programs linked to apoptotic and/or necrotic cell death [318, 359, 360]. Consistent with this idea, we found that loss of the primary endoplasmic reticulum (ER) Ca^{2+} storage/binding protein, calreticulin (*crt-1)* protected against *swip-10* DA neuron degeneration (Fig. 38). Excessive activation of the Ca^{2+}-activated protease calpain-1, has been shown to lead to cellular damage, including neurodegeneration, in both mammals and *C. elegans* [361-363]. In keeping with these findings, a loss of function mutation of *clp-1,* the *C. elegans* calpain-1 ortholog, significantly attenuated the DA neuron degeneration of *tm5915* animals (Fig. 38). Additionally, we determined that loss of both *crt-1* and *clp-1* resulted in enhanced suppression of *swip-10* DA neuron degeneration above loss of individual aspects of intracellular Ca^{2+} signaling (Fig. 38). Together, these results support the hypothesis that inappropriate or excessive elevations of intracellular Ca^{2+} support *swip-10* DA neurodegeneration.

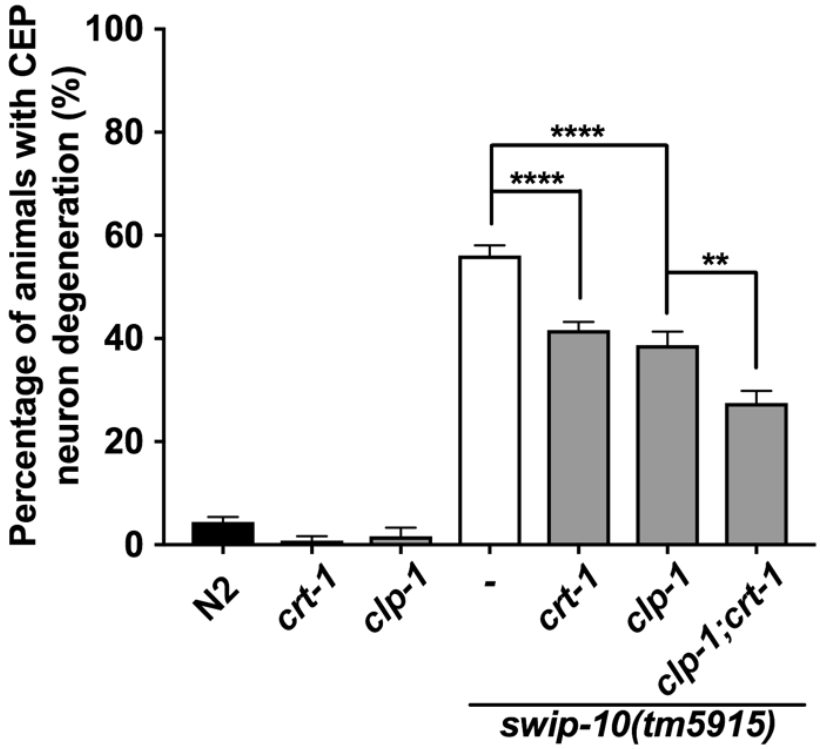

Fig. 38. Contributions of changes in intracellular Ca^{2+} to *swip-10* induced DA neuron degeneration. Calreticulin (*crt-1*) and calpain-1 (*clp*-1) mutations suppress *swip-10(tm5915)* induced DA neurodegeneration, and loss of both *crt-1* and *clp-1* enhances suppression of *swip-10(tm5915)* DA neuron degeneration. Analyzed by one-way ANOVA and Sidak's post-tests, ** and **** indicates a $P<0.01$ and <0.0001 respectively, error bars represent ± SEM, with n=105-150 animals per strain.

Assessing modes of cell stress in *swip-10* mutants

In mammals, aberrant excitotoxic Ca^{2+} signaling can generate reactive oxygen species (ROS) leading to activation of cell stress pathways that drive neuronal cell death [364, 365]. To explore this idea, we inspected *swip-10* animals for signs of oxidative stress by monitoring reporter expression from $P_{gst\text{-}4}$*::*GFP. The *gst-4* gene encodes a glutathione-s-transferase, and is a target for the ROS responsive transcriptional regulator SKN-1(*C. elegans* Nrf2 ortholog) [339, 366]. As shown in Fig. 39, *tm5915* animals basally demonstrate a significant elevation in $P_{gst\text{-}4}$*::*GFP expression. *swip-10* mutants are responsive to the known oxidative stress inducer, paraquat, with an increase in $P_{gst\text{-}4}$*::*GFP expression similar to paraquat induced $P_{gst\text{-}4}$*::*GFP expression in N2 animals, for the 2 μM paraquat concentration used (Fig. 39). As a measure of ER stress, we monitored the transcriptional reporter, $P_{hsp\text{-}4}$*:*GFP [340, 342]. Although *tm5915* animals did not show indications of basal ER stress with this marker (Fig. 40), they were more sensitive to the pharmacological ER stressor, tunicamycin, compared to N2 animals (Fig. 40). Although not explored extensively, we sought preliminary data to implicate a mechanism responsible for the observed *swip-10* loss induced basal expression of the $P_{gst\text{-}4}$*::*GFP. Environmental stress such as heat shock, and pharmacological oxidative stress inducers, including paraquat, have been shown to induce expression of detoxifying enzymes such as GST-4 [367], and oxidative stress has been shown to cause DAF-16 translocation from the cytoplasm to the nucleus to induce expression of detoxifying enzymes [343, 368]. Under basal conditions, *tm5915* animals, show no change in the percentage of animals with partial or complete DAF-16 translocation to the nucleus compared to N2 (Fig. 41).

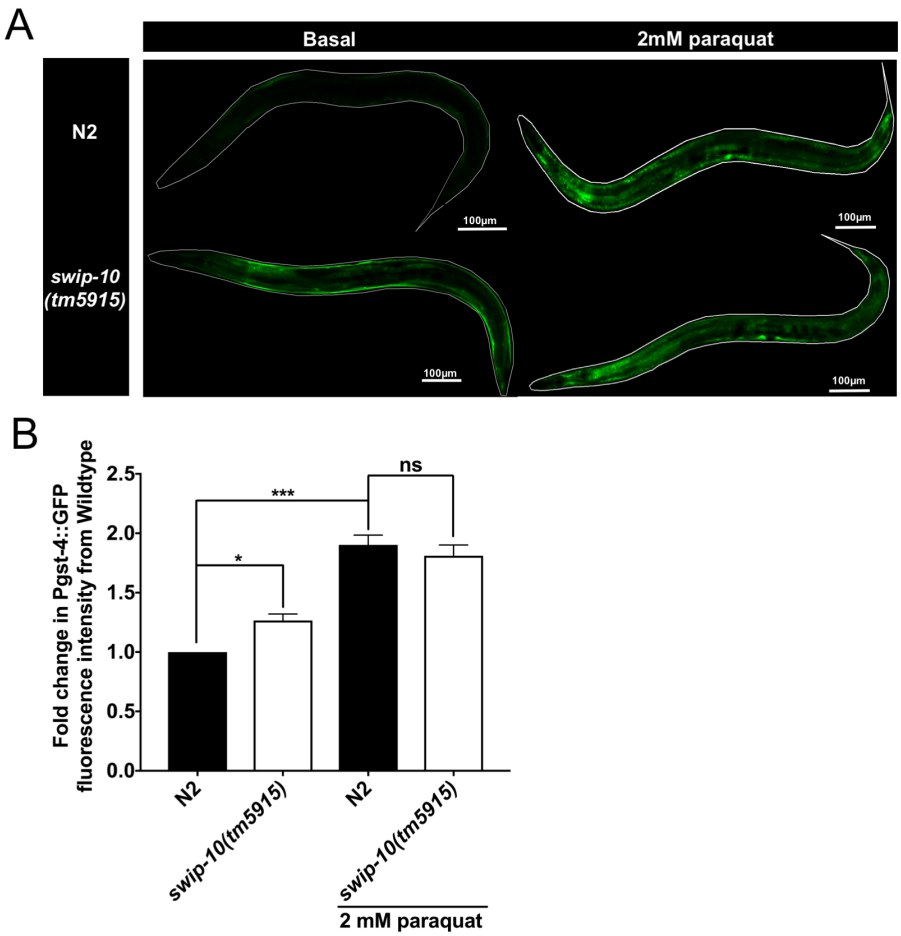

Fig. 39. Loss of *swip-10* induces oxidative stress under basal conditions. A. Representative images of gravid adult, whole body oxidative stress reporter, *dvIs19*[p_{gst-4}:GFP]. Fluorescence for basal N2 and *swip-10* animals and N2, and *swip-10* animals grown on NGM/OP50 plates with 2 mM paraquat are presented, scale bar is 100 µm. B. Normalized reporter fluorescent intensity quantification reveals a significant increase in basal fluorescence in *swip-10* mutants. Both N2 and *swip-10* animals significantly respond to the oxidative stressor, paraquat, and at this concentration of paraquat, N2 and *swip-10(tm5915)* normalized reporter fluorescent intensities are not significantly different. Analyzed by one-way ANOVA and Sidak's post-tests, * and *** indicates a $P<0.05$ and <0.001 respectively, ns = non-significant ($P>0.05$), error bars represent ± SEM, with n=105-150 animals per strain.

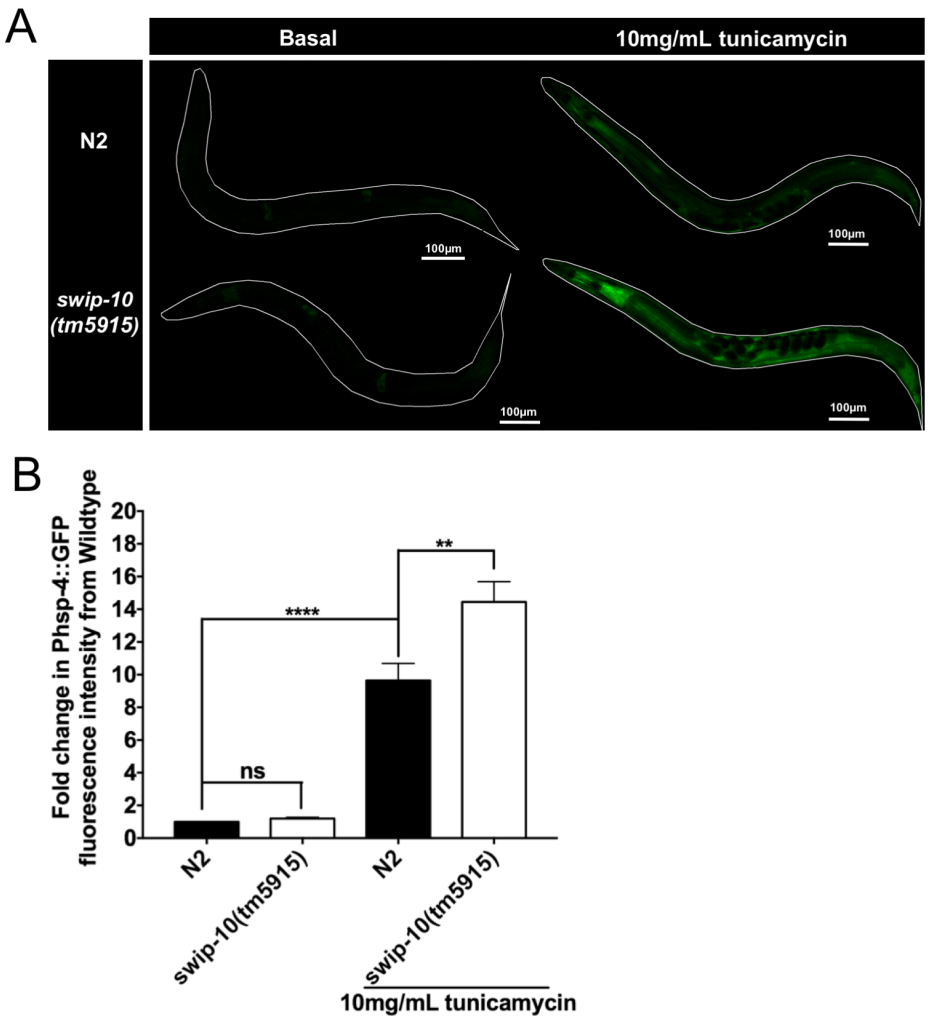

Fig. 40. Loss of *swip-10* increases sensitivity to ER stress. A. Representative images of gravid adult, whole body ER stress reporter, *zcIs4*[p_{hsp-4}:GFP]. Fluorescence for basal N2 and *swip-10* animals and N2, and *swip-10* animals grown on NGM/OP50 plates with 10 mg/mL tunicamycin are presented, scale bar is 100 µm. B. Normalized reporter fluorescent intensity quantification reveals no change in basal ER stress in *swip-10* mutants. Both N2 and *swip-10* animals significantly respond to the ER stressor, tunicamycin, with *swip-10* mutants significantly more sensitive to tunicamycin. Analyzed by one-way ANOVA and Sidak's post-tests, ** and **** indicates a $P<0.01$ and <0.0001 respectively, ns = non-significant ($P>0.05$), error bars represent ± SEM, with n=105-150 animals per strain.

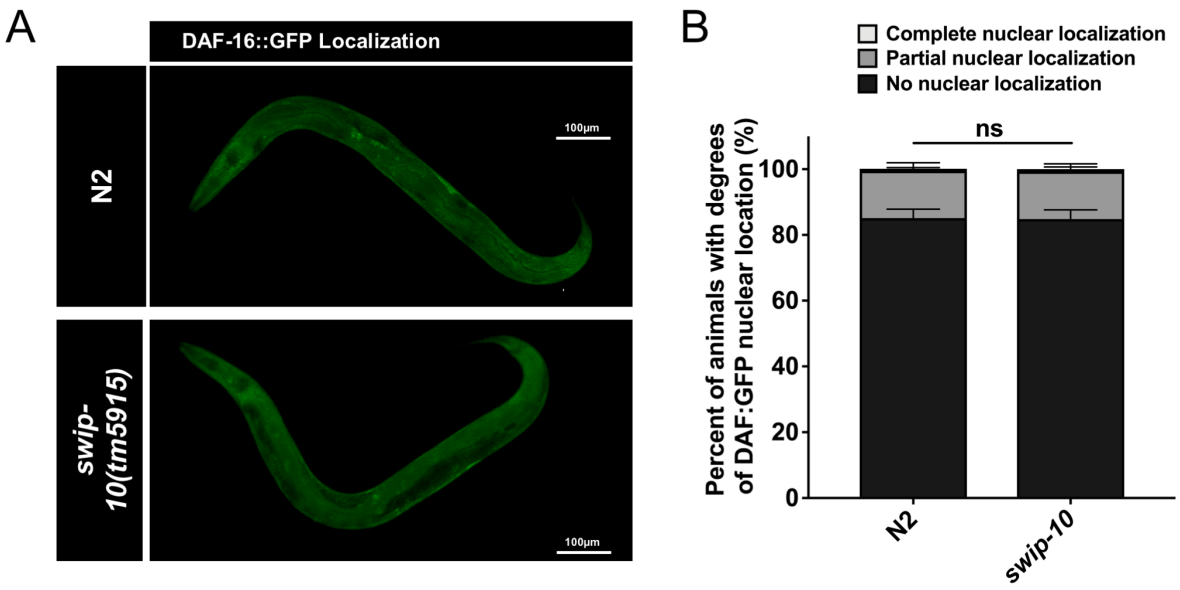

Fig. 41. Loss of *swip-10* does not result in basal changes in DAF-16 nuclear translocation. A. Representative images demonstrate that basally, in N2 and *swip-10ltm59159)* mutant animals, DAF-16::GFP localizes to the cytoplasm. B. Stacked graph representing the percentage of *C. elegans* with DAF-16::GFP no, partial, or complete nuclear localization, demonstrating no difference in DAF-16::GFP localization between N2 and *swip-10(tm5915)* mutants. Analyzed by one-way ANOVA and Sidak's post-tests, ns = non-significant (P>0.05), error bars represent ± SEM, (n=8 independent experiments, 50 animals/experiment per strain).

Apoptotic method of *swip-10* DA neuron cell death

Glu-induced excitotoxic cell death has been reported to arise from multiple mechanisms, including necrosis, autophagy and apoptosis [369], processes that also contribute to cell death in the nematode [344]. Cells dying by necrosis exhibit cell swelling and vacuolization [344], which we do not observe in *swip-10* animals (Fig. 42E-H). In contrast, as described in Fig. 24, DA neurons in *swip-10* mutants display blebbing or breaks in processes (Fig. 24B-C) and shrunken soma (Fig. 24D), features characteristic of apoptosis [370]. Consistent with this idea, we found that loss of function *ced-4* and *ced-3* mutants, well-known contributors to programmed cell death [291], significantly suppressed *tm5915* DA neuron degeneration across all individual indices of degeneration and the total measure of DA neurodegeneration (Fig. 43). Additionally, we found that gain of function *ced-9* mutant animals also a well-known regulator of apoptosis [301], significantly suppressed the more severe measures of DA neuron degeneration, shrunken and missing cell soma, as well as the total degeneration phenotype of *tm5915* mutant animals (Fig. 43). Interestingly, *ced-9, ced-4,* and *ced-3* mutants most robustly suppressed the missing CEP soma phenotype of *swip-10* loss induced DA neurodegeneration (reduced by 45%, 83%, and 65% respectively) (Fig. 43C). Apoptosis in the context of normal developmental programmed cell death is tightly coupled to cell corpse engulfment [371], with two partially-redundant and parallel pathways involving *ced-1/ced-6* [372, 373] and *ced-10* [374] responsible for recognition of dying cells and initiation of cell corpse clearance. Little is known concerning the integration of death and engulfment programs in relation to DA neuron cell death, though Offenburger recently reported contributions from both *ced*-6 and *ced-10* linked engulfment mechanisms in

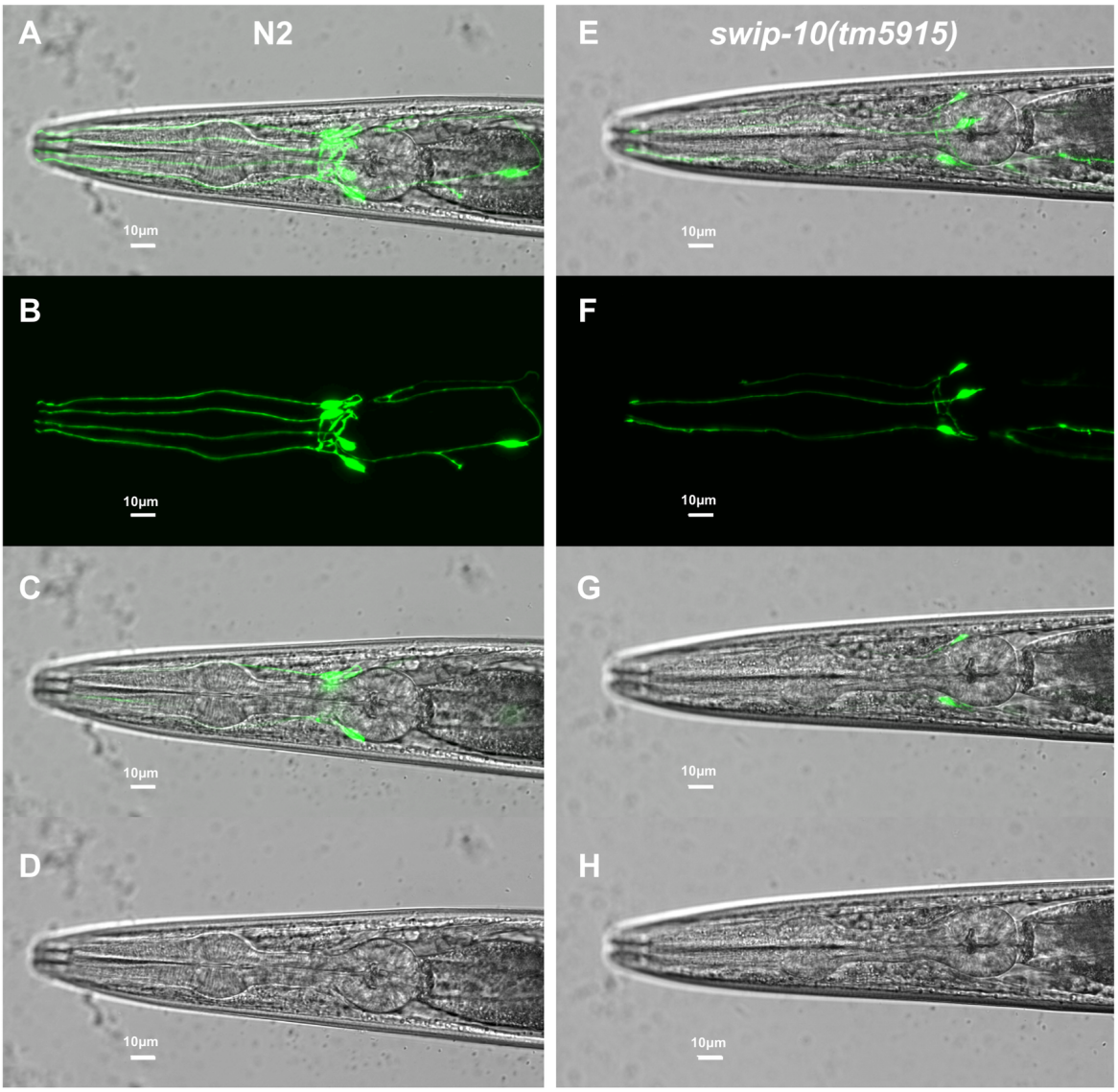

Fig. 42. *swip-10* mutants do not display gross morphological characteristics of necrotic cell death. Single-plane phase contrast images merged with maximum intensity projection confocal image show the relative positions of the CEP DA neurons to the terminal bulb of the pharynx in A. N2 and E. *swip-10(tm5915)* animals. B. and F. show the maximum fluorescence intensity projection confocal image of N2 and *swip-10(tm5915)* animals respectively. C. and G. show the merged single plane phase contrast image and corresponding single plane GFP confocal image at a plane where 1 or more CEP cell soma are in focus for N2 and *swip-10(tm5915)* animals respectively. D. and H. show the single plane phase contrast images for N2 and *swip-10(tm5915)* animals respectively, demonstrating no visible vacuolated or altered cellular structures. Scale bar of 10 microns for A-H.

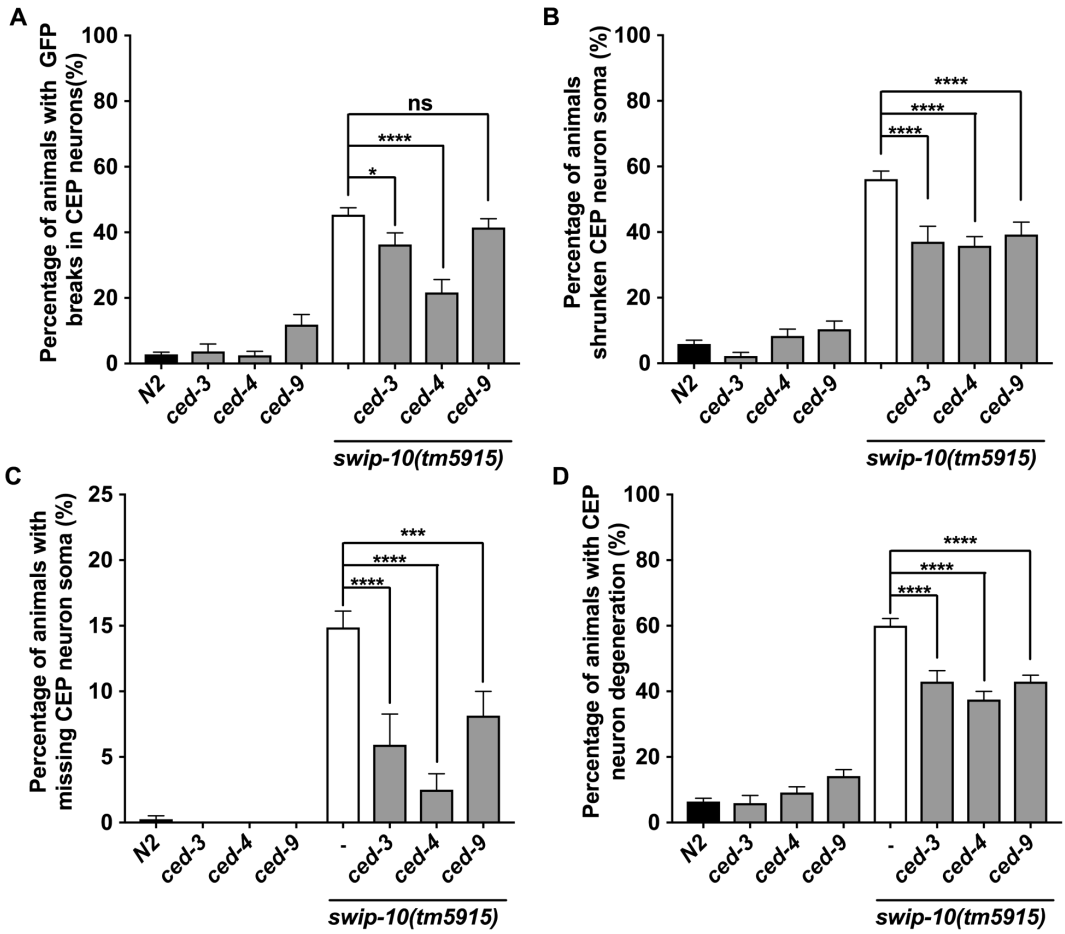

Fig. 43. Genetic evidence for involvement of an apoptotic cell death program underlying DA neuron degeneration in *swip-10* animals. Genetic disruption of the apoptotic cell death pathway, via loss of *ced-3* or *ced-4* or gain of function mutation to *ced-9* significantly reduces *swip-10* mutant CEP DA neuron degeneration, with the most robust suppression of missing CEP soma. Quantification of the components of CEP DA neuron degeneration for A. truncations/breaks in GFP, B. shrunken CEP soma, C. missing CEP soma, and D. total degeneration phenotype, inclusive of all three degeneration measures. *, ***, and **** indicates $P<0.05$, $P<0.001$, and $P<0.0001$ respectively, and ns = non-significant ($P>0.05$), error bars represent ± SEM, with n=105-150 animals per strain.

6-OHDA induced DA neuron degeneration [375]. In contrast, we found that genetic disruption of individual genes associated with *ced-1/ced-6* and *ced-10* had no effect on measures of *swip-10* DA neuron degeneration (Fig. 44). These findings suggest that *swip-10* DA neuron degeneration arises from the activation of a cell-autonomous apoptotic pathway, one that draws little observable support from known engulfment mechanisms.

Discussion

Overall, our findings reveal that loss of glial-expressed *swip-10* results in DA neuron degeneration through a process supported by excess Glu signaling through Ca^{2+}-permeant ionotropic Glu receptors and Ca^{2+}-dependent cell death mechanisms that engage apoptotic cell death pathways, as summarized in Fig. 45.

Having generated evidence for an age-dependent degenerative process impacting the morphology of *swip-10* DA neurons, we pursued mechanistic studies through a combination of genetic and imaging techniques. Such approaches have provided for a systematic elucidation of mechanisms underlying both programmed and environmentally-triggered cell death [160, 291, 296, 376, 377]. In addition to the apoptotic pathways that drive programmed cell death during development, molecular determinants of later stage necrotic neuronal death, that arise as a result of the constitutive activity of mutant ion channels [314, 317] and ligand-gated Glu receptors [378], have been investigated. A potential role for excess Glu signaling in *swip-10* DA neuron degeneration seemed plausible given the contribution of Glu receptors and Glu transporters to Swip reported in our prior study [146]. In this regard, the groups of Driscoll and Mano have provided evidence that necrotic cell death arises with excess Glu signaling that occurs from a

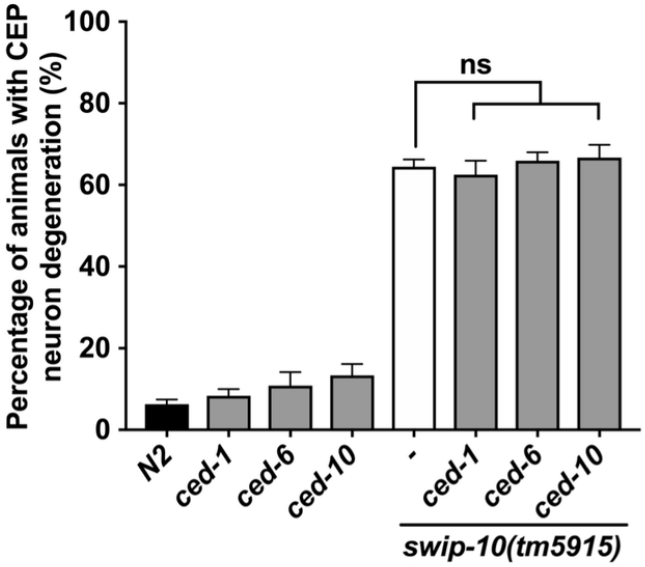

Fig. 44. Genetic evidence for *swip-10* degeneration engagement of apoptotic genes independent of the cell-corpse engulfment of programmed cell death. Genetic disruption of genes involved in cell-corpse engulfment had no effect on the observed DA neuron degeneration of *swip-10* mutants. Analyzed by one-way ANOVA with Sidak's post-tests, ns = non-significant (*P*>0.05), error bars represent ± SEM, with n=105-150 animals per strain.

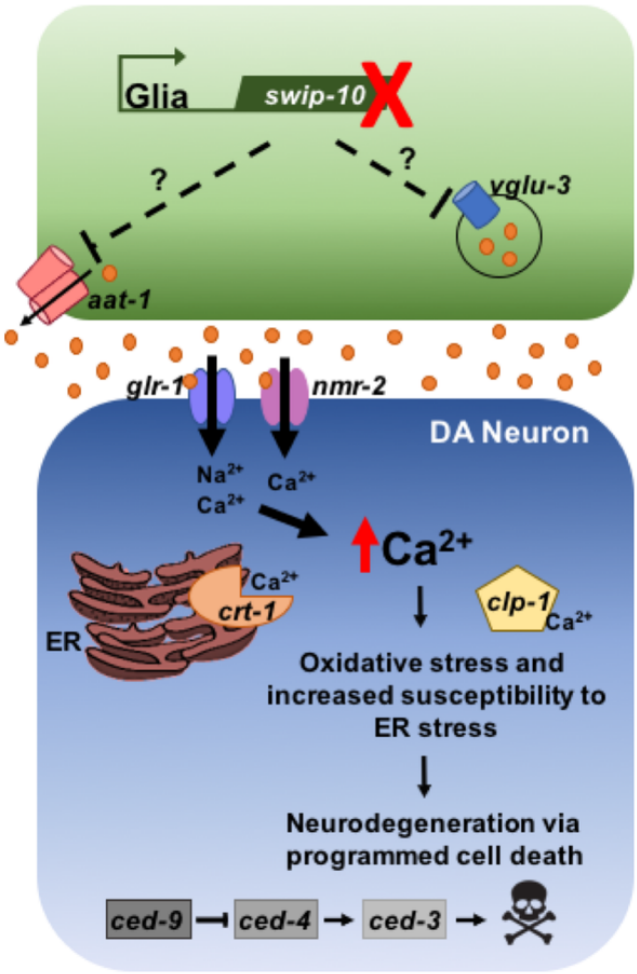

Fig. 45. A suggested mechanism of *swip-10* Glu-induced excitotoxic DA neuron degeneration. Our findings are consistent with glial expressed *swip-10* leading to an elevation of extracellular Glu arising from changes in *aat-1* mediated Glu/Cys exchange or *vglu-3* mediated vesicular Glu release, resulting in the involvement of excess Glu activation of the Ca^{2+}-permeable iGluRs, *nmr-2* and *glr-1.* Elevated tonic iGluR stimulation then drives pathological elevations in intracellular Ca^{2+}-levels, increases cellular stress and activates apoptotic cell death pathways.

combined loss of Glu clearance and a hyperactive, constitutively active form of the alpha subunit of the G-protein, G_s [321-323]. Although *swip-10* DA neuron death shares features associated with the degeneration described in Mano's studies, specifically the contributions from the iGluR, *glr-1* (Fig. 36A), and the intracellular Ca^{2+} sequestering protein, *crt-1* (Fig. 38), our analysis also reveals a number of differences. Thus, besides a lack of morphological evidence of swollen, vacuolated soma seen in prior studies (Fig. 42), we found no evidence for a contribution to *swip-10* induced DA neuron degeneration of the adenyl cyclase ortholog, *acy-1,* nor could we implicate the autophagy-associated, cell death protein kinase, *dapk-1* (Fig. 46) [321, 323].

We also obtained evidence that the damaging effects of *swip-10* mutation are quite distinct from those observed with 6-OHDA induced DA neuron cell death. As a DA neuron specific toxin, 6-OHDA induced DA neuron degeneration is a commonly used in mammalian and *C. elegans* model for Parkinson's disease. Similar to the mammalian mechanism of 6-OHDA toxicity, Nass and colleagues demonstrated that in the nematode 6-OHDA is transported selectively into DA neurons via the DA transporter, DAT-1, and genetic loss of *dat-1* protects against 6-OHDA neurodegeneration [52, 156]. Morphologically, *swip-10* mutant induced, progressive DA neuron degeneration resembles the morphological hallmarks of 6-OHDA induced degeneration. In *swip-10* mutants, DA neuron degeneration progressively worsens from early morphological aberrations, such as dendritic truncations and breaks in dendritic GFP, to the later, more severe measures of degeneration, shrunken/rounded soma, and ultimately missing soma (Fig. 29). Similarly, the earliest and most readily detectible morphological changes due to 6-OHDA toxicity include blebbing of the CEP dendrites and rounding of the CEP soma,

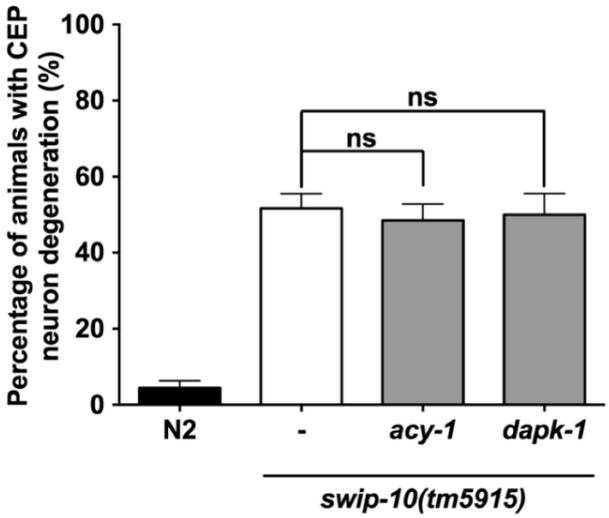

Fig. 46. Mutation of genes previously implicated in Glu-dependent necrotic cell death do not alter *swip-10* induced DA neuron degeneration. Data were analyzed by one-way ANOVA with Sidak's post-tests, ns = non-significant (P>0.05), error bars represent ± SEM, with n=105-150 animals per strain.

with later observation of complete loss of GFP expression in the CEP cell bodies [52]. Despite the morphological parallels in the progression of DA neuron degeneration, our data demonstrate that the mechanism driving DA neuron cell death in *swip-10* mutant animals is distinct from the mechanism of 6-OHDA DA neuron cell death. For example, the degeneration of DA neurons that arises within a day following 6-OHDA administration to wildtype worms lacks contributions from genes that participate in programmed cell death mechanisms [52], whereas, as we discuss below, contributions of these genes are evident in the *swip-10* model. Moreover, recent studies indicate that *ced-6* and *ced-10* dependent engulfment pathways support 6-OHDA induced loss of DA neurons [375], whereas we found no contribution of these engulfment genes to *swip-10* effects (Fig. 44). Moreover, Offenburger and colleagues have reported that 6-OHDA induced DA neuron death is exacerbated by mutation of the Ca^{2+} chaperone *crt-1* whereas we demonstrated that *crt-1* mutation confers neuroprotection in the *swip-10* model [379]. Together, these findings indicate that the DA neuron degeneration induced by *swip-10* mutation is an altogether unique form of neural degeneration as compared to prior glutamatergic and exogenous neurotoxin models.

Our prior studies [146] assessing Swip behavior in *swip-10* mutants provided evidence of perturbed glial control of extracellular Glu that we hypothesized was responsible for the iGluR and mGluR dependence of Swip in these animals. We therefore considered the possibility that perturbed buffering of extracellular Glu by *swip-10* glia also underlies DA neuron degeneration. Mammalian literature emphasizes the critical role of glial Glu buffering mechanisms as protective against Glu excitotoxicity. As first described by Olney and colleagues, Glu excitotoxicity derives from excessive synaptic Glu acting

on post-synaptic iGluRs [380-382], a process recapitulated by the actions of iGluR agonists such as kainic acid and ibotenate [383-385]. Moreover, inhibition of Glu transporters and increased extracellular Glu recapitulates the pathological hallmarks of PD in animal models, including DA neuron degeneration [386]. Our findings that mutations in the Ca^{2+} permeant iGluRs, *nmr-2 and glr-1,* protect against *swip-10* DA neuron degeneration (Fig. 36A), that overexpression of these receptors leads to DA neuron degeneration in wildtype animals (Fig. 36C), and overexpression of these receptors exacerbates the DA neuron degeneration of *swip-10* mutants (Fig. 37), provides strong supportive evidence that glial mechanisms dictating the availability of extracellular Glu are likely disrupted in *swip-10* animals.

Mammalian glia have been reported to modulate extracellular GLU by vesicular release [387], GLU-permeable channels [388], synaptic clearance of Glu by Na^{+}-coupled Glu transporters (GLTs) [241], and extrasynaptic Glu buffering by the cystine/Glu exchanger (xCT) [255, 266]. We found that a mutation in the vesicular Glu transporter *vglu-3* attenuates *swip-10* DA neuron degeneration (Fig. 34A). We were surprised that an *eat-4* mutation did not contribute to *swip-10* induced degeneration, as such a mutation reduced Swip behavior [146]. Although the expression pattern and role for *vglu-3* is undetermined, these findings raise the possibility that EAT-4 supports Glu signaling in the neural circuitry that drives DA neuron excitation in response to water, whereas VGLU-*3* contributes to Glu release directly onto DA neurons, including SWIP-10 expressing glia, and drives tonic activation of Glu receptors on DA neurons and over time, excitotoxicity. Consistent with this model, distinct Glu receptors support Swip (GLR-4*,* GLR-6 and MGL-1) versus DA neurodegeneration (GLR-1 and NMR-2). Although we did not observe DA

neurodegeneration with genetic loss of single GLT orthologs in the nematode (Fig. 34B, unlike Swip [146], this may be due to genetic redundancy among the six GLTs. Indeed, studies by the Driscoll lab demonstrated that loss of one or two GLTs is insufficient to drive Glu-dependent neurodegeneration [389]. In contrast to our inability to implicate specific GLTs, we found that genetic disruption of the xCT related gene, *aat-1,* significantly reduced *swip-10* DA neuron degeneration (Fig. 34C). As with *vglu-3*, the expression pattern for *aat-1* in the worm is undefined, and thus additional studies are needed to determine site(s) of expression that contribute to our results. The effects of *aat-1* mutation were not additive with those of *vglu-3*, suggesting that both genes act to support DA neurodegeneration through a common mechanism (Fig. 35), which we propose is through the control of tonic, extracellular Glu providing tonic excitation of DA neuron expressed Glu receptors. Finally, it is important to note that mammalian xCT is upregulated by the beta lactam antibiotic ceftriaxone [267, 277, 390], which we have shown binds directly to the putative *swip-10* ortholog MBLAC1 [182]. Moreover, research, initiated by findings of Rothstein and colleagues [202], has demonstrated that ceftriaxone is neuroprotective, including in models of DA neuron degeneration [276].

Although not exclusive, Glu-induced neural degeneration often involves activation of Ca^{2+}-permeable NMDA type iGluRs [209, 391, 392] and, as noted, our studies demonstrate an important contribution of Ca^{2+}-permeable *C. elegans* iGluRs, the NMDA-type iGluR, *nmr-2*, as well as the AMPA-type iGluR, *glr-1* in *swip-10* neural degeneration [358] (Fig. 36A). Expression profiling data provides evidence that *nmr-2* and *glr-1* are expressed in DA neurons [393]. Since *swip-10* mutant animals with loss of both *nmr-2* and *glr-1* do not demonstrate enhanced suppression of DA neural degeneration as

compared to single receptor mutations (Fig. 36B), we suggest that the flux of Ca^{2+} through one of these receptors is sufficient to increase intracellular Ca^{2+} to initiate downstream signaling pathways that lead, over time, to neurodegeneration. Aberrant intracellular Ca^{2+} regulation and signaling has been implicated in excitotoxic cell death [219], with evidence supporting a role for Na^{+}/Ca^{2+}-permeable degenerin/epithelial sodium channels (DEG/ENaCs) [148, 222, 223], Ca^{2+}-dependent proteases such as calpain [225, 226], and deficiencies in ER Ca^{2+} buffering [317, 318] in cell death mechanisms. We found that disrupting ER Ca^{2+} storage, by mutation of *crt-1*, or mutation of the *C. elegans* calpain ortholog, *clp-1,* significantly reduced *swip-10* DA neural degeneration (Fig. 38). Additionally, we found combined loss of *crt*-1 and *clp*-1 resulted in enhanced suppression of *swip-10* DA neural degeneration (Fig. 38), suggesting *swip-10* dysregulated intracellular Ca^{2+} signaling leading to cell death arises via activation of Ca^{2+}-dependent proteins, such as calpain, and suggests that in *swip-10* mutants Ca^{2+} normally sequestered in the ER may be released and cause further cell damage.

Ca^{2+} dysregulation following excessive Glu stimulation has also been shown to engender multiple indications of cell stress including oxidative stress and ER stress [230, 394], which *swip-10* mutants display. The observed increase in the basal level of oxidative stress throughout the entire *swip-10* mutant animal supports that loss of *swip-10* does not selectively affect the viability of the DA neurons (Fig. 39). Although we do not see increased sensitivity to the pharmacological inducer of oxidative stress, paraquat, we suspect that this could be a result of a maximum response for the selected paraquat concentration in our experimental conditions. Although *swip-10* mutants did not display basal, global ER stress, they were more sensitive to the ER stress inducer, tunicamycin

(Fig. 40). These findings suggest that *swip-10* mutant animals retain the ability to regulate normal ER function despite excitotoxic signaling, but an added stressor overwhelms *swip-10* mutant animals' capacity to protect against ER stress, thus rendering *swip-10* mutants more sensitive to ER stress. As in mammals, there are several *C. elegans* neuroprotective pathways to protect against oxidative and ER stress, including induced transcription of detoxifying enzymes. Once such pathway in the nematode is through the insulin signaling pathway and translocation of DAF-16 to the nucleus to induce expression of enzymes such as GST-4. Though our studies exploring *swip-10* mutant induction of stress pathways are in their infancy, we do not observe basal changes in DAF-16 localization compared to N2 (Fig. 41), suggesting that the basal oxidative stress we observe in *swip-10* mutants does not engage the DAF-2/DAF-16 signaling mechanism although more thorough, future studies are required to definitively rule out a role for DAF-16 in *swip-10* induced oxidative stress.

Finally, although acute Glu excitotoxicity has been more typically associated with necrosis [207, 209], evidence suggests that chronic dysregulation of Glu signaling and altered intercellular Ca^{2+} homeostasis can lead to activation of apoptotic pathways [395, 396], and a recent study by Anilkumar and colleagues has demonstrated that external factors, such as nutrient availability, determine whether or not excess Glu signaling triggers apoptotic or necrotic cell death [217]. Consistent with this idea, genetic disruption of apoptosis in *C. elegans* [291] significantly reduced the DA neurodegeneration of *swip-10* mutants (Fig. 43). *ced-9, ced-3,* and *ced-4* mutation most robustly suppress the missing CEP soma measure of *swip-10* DA neuron degeneration (Fig. 43C). We suggest this finding provides support for progressive DA neurodegeneration, such that as *swip-10*

DA neuron experience excitotoxic stress and viability is reduced, the dendrites become truncated and/or broken, and ultimately apoptotic mechanisms of cell death are engaged, resulting in missing CEP soma. The progressive DA neuron degeneration we detect in *swip-10* animals supports the occurrence of a chronic insult and thus is in line with our genetic findings of apoptotic program engagement. However, our data suggests that *swip-10* involvement of apoptotic cell death associated genes differs from the involvement of these genes in developmental programmed cell death, as loss of genes critical for cell-corpse engulfment during programmed cell death did not alter the levels of *swip-10* DA neuron degeneration (Fig. 44). Although lack of a reliance on engulfment genes could be a reflection of the partial redundancy of the two major engulfment pathways, we suspect that these findings are indicative of a slower engagement of apoptotic genes in the *swip-10* model. Additionally, the majority of our assays are conducted at a mid-point, with degeneration in progress, to capture various degrees of degeneration in *swip-10* animals, it is possible that we have simply not assessed the correct temporal window for engulfment.

Although we present clear evidence for a significant role of excess Glu signaling in the degeneration of *swip-10* DA neurons, other mechanisms besides changes in extracellular Glu homeostasis are likely to contribute to our observations since Glu homeostasis and signaling mutants afford incomplete suppression of *swip-10* DA neurodegeneration. The elucidation of the normal role and genetic pathway for wildtype *swip-10* in *C. elegans* glial cells will likely clarify other contributors to *swip-10* induced neural degeneration. For example, mammalian glia have been shown to support neurons by buffering ions such as potassium (K^+) and hydrogen (H^+) [397], and by providing

metabolic support via lactate, glutathione, and ATP shuttling [236]. Although only limited data speaks to glial-neuronal crosstalk in worms, we suspect that one or more of these mechanisms contribute to the diminished viability of DA neurons in *swip-10* animals. As our transcriptional stress reporter data indicate a systemic increase in cellular stress mechanisms, it seems entirely likely that the perturbations induced by *swip-10* mutation extend beyond the deficits observed in CEP (and OLL) neuron viability. Since wholesale degeneration is not evident, we suspect that the premature degeneration of DA neurons reflects a more dependent relationship of these cells on glia. The selective loss of nigrostriatal DA neurons in idiopathic PD has been suggested to derive from an intrinsic vulnerability to stress, possibly arising from the reactivity of DA itself, as well as inefficient anti-oxidant protection, ultimately rendering these cells more vulnerable than others to Glu-induced cell death [398]. Since genetic elimination of the capacity to synthesize DA did not reduce *swip-1*0 DA neuron degeneration, we feel it more likely that excess Glu signaling drives degeneration due to a parallel loss of glial metabolic or trophic support required by DA neurons.

In summary, our findings reveal a previously unreported dependence of DA neurons on *C. elegans* glia, one that when disrupted leads to neuronal degeneration. DA degeneration triggered by glial loss of *swip-10* appears to be progressive and dependent on excess Glu signaling through Ca^{2+} permeant iGluRs. We propose that these effects lead to perturbed intracellular Ca^{2+} homeostasis and, progressively, the engagement of apoptotic cell death pathways. Our work adds support to studies in mammals that indicate a critical role of proper glial function in DA neuron viability [399-402] and reveals a new worm model of Glu excitotoxicity, one likely amenable to pharmacological manipulation

that could provide insights to novel therapeutics to treat human neurodegenerative disorders.

Chapter VI

GLOBAL UNTARGETED SERUM METABOLOMIC ANALYSES NOMINATE METABOLIC PATHWAYS DEPENDENT ON THE EXPRESSION OF THE ORPHAN METALLO-β-LACTAMASE, MBLAC1[3]

Introduction

Despite the availability of a human genomic blueprint for nearly two decades, over 50% of proteins remain to be functionally annotated [403-405]. Many of these undefined proteins have predicted structural domains that suggest a potential, but undefined, physiological function. Both SWIP-10 protein, and its putative mammalian ortholog, MBLAC1, contain a single metallo β-lactamase (MBL) domain [146, 406]. Supporting the hypothesis that both SWIP-10 and MBLAC1 proteins function as enzymes, the MBL domains of both proteins possess the core motif (HxHxDH) found in prokaryotic and eukaryotic metallo-hydrolases that supports the coordination of metal ions to allow water polarization and substrate hydrolysis [407, 408]. The substrates for both SWIP-10 and MBLAC1, however, have yet to be identified, and further progress on their contribution to cell physiology will require their identification and elucidation of the molecular pathways within which they act.

In eukaryotes, the MBL domain has been repurposed to support hydrolysis of a diverse array of substrates ranging from intermediary metabolites (i.e. glyoxalase II

[3] Adapted from Gibson CL, Codreanu SG, Schrimpe-Rutledge AC, Retzlaff CL, Wright J, Mortlock DP, et al. Global untargeted serum metabolomic analyses nominate metabolic pathways dependent on expression of the orphan, metallo β-lactamase, MBLAC1. Molecular Omics. *Resubmitted*.

hydrolyzes the toxic 2-oxoaldehyde, methylglyoxal) and lipids to RNA and DNA [181, 406, 409]. As such, prediction of the substrate(s) targeted by SWIP-10/MBLAC1 remains a challenge.

In theory, clues to potential SWIP-10/MBLAC1 substrates and associated metabolic pathways may be gathered through evaluation of molecular differences emerging from a comparison of normal animals and animals deficient in enzyme expression. Although we have significant functional information in worms concerning the cellular and physiological impact of *swip-10* mutations, the gene is expressed in a small number of cells, making a biochemical comparison between wildtype and mutant strains problematic. In contrast, the murine *Mblac1* gene is widely expressed. Thus, we opted to characterize biochemical differences between wildtype (WT) and *Mblac1* knockout (KO) mice, produced using a CRISPR/Cas9 approach [410, 411]. Here, we report both our successful generation of viable *Mblac1* knockout (KO) mice and our efforts to use these animals to investigate the *in vivo* biochemical impact of loss of MBLAC1 expression.

Here we present the results of our efforts to interrogate the serum metabolome of MBLAC1 KO and age-matched WT mice. To resolve serum small molecules responsive to loss of MBLAC1 expression, we implemented an ultra-performance liquid chromatography coupled to mass spectrometry (UPLC-MS/MS)–based analysis. We report the presence of unique biosignatures that distinguish the sera of MBLAC1 KO from WT mice, with replicated, over-representation of features linked to primary bile acid biosynthesis, and linoleate metabolism. We discuss these networks in the context of the emerging biology of the MBLAC1 ortholog SWIP-10, as well as the neuroprotective actions of chronic Cef administration.

Materials and Methods

Generation of Mblac1 KO mice

Initial untargeted metabolomics experiments and generation of the Mblac1 KO mice were performed under a protocol approved and annually reviewed by the Vanderbilt Institutional Animal Care and Use Committee. For a subsequent pathway validation metabolomic study, experiments were performed under a protocol approved and annually reviewed by the Florida Atlantic University Institutional Animal Care and Use Committee. In all experiments, mice were housed on a 12:12 LD cycle with food and water available *ad libitum*. To implement a CRISPR/Cas9 based strategy for producing *Mblac1* KO mice, we utilized software developed in the Zhang laboratory (Massachusetts Institute of Technology, http://crispr.mit.edu.proxy.library.vanderbilt.edu) to evaluate sequences in the first exon, where we identified an optimal protospacer adjacent motif (PAM) sequence located 43-45 bp 3' of the ATG start site. We generated a guide RNA with sequence that matched the protospacer adjacent to the PAM - 3' to 5': GGAAACGACCGCAGGTCGCCG (PAM site underlined). Sense and antisense oligonucleotides (Sigma Aldrich, St. Louis, MO) encoding the guide RNA were annealed and inserted into the plasmid pX330, a gift from Feng Zhang (Addgene plasmid #42230) which also encodes CAS9 [412]. Injection of the plasmid into C57BL6/J embryos was performed in the Vanderbilt ES/Transgenic Mouse Core. From these injections one male pup was identified as having a 5 bp deletion at the targeted site, deleting bp 46-50, and another male pup was identified as having a 14 bp deletion at the targeted site, deleting bp 44-57, as verified by Sanger sequencing (Genewiz). KO mice referred to in the present

study represent progeny of the 5bp deletion founder. Genotyping of MBLAC1 KO mice was performed by TransnetYX, Inc (Cordova, TN, USA) using separate PCR reactions to genotype for WT (forward primer: GACAGCGATAGTTTAGTTTC, and reverse primer: TTGCTGGCGTCCAGCGGC), 5 bp deletion MBLAC1 KO (forward primer: GACAGCGATAGTTTAGTTTC and reverse primer: TCCCTGGCGTCCAGCGGC) and 14 bp deletion MBLAC1 KO (forward primer: CGAGCCCCTGCATCCT and reverse primer: GCCGCGCAGCAGAAC). KO mice were mated with WT C57BL6/J females and heterozygous KO pups were outcrossed to C57BL6/J mice for 3 additional generations to limit the presence of off-target mutations in mice used for analysis.

Evaluation of MBLAC1 protein expression by western blotting

All chemicals used in tissue homogenization and immunoblotting assays, unless otherwise specified, were obtained from Sigma-Aldrich (St. Louis, MO, USA). For western blots, male mice were killed by rapid decapitation and whole brains were removed to an ice-cold metal plate and dissected into specific regions. Freshly dissected brain regions were homogenized in RIPA buffer (50 mM Tris, pH 7.4, 150 mM NaCl, 1 mM EDTA, 1% TRITON X-100, 1% sodium deoxycholate, 0.1% SDS) with a Dounce homogenizer and then solubilized for 1 hr at 4°C while rotating. Protein lysates were centrifuged at 4°C for 30 min at 15,000*xg* to remove insoluble material. Protein concentrations of supernatants were determined using the BCA method (ThermoFisher, Waltham, MA, USA) and 40 µg of brain (cortical tissue) protein and 60 µg of liver protein was separated by 10% SDS-PAGE, transferred to PVDF membranes (Miillipore Sigma, Billerica, MA, USA). Membranes were blocked using 5% dry milk in TBS/0.1% Tween (TBST) for 1 hr at room

temperature (RT) prior to incubation with affinity-purified MBLAC1 #4980 antibody (1:1000 dilution in 5% milk with TBST – incubated overnight at 4°C followed by 4 x 5 minutes with TBST) [182]. HRP-conjugated, mouse anti-rabbit secondary antibody (Jackson ImmunoResearch, West Grove, PA) was used at 1:10000 dilution. β-actin was detected using a 1:20,000 dilution of β-actin-HRP antibody (Sigma-Aldrich, St. Louis, MO). Immuno-reactive bands were identified by chemiluminescence (Clarity, BioRad, Hercules, CA, USA) and imaged with an LAS4000 imager (GE Healthcare Life Sciences, Pittsburg, PA, USA) and analyzed with associated ImageQuant™ software (GE Healthcare Life Sciences, Pittsburg, PA, USA).

Serum sample preparation

Our initial untargeted study made use of the serum collected from three, age- (12-16 wks) and sex-(female) matched WT and KO mice. WT mice were commercially obtained C57BL/6J mice (Jackson Labs, Bar Harbor Maine, USA). Our subsequent pathway validation study reported is derived from serum collected from four sex-(female) matched WT and KO littermates (aged 12-16 weeks). Following rapid decapitation of mice, 0.5-0.75 mL trunk blood (blood immediately collected from the body at the site of decapitation) was collected, allowed to coagulate on ice for 30 min and centrifuged (15 min at 5,000 rpm). Serum (50 µL) was collected into fresh tubes followed by addition of ice cold 80% methanol (5x by volume), then stored at -80°C overnight. On the next day samples were centrifuged at 10,000 rpm for 15 min to eliminate precipitate proteins. This methanol precipitation step was repeated and the metabolite containing supernatant was dried via speed-vacuum and stored at -80°C until analysis.

Global, untargeted UPLC-MS/MS analysis

For mass spectrometry analysis, dried extracts were reconstituted in 100 µL of acetonitrile/water (80:20, v/v) and centrifuged for 5 min at 15,000 rpm to remove insoluble material. Quality control (QC) samples were prepared by pooling equal volumes from each experimental sample. Full MS (FMS) data was acquired for this QC pool, in both HILIC-POS and HILIC-NEG methods, to use as a retention time alignment reference within Progenesis QI for subsequent normalization and data quantitation. MS/MS acquisitions for pooled QCs were run to assess instrument performance over time and used for feature annotation (described below).

MS analyses were performed on a Q-Exactive HF hybrid mass spectrometer (Thermo Fisher Scientific, Bremen, Germany) equipped with a Vanquish UHPLC binary system and autosampler (Thermo Fisher Scientific, Germany). Extracts (5uL injection volume) were separated on a SeQuant ZIC-HILIC 3.5 µm, 2.1 mm × 100 mm column (Millipore Corporation, Darmstadt, Germany) held at 40°C. Liquid chromatography was performed at a 200 µL min^{-1} using solvent A (5 mM ammonium formate in 90% water, 10% acetonitrile) and solvent B (5 mM ammonium formate in 90% acetonitrile, 10% water) with the following gradient: 90% B for 2 min, 90-40% B over 16 min, 40% B held 2 min, and 40-90% B over 10 min, 90% B held 10 min (gradient length 40 min). Full MS analyses were acquired over a mass range of m/z 70-1050 under an ESI positive profile mode and separately under an ESI negative profile mode. Full mass scan was used at a resolution of 120,000 with a scan rate at ~3.5 Hz. The automatic gain control (AGC) target was set at 1×10^6 ions, and maximum ion injection time (IT) was at 100 ms. Source ionization

parameters were optimized with the spray voltage at 3.0 kV, and other parameters were as follows: transfer temperature at 280 °C; S-Lens level at 40; heater temperature at 325 °C; Sheath gas at 40, Aux gas at 10, and sweep gas flow at 1. Data dependent (DD) MS/MS spectra were acquired using a data dependent scanning mode in which one full MS scan (m/z 70-1050) was followed by 2 MS/MS scans. MS/MS scans are acquired in profile mode using an isolation width of 1.3 *m/z*, stepped collision energy (NCE 20, 40, 60), and a dynamic exclusion of 6 s. MS/MS spectra were collected at a resolution of 15,000 with an AGC target set at 2×10^5 ions, and IT of 100 ms. To assess instrument performance and reproducibility throughout our experimental run sequence, we monitored the retention times and peak areas for a subset of identified endogenous molecules (n=10) observed in the QC pool runs (visualized using Skyline (www.skyline.ms)(MacLean, Tomazela et al. 2010)). These data (Fig. 47-50) demonstrate the reliability of our UPLC-MS/MS platform.

Metabolite data processing and analysis

UPLC-MS/MS raw data were imported, processed, normalized, and reviewed using Progenesis QI v.2.1 (Non-linear Dynamics, Newcastle, UK). All FMS sample runs were aligned against a FMS QC pool reference, with alignment to the reference being ≥ 97% aligned, demonstrating the reproducibility of the HILIC column separation method. Peak picking, with a minimum threshold of 250,000 ion intensity, was performed for individual aligned runs based on an aggregate run (representative of all ion peaks detected in all samples). Unique ions (retention time and m/z pairs) were grouped (a sum

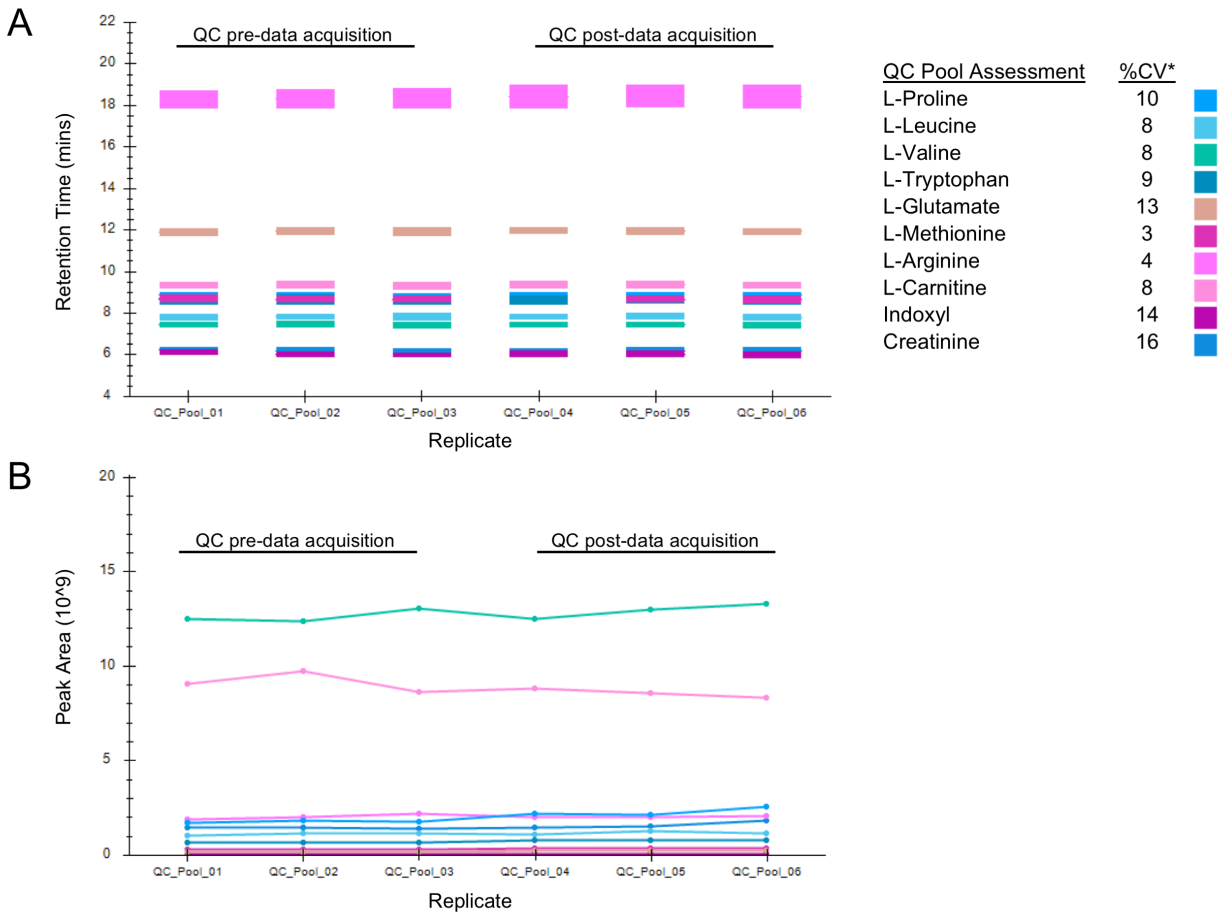

* %CV was calculated within Progenesis QI by normalizing to all features.

Fig. 47: Comparison of ten endogenous molecules in replicate injections of a pooled sample for QC assessment prior to and after the experimental sample data acquisition for *HILIC-POS collection, discovery sample set*. A. The retention time and B. peak area for the ten endogenous compounds are reliable and reproducible (compound legend indicates respective %CVs). Figures were generated in Skyline software.

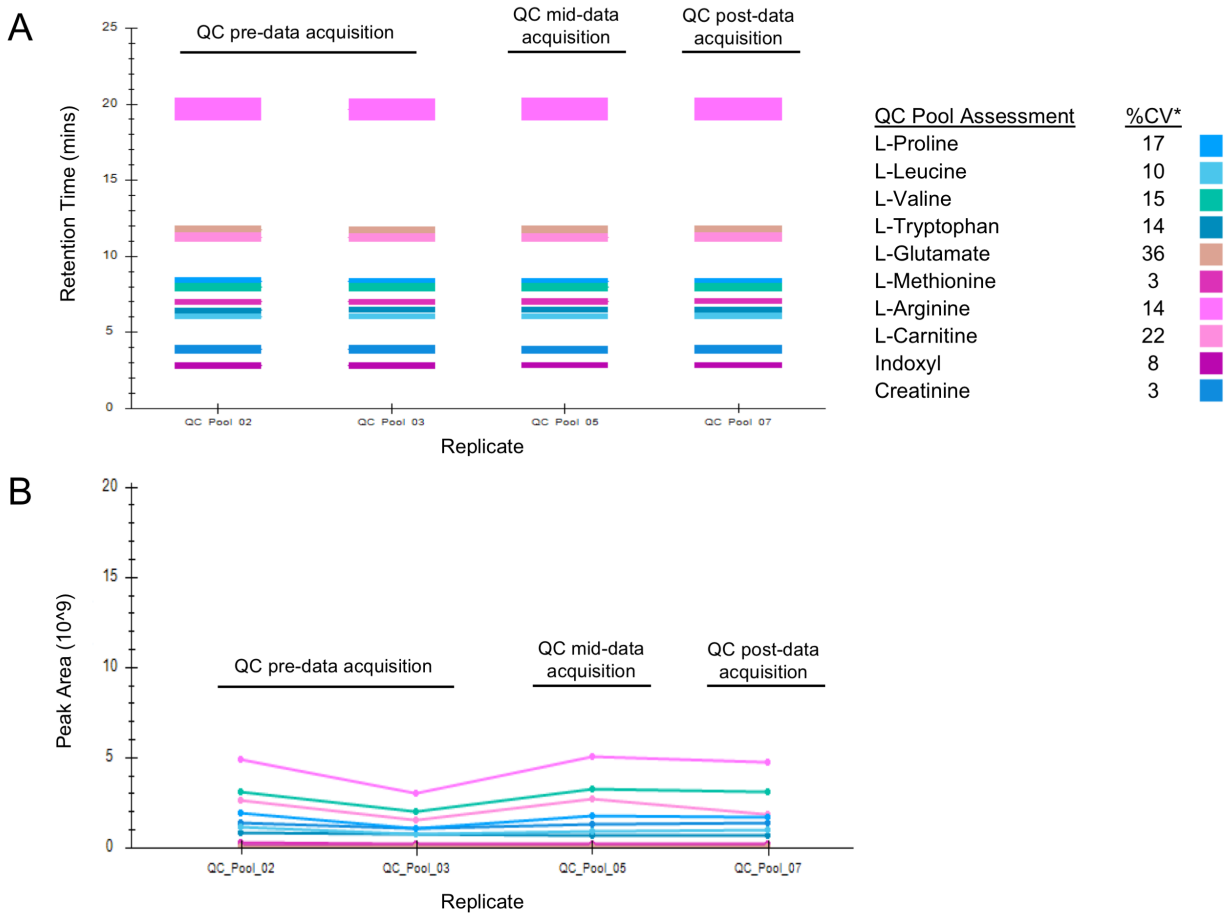

* %CV was calculated within Progenesis QI by normalizing to all features.

Fig. 48: Comparison of ten endogenous molecules in replicate injections of a pooled sample for QC assessment prior to, during, and after the experimental sample data acquisition for *HILIC-POS collection, validation sample set*. A. The retention time and B. peak area for the ten endogenous compounds are reliable and reproducible (compound legend indicates respective %CVs). Figures were generated in Skyline software.

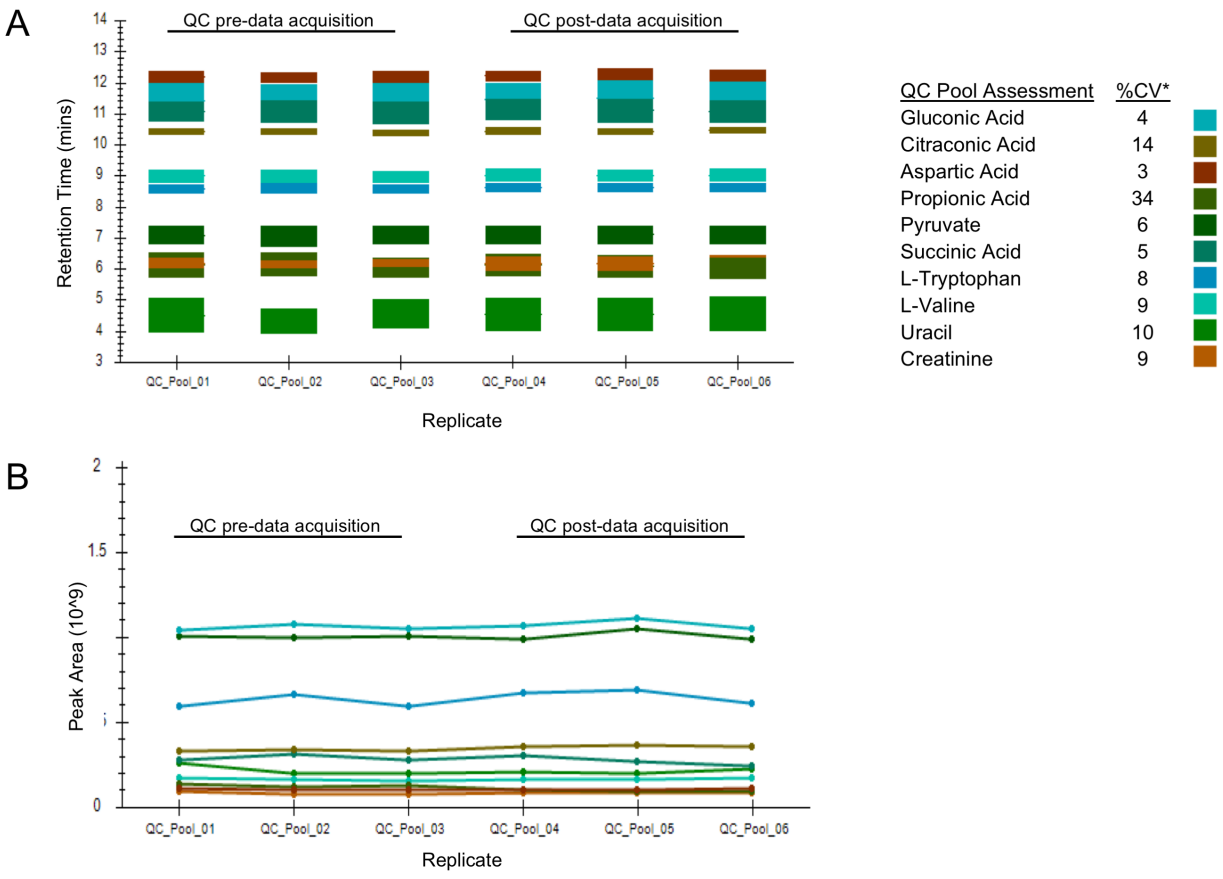

* %CV was calculated within Progenesis QI by normalizing to all features.

Fig. 49: Comparison of ten endogenous molecules in replicate injections of a pooled sample for QC assessment prior to and after the experimental sample data acquisition for *HILIC-NEG collection, discovery sample set*. A. The retention time and B. peak area for the ten endogenous compounds are reliable and reproducible (compound legend indicates respective %CVs). Figures were generated in Skyline software.

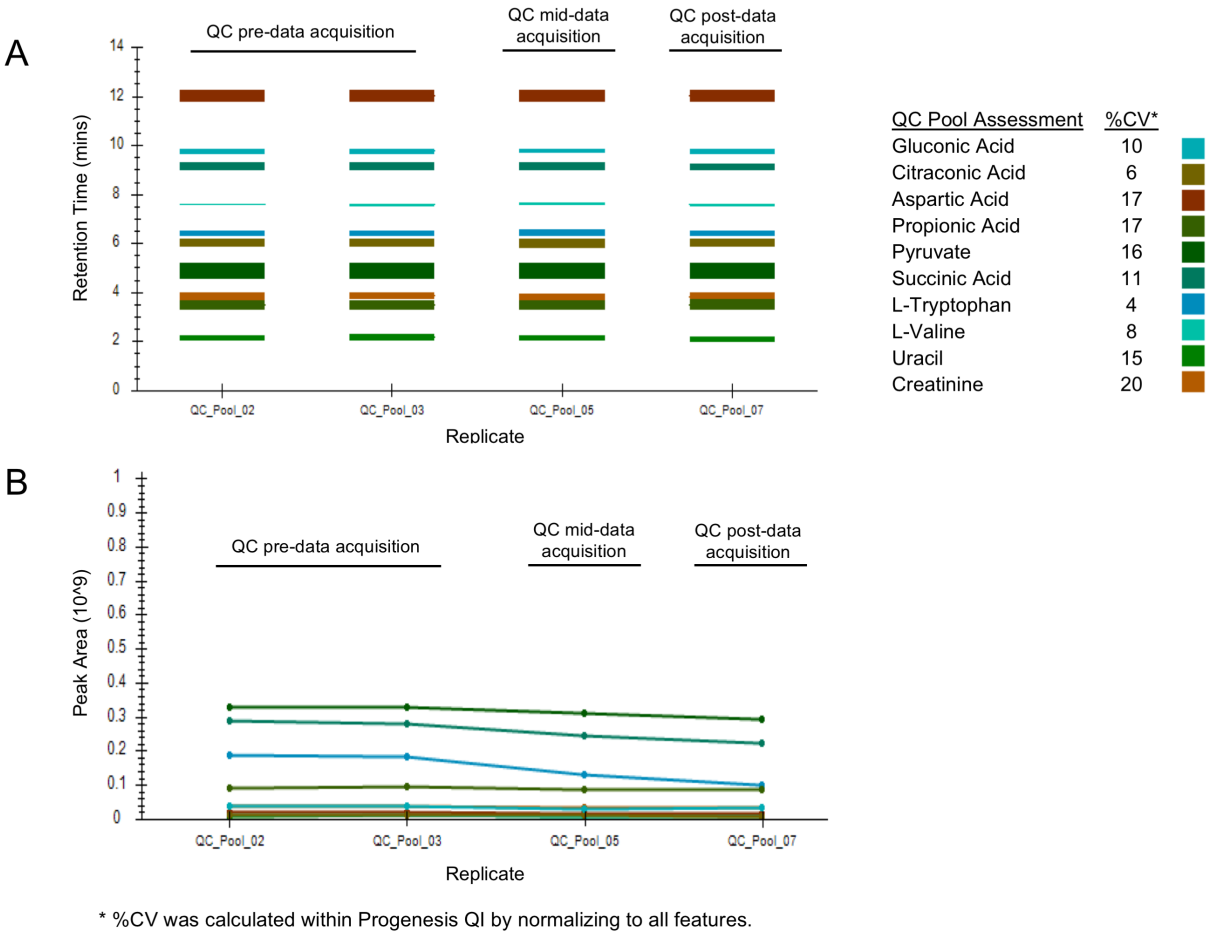

* %CV was calculated within Progenesis QI by normalizing to all features.

Fig. 50: Comparison of ten endogenous molecules in replicate injections of a pooled sample for QC assessment prior to, during, and after the experimental sample data acquisition for *HILIC-NEG collection, validation sample set*. A. The retention time and B. peak area for the ten endogenous compounds are reliable and reproducible (compound legend indicates respective %CVs). Figures were generated in Skyline software.

of the abundancies of unique ions) using both adduct and isotope deconvolutions to generate unique “features” (retention time and m/z pairs) representative of unannotated metabolites. Data were normalized to all features using Progenesis. Briefly, all runs have a measurement for every feature ion, therefore a ratio can be taken for the feature ion abundance in a particular run relative to the value in the normalization reference. Progenesis applies a Log10 transformation to the ratio to yield a normal distribution on all ratio data within each run for all samples, and scalar estimations shift the Log10 distributions onto that of the normalization reference. Resulting FMS data was utilized for relative quantitation. The minimum percent coefficient of variance (%CV) was determined for all features across sample groups. Data was exported to EZ Info (Umetrics Software) and unsupervised (% of mean) Principle Components Analysis (PCA) was used to visualize clustering of data groups prior to statistical tests of significance. Additionally, within Progenesis QI, One-way analysis of variance (ANOVA) was used to assess significance between WT and KO groups and returned a *P*-value for each feature (retention time_m/z descriptor), with a nominal *P*-value ≤0.05 taken as significant. Significant features were further filtered using a fold change threshold calculated by Progenesis from combined abundance data, with a cutoff of FC ≥ $\left|1.2\right|$ deemed as significant. Visualizations of dysregulated metabolites were represented by volcano plots ($\log_2$ (fold change) vs. $-\log_{10}$ (*P*-value)). Tentative and putative annotations were determined within Progenesis using accurate mass measurements (< 5 ppm error), isotope distribution similarity, and manual assessment of fragmentation spectrum matching (when applicable) from the Human Metabolome Database (HMDB) [413], Metlin [414], MassBank [415], and the National Institute of Standards and Technology (NIST)

database [416]. Additional putative annotations were assigned using Compound Discoverer 2.0 (Thermo Scientific, Waltham, MA, USA). Briefly, the DDA data was uploaded to Compound Discoverer 2.0, deconvoluted to group isotopes/adducts of the same feature, and features were assigned an m/z Cloud spectral match score based on feature spectral matches against the mzCloud [417] spectral libraries [418]. Within Progenesis, individual fragmentation (MS/MS) spectra peak shape and intensity of the putatively identified statistically significant features were visually assessed for quality control. For Level 3 confidence features (i.e., annotations supported by MS1 level data that may match multiple candidate annotations), *mummichog* 2.0 (www.mummichog.org/index.html) [419] was utilized to rank the most likely species within our samples. *mummichog* 2.0 predicts biological activity from MS1 data rather than formal manual curation of MS-2-dependent identifications. The MetaboAnalyst 3.0 program (www.metaboanalyst.ca/) was used for pathway and metabolite set enrichment analyses using the list of statistical significance annotated features in the discovery dataset [418, 420]. KEGG metabolite pathways were visualized using Cytoscape 3.4.0 (The Cytoscape Consortium, USA). Increased confidence in the annotation of many features was achieved by manually assessing spectral match and RT consistencies between experimental data and chemical standards within a curated in-house library. Chemical standards (purchased from Sigma Aldrich (St. Louis, MO) unless otherwise specified) were prepared at a concentration of 10 ng/uL in acetonitrile/water (80/20, v/v).

Validation of pathway disruptions via metabolomic UPLC-MS/MS analysis

UPLC-MS/MS raw data were imported, processed, normalized, and reviewed using Progenesis QI v.2.1 as described in detail above for the initial discovery dataset. After the raw data was imported and processed in Progenesis, *mummichog* 2.0 [419] was used to perform pathway enrichment analysis by predicting biological activity from MS1 data allowing a focused assessment and validation of specific pathways sensitive to *Mblac1* KO.

Results and Discussion

Generation and validation of MBLAC1 KO mice

To eliminate expression of MBLAC1 *in vivo* and initiate a metabolomic interrogation of MBLAC1-linked pathways, we used a non-homologous end joining (NHEJ) CRISPR/Cas9 strategy to introduce deletions in the *Mblac1* gene, disrupting sequences that encode the N-terminus of the MBLAC1 protein as described in the Methods [421, 422]. This effort yielded two different deletion lines with either 5 bp or 14 bp deletions. The studies described in this report, derive solely from experiments with mice that harbor the 5 bp deletion, which lies 46 bp downstream of the MBLAC1 protein start site (Fig. 51A). The resulting frame shift results in the generation of 27 amino acids of ectopic sequence prior to strand termination (Fig. 51B). As shown in Fig. 51C, immunoblots of brain (cortical tissue) and liver extracts prepared from 5 bp deletion-containing KO mice, using affinity-purified MBLAC1 antibody, demonstrated complete loss of the 27 kDa band predicted to encode MBLAC1 protein (Fig. 51C) [182]. Whereas a more detailed characterization of the phenotypes of the MBLAC1 KO animals will be

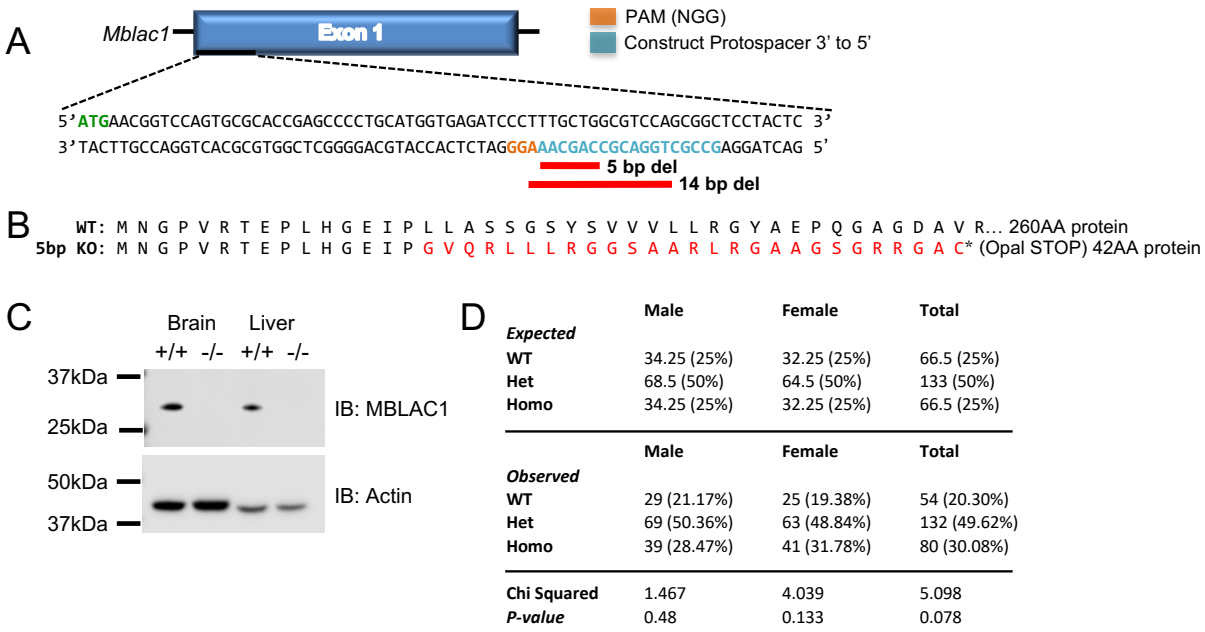

	Male	Female	Total
Expected			
WT	34.25 (25%)	32.25 (25%)	66.5 (25%)
Het	68.5 (50%)	64.5 (50%)	133 (50%)
Homo	34.25 (25%)	32.25 (25%)	66.5 (25%)

	Male	Female	Total
Observed			
WT	29 (21.17%)	25 (19.38%)	54 (20.30%)
Het	69 (50.36%)	63 (48.84%)	132 (49.62%)
Homo	39 (28.47%)	41 (31.78%)	80 (30.08%)
Chi Squared	1.467	4.039	5.098
P-value	0.48	0.133	0.078

Fig. 51: CRISPR/Cas9 generation of the MBLAC1 KO mouse. A. Gene diagram depicts the target sequence used to direct DNA cut sites in the *Mblac1* genomic sequence. The protospacer adjacent motif (PAM) and protospacer sequences are highlighted and 5 bp deletion and 14 bp deletion of the KO are underlined. B. Beginning of the protein sequences for WT and the 5 bp MBLAC1 KO, highlighting the frameshift/missense amino acid sequence and early truncation of the 5 bp MBLAC1 KO line generated and used in the present study. C. MBLAC1 immunoblot of protein lysates prepared from WT and KO brain (cortical tissue) and liver tissue. MBLAC1 KO mouse tissue lacks the specific 27 kDa MBLAC1 band. Work performed in collaboration with Jane Wright (MBLAC1 KO mouse generation) and Cassie Retzlaff (western blots).

provided in future reports, we note here that the founder mouse, as well as subsequent heterozygous and homozygous KO progeny, were viable, produced offspring at normal Mendelian ratios (Fig. 51D), and exhibited no visible physical or behavioral abnormalities.

Our discovery experimental design, from serum collection through data analysis, is depicted in Fig. 52. Serum samples were collected from WT and MBLAC1 KO mice and metabolites were separated by polarity using HILIC-POS and -Neg UPLC-MS/MS. For confidence in metabolite detection and putative identification of features, we pursued two complementary data processing and analysis platforms, Progenesis QI and Compound Discoverer 2.0 as described in Methods. Briefly, Progenesis QI was used for peak-picking, normalization and statistical analysis to determine uniqueness of MBLAC1 KO and WT sera metabolomes. Both Progenesis QI and Compound Discoverer 2.0 were used to assign annotations to features of interest based on database searches and spectral library matching. The compiled list of annotated, significantly regulated features was subsequently analyzed by MetaboAnalyst 3.0. where we assessed enrichment of known metabolic pathways. This approach was designed to identify metabolic pathways affected by loss of MBLAC1 expression, and thereby provide a physiological context for contributions of MBLAC1 subtrate(s).

Elucidation of an MBLAC1-dependent serum metabolome

UPLC-MS/MS methods are now commonly used for metabolomic studies owing to their high-resolution and sensitivity capabilities [423]. As many endogenous metabolites found in serum samples are expected to be polar/hydrophilic, we initiated our efforts using HILIC to retain and resolve polar analytes [424, 425]. We used both HILIC-positive (POS)

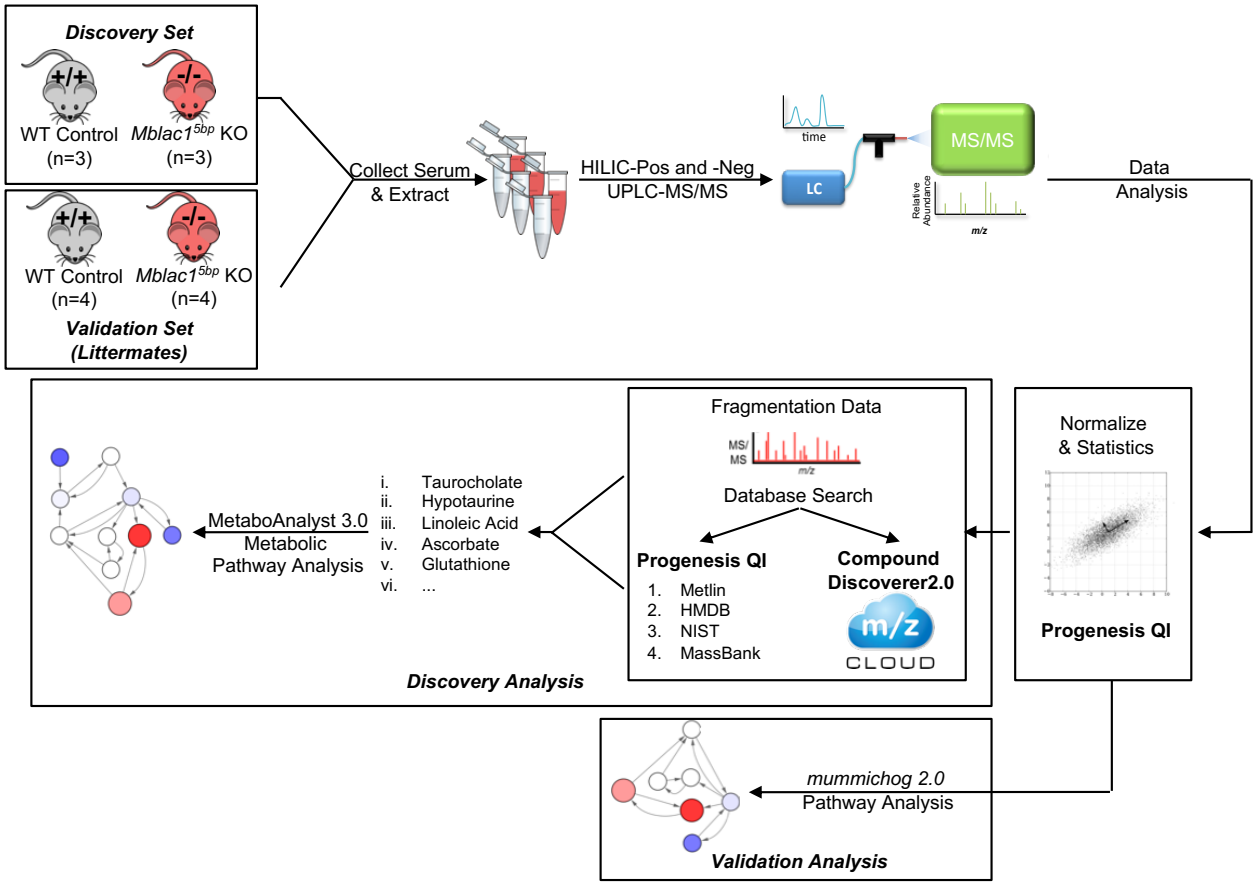

Fig. 52: Illustration of the workflow for the global, untargeted MBLAC1 KO serum metabolomic discovery and validation studies. The workflow begins with serum sample preparation from age- and sex-matched controls for the discovery set, and serum sample preparation from littermate age- and sex-matched controls for the validation set. This diagram illustrates the steps required for the discovery-based analysis of a multidimensional dataset across several analysis platforms to curate tentative and putative feature annotations and prioritize metabolic pathways altered by loss of MBLAC1. Additionally, this illustration describes the validation analysis to identify replicable metabolic pathways sensitive to MBLAC1 loss.

ion mode (Fig. 53A) and HILIC-negative (NEG) ion mode (Fig. 53B) MS methods to increase the molecular breadth of detected metabolites. Future studies may benefit from complementary reverse-phase liquid chromatography (RPLC)-MS methods [426]. In Fig. 53A-B, we show representative total ion chromatograms for serum samples derived from WT and KO mice. We used the Progenesis QI data processing platform, to inspect these runs for reproducible, genotype-dependent differences by normalizing to all feature abundances (each feature abundance is a sum of feature ion abundances comprised of grouped adduct forms). While not a direct indicator of efficacy, these analyses detected many molecular features (with unique mass to charge ratios (m/z)) in our data set, 2002 features in HILIC-POS and 2336 features in HILIC-NEG. Within Progenesis QI, feature sample variance is defined by the minimum percent coefficient of variance (min %CV) from any experimental group such that a low %CV value represents less abundance variance among biological samples. Based on other untargeted metabolomic studies [427, 428], we considered features with a min %CV ≤30% as having acceptable abundance variation, with 69% of the features in HILIC-POS have a min %CV ≤30% and 57% of the features in HILIC-NEG have a min %CV ≤30%. The binning of features by min %CV ranges is shown in Fig. 54. Subsequent, unsupervised PCA of these data revealed clear and consistent segregation of WT and KO biological replicates (Fig. 53C-D) distinct from the QC-pooled reference sample.

Next, a one-way ANOVA was used to nominate features that demonstrated genotype-dependent abundance differences between WT and KO samples, with a nominal *P*-value of ≤0.05 taken as significant. For HILIC-POS data, ANOVA analysis revealed 326 features as significant, 16% of the total number of features. For samples

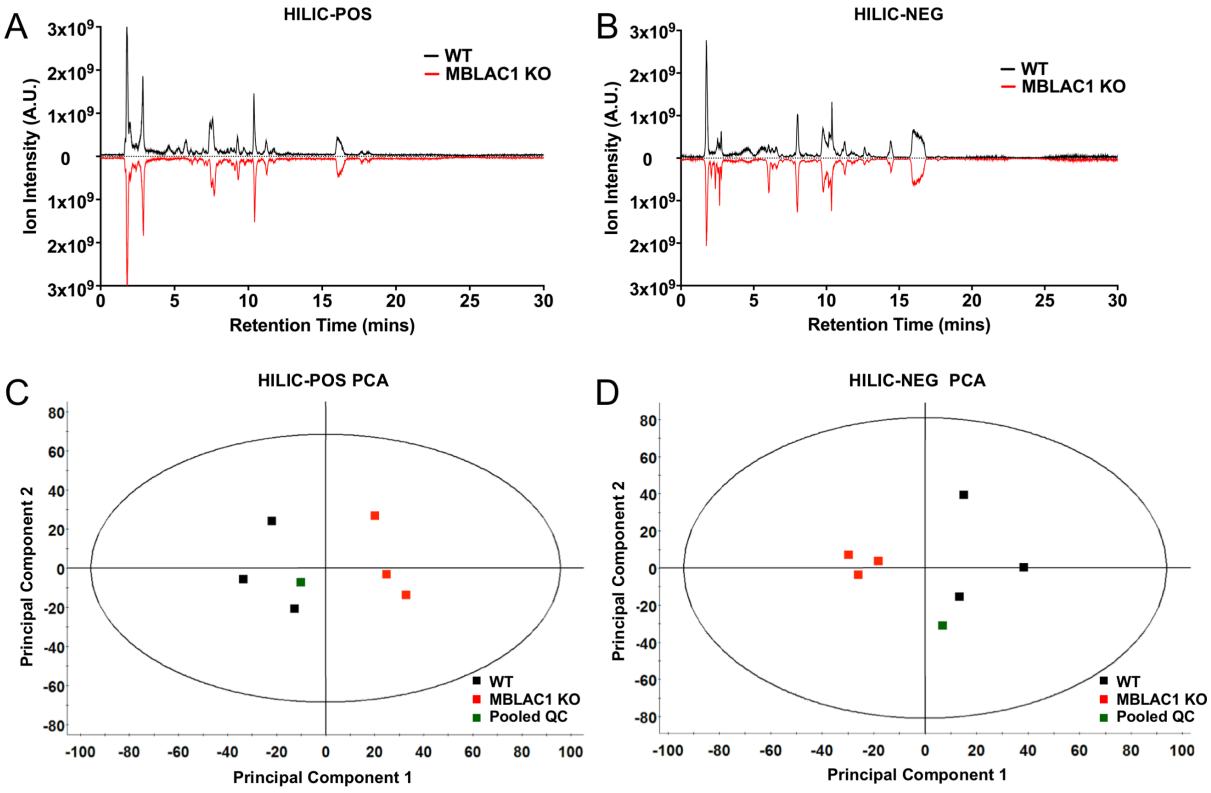

Fig. 53: Data representative of the UPLC-MS/MS characterization of WT and MBLAC1 KO serum and multivariate statistical analysis. Representative total ion chromatograms separated by A. HILIC-POS ion mode and by B. HILIC-NEG ion mode, WT shown in black and MBLAC1 KO shown in red. Global, unsupervised, principal component analysis (PCA) of the C. HILIC-POS and D. HILIC-NEG data illustrating distinct metabolic profiles observed between the WT control samples (black) and the MBLAC1 KO samples (red) with the alignment reference QC sample (green).

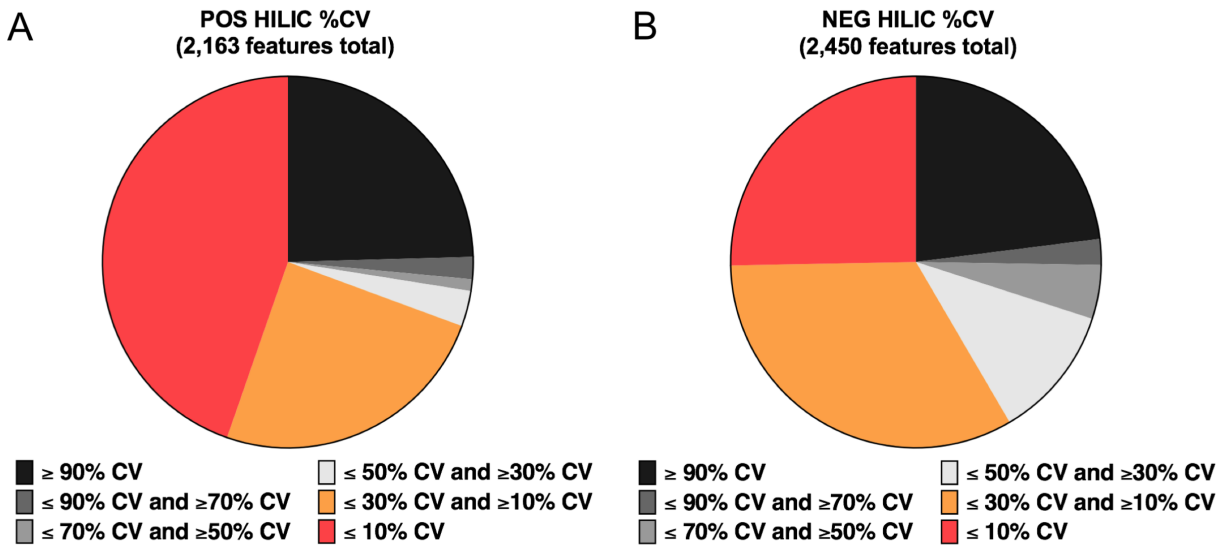

Fig. 54. Features detected by untargeted UPLC-MS/MS approach binned according to minimum percent coefficient of variance (min %CV). A. HILIC-POS and B. HILIC-NEG. For both ion modes, about 60% of the detected features have a min %CV ≤ 30%.

analyzed by HILIC-NEG, 287 features, 12% of the total, reached significance. These features are displayed in Volcano plots in Fig. 55, showing significance on the x-axis and magnitude of change on the y-axis, and highlighting the upper, outer features for prioritization for subsequent identification and pathway analysis. In these discovery experiments, we used a liberal fold change [(FC) ≥ |1.2|] as our filtering threshold, based on previous plasma metabolomics studies [429]. Supplementary Tables 5 and 6 (Appendix A) summarize the features significantly dysregulated between WT and KO samples from HILIC-POS and -NEG respectively.

Nomination of biomarkers of loss of MBLAC1 expression

Metabolite identification was pursued for significant features, with a nominal *P*-value ≤0.05 and a FC ≥ |1.2|. The experimental m/z measurement of each feature was queried against several published metabolite databases (i.e., HMDB, MassBank, Metlin, NIST, mzCloud) to match feature m/z within a ± 5 ppm window. We assigned various levels of confidence to our metabolite annotations (Table 3) based on the levels of metabolite identification first outlined by Sumner et al. 2007 and the Metabolomics Standard Initiative [430, 431], and the more recent adaptations of this approach [418, 432]. Several of the prioritized molecules do not match any current database entries, either representing novel metabolites (unknown unknowns) or unknown degradation or breakdown products that are absent from existing databases. These are classified most broadly as level 5 (L5) for a feature annotated with a unique m/z. A subset of the significantly regulated molecules in our data, classified as level 4 (L4), could be assigned multiple potential molecular formulas and thus render multiple candidate annotations.

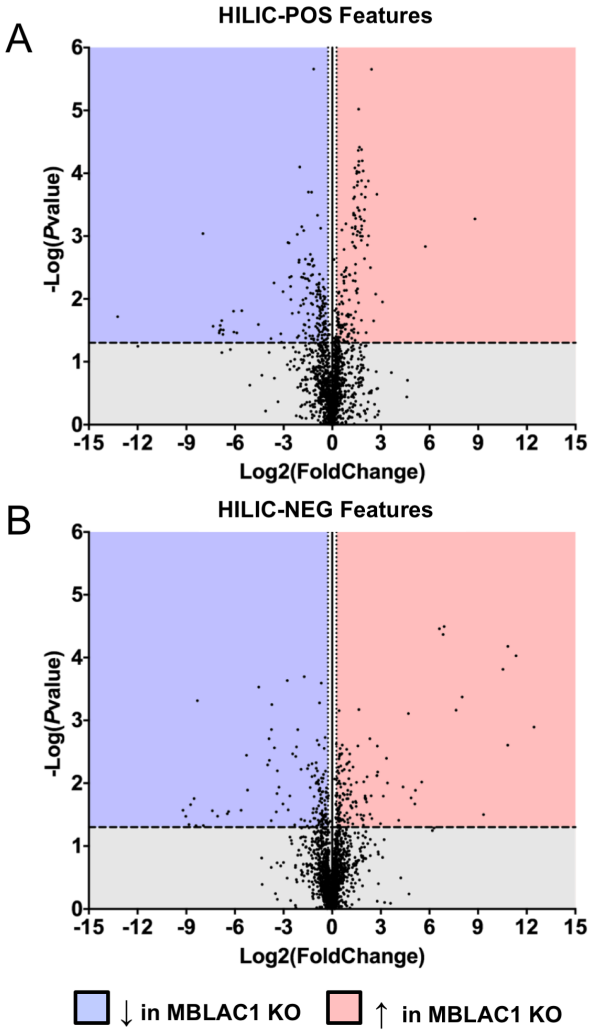

Fig. 55: Volcano plots of UPLC-MS/MS datasets. A. HILIC-POS and B. HILIC-NEG combining the statistical test (y-axis: -log *(P*-value)) and the magnitude of the change (x-axis: (log 2(FC)) of metabolites on a scatter plot. Points in the blue shaded area represent metabolites with a *P*-value <0.05, and FC<-1.2 in MBLAC1 KO samples. Points in the red shaded area represent metabolites with a *P*-value <0.05, and FC> 1.2 in MBLAC1 KO samples.

	Initial Untargeted UPLC-MS/MS						
Pathway	**Name**	**Formula**	**KEGG ID**	**Mol. Wt.**	**Retention Time (mins)**	***P*-value**	**Confidence level**
Taurine and hypotaurine metabolism	**Pyruvic acid****	C3H4O3	C00022	88.0160	6.974	0.552	L3
	L-alanine	C3H7NO2	C00041	89.0477	10.435	0.667	L2
	Taurine	C2H7NO3S	C00245	125.0146	11.111	0.770	L2
	Hypotaurine	C2H7NO2S	C00519	109.0197	10.834	0.558	L1
	3-Sulfinoalanine	C3H7NO4S	C00606	153.0096	8.552	0.306	L2
	Taurohyocholic acid*/Taurocholic acid*	C26H45NO7S	**C15516**/C05122	515.2917	5.294/5.811	0.032/0.035	L3
	2-Hydroxyethanesulfonate	C2H6O4S	C05123	125.9980	9.039	0.003	L2
Primary bile acid biosynthesis	**Glycine**	C2H5NO2	C00037	75.0320	11.348	0.846	L1
	Taurine	C2H7NO3S	C00245	125.0144	11.120	0.770	L2
	Cholic acid	C24H40O5	C00695	408.2880	2.723	0.206	L2
	Chenodeoxycholic acid*/Deoxycholic acid*	C24H40O4	**C02528**/C04483	392.2927	1.794	0.455	L3
	Chenodeoxycholic acid*/**Deoxycholic acid***	C24H40O4	C02528/**C04483**	392.2927	2.395	0.027	L3
	Taurohyocholic acid*/**Taurocholic acid***	C26H45NO7S	C15516/**C05122**	515.2917	5.294/5.811	0.032/0.035	L3
	Taurochenodeoxycholic acid	C26H45NO6S	C05465	499.2967	2.776	0.027	L2
Glutathione Metabolism	**L-glutamate**	C5H9NO4	C00025	147.0532	11.913	0.383	L1
	Glycine	C2H5NO2	C00037	75.0320	11.348	0.846	L1
	Ascorbic acid**	C6H8O6	C00072	176.0321	13.798	0.009	L2
	Ornithine	C5H12N2O2	C00077	132.0899	11.804	0.192	L2
	gamma-L-Glutamyl-L-cysteine**	C8H14N2O5S	C00669	250.0623	6.534	0.193	L3
	Pyroglutamic acid	C5H7NO3	C01879	129.0426	12.642	0.010	L2
	Dehydroascorbic acid**	C6H6O6	C05422	174.0164	12.542	0.007	L3
Linoleic acid metabolism	**Linoleic acid**	C18H32O2	C01595	280.2402	1.768	0.040	L2
	13(S)-HpODE	C18H32O4	C04717	312.0230	1.895	0.095	L2
	13(S)-HODE*/ 9(10)-EpOME*	C18H32O3	**C14762**/C14825	296.2347	1.833	0.069	L3
	13-OxoODE**	C18H30O3	C14765	294.2195	1.829	0.018	L3
	13(S)-HODE*/ **9(10)-EpOME***	C18H32O3	C14762/**C14825**	296.2347	1.833	0.069	L3

* Isomeric metabolites cannot be differentiated in our data by MS2 or retention time, thus both potential candidates are indicated and denoted as L3.

** L3 confidence level indicates that a feature has multiple candidate identifications. Mummichog 2.0 was used to rank the most likely species, denoted in Table 1.

Table 3: Metabolites of the identified pathways of interested to be confirmed and utilized for a future targeted Mblac1 KO metabolomics studies. ID levels for each listed metabolite is based on the degree of confidence of putative identification (based on database identification and fragmentation data supporting ID) described in Sumner et al., 2007 [430] and Schrimpe-Rutledge et al., 2016 [418]. Metabolites significantly reduced in MBLAC1 KO serum are highlighted in blue, and those significantly elevated in MBLAC1 KO serum are highlighted in red.

Level 3 (L3) features are classified based on a confident molecular formula and accurate mass. We assigned tentative identifications to many L3 features by using *mummichog* 2.0 to predict the species found in our samples, and denoted these putative annotations in Table 3. Features are classified as level 2 (L2) when experimental fragmentation data is consistent with a spectral library match upon manual assessment and curation, rendering a putative identification (Supplementary Figs. 60-71, Appendix A). We have in-house experience that pure reference standards generate match scores ranging from 20/100 to >99/100 against external spectral libraries. Thus, we set an arbitrary threshold of 45/100 to facilitate curation. A lower fragmentation score match was accepted for features with a low (<100) m/z that matched a single metabolite, in which case the low fragmentation score is likely a result of minimal fragmentation as well as potential MS/MS fragments being below the detection limit of our instrumentation platform. Together, Progenesis QI and Compound Discoverer 2.0 facilitated annotations for 16% (92 out of 593) of the significantly different features. The highest identification, confidence level (L1), is achieved by comparison of experimental data with that of a standard reference compound to confirm the structure with retention time, isotope pattern, and fragmentation.

Nomination of MBLAC1-dependent metabolic pathways

To identify metabolic pathways altered by MBLAC1 KO, we pursued analysis with features of interest exhibiting moderate to high confidence levels of identification (L1-L3). MetaboAnalyst 3.0 [420, 433] was used to map the 92 significantly dysregulated, putatively-identified metabolites to Kyoto Encyclopedia of Genes and Genomes (KEGG) defined pathways. The most over represented KEGG pathways are highlighted in

Fig. 56A. After identifying these dysregulated pathways, we determined the total coverage of each pathway that was identified in our dataset which allowed us to increase our confidence in KEGG pathway assignment (Fig. 56B). HILIC-MS/MS provides effective retention, separation, and elution of polar molecules and consequently, lower representation of non-polar molecules is expected, and thus we would not expect to obtain full coverage of metabolic pathways. Several pathways, however, were identified as warranting further inspection, including taurine and hypotaurine metabolism, primary bile acid biosynthesis, glutathione metabolism, and linoleate metabolism.

The KEGG defined pathway for taurine and hypotaurine metabolism overlaps at multiple points with the pathway supporting primary bile acid homeostasis. The pathway intersection (containing 31 metabolites) is highlighted in our user-defined, hybrid “taurine, hypotaurine and primary bile acid metabolism” pathway (Fig. 57A) with the highest (68%) coverage of metabolites in our dataset. Furthermore, 16% of the metabolites (i.e., 5 features) in this combined pathway are putatively identified as significantly reduced in KO samples (Fig. 57A and Table 3) with large fold changes (i.e. Taurochenodeoxycholic acid FC = |49.1|) observed, underscoring these pathways as particularly sensitive to the absence of MBLAC1 expression. Furthermore, the two linked pathways noted can also be associated with glutathione (GSH) metabolism. Thus, although no change is observed in cysteine, this amino acid is a key precursor to the synthesis of taurine related metabolites and is also a key amino acid in the GSH pathway, which MetaboAnalyst 3.0 KEGG pathway analysis revealed to be significantly impacted by loss of MBLAC1 expression, with 8% (3 features) of KEGG GSH metabolites altered in KO serum (Fig. 57B and Table 3). Lastly, our MetaboAnalyst 3.0 KEGG pathway analysis identified

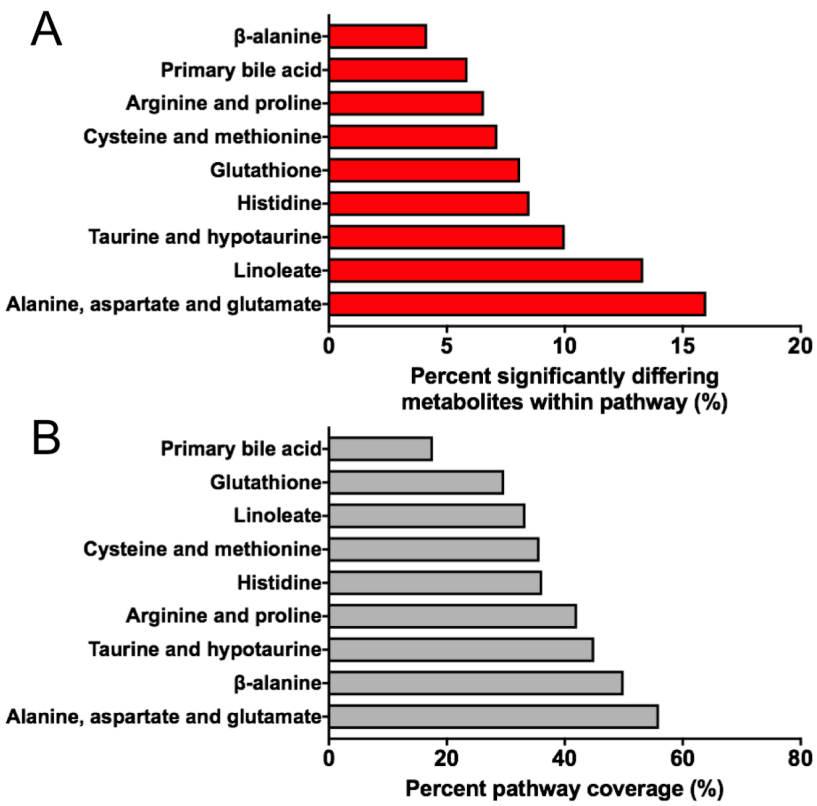

Fig. 56: MetaboAnalyst 3.0 identified metabolic pathways significantly altered by loss of MBLAC1. A. The percent differing metabolites (number of metabolites in pathway with *P*-value ≤0.05 and FC ≥|1.2| out of the total number of KEGG specified metabolites in the metabolic pathway. B. Percent of total pathway coverage determined by the number of metabolites found in serum metabolite samples (both significantly different and unchanged metabolites) / total number of KEGG specified metabolites in the metabolic pathway.

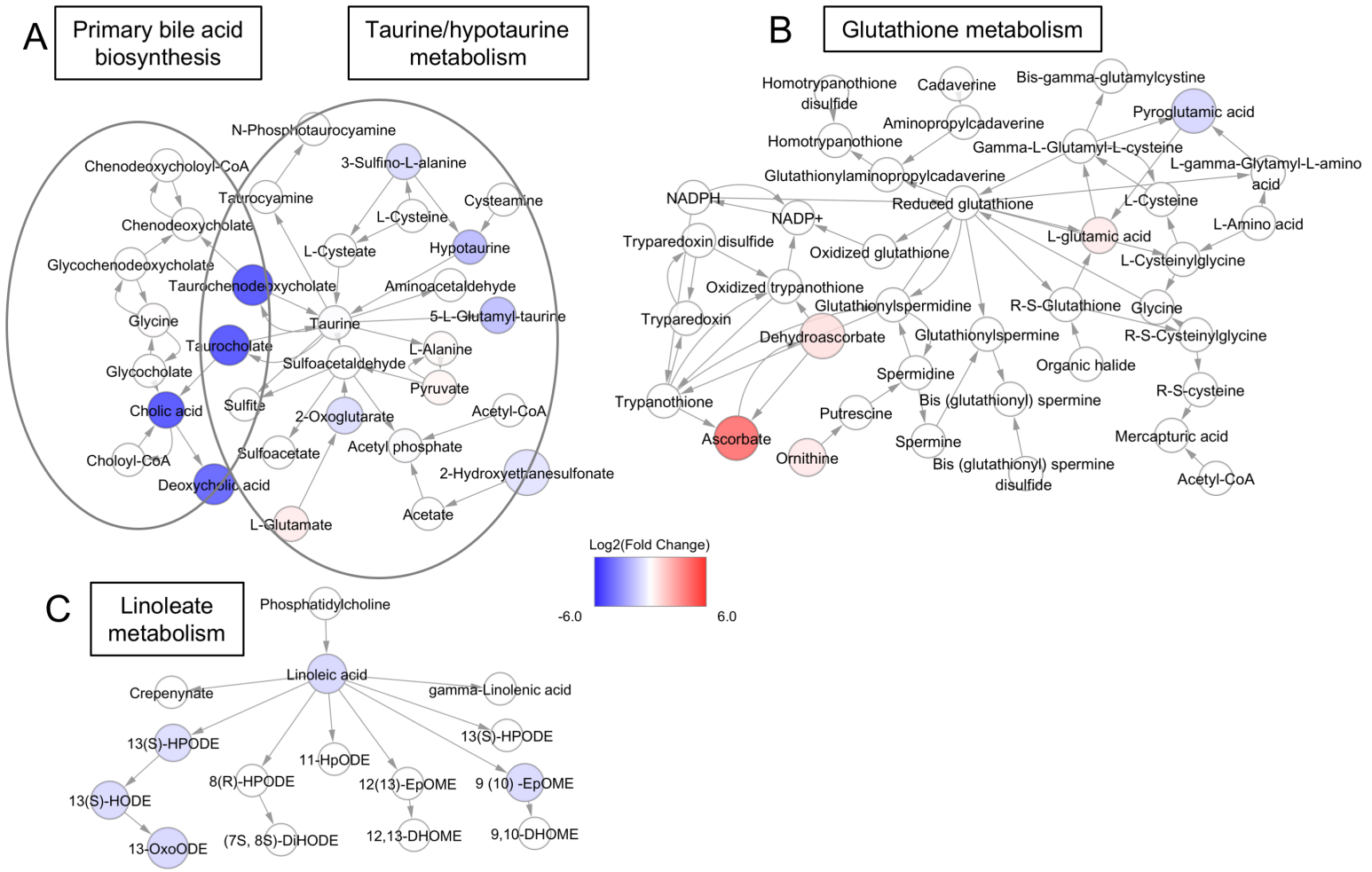

Fig. 57: Loss of MBLAC1 disrupts the abundance of metabolites residing in several KEGG defined metabolic pathways. A. The user-defined intersection between taurine and hypotaurine metabolism and primary bile acid biosynthesis metabolic pathways based on individual KEGG pathways. B. The KEGG-defined glutathione metabolism pathway. C. The KEGG-defined linoleate metabolism pathway. All metabolic pathways are visualized via Cytoscape 3.4 (Arrows denote enzymatic directionality defined by KEGG). Metabolites are colored per their FC abundance differences (blue indicates decreased abundance in MBLAC1 KO, red indicates increased abundance in MBLAC1 KO).

linoleate metabolism, depicted in Fig. 57C, as a pathway with changes in a sizable number of metabolites detected (40% total metabolic pathway coverage (Fig. 56A) and identified to have 13% over-representation of significantly dysregulated metabolites (Fig. 56B). Together these findings encouraged a follow up experiment of MBLAC1 KO metabolic changes to validate the impact of the *Mblac1* KO on the metabolic pathways highlighted above (pathways of interest).

Validation of metabolic pathway disruptions induced by loss of MBLAC1

Using an independent set of serum samples prepared from four age- and sex-matched (female) littermate MBLAC1 KO and four WT mice, we conducted a follow-up metabolic pathway based analysis to provide preliminary validation of MBLAC1 sensitive metabolic pathways determined from our initial age and sex-matched, but non-littermate derived serum samples. Our validation dataset corroborated the presence of 80% (19/24) of the unique features putatively identified in pathways of interest (Table 4) in the discovery set of serum samples by Progenesis QI, though some features were not detected. Utilizing our second set of serum samples to pursue validation of our discovery dataset at the specific metabolic pathway level, we again used *mummichog* 2.0, to determine the metabolic pathways impacted by loss of MBLAC1 (Fig.53) [419]. The software predicted bile acid biosynthesis (*P*-value =0.042, 5 significant features out of 18 pathway features) and linoleate metabolism (*P*-value =0.0002, 7 significant features out of 14 pathway features), reproducing two of the pathways from our initial discovery findings that the top metabolic pathways affected by loss of MBLAC1 include primary bile acid biosynthesis and linoleate metabolism (Table 4). Multiple other pathways were

Network Activity Prediction Analysis				
Ion Mode	Pathway Name	signficant features within	# features within pathway	*P*-value
HILIC-POS	N-Glycan biosynthesis	2	2	0.004
	Hexose phosphorylation	3	5	0.004
	Fructose and mannose metabolism	3	5	0.004
	Arginine and proline metabolism	7	26	0.009
	Urea cycle/amino group metabolism	9	38	0.010
	Chondroitin sulfate degradation	2	3	0.010
	Glycosphingolipid biosynthesis - ganglioseries	2	3	0.010
	Glycosphingolipid biosynthesis - globoseries	2	3	0.010
	Caffeine metabolism	2	3	0.010
	Heparan sulfate degradation	2	3	0.010
	Starch and sucrose metabolism	2	3	0.010
	Vitamin B3 (nicotinate and nicotinamide) metabolism	4	12	0.013
	Glycolysis and glucogenesis	2	4	0.022
	Keratan sulfate degradation	2	4	0.022
	N-Glycan degradation	2	4	0.022
	Pentose phosphate pathway	2	4	0.022
	Galactose metabolism	3	9	0.026
HILIC-NEG	Linoleate metabolism	7	14	0.000
	C21-steroid hormone biosynthesis and metabolism	5	12	0.006
	Glycosphingolipid biosynthesis - ganglioseries	2	2	0.010
	Fructose and mannose metabolism	4	10	0.018
	N-Glycan biosynthesis	2	3	0.026
	Glycosphingolipid biosynthesis - globoseries	2	3	0.026
	Omega-3 fatty acid metabolism	2	3	0.026
	Hexose phosphorylation	3	7	0.029
	N-Glycan degradation	3	7	0.029
	Bile acid biosynthesis	5	18	0.042
	De novo fatty acid biosynthesis	5	18	0.042
	Keratan sulfate degradation	3	8	0.044

Validated pathways sensitive to MBLAC1 KO

Table 4: Network activity prediction analysis validates metabolic pathways sensitive to constitutive loss of MBLAC1. Serum samples from a second cohort of mice were analyzed by *mummichog* 2.0[419] to determine the global metabolic pathways altered in the context of MBLAC1 KO for HILIC-POS and HILIC-NEG. This analysis supported the previous metabolic pathways identified by MetaboAnalyst 3.0 as significantly altered by KO of MBLAC1 (highlighted in green).

nominated as significantly impacted by MBLA1 KO, though almost all of these derive from 2-3 molecules within their designated network. A notable exception is a pathway linked to urea cycle/amine group metabolism, where 9 of 38 features were nominated, though this pathway had not been identified in our earlier discovery analysis. In our validation analysis, we did not identify a significant perturbation of GSH metabolism following loss of MBLAC1. As the bile acid synthesis pathway, which retained significance, shares molecules with that of the GSH metabolic pathway, we suspect that the lack of significance of the latter network likely reflects an overall weaker effect of Mblac1 genotype that becomes insignificant in the context of the more stringent, littermate based design of the validation experiment. Alternatively, this difference could derive from unknown variables associated with animal housing and husbandry at the two sites where samples were derived.

Potential significance of perturbation of taurine-derived metabolites within the primary bile acid biosynthesis pathway

As noted above, MBLAC1 KO appears to result in a consistent reduction in the abundance of many taurine derived metabolites such as taurochenodeoxycholic acid and taurocholate (Fig. 57A) that reside in the primary bile acid metabolism pathway. Indeed, these features represent the most significantly altered and putatively identified metabolites in our dataset, with the greatest magnitude of change due to loss of MBLAC1 (Table 5 and 6, Appendix A). Our pathway validation data provided additional support for bile acid biosynthesis and taurine derived metabolites as highly sensitive to MBLAC1 expression (Table 4). Taurine and related metabolites have many important biological

roles, ranging from essential contributions to bile acid conjugation in the liver, to the regulation of cardiac and skeletal muscle function, and evidence suggests that they can cross the blood brain barrier and regulate neurotransmission [434, 435]. Taurine has been shown to be as protective against oxidative stress induced cell death in peripheral tissues such as liver in several animal models of hepatotoxicity [436, 437]. Likewise, tauroursodeoxycholic acid (TUDCA), a bile acid derivative of taurine, has been shown to be neuroprotective in *in vitro* and *in vivo* models of cell death such as retinal degeneration by reducing cellular stress and preventing release of pro-apoptotic factors [438-440]. Therefore, loss of these molecules from the serum of MBLAC1 KO mice may indicate a role played by the MBLAC1 substrate in triggering pathways protective against cell stress and cell death. This is an interesting conclusion in the context of the reported neuroprotective action of Cef [202, 441, 442], which we have determined to bind MBLAC1 [182], likely as a functional antagonist due to the β-lactam structure of Cef. Chronic Cef treatment of cells has been reported to act via a Nrf2 pathway to induce expression of the cysteine/Glu exchanger and the Na^+-dependent Glu transporters that can diminish the threat of excitotoxic insults and oxidative stress [277]. We hypothesize that short term Cef blockade of MBLAC1 is detected as a stressful event by Nrf2, whereas the lifelong absence of MBLAC1 may preclude cells from mounting an appropriate stress response, as revealed in the bile acid pathway molecules lacking in the serum of Mblac1 KO mice.

Potential significance of alterations in linoleate metabolism

In our validation analysis, we confirmed that linoleate metabolism is one of the metabolic pathways sensitive to loss of MBLAC1 (Fig. 57C and Table 4). Linoleic acid is

an essential poly-unsaturated, omega-6 fatty acid (PUFA) primarily known as a precursor for the biosynthesis of arachidonic acid. Alterations in linoleic acid levels have been associated with a wide variety of health consequences ranging from perturbations in skin and hair health, as well as obesity and cardiovascular disease [443-445]. As our ongoing and future efforts are focused on identifying a role for MBLAC1 in the brain, we particularly note that linoleic acid crosses the blood-brain barrier [446, 447], and that brain levels of linoleic acid and derived fatty acids are resistant to dietary fluctuations in linoleate intake, suggesting that precise control of linoleic acid abundance in the brain is essential for normal brain function [448, 449]. Moreover, linoleic acid and other PUFAs have been reported to be reduced in patients with Alzheimer's disease, multiple sclerosis, mood disorders [450-452], and a recent metabolomics study of serum from subjects with epilepsy identified reductions in linoleic acid and its metabolites [453]. This body of work supports the hypothesis of Cocchi et. al., suggesting that reduced membrane linolenic acid concentrations in neurons and glia may reflect a pathological state [454]. In this regard, as we observe changes in the metabolites of the linoleic acid metabolism pathway in MBLAC1 KO mice (Fig. 57C), we hypothesize that MBLAC1 KO mice may be more susceptible to abnormal brain health, a hypothesis that can be assessed through disease-mimicking pharmacological and genetic challenges.

Study limitations and future directions

We acknowledge that there are several limitations to utilizing a global, untargeted metabolomic approach as a pilot study determine the metabolic pathway disrupted by genetic loss of an orphan enzyme. However, our data suggests that knock-out of Mblac1

is sufficient to significantly alter the murine serum metabolome and provides directionality to subsequent targeted analyses. The biggest limitation to this study is the small sample size and resultant challenges in drawing definitive conclusions without the statistical power of a larger sample size. However, despite the low number of biological replicates, we are able to identify replicable metabolic pathways reliant on MBLAC1. Rather than increase the “N” associated with our initial discovery analyses, we decided to pursue validation experiments using age- and sex-matched, littermate control WT mice as a more rigorous WT control that was unavailable when the discovery experiment was performed, due to the early stage of our MBLAC1 KO colony. The inclusion of an independently conducted validation study provides the opportunity to evaluate whether the pathways identified in the discovery phase of our efforts are strong enough to survive attempts at replication in a separate co-hort of mice. We also note that, in between the discovery and validation studies, the laboratory relocated, so we must also consider false negative results that may have arisen from differences in animal housing and husbandry.

Global, untargeted metabolomic studies are becoming increasingly popular as exploratory, hypothesis-generating experiments that provide an unbiased opportunity to uncover networks perturbed by genetic, pharmacological or environmental insults [455-459]. Importantly, metabolomic approaches can provide key data that allow for the “de-orphanization” of enzymes [460, 461]. Our samples for analysis, however, only derive from serum, which collects molecules from all tissues and thus may be seen as limiting the specificity of our conclusions. Serum is a frequent source of material for such studies, owing to its relative ease of preparation and ability to report system-level biochemical changes without assumptions as to specific sites of gene/drug action. Serum has also

been utilized to search for pathological biomarkers and insults arising from genetic mutations [462-464]. Finally, serum is also a reasonable starting point for the current analyses as *Mblac1* mRNA is expressed widely, including expression in both brain and peripheral tissues [146].

As a pilot study, with restricted serum sample availability, we selected a metabolite extraction method and metabolite separation column (HILIC) well suited to retention and separation of polar metabolites typically found in the predominately aqueous serum [424, 465]. We utilized a methanol (MeOH) protein precipitation step, in which polar metabolites are retained in the MeOH supernatant, subsequently dried down, and resuspended for analysis by mass spectrometry. It is likely that some hydrophobic metabolites and lipids are lost in the protein pellet or not retained by the HILIC column, which is primarily used for the separation and elution of polar compounds [425, 466, 467]. In future metabolomic experiments we will use complementary extraction methods as well as RPLC to increase the breadth of compound coverage thus expanding the analysis presented here.

An inherent challenge to investigating an orphan enzyme, is designing simple yet powerful hypothesis generating pilot studies that will inform future studies without leading to pursuit of false positives. Our knowledge of Mblac1 is derived from our previous studies demonstrating a role for the *C. elegans* ortholog of MBLAC1, SWIP-10*,* in Glu signaling [146, 468], and our study showing a specific and selective binding interaction between MBLAC1 and Cef, a β-lactam antibiotic with non-microbial, neuroprotective actions [202, 469, 470]. Cef affords neuroprotection in many brain disorders by preventing pathology such as oxidative stress and excitotoxicity arising from dysregulated Glu signaling. Cef regulates astroglial expression of multiple Glu transporters, specifically the Na^+-

dependent Glu transporter EAAT2/GLT1 (SLC1A2) and the cysteine/Glu exchanger (xCT, *SLC7A11*) [202, 277]. We are currently pursuing experimental studies to test our hypothesis that MBLAC1 plays a role in mediating the neuroprotective actions of Cef. To this we will conduct biochemical studies to determine if constitutive loss of MBLAC1 affects the expression of the Glu transporters regulated by Cef, and we will conduct behavioral studies on MBLAC1 and KO mice treated with saline or ceftriaxone, to see if constitutive loss of MBLAC1 disrupts the behavioral phenotypes associated with Cef treatment (i.e. how do MBLAC1 KO mice respond to cocaine sensitization and reinstatement paradigms). We chose not to include Cef treated WT and MBLAC1 KO mice in the presented untargeted metabolomics experiments as we wanted an unbiased study aimed at de-orphanizing MBLAC1, and identifying endogenous biologically relevant pathway(s) reliant on MBLAC1, independent of Cef, to guide future research.

Conclusion

Using an unbiased metabolomic approach, based on an UPLC-MS/MS, we evaluated serum metabolome changes arising from constitutive elimination of MBLAC1, an enzyme of yet undetermined function. Ninety-two annotations were assigned to features of interest that significantly differed in abundance in the serum of MBLAC1 KO mice compared to WT controls. MetaboAnalyst 3.0 and KEGG pathway analysis nominated multiple metabolic pathways impacted in the KO, with several linked to neuroprotective, oxidative stress reducing pathways. In an independent validation study, we confirmed the impact of MBLAC1 on bile acid biosynthesis and linoleate metabolism, pathways that share cell protective actions in the face of metabolic and oxidative cellular

stress. Our studies designate metabolic pathways that should be pursued in future targeted analyses and that may ultimately reveal the endogenous substrate(s) for MBLAC1/SWIP-10. We speculate that the reported neuroprotective actions of Cef, a demonstrated MBLAC1 ligand, may derive from the induction of cell defense mechanisms such as those designed to limit oxidative stress, effects that cannot be sustained in the context of a full loss of the enzyme.

Chapter VII

CONCLUSIONS AND FUTURE DIRECTIONS

Summary and Conclusions

The studies described here demonstrate the power of using *C. elegans* as a model to characterize conserved genes. Due to its genetic tractability, transparent cuticle, and highly described/ stereotyped nervous system development and structure, the nematode is an excellent model to study genetic regulation of neuronal morphology and degeneration. Our studies reveal that loss of glial-expressed *swip-10* induces cell non-autonomous, progressive, age-dependent DA neuron degeneration in the worm. Additionally, we provide initial evidence that the role for *swip-10* in glial maintenance of neuronal viability is not limited to DA neurons but likely extends to other neuronal types with close apposition to glial support cells in the worm, as loss of *swip-10* results in degeneration of the glial-ensheathed OLL neurons but not the BAG neurons. Our previous *swip-10* studies revealed that the hyperdopaminergic behavior observed in *swip-10* mutants arises due to DA neuron hyperexcitation and increased DA secretion due to altered Glu signaling mechanisms [146]. These findings, in concert with the mammalian literature describing a critical glial role in regulating extracellular Glu availability, led to our hypothesis that the DA neuron degeneration observed in *swip-10* mutants arises due to excitotoxic Glu signaling and activation of cell death mechanisms. The data described in the chapters above, demonstrate that disrupting Glu signaling via loss of the vesicular Glu transporter, *vlgu-3,* or loss of the putative xCT homolog, *aat-1,* significantly attenuates the DA neuron degeneration of *swip-10* mutant animals. Our strongest evidence

supporting *swip-10* loss induced Glu excitotoxicity, is that loss of the Ca^{2+}-permeable ionotropic Glu receptors, *nmr-2* and *glr-1,* significantly reduced *swip-10* DA neurodegeneration, and selective overexpression of these Glu receptors in wildtype DA neurons induced neurodegeneration. In the pursuit of defining a *swip-10* mutant induced Glu excitotoxicity model, we provide a mechanistic framework for the observed reduced DA neuron viability and cell death. In keeping with mammalian Glu excitotoxicity literature, we demonstrate that *swip-10* loss induced DA neurodegeneration results in dysregulated intracellular Ca^{2+}, as genetic disruption to ER Ca^{2+} storage or loss of the Ca^{2+}-dependent protease, *clp-1*, significantly and in combination, additively suppress *swip-10* DA neuron degeneration. Using fluorescent stress reporters, we provide evidence that *swip-10* mutant animals experience increased levels of basal oxidative stress and are more susceptible to ER stress inducers, suggesting that loss of glial-expressed *swip-10* has a more global effect on *C. elegans* health, and that the DA neurons are likely more intrinsically reliant on glial neuronal support. The observed progressive, age-dependent DA neuron degeneration of *swip-10* mutants is reminiscent of mammalian models of chronic Glu excitotoxicity suggesting that cell death occurs via an apoptotic mechanism. In addition to *swip-10* mutants lacking the distinct morphological features of necrotic cell death (including cell swelling and vacuolization), our data demonstrates that mutations to canonical genes in the apoptotic cell death pathway (*ced-9, ced-4,* and *ced-3)*, suppress *swip-10* mutant DA neurodegeneration. Lack of observed involvement of programmed cell death cell-corpse engulfment pathways, indicates that *swip-10* mutant DA neuron degeneration via apoptosis is distinct from the engagement of apoptosis that occurs during developmental cell death. In conclusion, *swip-10* induced neuronal degeneration

provides a novel model of glial regulated, Glu-induced excitotoxicity in the worm, and this model is highly amenable to genetic manipulation to further understand the molecular mechanism of glial support of neuronal viability as well as chronic Glu-induced cell death mechanisms.

Discerning novel roles for conserved genes in the worm provides valuable insight to the potential roles of previously undescribed genes in the mammalian brain. Previously we identified the mammalian ortholog of SWIP-10 to be the metallo β-lactamase domain contain protein, MBLAC1 [146]. The discovery of a *C. elegans* glial regulator of neuronal signaling with homology to a mammalian protein with a putative enzymatic domain theorized to interact with β-lactam rings, resonated with the recently described neuroprotective upregulation of glial Glu transporters by the β-lactam antibiotic, Cef. Despite extensive work demonstrating the neuroprotective effects of Cef across a broad spectrum of brain disorders, the target(s) of Cef was, until recently, unknown. A study by Retzlaff and colleagues, demonstrates that Cef interacts specifically and selectively with MBLAC1 in murine brain lysates [182]. This interaction supports our hypothesis that the neuroprotective upregulating of Glu transporter expression by Cef mechanistically originates via Cef interaction with MBLAC1, likely disrupting MBLAC1 from interacting with an endogenous substrate. Ongoing studies aim to further characterize the MBLAC1/Cef interaction, and using CRISPR/Cas9 methods we created the MBLAC1 KO mouse model. One of the primary objectives of utilizing the MBLAC1 KO model is to determine the endogenous enzymatic substrate(s) of MBLAC1 or the identify the metabolic pathway(s) sensitive to loss of MBLAC1. To this end we employed a global, untargeted metabolomics approach and found that the sera of MBLAC1 KO mice are

distinct from their WT counterparts. These studies provide evidence that the metabolic pathways, taurine/hypotaurine metabolism, primary bile acid biosynthesis, and linoleic acid metabolism are sensitive to loss of MBLAC1, as the abundancies of several metabolites within these pathways are altered by loss of MBLAC1. Strikingly, as described in the previous chapter, metabolites within these pathways have been associated with brain disorders and cell stress mechanisms. These pathways will be pursued in future targeted analyses, which may reveal the substrate(s) for MBLAC1/SWIP-10.

The characterization of *swip-10* in the nematode and pioneering studies utilizing the MBLAC1 KO mouse model suggest a role for SWIP-10/MBLAC1 in pathways associated with monitoring and regulating cell stress, including Glu homeostasis and excitotoxicity prevention as well as taurine-related metabolite neuroprotection. Using model organisms, including the nematode and rodents, allowed us to identify and initially characterize a target potentially relevant in the context of a variety of human brain disorders including neurodegenerative diseases. By further exploiting these model systems using more advanced neurophysiological approaches (electrophysiology, optogenetics, Ca^{2+} signaling dynamics, etc) we can more fully describe a functional role for SWIP-10/MBLAC1, ideally presenting these proteins as drugable targets to impart neuroprotection in the CNS.

Future Directions to Further Characterize *swip-10* in *C. elegans*

Assess a potential developmental role for *swip-10*

The studies described above provide evidence for the progressive, age-dependent DA neuron degeneration induced by genetic loss of *swip-10.* Our explorations into the neurodegenerative phenotype of *swip-10* mutants are very informative but by no means comprehensive. Perhaps the most apparent future direction, given the evidence of *swip-10* mutant DA neurodegeneration as early as L1, is to evaluate CEP neuron development during embryogenesis. Our findings indicate that *swip-10* may play a biphasic role in regulating DA neuron viability, first a developmental role, and a second, later role in maintaining neuronal health. Interestingly, unreported findings by Hardaway indicate that the *swip-10* expression pattern changes, with highest embryonic *swip-10* expression in the hypodermis, and predominately glial expression by the L4 stage that persists in adult animals, suggesting this change in expression may be relevant to age-dependent roles for *swip-10*. To initiate developmental studies, we will use fluorescence light microscopy to assess the morphology of the CEP DA neurons of N2 and *swip-10* mutant animals during embryogenesis. We are interested in determining the temporal requirement for *swip-10* in the context of either the hyperdopaminergic, Swip phenotype or DA neuron degeneration. To address this question, we can genetically create an knock-in nematode model, such that wildtype *swip*-10 expression could be induced at various developmental stages (i.e. induced expression by heatshock-sensitive promotors) to determine when *swip-10* expression is required to rescue mutant *swip-10* phenotypes. Additionally, using methods described below, gene expression profiling of *swip-10*-expressing cells of N2 and *swip-10* mutant animals, across various developmental stages, may reveal different

gene expression profiles early in development versus the gene expression profile observed in adult animals.

Future experiments to assess cellular stress pathways in *swip-10* mutant animals

As described in a previous chapter, we have demonstrated that *swip-10* mutant animals display increased basal oxidative stress and increased sensitivity to ER stress. These assays were conducted using transcriptional reporters to assess gene expression levels of genes whose expression increases under genetic or environmental stress conditions, *gst-4* and *hsp-4* expression increases under oxidative and ER stress respectively. To more fully characterize *swip-10* loss induced indices of cellular stress, a more complete assessment of stress reporters can narrow down selective types of stress associated with *swip-10* mutation. For example, in future, we will assay the engagement of SKN-1 transcriptional regulation of detoxifying enzymes, in *swip-10* mutant stress susceptibility. SKN-1 is of particular interest in future studies as it is the nematode ortholog of the mammalian transcriptional regulator Nrf2 [471]. Under basal WT conditions, Nrf2 (SKN-1) is retained in the cytosol by interaction with Keap1 (mammals), exposure to oxidants and electrophiles results in Keap1 release of Nrf2 and subsequent Nrf2 translocation to the nucleus where it interacts with DNA sequence antioxidant response elements to increase expression of detoxifying enzymes and proteins [472, 473]. Relevant to our studies, Cef treatment results in Nrf2 mediated increased expression of the cystine/Glu exchanger (xCT) as a means to increase GSH production in a mouse derived hippocampal cell line [277]. Using a translational reporter, we can assess the localization of SKN-1::GFP (cytosolic or nuclear) in *swip-10* mutant animals compared to

N2, under basal or pharmacologically induced stress [474] to determine if loss of *swip-10* induces engagement of antioxidant and stress defense pathways. We will also use a gain of function *skn-1* mutant to determine if increasing expression of detoxifying enzymes and proteins will suppress *swip-10* mutant DA neuron degeneration.

We provide evidence for basal levels of oxidative stress in *swip-10* mutants and future studies will determine if the observed oxidative stress is associated with mitochondrial dysfunction. Oxidative stress is characterized by increased levels of reactive oxygen species (ROS) which can be derived from Glu excitotoxic signaling, environmental toxicant exposure, and dysfunction of normal cellular detoxifying pathways. Oxidative stress can induce mitochondrial dysfunction, damaging the mitochondrial respiratory change, and can trigger increases mitochondrial derived ROS, which has been associated the pathology of several neurodegenerative disorders [475]. Again, we can take advantage of the genetic-tractability and transparency of *C. elegans,* to assess mitochondrial morphology and mitochondrial fusion and fission, especially as mitochondrial fission was shown to play a role in apoptosis and neurodegenerative diseases. Globally, we can use fluorescence microscopy to visualize mitochondrial dynamics using mitochondrial membrane potential-sensitive dyes such as MitoTracker Red or methyl-rhodamine B in *swip-10* mutants versus N2 [476]. Using cell specific promotors, we can assess mitochondria using Mito:GFP expressed selectively in glia or DA neurons of *swip-10* mutant and N2 animals [476]. With our data supporting *swip-10* loss induced Glu excitotoxicity resulting in apoptotic DA neuron degeneration, we hypothesize that loss of *swip-10* results in damaged mitochondria within DA neurons.

Though monitoring the mitochondrial morphology would be informative and suggest a role for mitochondrial dysfunction in *swip-10* mutants, in order to support a mitochondrial role in *swip-10* loss induced oxidative stress, we can envisage experiments designed to assess cellular respiration and ATP production as a measure of mitochondrial/metabolic health in *swip-10* mutants. In order to measure, *in vivo*, fundamental parameters of the mitochondrial respiratory chain (ATP-linked respiration, basal oxygen consumption, spare respiratory capacity and proton leak) in *swip-10* mutants compared to N2, we propose utilizing the Seahorse XFe24 analyzer (Agilent) previously used to measure mitochondrial function in genetic and pharmacological models of mitochondrial dysfunction in *C. elegans* [477, 478].

In the past, we have shied away from assessing metabolic processes in the whole animal, with the caveat that *swip-10* expression is limited to a relatively small number of cells and changes induced by loss of *swip-10* may be masked by the contribution of whole animal metabolic processes, however our whole animal oxidative stress marker data demonstrates that loss of *swip-10* induces basal changes that are evident by assessing the entire animal. We have initiated a collaboration with the Miller lab at Emory University, whose recent work includes improving the biological metabolic map for *C. elegans* metabolites, to conduct a high-resolution metabolomics analysis to identify potential metabolic pathway differences between N2 and *swip-10* mutant animals.

Future directions to identify a glial, cell-autonomous genetic pathway for *swip-10*

Our studies describe a cell non-autonomous role for *swip-10* in glial-mediated support of DA neuron viability, however the precise cell autonomous role of *swip-10*

remains unknown. We hypothesize that SWIP-10 acts in *C. elegans* glia to maintain Glu homeostasis and glial support of neuronal morphology and function. One approach to identifying a role for *swip-10* is a candidate gene approach, where a list of candidate genes thought to act in a *swip-10*-related pathway based on previous data are assessed for Swip behavior and/or DA neuron degeneration. More recently, mammalian models of Parkinson's disease implicate astrocytic dysfunction in contributing to DA neuron degeneration as summarized in Fig. 58. Also, mammalian literature, and more recently, *C. elegans* studies indicate that glia play important roles in supporting neuronal health through trophic support such as lactate shuttling and glutamine provision as well as ion buffering and Glu homeostasis. For example, in the mammalian brain, glycolysis-produced lactate is shuttled from astrocytes and oligodendrocytes to neurons as a substrate for oxidation and ATP production [479]. Researchers demonstrate the importance of the astrocyte-neuron lactate shuttle, as pharmacological inhibition of the monocarboxylate transporter (MCT-1), responsible for lactate uptake in neurons, results in impaired memory processing and deficits in long- term memory formation [480, 481] and astrocytic lactate shuttling-related gene expression declines with age in humans [482]. Using BLAST nucleotide sequence alignment and protein sequence alignment tools, 7 *C. elegans* genes (*mct-(1-7) and slcf-1)* have been identified as belonging to the monocarboxylate transporter (SLC16) superfamily that contains the mammalian astrocytic and neuronal plasma membrane lactate transporters [483] (wormbase.org). In a candidate gene approach, we would assess loss of function mutation alleles in these genes for paralysis behavior and DA neurodegeneration, and additionally determine the effects of combined genetic loss of *swip-10* and these putative monocarboxylate

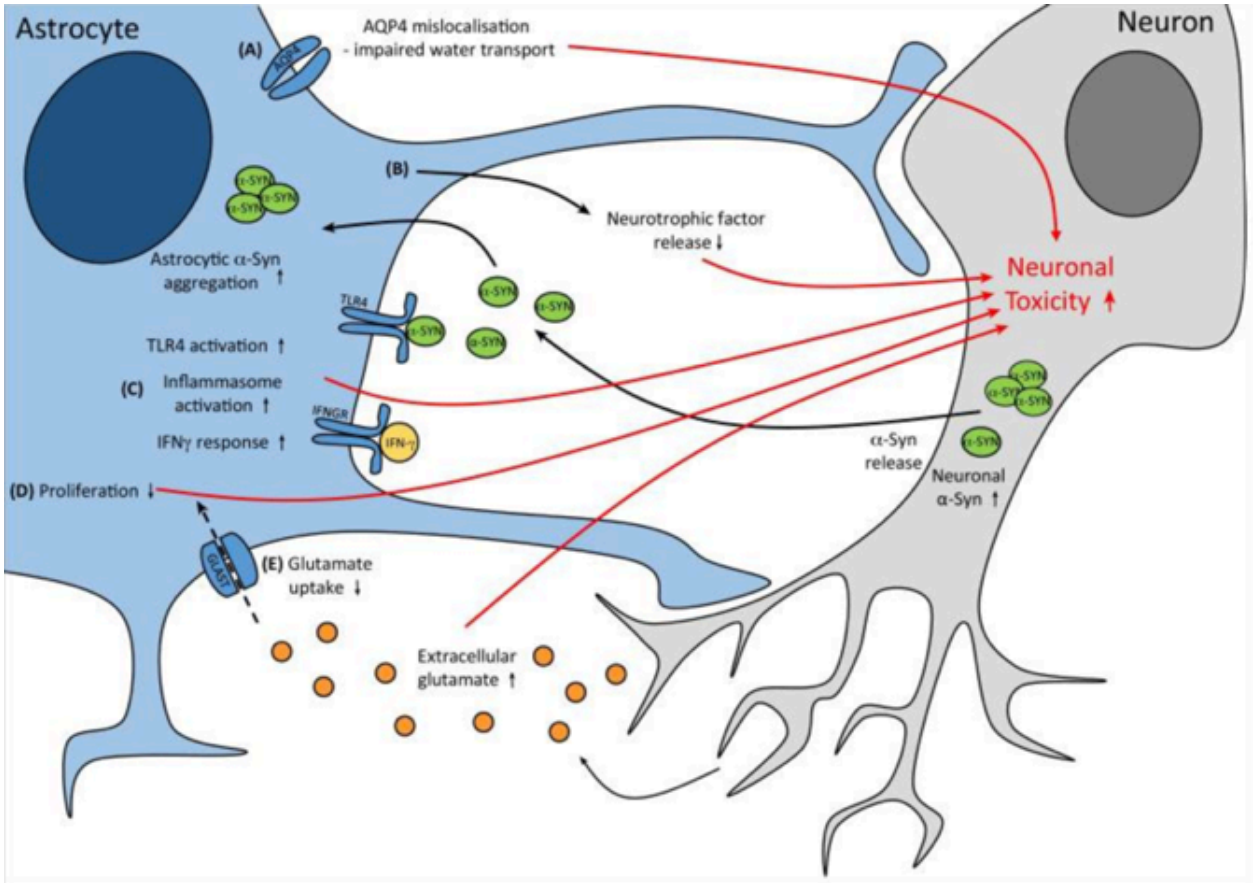

Fig. 58. Cartoon depicting the contributions of astrocyte dysfunction to neural toxicity in the context of Parkinson's Disease. This schematic depicts the five main mechanisms by which astrocyte dysfunction elicits neuronal toxicity. (Figure from Booth et al., 2017).

transporters. In order to further prioritize among paralogs, we will review the literature for known expression patterns, for example, *mct-6* could prioritized above the other paralogs as it is putatively expressed within the *C. elegans* nervous system. The example of lactate shuttling between glial and neurons is only one of example of a glial pathway we will assess via a candidate approach. The candidate gene approach, however, is biased as the researcher must select the genes/ mutants for assessment, therefore an unbiased approach may be better suited to the elucidation of a *swip-10* related genetic pathway.

One unbiased approach to identifying a functional cell-autonomous role for *swip-10*, is the implementation of a glial specific suppressor screen. Starting with a known mutation and a readily observable phenotype, a suppressor screen is used to identify second-site mutations that suppress the original mutant phenotype, and reveal additional information about the genetic path or gene of interest [484]. Recently, as an alternative to traditional mutagenesis based screens, RNA-mediated interference (RNAi) methods are used in forward genetic screens and suppressor/enhancer screens [485-487]. The advantages of a RNAi feeding screen are 1) the convenience of simply feeding animals *E. coli* expressing a library of dsRNA and 2) that the molecular identify of the suppressing clones are known, however one caveat is that RNAi inactivation of genes is not always effective. In order identify a glial-specific role for *swip-10,* a glial-specific RNAi feeding suppressor screen could be envisioned. A global RNAi suppressor screen was utilized to identify transcriptional regulators of an amphid sheath glial specific expressed gene [488], however, to date, a glial-cell specific RNAi screen has not been reported. Adapting the techniques described for tissue- and neuron- specific RNAi screens, using the pan-glial promoter, $p_{ptr\text{-}10,}$ to restore RNAi transport and efficacy selectively to glial cells on a RNAi

resistant- and *swip-10*- mutant background strain may reveal a functional genetic interactor with *swip-10* [489, 490]. Assessing clones for suppression of the *swip-10* mutant induced DA neuron degeneration phenotype is technically challenging and time consuming as individual clones need to be immobilized on sides, imaged by fluorescence light microscopy, and recovered. Therefore, a two-tier suppressor screen is better suited for *swip-10* mutants, first using the Swip phenotype to quickly identify glia-specific genetic suppressors of *swip-10* mutant paralysis, and an additional phenotype screening step to identify which paralysis suppressors also suppress the *swip-10* mutant DA neuron degeneration phenotype. While we have not yet determined if the extent of the impact of *swip-10* loss on the truncation of other ciliated neurons, such as the amphid neurons, we propose utilizing the ciliated neuron DiI dye filling method [329, 491], previously described to identify mutants with cilia defects, as a quicker, alternative method for the secondary phenotypical screening step. The two-tier suppressor screen strategy presents a caveat that we would miss mutants that selectively suppress *swip-10* mutant DA neurodegeneration but not Swip. Using a glial-cell specific RNAi approach will help overcome the caveat of finding already known cell non-autonomous suppressors of *swip-10* phenotypes. For example, a traditional suppressor screen may reveal a mutation to *cat-2,* a gene previously shown to suppress the paralysis behavior of *swip-10* mutants but not the DA neurodegeneration phenotype. As *cat-2* expression is limited to the DA neurons of the worm, a glial-specific RNAi approach would eliminate identification of downstream DA neuron viability genes or DA signaling genes (i.e. DA neuron expressed Glu receptors, or the DA receptor, *dop-1)*. While our current data supports differences in downstream mediators of *swip-10* mutant induced paralysis versus DA

neurodegeneration, our data also supports that both phenotypes are reliant on dysregulated Glu signaling and glial expression of SWIP-10. Ideally, a suppressor screen will reveal close genetic interactors with the *swip-10* gene such that both phenotypes are robustly suppressed, and provide new insight to a glial function for *swip-10.*

An alternative, unbiased approach to identify glial-specific changes due to loss of *swip-10* is to compare the glial gene expression profiles of *swip-10* mutants to wildtype animals [492]. Cell-type specific gene expression profiling was previously utilized to identify genes specifically expressed in various tissue such as the pharynx, male tail rays, neurons and others [493-495]. Early gene expression profiling studies utilized mRNA microarrays to detect mRNA level changes in transcripts corresponding to existing genomic sequence information. More recently, Spencer and colleagues describe the use of RNA-sequencing to transcriptionally profile specific *C. elegans* cell types (SeqCeL), which has reduced background signal compared to the tiling array method and facilitates investigation of known and previously unknown transcript levels [495], therefore in order to promote discovery of all transcriptional changes due to glial *swip-10* loss, RNAseq gene expression profiling is the preferred method. Heretofore, researchers isolated tissue specific mRNA transcripts via two methods 1) RNA immunopurification, such that cytosolic mRNAs are isolated via affinity tag purification, where an epitope tagged RNA binding protein is expressed selectively in the cell-type of interest, and after immuno-precipitating the protein-mRNA complex, the mRNA is isolated for subsequent microarray or RNAseq analysis; or 2) Fluorescence Activated Cell Sorting (FACS), such that following whole nematode dissociation, cell-type specific promoter driven fluorescent markers are used to isolate cell of interest using FACS, and from these FACS separated

cells, mRNA can be purified and analyzed by microarray or RNAseq. Unique challenges and caveats are associated with these two complementary methods, for example the mRNA tagging approach is associated with higher levels of non-specific RNA species [496] and the FACS approach requires the dissociation of cells from their native context, potentially inducing gene expression changes. Recently, Heiman and colleagues described a new method for the isolation of cell-type-specific mRNA for *in situ* profiling of gene expression termed Translating Ribosome Affinity Purification (TRAP) [497]. Briefly, cell-type-specific promotors are used to drive expression of EGFP-tagged ribosomes in cells of interest for affinity purification of translating ribosomes bound to translated mRNAs and subsequently, these mRNAs are purified for analysis (qPCR, microarray, or RNAseq) [497]. The TRAP method for cell-type specific gene expression profiling has been utilized in *C. elegans* [498], and we propose that future *swip-10* studies would benefit from the implementation of TRAP to determine the gene expression profile differences between *swip-10* mutant glia compared to wildtype. Additionally, Gracida and Calarco already describe a *C. elegans* transgenic strain with DA-neuron specific EGFP tagged ribosomes [498], and crossing this strain with *swip-10* mutants will allow us to either profile the global DA neuron gene expression profile of *swip-10* mutant animals, or isolate DA neuron specific mRNA for qPCR evaluation of gene transcript levels for genes we have previously described as playing a role in *swip-10* loss induced DA neuron degeneration, such as Glu receptor genes or apoptotic genes.

Future Directions to Further Characterize Mammalian MBLAC1

Alternative methods to identify the MBLAC1 substrate(s)

The global, untargeted metabolomics approach used to identify metabolic pathways sensitive to loss of MBLAC1 provided several pathways to investigate as reliant on normal Mblac1 function, however as addressed above there are several caveats to hypothesis-generating untargeted approaches. Recently, we initiated a new experimental design coupling affinity captured MBLAC1 incubation with brain lysates to mass spectrometry-based small molecule detection, with the specific aim of identifying the specific endogenous MBLAC1 substrate(s) or immediate enzymatic product(s). Although not shown here, we can successfully express and purify HA tagged MBLAC1 from HEK 293t cells, and couple the enzyme to HA beads, and we demonstrated that MBLAC1 retains the ability to interact with Cef despite conjugation to HA beads, suggesting some level of retained function. We will acutely incubate MBLAC1 conjugated beads and unconjugated control beads with freshly prepared MBLAC1 KO mouse cortical brain lysate. Following incubation, we will remove the beads, precipitate out the proteins and obtain the high-speed small molecule containing supernatant. These supernatants will be dried down and re-suspended in appropriate buffers for positive and negative ion mode HILIC and RPLC chromatographic separation methods for LCMS/MS, allowing for comprehensive metabolite coverage. We hypothesize that the MBLAC1 KO brain lysate lacks the immediate product of putative MBLAC1 enzymatic activity, and following acute incubation of KO lysate with MBLAC1 conjugated beads should result in either decreased abundance of the substrate(s) for MBLAC1 or increased abundance of the product of MBLAC1 enzymatic activity. As we do not know the identity of the substrate(s)/products(s)

of MBLAC1, using untargeted metabolomics to assess abundancy differences in small molecules exposed to MBLAC1 beads or control beads allows us remain unbiased, and query both known metabolites and unidentified metabolites.

Mblac1 does not hydrolyze prokaryotic β-lactamase substrates via established colorimetric assays (unpublished findings by Hardaway), however, by exploiting the previously described binding interaction between MBLAC1 and the β-lactam antibiotic, Cef [182], we can envision designing competitive displacement assays to identify the endogenous substrate(s) of MBLAC1. While we have not fully characterized the Cef-MBLAC1 binding interaction, using BSI, Retzlaff and colleagues determined that MBLAC1-Cef binding, over a range of Cef concentrations, fit well to a single site binding equation with a K_D of about 2μM [182]. Briefly, this method would monitor the displacement of radio-labeled Cef bound to MBLAC1 in the presence of increasing concentrations of crude small molecule extracts prepared from brain lysates. In order to further narrow down the types of endogenous small molecules interacting with MBLAC1, the small molecule extracts can be purified into fractions based on polarity and molecular mass using column chromatography [499]. After identifying a particular fraction(s) that displaces radiolabeled-Cef binding from MBLAC1, the metabolites within the fraction can be determined via mass spectrometry, and pure standards can be utilized in competition binding assays to validate the endogenous small molecule substrate(s) that interact with MBLAC1. There are several caveats to this biochemical substrate identification technique including troubleshooting the purification of active MBLAC1 protein for these binding studies and the high cost of creating and using radiolabeled Cef in competition assays

when the binding affinity between Cef and MBLAC1 is in the micromolar range, rather than the nanomolar range better suited to displacement/competition binding assays [500].

Future directions utilizing the MBLAC1 KO mouse model

As described in a previous chapter, we generated a CRISPR/Cas9 mediated MBLAC1 KO mouse model to characterize, *in vivo*, the biochemical and behavior consequences to constitutively loss of MBLAC1 expression. Heterozygous and homozygous MBLAC1 KO animals are viable, reproduced normally, and display no overt physical or behavioral abnormalities (assessed by a modified Irwin-screen) [501]. This mouse model presents a large variety of future directions, and here I will briefly describe several ongoing or top priority experimental pursuits.

In the chapters above, we extensively describe the nematode DA neural degeneration induced by loss of *swip-10*. To expand our initial characterization of the MBLAC1 KO mice, we will assess the DA neuron morphology of KO vs WT animals. Given that the KO animals display no overt phenotypes, including no signs of movement aberrations associated with mouse models of PD, MBLAC1 KO animals may not display overt signs of DA neuron degeneration, however we will also examine the MBLAC1 KO mice for sensitivity to neurotoxins such as 6-OHDA and MPTP. Given our hypothesis that constitutive loss of MBLAC1 may result in a reduced capacity to handle cell and oxidative stress, MBLAC1 KO mice may be more sensitive to neurotoxins, displaying more severe phenotypes at a lower concentration of neurotoxin than their WT counterparts.

We have initiated biochemical investigations to determine the tissue biogenic amines levels in MBLAC1 KO mice versus WT littermate controls. As described in our

previous studies, *swip-10* mutant animals have reduced DA content compared to WT [180], therefore determining the content of DA and its metabolites across various brain regions may provide initial support of a conserved role for MBLAC1 in alterations in DA availability/signaling. Tissue level biogenic amine content and amino acid levels, such as Glu, can be readily detected using HPLC methods. As measuring synaptic DA or Glu *in vivo* in the worm is not feasible, in future, we may employ an *in vivo* microdialysis technique coupled to HPLC methods to monitor synaptic neurotransmitter release, comparing basal levels and release of DA and/or Glu in WT and MBLAC1 KO animals (van der Zeyden et al., 2008). Microdialysis-HPLC coupled methods were utilized by Trantham-Davidson and colleagues to demonstrate that Cef restores basal Glu levels in cocaine self-administering rats and Cef treatment attenuates the observed Glu increase during a cocaine-primed reinstatement test [441]. As our MBLAC1 studies progress, we can determine if constitutive loss of MBLAC1 disrupts the previously described biochemical changes attributed to chronic Cef treatment. Along these lines we will use specific antibodies and immuno-blotting techniques to evaluate the expression of proteins previously shown to be sensitive to Cef treatment, in particular GLT-1 and xCT [202, 442], in protein lysates prepared from WT and MBLAC1 KO brain regions.

In addition to the literature supporting the neuroprotective biochemical effects of Cef, such as restoring Glu transporter protein expression and restoration of basal Glu levels, there is a substantial body of work describing the behavior changes associated with Cef treatment *in vivo.* We propose that Cef interaction with MBLAC1 (depicted in Fig. 59) may be responsible for imparting neuroprotection in a variety of behavioral paradigms, such as reducing behavioral deficits associated with excitotoxic cell death [202] and

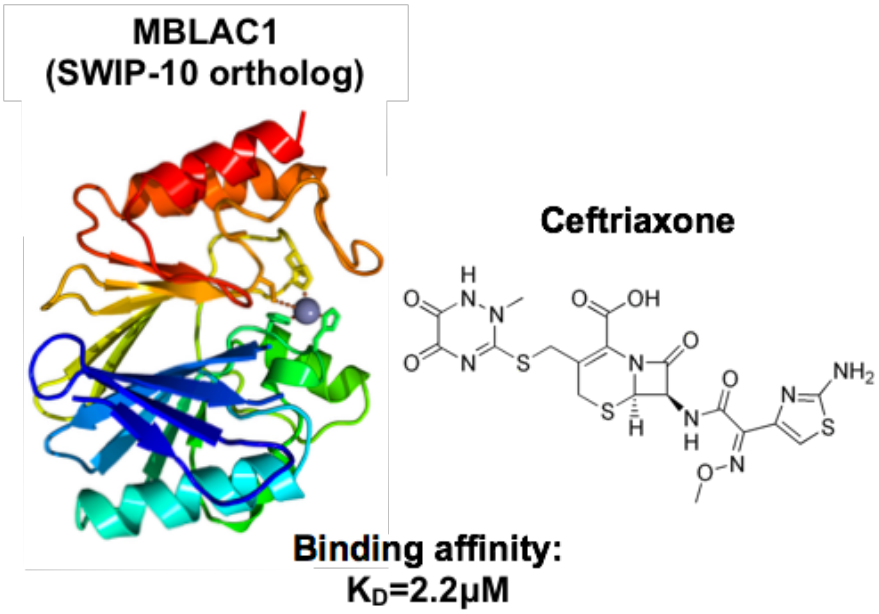

Fig. 59. Schematic depicting the specific and high affinity interaction between MBLAC1 and the neuroprotective β-lactam antibiotic, ceftriaxone. (Figure adapted from Retzlaff et al., 2017).

preventing psychostimulant reinstatement [275]. Following this hypothesis, will utilize MBLAC1 KO and WT littermate controls to determine if loss MBLAC1 expression disrupts the Cef induced restoration of WT-like behavior first in a locomotor sensitization to cocaine paradigm [502] with following investigations utilizing a cocaine self-administration and reinstatement paradigm [441].

Appendix A

SUPPLEMENTARY MATERIAL FROM THE UNTARGETED METABOLOMIC STUDY OF MBLAC1 KO AND WT SERA[4]

The data here includes the supplemental material relating to the untargeted serum metabolomics study of MBLAC1 KO and WT mice. Tables 5 and 6 provide the full list of features significantly dysregulated between MBLAC1 KO and WT serum samples from HILIC-POS and HILIC-NEG respectively. In future, these datasets may be useful in comparing results from targeted metabolic approaches designed to assess MBLAC1 KO induced changes to specific metabolic pathways such as bile acid biosynthesis and linoleic acid metabolism. Many of the significantly dysregulated features with large fold changes in abundancy due to loss of MBLAC1 were unidentified/ not annotated in our untargeted metabolomics approach, but these features may be important in future studies. As described in chapter VI, in order to assign higher levels of confidence in feature annotation (L2), we compare the fragmentation spectra (MS/MS data) of experimentally obtained data with the fragmentation spectra available from several databases, as well as assess spectra obtained from chemical standards within an in-house chemical library. Figures 60-71 show the spectral matches for putatively annotated features of the L2 and L1 confidence levels described in Table 3.

[4] Adapted from Gibson CL, Codreanu SG, Schrimpe-Rutledge AC, Retzlaff CL, Wright J, Mortlock DP, et al. Global untargeted serum metabolomic analyses nominate metabolic pathways dependent on expression of the orphan, metallo β-lactamase, MBLAC1. Molecular Omics. In revision.

Appendix A: Table 5: HILIC-POS

Putative identification	Mass to charge ratio (m/z)	Retention time (min)	ANOVA nominal *P*value	Fold Change (relative to KO)	Coefficient of Variance (% min CV)	Maximum Abundance
	72.0808	24.3304	0.0008	1.5097	2.65	1527.9695
	84.9113	15.5174	0.0208	1.2970	6.27	59760.4019
	86.0601	3.0987	0.0056	1.6484	8.15	25196.5012
Piperidine	86.0964	7.8332	0.0163	1.2849	6.99	97875.8230
	86.9087	15.5174	0.0178	1.2859	5.12	26318.1293
	90.0550	25.9629	0.0081	1.3095	4.79	285.7980
	90.0550	25.7472	0.0257	1.3041	4.63	120.0458
	102.0338	21.4942	0.0010	3.6246	2.05	15575.7780
	102.0339	20.1411	0.0006	3.9267	3.34	46155.6713
	102.0662	6.0664	0.0458	1.3123	3.09	36995.2371
	102.0914	17.7501	0.0382	-1.2137	3.33	41998.5576
	103.5480	6.0971	0.0388	-2.3249	17.78	19545.4642
	110.0713	14.2781	0.0030	-2.2716	9	52273.8934
	112.0505	22.4858	0.0185	-1.4408	5.01	848.9945
Uracil	113.0345	4.8326	0.0119	1.5763	5.5	35935.3869
	113.0509	6.0971	0.0430	-2.4483	18.89	44568.2828
	118.0650	17.1449	0.0093	-2.0016	12.46	230.5511
	118.1226	20.9556	0.0260	-3.2038	7.79	60.5905
Phenylethanolamine	120.0808	21.8640	0.0045	-3.7220	20.93	157.8819
	121.0720	6.0708	0.0104	2.0676	18.99	11538.5787
	122.0812	10.2071	0.0302	-1.3135	5.83	8582.6247
	122.5538	6.0840	0.0218	-2.7261	4.75	73452.5597
	125.9862	9.2787	0.0004	2.9679	5.14	1115138.4580
	128.1070	2.4502	0.0005	443.9184	1.88	457442.7315
Pyroglutamic acid	130.0500	12.6417	0.0098	-1.6532	7.09	19733.1430
Isoquinoline	130.0652	8.6000	0.0308	-1.4577	9.18	11636.4586
	131.0532	25.4295	0.0112	8.5494	18.64	3.5737
Isoleucine	132.1019	7.8288	0.0203	1.2494	7.02	1217198.3970
Beta-Leucine	132.1020	6.9833	0.0044	1.8026	3.81	57713.3395
Asparagine	133.0608	11.5800	0.0201	-1.9034	14.2	155042.5263
Ornithine	133.0972	18.0221	0.0094	-1.3621	3.41	134476.5912
	133.1052	22.1486	0.0411	-4.4619	36.36	57.0306
	133.1053	7.8332	0.0223	1.2431	6.81	84064.7167
Aspartic acid	134.0448	12.1474	0.0286	1.5079	4.71	18705.6345
2-Oxindole	134.0600	5.9915	0.0084	6.4142	16.41	35651.4697
3-hydroxynorvaline	134.0812	3.6866	0.0260	1.2676	8.25	47303.4018
	134.1175	22.3807	0.0007	-1.6468	4.82	351.5656
	136.0481	20.1937	0.0246	-1.9074	1.91	359.4855
	136.0481	21.5074	0.0280	-2.6921	6.47	252.7366
	137.0458	21.8903	0.0008	-3.3856	11.94	346.7277
6-Methylnicotinamide	137.0710	9.4145	0.0010	2.8755	13.44	113229.0988
	138.0549	21.9910	0.0251	-1.7770	8.95	113229.0988
	138.0549	23.2658	0.0206	-1.7132	14.47	499.3708
	138.0550	6.2158	0.0423	2.2970	12.41	359.7119
Trigonelline	138.0550	7.9563	0.0314	2.2603	7.51	11230.4328
Urocanic acid	139.0502	23.8801	0.0283	-1.3562	9.11	560.0547
	139.0502	22.5384	0.0076	-1.6784	6.61	1509.9422

	139.0502	19.8774	0.0058	-1.7691	9.07	2096.3818
	139.0502	18.5301	0.0076	-1.8629	11.28	2999.5175
	139.0584	7.9519	0.0319	2.3045	8.23	60694.8195
	140.0706	7.2810	0.0002	3.4767	2.34	27609.5768
	141.0659	9.2306	0.0069	2.9551	1.21	66428.1188
	142.9386	14.4883	0.0005	-1.8773	6.26	28638.5131
	143.9969	22.0391	0.0004	3.1270	2.22	844610.0416
	144.0656	12.6417	0.0333	-1.5411	4.86	212221.4363
	145.1052	22.3588	0.0102	-5.8816	10.87	33.5617
	145.1052	20.9819	0.0013	-6.6723	20.13	62.7757
4-Indolecarbaldehyde	146.0601	8.5956	0.0093	-1.6577	6.52	22938.8431
	146.0924	26.1775	0.0253	1.8395	10.04	54.2462
	146.1176	8.9503	0.0051	1.6383	3.26	10597.2192
	147.0765	12.6636	0.0085	-1.7145	4.98	65514.6191
	148.0604	27.2481	0.0455	-1.4232	7.1	86.2407
	148.0969	8.3460	0.0032	1.8251	3.33	13933.0070
	149.0186	20.3294	0.0009	-251.6765	15.34	276.8682
Methionine	150.0584	3.0987	0.0035	1.7578	9.44	133815.6424
	151.0353	21.3059	0.0041	-2.3191	12.49	2802998.3220
	151.0391	10.1808	0.0448	1.6120	17.22	16717.4903
	153.0659	3.5415	0.0254	1.6873	7.48	1210138.8260
	154.0693	3.5415	0.0260	1.7099	8.15	92614.0237
Histidine	156.0769	14.2694	0.0025	-2.4030	8.34	1754177.0270
Histidine	156.0769	12.9139	0.0107	-1.9207	15.01	656943.8390
Histidine	156.0769	17.5875	0.0002	-2.4286	7.34	118857.1933
	156.9841	10.3647	0.0005	3.2622	10.6	113178.0513
4,4'-Bipyridine	157.0761	8.5869	0.0091	-1.4519	2.99	47635.1287
	157.0802	14.2694	0.0023	-2.3341	7.36	127742.4635
	158.9811	10.3472	0.0005	3.4214	8.69	31546.9234
	159.0277	20.4827	0.0000	-2.2228	2.37	233.2619
Hydroxymethyl-5,5-dimethylhydantoin	159.0765	11.7825	0.0169	-1.6381	11.07	432814.5646
	159.0917	22.5909	0.0131	-1.8824	7.51	229.4109
1,5-Naphthalenediamine	159.0917	8.5956	0.0120	-1.4035	5.1	164181.4598
	159.1208	21.9165	0.0274	-2.0365	20.96	210.2518
	159.1209	20.5089	0.0066	-2.9371	20.97	134.4952
Trigonelline	160.0370	7.9957	0.0180	2.2066	20.85	204796.4498
	160.0798	11.7825	0.0184	-1.7235	13.72	29276.8428
	160.0951	8.5869	0.0225	-1.3321	4.22	20297.0346
	160.0969	8.7576	0.0070	-1.3960	5.99	54350.7068
	160.0969	3.0812	0.0073	1.8385	10.03	100948.6660
Acetyl-β-methylcholine	160.1332	9.0773	0.0004	2.4929	7.01	7404291.8100
N. epsilon-methyl-l-lysine	161.1285	16.5788	0.0406	1.2864	1.71	187535.4151
	161.1365	9.0729	0.0005	2.4906	7.18	674108.0717
	162.1123	23.4366	0.0132	-1.3923	6.44	1053.6724
7-Methylguanine	166.0724	6.3647	0.0078	1.3395	3.9	13446.5150
	166.0863	21.8596	0.0373	-1.4187	8.83	4186.6128
	167.0128	9.3619	0.0052	2.6850	6.59	12399554.4800
	167.0895	23.1598	0.0137	-1.7285	14.98	197.7171
	168.0656	3.4189	0.0408	1.3963	3.02	118122.0100
	168.9607	10.3472	0.0002	4.0787	13.62	39181.3629
3-Methylhistidine	170.0925	11.0283	0.0259	-1.4575	11.78	185237.0920
	171.1128	6.0577	0.0287	-1.4204	11.91	95477.5259

	171.1129	10.2071	0.0248	-1.3428	3.26	5933.1285
Citrulline	176.1030	11.7825	0.0146	-1.6769	12.54	1713598.8360
	176.1282	8.0570	0.0040	-1.7260	4.73	62088.9565
	176.1282	9.9049	0.0007	2.6891	3.76	24988.2374
	177.1063	11.7825	0.0156	-1.6964	12.99	113904.0181
	178.0897	2.5685	0.0202	2.5059	3.31	38704.2115
	180.0994	21.9691	0.0001	-4.0221	2.47	173.0888
	180.0994	20.5659	0.0002	-2.7754	2.17	160.0383
	181.0260	17.7944	0.0004	3.9708	2.1	1802.6445
	185.0234	9.1780	0.0004	3.1523	10.68	26646.3552
	185.0235	8.7270	0.0074	2.7752	7.97	7579.7091
	186.0186	21.5030	0.0032	5.1092	29.07	171.6159
	188.0705	22.5909	0.0026	-4.1739	12.35	1894.0624
	188.0706	23.9601	0.0049	-1.4890	5.61	5168.9108
Trans-3-Indoleacrylic acid	188.0707	8.5956	0.0149	-1.5147	9.36	502369.1469
	188.1282	8.2628	0.0016	1.6481	4.28	52867.7668
	189.0739	8.5956	0.0118	-1.4813	5.91	66852.1910
N-Acetylglutamic acid	190.0710	12.6417	0.0009	-4.4546	16.19	90436.0654
	193.9737	15.9247	0.0012	3.4638	8.38	16007.5213
	194.0812	19.7187	0.0100	-1.3963	7.26	446.2450
Phenylacetylglycine	194.0813	5.6266	0.0010	4.7199	9.35	159655.7546
	196.1544	2.5904	0.0219	3.4807	35.16	24978.1814
N-Acetylornithine	197.0898	10.0801	0.0171	-2.8528	14.77	236639.8666
	198.0106	10.3297	0.0009	3.2813	7.9	128239.4865
	198.0973	9.7955	0.0238	1.3044	8.09	49264.6020
	200.0077	10.3297	0.0010	3.3413	13.46	53932.5720
	200.0443	10.1940	0.0193	1.9934	18.77	43445.3835
3-Amino-5-morpholinomethyl-2-oxazolidinone	202.1187	7.7408	0.0278	1.3616	1.63	94536.9337
	203.0525	24.0083	0.0071	-1.7794	8.31	963.2424
	203.0525	24.3448	0.0083	-2.2814	13.34	232.1943
	203.0526	10.1808	0.0122	1.3629	5.18	965813.4034
	204.1229	22.9650	0.0081	-2.5421	20.82	156.6340
	204.1230	21.5906	0.0063	-5.9464	10.57	393.8988
	204.1344	8.4292	0.0262	1.5297	5.04	45288.0000
	205.0925	16.5394	0.0090	1.4937	7.26	31803.8072
	205.0971	22.5909	0.0318	-3.4646	14.82	98.6836
L-Tryptophan	205.0972	8.5956	0.0138	-1.5205	8.75	1587172.9730
	206.1006	8.5869	0.0129	-1.5523	8.91	194164.5283
	208.0394	9.3619	0.0028	2.7061	8.36	3972270.1760
Kynurenine	209.0922	8.1665	0.0074	-1.9649	5.52	43337.3666
	209.1384	1.9986	0.0357	1.4366	1.73	297633.9539
	209.9873	10.3297	0.0007	3.5180	11.08	55465.0656
	211.0391	8.0439	0.0396	1.9867	8.01	252318.4061
	211.9843	10.3122	0.0008	3.4911	7.76	28969.6339
	212.1004	11.2035	0.0377	-1.5556	12.06	29034.0494
Acetylarginine	217.1296	10.6979	0.0020	-2.5566	5.89	40209.9826
	218.0925	8.5869	0.0059	-1.9389	10.18	86385.1647
	218.1136	11.7558	0.0170	-5.5326	23.5	38462.8449
	218.9748	14.4883	0.0008	2.9675	5.41	46369.3364
	218.9843	12.6417	0.0002	2.5866	7.26	104161.3225
	219.0177	10.1808	0.0000	3.0887	1.78	21399.2071
N-(1-deoxy-1-fructosyl)glycine	220.0816	12.6417	0.0051	-2.6983	20.89	132361.8612

	220.1179	22.5909	0.0488	-8.7455	7.46	19.6660
	220.1179	21.1921	0.0255	-23.6202	56.94	98.8283
	220.5576	10.1852	0.0305	1.7415	9.93	52106.6322
	220.9346	16.4115	0.0005	2.6254	6.05	339451.6681
N-Acetyl-D-galactosaminitol	224.1129	13.2948	0.0047	-3.1589	5.4	856291.6159
	225.0547	6.3428	0.0175	1.9483	1.54	129068.8627
	225.1163	13.3036	0.0040	-3.3562	6.02	73821.1661
	226.0499	11.2472	0.0001	3.5945	6.98	127997.2504
	226.1649	2.0030	0.0327	1.4332	4.06	193532.5957
	232.1543	21.5512	0.0352	-3.1353	21.01	196.7651
	234.0770	24.0083	0.0065	-1.4622	4.05	7154.7143
	234.0770	24.3217	0.0169	-1.3343	7.21	6508.1870
	234.0770	22.6172	0.0118	-2.4543	11.83	7054.3141
	234.0770	23.0985	0.0085	-1.6827	10.23	5093.0352
	234.0771	22.2975	0.0177	-2.2727	13	175090.3796
	234.0771	10.1370	0.0456	1.2698	7.49	1074703.2330
	235.0804	11.3699	0.0174	1.5141	12.63	82809.0030
	235.0805	10.1414	0.0423	1.2851	8.04	90808.2970
	235.1651	21.4592	0.0231	-1.4069	11.14	310.3121
	236.0729	10.1414	0.0493	1.2533	6.5	49331.2710
	240.1805	2.3845	0.0455	2.6564	14.25	142321.5451
	241.0496	8.8277	0.0493	1.8123	5.81	41365.6592
	242.9253	30.2278	0.0179	2.0081	21.24	121.5675
	243.0653	8.9284	0.0006	1.7853	0.73	31049.0823
2-Fluoro-6-(4-methoxyphenoxy)benzonitrile	244.0793	8.0395	0.0284	1.3192	7.83	125739.2037
	246.0221	11.1071	0.0001	3.4987	7.56	118036.1375
N-Acetyl-D-galactosaminitol	246.0949	8.7489	0.0065	-1.8095	9.84	174654.8642
	246.1699	19.7494	0.0007	-3.6919	11.41	282.4559
	246.1700	21.1658	0.0084	-1.8851	4.59	787.1396
N-Acetyl-DL-tryptophan	247.1078	6.3428	0.0042	-2.4639	12.03	122502.9659
	249.0456	9.7955	0.0256	-3.3418	29.27	225555.2801
	249.0457	10.1808	0.0388	-2.6350	28.43	127665.7877
	250.0510	11.6638	0.0073	1.6769	11.63	82423.0785
	252.0656	8.0395	0.0477	1.9183	10.7	169682.2730
Muramic acid	252.1078	11.4925	0.0023	-3.1686	6.9	294734.3357
	255.9441	9.1561	0.0001	4.6616	9.41	69971.6374
	256.1307	19.8292	0.0024	-4.1212	21.85	5670.6077
	256.1307	21.2402	0.0028	-2.8244	8.87	7050.5758
	260.0013	14.4883	0.0015	2.7162	4.21	86413.6318
Hexanoylcarnitine	260.1857	5.3201	0.0485	-1.5227	4.73	452802.3734
	262.1649	7.5044	0.0442	-1.3049	4.73	117010.5394
	262.8880	14.4664	0.0028	-2.6307	13.46	44204.5315
	263.0850	25.9323	0.0233	1.3026	6.89	945.9356
	265.0232	9.7823	0.0001	2.8607	3.99	578896.0953
	265.0232	10.1896	0.0000	3.1879	6.62	436771.2469
	266.1863	2.0952	0.0243	-1.4961	8	87949.2892
	267.0765	11.2560	0.0000	3.4924	7.17	81473.9106
N5-(4-Methoxybenzyl)glutamine	267.1339	9.3182	0.0051	2.4413	2.46	35569.9041
N-(1-Deoxy-1-fructosyl)serine	268.1027	12.6417	0.0048	-2.8838	22.09	50167.5354
	276.1443	10.5837	0.0056	-1.7616	6.69	24909.3274
	280.1544	5.8683	0.0002	6.7137	9.59	85078.0937
	281.2475	1.7184	0.0045	1.6335	0.51	41234.3942

	288.9219	16.3764	0.0002	2.9128	2.71	1072933.3060
	290.0758	9.7955	0.0480	1.6566	20.72	64068.3349
	290.0759	10.1983	0.0080	2.8555	7.59	39609.3846
	290.1598	5.7405	0.0015	53.5854	6.34	124821.1447
	296.0209	10.1940	0.0003	2.4935	7.13	177189.2705
	296.9707	9.1868	0.0014	4.4974	10.44	622783.7509
	296.9707	8.4117	0.0345	4.2427	12.95	272770.7159
	298.0179	10.1940	0.0001	2.6329	4.41	54225.3070
	305.5881	10.1983	0.0039	2.6634	8.01	10202.0532
Cytidine monophosphate	306.0496	9.7867	0.0001	2.8331	3.99	713444.4227
	306.0496	10.1896	0.0001	3.1219	6.54	364876.7289
	307.9975	10.2421	0.0000	3.0403	6.29	38997.2949
	309.0493	10.1764	0.0001	3.1551	5.59	103575.6782
	309.0493	9.8042	0.0009	2.4400	11.06	132448.7939
	309.1290	26.9318	0.0261	1.4201	7.42	224.3408
	309.1290	27.0993	0.0332	1.5076	13.83	265.1554
	309.1291	11.7251	0.0044	-5.7711	14.15	1131586.5380
	309.1292	11.5625	0.0045	-3.4984	23.61	861836.9430
	309.1292	12.6680	0.0123	-2.3209	18.46	321470.6683
	309.9945	10.2421	0.0001	3.0693	6.97	24396.4703
	310.0574	6.3428	0.0475	1.2234	4.36	146023.9123
	310.1325	11.7295	0.0045	-6.2037	13.01	161500.5683
	312.9528	10.2377	0.0304	-1.2831	5.38	18906.4671
9-Decenoylcarnitine	314.2325	3.1338	0.0190	-1.5900	7.94	184895.9756
Decanoylcarnitine	316.2483	3.0243	0.0191	-1.6039	6.87	128888.3498
	331.0924	11.2472	0.0008	2.6628	5.49	168308.8444
	331.1111	11.5757	0.0013	-6.3516	21.51	709074.0270
	343.9966	8.0439	0.0342	2.5197	13.04	95898.5223
	345.2060	2.1302	0.0347	3.0101	19.94	64530.7750
	351.1986	11.8000	0.0164	-4.2033	31.23	63398.6294
	353.0226	6.0796	0.0224	5.8393	11.58	130820.5570
	356.9093	16.2225	0.0023	3.9565	8.56	62129.4052
3-Beta-Hydroxy 5-cholenoic acid	357.2787	2.4108	0.0359	-9.0123	12.12	170272.7135
	367.1500	10.2071	0.0098	-3.0953	10.6	57654.5831
	385.0230	8.0526	0.0301	2.5213	15.57	92387.9515
	389.0431	6.3428	0.0160	2.7103	3.66	118566.6699
	395.0248	11.0984	0.0115	3.0744	12.66	70269.1407
O-Palmitoleoeoylcarnitine	398.3265	2.8049	0.0315	-1.7906	3.07	411580.6742
	399.0811	10.1896	0.0001	2.9738	4.28	81030.3740
	400.2363	17.0344	0.0154	-47.8724	89.27	175.4606
	402.3578	2.9188	0.0400	1.9019	16.49	48283.3917
	413.9982	11.1071	0.0005	2.7184	1.97	99034.3286
	418.0544	10.1764	0.0000	5.3538	4.75	108739.0114
	424.8967	16.2575	0.0001	3.7398	5.3	521237.3083
	432.2240	1.8454	0.0497	-1.6887	19.42	17557.9825
	432.2376	15.8765	0.0474	1.7155	19.07	3425.3245
	435.0577	10.1940	0.0013	2.3688	6.04	222122.1189
	437.0548	10.1940	0.0014	2.5516	5.64	69784.0881
	445.0865	10.1896	0.0002	2.5422	0.28	169544.6088
	445.0865	9.8042	0.0007	2.3335	9.46	202871.3361
LysoPE(16:0/0:0)	454.2928	3.1868	0.0290	1.4517	5.58	1921929.1770
	456.1071	11.2210	0.0041	1.4884	6.42	67679.4105

	460.2691	1.7534	0.0177	2.0028	18.97	3383562.3140
	462.2672	5.7803	0.0308	-117.8194	16.33	735044.6422
	477.1618	11.2648	0.0041	2.0787	8.16	240952.5565
Taurocholic acid	480.2779	5.6748	0.0338	-66.9070	13.47	4249432.6640
	494.3242	2.8837	0.0494	-1.2209	6.44	3777191.9810
	496.2734	2.9144	0.0100	-6270367.6742	11.64	768638.4006
	496.4208	1.7359	0.0319	-1.2080	3.89	90960.1046
Taurodeoxycholic acid	500.3041	3.4671	0.0157	-67.9795	9.18	15338520.0400
LysoPE (20:4/0:0)	502.2927	2.9451	0.0111	1.4954	4.34	1430033.2480
LysoPC(O-18:1/0:0)	508.3763	2.8618	0.0184	1.8463	3.2	173835.1744
Taurocholic acid	516.2991	5.8110	0.0348	-59.1276	12.75	12881412.1600
Taurocholic acid	516.2991	5.2938	0.0323	-124.1226	12.53	10241569.7100
	518.3047	5.8110	0.0368	-107.0283	16.55	346920.1167
LysoPC(18:1)	522.3459	2.8750	0.0104	-3.5137	4.49	191992.2924
LysoPE(20:4/0:0)	524.2751	2.9669	0.0037	1.6688	7.36	153161.0696
LysoPE(20:3/0:0)	526.2929	2.9232	0.0281	1.5831	14.74	3346118.4420
	531.3099	2.9100	0.0191	-9598.9417	77.59	337047.0832
	531.3100	19.1694	0.0002	4.1366	3.93	37361.0245
	531.3100	4.7669	0.0265	-120.4138	9.59	858644.7160
	531.3101	3.8098	0.0222	-112.5155	3.3	2518978.9320
	533.3255	5.8110	0.0312	-104.8941	14.49	32257473.3200
	533.3256	5.2938	0.0348	-125.5704	11.24	9328470.4510
	535.3309	5.8110	0.0272	-162.7887	15.08	1283473.3730
PC(19:0/0:0)	538.3868	2.7217	0.0029	-2.1878	4.39	789146.5787
	548.2749	2.9275	0.0042	2.1214	11.78	156413.9815
	552.4026	2.6736	0.0337	-1.7089	3.03	669659.2306
	554.3186	2.6079	0.0428	-13.7141	13.57	172372.0757
	575.1424	11.7470	0.0420	-3.1168	23.02	136939.8644
	575.4669	1.7096	0.0107	-1.5161	5.65	74650.1050
	576.3320	1.6877	0.0257	2.3018	21.85	155257.0983
	584.4734	1.7359	0.0425	-1.2281	3.87	64900.7151
PC(16:0/5:0(CHO))	594.3767	2.3977	0.0292	-1.8902	20.74	157721.8480
	599.3400	8.2716	0.0120	-3.4079	11.85	5812329.2970
	600.4683	1.7359	0.0372	-1.7911	16.45	74731.2088
	601.3464	8.2716	0.0128	-3.8649	13.98	274445.9963
	621.3219	8.1446	0.0077	-8.2267	14.56	612193.8903
PC(16:0/9:0(CHO))	650.4392	2.2090	0.0264	-1.6782	16.74	612841.5591
	675.5437	2.4853	0.0396	-1.8578	3.24	345179.9695
PS(P-16:0/13:0)	678.4705	2.1608	0.0447	-1.8680	16.77	287422.3268
	689.5593	2.4196	0.0452	-2.2085	6.2	826867.0542
	726.5301	1.6395	0.0358	2.0477	6.46	757434.6709
	758.2215	16.9940	0.0424	-1.5552	17.64	14996.9020
	761.3928	8.9635	0.0056	-12.0677	20.24	440764.5039
	773.0775	11.0984	0.0432	-2.2131	26.51	140967.6458
PC(16:0/18:2(11Z,13Z))	780.5533	1.9899	0.0119	-1.3117	2.89	8102151.3070
	800.6167	1.9461	0.0388	-4.2020	9.29	434972.1395
	832.2404	1.6395	0.0479	1.3624	5.24	2698869.6870
	1021.6252	2.9100	0.0370	1.9712	19.45	203859.8066
	1029.6874	2.8356	0.0368	-1.3550	5.44	145463.4559

Table 5. HILIC-POS ion mode features with a *P*-value <0.05 and FC ≥ |1.2|. Many of the genotype-dependent features, assigned unique m/z, remain unidentified using the data analyses described in the text. These molecular features are reported both for completeness and as reference points for future studies.

Appendix A: Table 6: HILIC-NEG						
Putative identification	**Mass to charge ratio (m/z)**	**Retention time (min)**	**ANOVA nominal *P*value**	**Fold change (relative to KO)**	**Coefficient of Variance (% min CV)**	**Maximum Abundance**
	79.9570	2.6884	0.0161	8.8829	59.04	2463.2541
	79.9571	2.3683	0.0002	1480.0348	17.26	2200.0673
	79.9571	6.0023	0.0159	4.0733	14.34	6818.7494
	87.0086	6.0420	0.0038	-4.7318	14.87	8915.7965
	88.9880	20.7710	0.0388	17.2295	67.72	1307.8757
	93.0343	2.6489	0.0066	6.9925	46.09	28199.8376
Sulfate	96.9599	14.4442	0.0166	-1.2722	3.67	978172.3007
	97.0042	8.8155	0.0034	1.5114	6.79	2449.9059
	97.0293	9.8127	0.0393	1.3072	10.24	3302.1746
	98.9557	14.4485	0.0119	-1.2770	3.25	44198.8961
	106.0408	13.7186	0.0374	-1.4557	6.33	60.8436
	106.0409	4.4868	0.0214	-8.1944	66.62	4248.2874
	106.0409	2.5260	0.0285	-10.9351	59.48	5352.8612
	106.0409	26.2068	0.0460	-1.8041	10.13	18552.9795
	106.0409	29.3988	0.0084	-1.4702	9.21	20337.8979
	107.0362	27.2757	0.0115	1.4473	1.8	961.9447
	107.0362	28.1162	0.0492	-2.3063	26.76	2373.6588
4-Methylphenol	107.0499	2.3683	0.0004	259.4036	15.19	18271.9300
Imidazole acetaldehyde	109.0405	26.2068	0.0481	-1.5667	10.83	1181.2989
2-Furoic acid	111.0086	14.2989	0.0157	1.2377	5.95	40046.9049
	114.0307	8.8155	0.0053	1.4418	6.87	7716.5786
3-Hydroxyvaleric acid	117.0555	4.7025	0.0025	1.5376	6.51	211849.3395
	117.0708	2.5304	0.0020	5.0136	17.47	40860.8548
	119.0348	8.5648	0.0363	1.3929	12.18	22090.3856
4-Hydroxybenzaldehyde	121.0293	3.7058	0.0093	1.3489	7.58	29047.9739
2-Hydroxyethanesulfonate	124.9912	9.0388	0.0028	-1.4049	2.82	50500.4717
4-Hydroxy-6-methyl-2-pyrone	125.0242	4.5353	0.0404	-2.5634	24.12	38793.6614
N-Acetylalanine	130.0508	7.7016	0.0223	1.4748	3.55	40749.9103
Isoleucine	130.0871	7.8243	0.0037	1.3687	2.05	199139.3285
DL-beta-leucine	130.0871	8.1176	0.0041	1.3403	5.44	105411.7415
	131.0349	12.3786	0.0464	1.2834	7.57	1306.8043
	131.0460	9.7689	0.0406	1.7067	4.18	14584.5517
	131.0905	7.8243	0.0028	1.4089	2.32	12898.5462
D-aspartic acid	132.0301	12.1587	0.0178	1.8744	8.01	46596.2451
L-aspartic acid	132.0301	20.5441	0.0464	3.8046	22.92	193.7417
	132.0450	6.0023	0.0199	4.3542	13.91	7942.7952
	133.0505	7.7192	0.0106	2.2384	4.01	5884.4360
	134.8946	18.8303	0.0084	1.2293	0.46	1136.5361
	141.0392	9.4436	0.0327	3.8618	21.62	9538.9853
	144.0025	9.4567	0.0297	1.8711	13.16	7498.1210
	144.0665	14.3339	0.0388	-1.2654	8.67	139.4714
	144.8695	10.2075	0.0304	-1.6660	7.26	21229.7807
3-Methylglutaric acid	145.0504	6.0201	0.0002	-3.3155	9.46	111698.5542
	145.0981	17.7387	0.0170	1.3844	7.88	260158.0208
	146.0246	2.2195	0.0442	2.4125	28.39	28266.9484
L-4-Hydroxyglutamate	146.0457	9.2497	0.0487	1.3511	7.13	6639.5919
	146.0458	20.2602	0.0100	1.2740	3.32	384.7539

	146.0821	8.7142	0.0349	1.2977	5.99	11030.2346
	146.1014	17.7387	0.0159	1.3976	7.66	17398.3656
	146.8666	10.2031	0.0403	-1.6611	11.17	21535.4547
	147.0661	6.1340	0.0491	1.3484	11.08	17375.8675
D-(-)-Lyxose	149.0453	7.1993	0.0429	-1.2725	3.8	9666.5846
D-(-)-Lyxose	149.0453	10.0889	0.0392	1.4475	10.68	57830.4890
	151.0399	5.6377	0.0315	2.9028	24.49	16893.1455
Orotic acid	155.0097	8.8592	0.0103	1.7313	11.98	6752.3903
	155.0712	2.6052	0.0254	-2.2322	23.23	10067.1902
	157.0364	8.8155	0.0102	1.4097	8.47	241852.2128
	157.0868	2.5085	0.0194	-1.6932	10	45062.4937
	157.9007	5.1895	0.0361	-2.1823	20.88	11951.2181
	158.0398	8.8023	0.0035	1.4687	7.24	11241.0982
	159.0409	10.4222	0.0317	-1.3897	11.02	6251.2269
Daminozide	159.0773	9.8259	0.0363	3.5325	20.94	11779.3137
	161.0454	9.8040	0.0250	1.2830	8.22	2723604.4620
	161.0454	18.1422	0.0276	1.2820	4.13	94882.3434
3-(4-Hydroxyphenyl)propionic acid	165.0555	3.7233	0.0117	-2.5589	23.76	158359.7077
Noradrenochrome o-semiquinone	166.0507	3.3730	0.0470	1.3066	6.92	25154.8528
Uric acid	167.0208	10.6109	0.0369	-1.5121	14.86	600403.9205
	167.0209	18.9424	0.0340	-1.3304	9.57	2234.9378
	172.8299	10.1681	0.0406	-1.2602	9.18	8798.0032
4-Phenolsulfonic acid	172.9911	2.6752	0.0076	6.7151	47.51	6330597.1140
cis-Aconitic acid	173.0089	12.5419	0.0069	1.3292	6.14	6712.9901
	174.9558	8.3497	0.0444	-1.4671	7.94	154508.6864
	174.9868	2.6665	0.0075	6.8452	47.38	277847.5865
	174.9975	2.6796	0.0099	10.6444	27.25	4749.2081
Ascorbate	175.0246	13.7985	0.0095	3.8646	30.93	15129.6630
N-Formylmethionine	176.0384	6.4632	0.0146	1.5927	2.13	13343.1001
	179.0560	18.1159	0.0260	1.3354	3.79	13274.3897
2,4-Dinitrophenol	183.0045	2.3640	0.0204	-1.5658	4.63	7204.5390
	183.1024	2.3946	0.0120	-1.6853	10.09	10857.0773
	185.0429	4.6539	0.0055	2.4356	8.51	49089.3782
	187.0068	2.3596	0.0000	97.7069	15.65	4761696.6280
	188.0101	2.3596	0.0000	114.6441	15.39	355503.8634
DL-alpha-Aminosuberic acid	188.0926	6.9824	0.0407	1.3492	8.92	9807.0479
	189.0025	2.3640	0.0000	120.3912	15.32	210000.8987
	189.0132	2.3552	0.0001	1825.6884	12.02	7529.0520
Phenylacetylglycine	192.0665	5.6640	0.0026	6.9120	23.62	353634.6842
	193.0697	5.6596	0.0040	10.1710	23.66	40709.9547
	194.9272	14.4442	0.0142	-1.2916	1.47	2317671.3280
Gluconic acid	195.0507	7.2080	0.0252	-1.3345	7.77	12206.6306
Gluconic acid	195.0508	11.6722	0.0353	1.2866	5.87	399076.0035
	195.1388	1.8946	0.0448	-1.4727	10.62	20734.1470
	196.0224	8.9950	0.0034	1.3747	3.56	6852.4739
	196.9230	14.4442	0.0136	-1.3024	1.6	197664.2736
	198.0745	7.7761	0.0055	1.3114	5.3	21240.2496
	199.0190	10.3345	0.0477	1.3822	13.28	45958.6888
N-Acetyl-aminooctanoic acid	200.1290	2.6708	0.0090	-1.7955	12.55	31523.6604
	201.0225	2.0877	0.0001	2592.6209	53.36	1848689.3340
	203.0559	11.2863	0.0479	-2.9126	14.73	30552.0367
	203.0559	10.1944	0.0059	-2.8762	19.72	3394.0507

D-(+)-Tryptophan	203.0824	8.5780	0.0221	-1.3611	7.86	423450.5591
Indole-3-lactic acid	204.0663	6.8147	0.0058	-1.9789	11.44	58188.1261
	204.0856	8.5780	0.0188	-1.3796	7.06	50339.9680
	204.9809	2.1713	0.0461	-4.9686	53.04	12781.1513
	207.0508	10.4791	0.0251	1.3009	8.14	1158068.8730
	207.0509	18.8260	0.0303	1.2602	4.03	38913.4362
	207.0509	18.2481	0.0369	1.2479	3.54	20293.6247
	209.0850	1.8596	0.0176	-1.5449	13.01	4677.2375
	209.9687	9.0475	0.0005	-1.7203	3.8	16618.9289
	211.1337	2.1801	0.0273	-1.5322	14.96	17826.2259
3-Indoxyl sulphate	212.0020	6.0201	0.0173	4.0662	13.98	9737671.1760
	213.0052	6.0154	0.0174	4.1838	14.06	986357.7973
	213.0855	17.7475	0.0261	1.2133	4.15	34525.4040
	213.1494	2.1100	0.0101	-1.9844	4.98	110731.2483
	213.9977	6.0110	0.0180	4.1774	14.64	476835.5745
	214.0084	5.9848	0.0383	3.7385	14.1	8165.7013
	214.0487	10.4572	0.0403	-1.7033	6.12	8300.6576
12-Hydroxydodecanoic acid	215.1649	2.0877	0.0152	-1.6423	11.4	52814.9569
	217.0173	2.0877	0.0008	25.9925	42.13	7534.2635
	217.0173	4.6539	0.0200	2.4233	29.88	53338.0732
	217.0295	18.6526	0.0493	1.3534	10.47	288.2223
	218.9819	8.0607	0.0455	-1.5992	9.24	36449.7649
	224.7626	9.9747	0.0176	-1.2024	5.04	6846.3369
	225.0239	8.8155	0.0063	1.5383	5.86	9682.1120
	225.0614	20.3183	0.0242	1.3604	6.66	3093.4898
	225.0615	18.1203	0.0208	1.3565	2.33	7167.4758
	226.1446	2.6008	0.0297	-1.5630	6.55	13774.1149
2'-Deoxyuridine	227.0671	4.7730	0.0177	1.9666	11.75	352474.6785
	227.1650	2.0702	0.0287	-1.9914	23.2	17273.6853
	227.2014	1.7983	0.0047	-1.9837	13.87	94235.7736
	228.0705	4.7112	0.0034	2.1236	14.64	43276.1979
	228.1601	2.5873	0.0138	-1.5464	3.74	5698.6131
	229.0020	10.4616	0.0049	-2.3680	8.83	8451.6618
	229.1805	2.0527	0.0377	-1.5612	14.88	15740.4235
	229.8606	5.1676	0.0152	1.9071	18.25	106450.4267
2,4-Dihydroxyacetophenone 5-sulfate	230.9965	2.5785	0.0002	-6.8160	6.47	19482.5660
	237.1493	2.0746	0.0129	-1.7733	9.51	21691.2456
Indole-3-carboxilic acid-O-sulphate	239.9970	2.7234	0.0005	-318.4697	29.91	47047.5522
	241.0916	18.1956	0.0481	1.3449	8.59	40828.2828
	242.0126	2.5917	0.0003	-23.1126	28.06	62926.1858
	242.0517	18.4254	0.0144	1.2242	3.06	744.1482
Pseudouridine	243.0619	8.1527	0.0007	1.3447	3.18	120672.4755
	243.1962	1.9253	0.0096	-1.9428	7.16	47625.4798
	245.0775	6.3581	0.0102	1.6437	4.27	13584.7034
N-Acetyl-DL-tryptophan	245.0927	6.2479	0.0052	-2.7479	6.18	72281.2950
	249.0318	2.5348	0.0036	-39.0426	25.84	21570.9225
	249.0877	6.0420	0.0026	-4.5924	25.85	46537.9157
	249.1160	1.8377	0.0393	-3.2556	44.67	24779.1309
	250.1241	1.9826	0.0064	-10.4267	43.69	42445.9994
	251.1285	6.5599	0.0354	-1.4534	9.54	42760.3354
	252.9478	2.6708	0.0315	647.8418	86.09	14742.2133
	253.0925	6.4720	0.0003	-1.5936	2.65	10783.6918

	253.0926	5.2508	0.0019	-1.3515	2.22	189075.1589
	253.1442	2.2720	0.0336	-1.4731	8.34	62281.2772
Palmitoleic acid	253.2170	1.7808	0.0078	-2.3848	17.43	741023.2017
Ascorbic acid-2-sulfate	254.9815	15.6392	0.0255	-1.9242	22.01	719.9750
	254.9942	2.3683	0.0025	1817.6010	36.81	15537.1762
	255.2327	1.7677	0.0073	-1.4515	8.38	2029174.5820
	259.1295	9.7908	0.0151	2.1678	13.46	8089.7206
	259.8390	14.4879	0.0465	-1.5905	6.57	19834.0029
	261.0980	2.4734	0.0006	-13.1732	11.6	144144.8107
	263.0437	4.9218	0.0195	2.7168	15.15	77241.5797
	263.0576	9.3424	0.0154	1.6888	6.82	43475.1816
	265.0732	9.3467	0.0376	1.5434	14.84	13028.1040
	265.1805	1.8903	0.0320	-1.5519	8.45	13754.5838
	267.1046	1.8377	0.0020	-14.8879	37.66	66043.7821
	267.1962	1.8596	0.0025	-1.7670	4.43	44613.8287
	269.0874	7.8987	0.0063	2.0951	14.35	26963.0214
	269.2119	1.8684	0.0021	-1.8971	6.75	131811.8347
16-Hydroxyhexadecanoic acid	271.2276	1.8596	0.0064	-1.8774	4.28	315917.4100
	273.0725	4.7594	0.0048	1.9197	13.4	791870.6193
	274.0759	4.7730	0.0046	2.0705	15.07	89217.1255
Norophthalmic acid	274.1042	12.4224	0.0317	1.3423	4.43	89197.0527
	275.1075	12.4267	0.0205	1.3956	4.66	9833.1131
	278.9156	2.0089	0.0261	-1.3272	2.64	31290.5097
13-Hydroxyabscisic acid	279.1234	1.8859	0.0050	1.8658	12.56	68914.3004
	279.1631	1.7107	0.0422	1.9687	11.25	76345.6819
Linoleic acid	279.2325	1.7677	0.0399	-1.6136	18.12	4410173.3990
	279.9892	5.9935	0.0234	2.7976	11.83	38562.2381
p-Cresol glucuronide	283.0819	7.3849	0.0007	200.4614	31.44	153066.7082
	283.2275	1.8465	0.0424	-1.7568	21.21	10406.0137
	285.2432	1.8640	0.0136	-1.4910	1.96	5656.2599
	290.0626	4.9087	0.0137	2.2445	10.56	92316.0704
	291.0829	6.3537	0.0060	1.6782	1.14	17667.3612
	292.6899	9.9528	0.0064	-1.3353	6.69	27701.1758
	292.9445	14.3033	0.0063	1.2597	2.21	94175.9672
13-OxoODE	293.2119	1.8290	0.0176	-1.6164	13.46	52971.1891
	299.2223	1.8202	0.0164	-2.1674	16.67	34792.6810
	301.2378	1.7764	0.0083	-1.5853	10.38	102994.4831
	302.6820	9.9441	0.0324	-1.3283	10.37	109091.1861
	303.1267	2.6008	0.0130	1.9519	13.59	10019.0101
	304.6798	9.9397	0.0414	-1.3204	11.22	159641.0499
	305.1424	2.5785	0.0026	3.0117	17.05	103471.4689
	306.6776	9.9397	0.0389	-1.3275	11.22	117830.7975
	307.1580	1.8202	0.0159	-6.1266	39.15	20371.2815
	307.1945	1.6799	0.0354	2.1406	22.76	95479.7318
	308.0983	8.9862	0.0097	2.8412	23.42	19006.3738
	308.6756	9.9441	0.0310	-1.3004	8.7	46846.2365
	310.1139	9.7689	0.0007	3.1271	7.67	8799.2921
	311.1092	9.7777	0.0326	1.7062	2.77	162476.4668
	311.1858	1.8815	0.0363	-2.0940	22.75	11739.5465
12,13-DiHOME	313.2381	1.8903	0.0076	-2.1094	16.22	157191.6765
	315.2535	1.8859	0.0230	-1.7902	12.89	31962.8451
	323.1893	1.6976	0.0228	2.2094	17.83	27358.8944

	323.2221	1.8027	0.0159	5.2889	40.79	7962.0882
	325.2377	1.7677	0.0104	-1.7904	15.39	76874.7269
	327.2532	1.7501	0.0319	-1.5483	11.26	201775.4366
	329.1754	1.8946	0.0296	-2.2827	26.14	16768.9709
	332.1094	8.1833	0.0170	-1.2307	2.46	12516.0660
	336.0523	10.6065	0.0479	-1.9376	23.55	14842.3449
	344.1344	7.8505	0.0085	2.0338	11.41	20462.5927
	345.2429	1.8202	0.0406	-1.5375	17.41	58479.7590
	346.0775	7.4024	0.0013	5602.6355	48.06	29900.1634
	346.9894	2.6446	0.0214	34.2469	22.49	105404.5862
	349.0383	1.8552	0.0027	-11.8190	31.05	15768.0943
	351.0539	2.2195	0.0384	1.5944	17.45	18452.8792
	351.2204	1.6799	0.0247	2.3301	24.49	49746.1361
	351.8278	1.7545	0.0014	-13.4028	28.07	69520.7268
	353.8257	1.7458	0.0034	-5.4201	24.83	90660.0420
	355.8237	1.7458	0.0043	-14.6483	33.45	67143.7439
	360.1479	2.5873	0.0287	-1.9720	20.64	17210.8090
Adhumulone	361.2015	1.6274	0.0374	-3.7953	39.05	23937.5621
	367.2153	1.7020	0.0236	2.2387	24.6	16884.7482
	377.0694	2.0833	0.0079	4.4343	14.36	31326.2977
	379.1756	2.1319	0.0387	-1.8231	22.98	38315.1890
12-Ketodeoxycholic acid	389.2692	2.1231	0.0146	-10.5894	46.62	51439.3893
Deoxycholic acid	391.2849	2.3946	0.0265	-6.5699	51.95	1271555.6700
	392.0473	2.6402	0.0172	29.1677	7.98	188548.5464
	395.2465	1.6799	0.0204	2.7878	25.18	40070.2287
	401.0749	10.1199	0.0184	1.5804	19.01	16587.4272
Indoxyl sulfate	425.0113	5.9629	0.0096	45.9841	21.99	274859.6181
Cysteineglutathione disulfide	425.0801	13.9976	0.0494	1.9968	15.91	65040.9617
	431.7359	1.6976	0.0269	-587.7488	159.22	30904.3652
	433.7339	1.7020	0.0473	-337.7808	126.66	28246.6543
	434.2363	1.8377	0.0130	-1.7140	7.56	177754.9858
	435.2744	2.1713	0.0393	-13.5603	47.15	49631.1714
	439.2726	1.6932	0.0317	3.4031	29.06	26724.6999
LysoPE(16:0/0:0)	452.2775	4.5747	0.0291	1.4180	11.95	100416.3578
Glycerophospho-N-palmitoyl ethanolamine	452.2776	2.8154	0.0468	1.3835	7.84	286564.4703
	458.1877	18.0931	0.0439	7.8849	64.04	8.5165
	470.0688	5.9410	0.0130	35.1084	5.49	505029.3275
	473.2680	2.3070	0.0051	-15.8256	40.14	45095.6005
	496.2730	2.6971	0.0306	-88.7313	106.83	1273298.7020
Taurochenodeoxycholic acid	498.2887	2.7759	0.0268	-49.1351	99.74	9996673.0720
	498.9294	1.5661	0.0095	-1.5333	10.29	509013.6642
	510.2520	2.7190	0.0220	-424.5775	103.69	152917.4938
	512.2678	2.7628	0.0334	-134.3214	78.69	60505.8581
	512.9589	1.6099	0.0133	-1.7486	11.9	3396404.1950
Taurohyocholate	514.2833	4.5222	0.0273	-167.7197	31.35	40151.1487
	514.2835	5.5848	0.0282	-83.8225	63.43	34863736.1200
PE(22:6/0:0)	516.2878	4.5660	0.0335	-521.8970	87.19	93867.1032
	524.2773	2.7759	0.0377	1.9347	17.78	608030.7137
2-[4,6-Bis(2,4-dimethylphenyl)-1,3,5-triazin-2-yl]-5-(octyloxy)phenol	530.2781	6.0639	0.0470	-246.4345	83.28	119514.1686
	538.3143	2.7759	0.0333	-1.3576	5.82	196626.9271
	545.3146	2.6971	0.0455	-456.8610	126.34	158935.7617

	562.9560	1.6099	0.0095	-1.8557	13.07	21189.2306
	582.2712	4.6058	0.0176	-365.8585	79.68	891759.1281
	582.2713	5.6070	0.0129	-37.3944	66.63	452355.1928
	597.3247	8.2227	0.0060	-3.7810	29.27	1754949.7590
	604.4608	1.7107	0.0023	-12155.2483	80.69	33071.3752
	613.3741	1.8465	0.0029	1.8621	9.09	22177.5278
	679.8444	18.7633	0.0365	5.4625	46.58	5.8398
	692.1083	5.9278	0.0115	20.6904	22.31	402492.9470
	697.4688	1.7896	0.0233	1.3773	7.47	1172561.8360
	759.3778	8.9600	0.0116	-9.7413	49.62	105776.7311
	888.5624	2.5785	0.0014	-4.3651	12.41	159152.2372

Table 6. HILIC-NEG ion mode features with a *P*-value <0.05 and FC ≥ │1.2│. Many of the genotype-dependent features, assigned unique m/z, remain unidentified using the data analyses described in the text. These molecular features are reported both for completeness and as reference points for future studies.

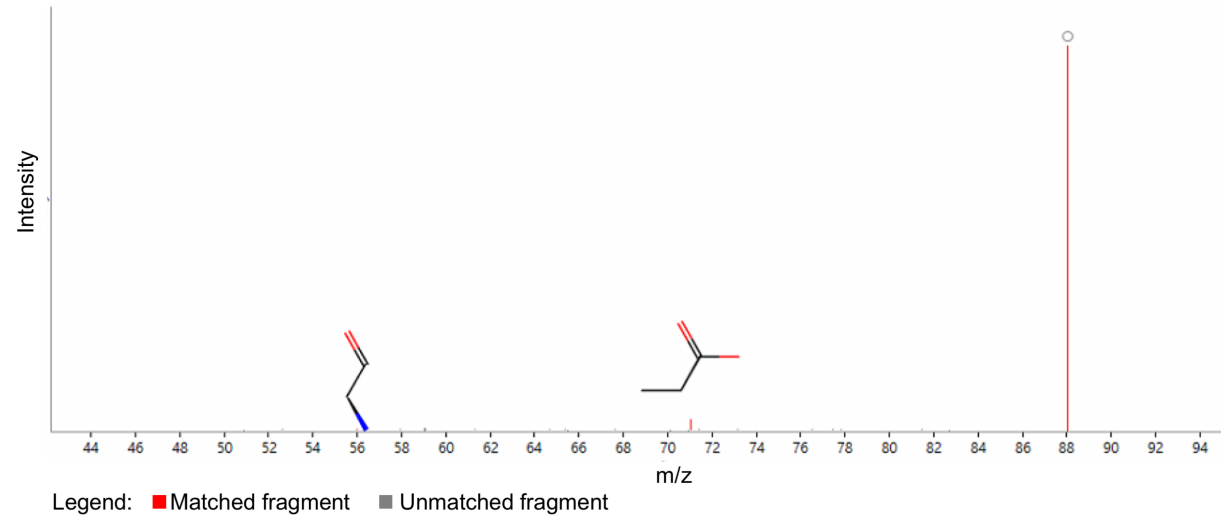

* Instrument method scans low end of mass range at 70 Da, therefore we do not expect ions to be detected below 70 Da.

Fig. 60: Experimentally measured (shown above): Putative identification: **L-alanine**
Progenesis Fragmentation Score: 17.7*
Reference (not shown) matched fragments in red): HMDB: **L-alanine**: C3H7NO2

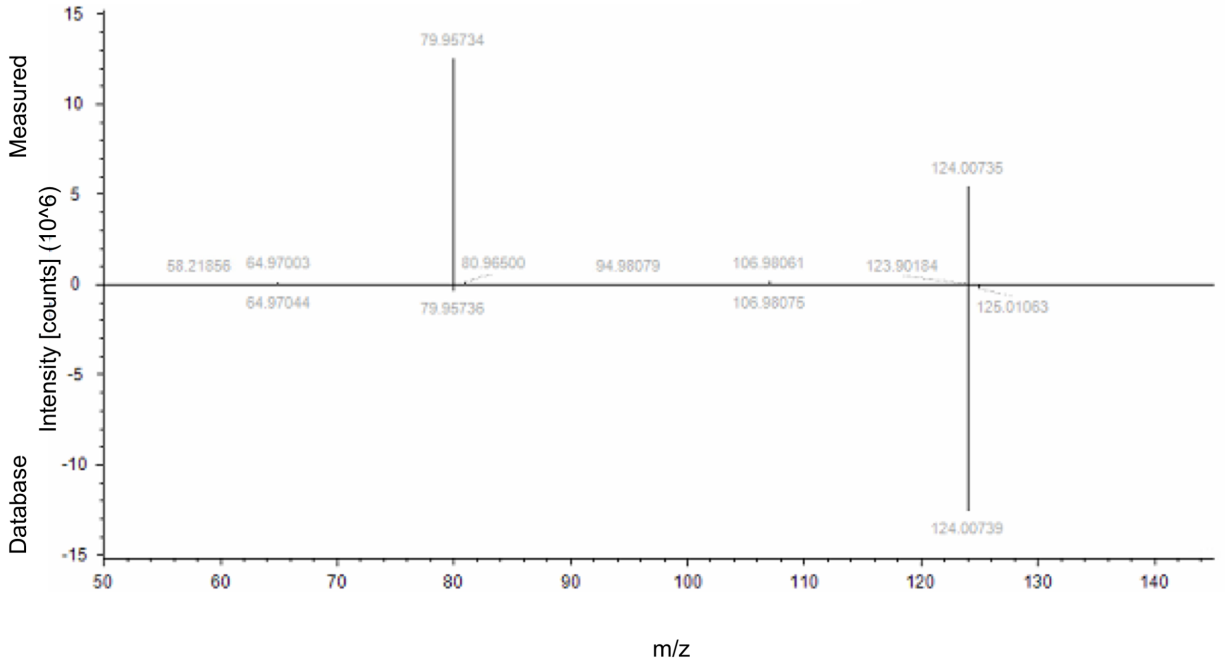

Fig. 61: Experimentally measured (Top): Putative identification**: Taurine**:
Compound Discoverer Fragmentation Score: 92.4
Reference (Bottom): mzCloud library: **Taurine**: C2H7NO3S

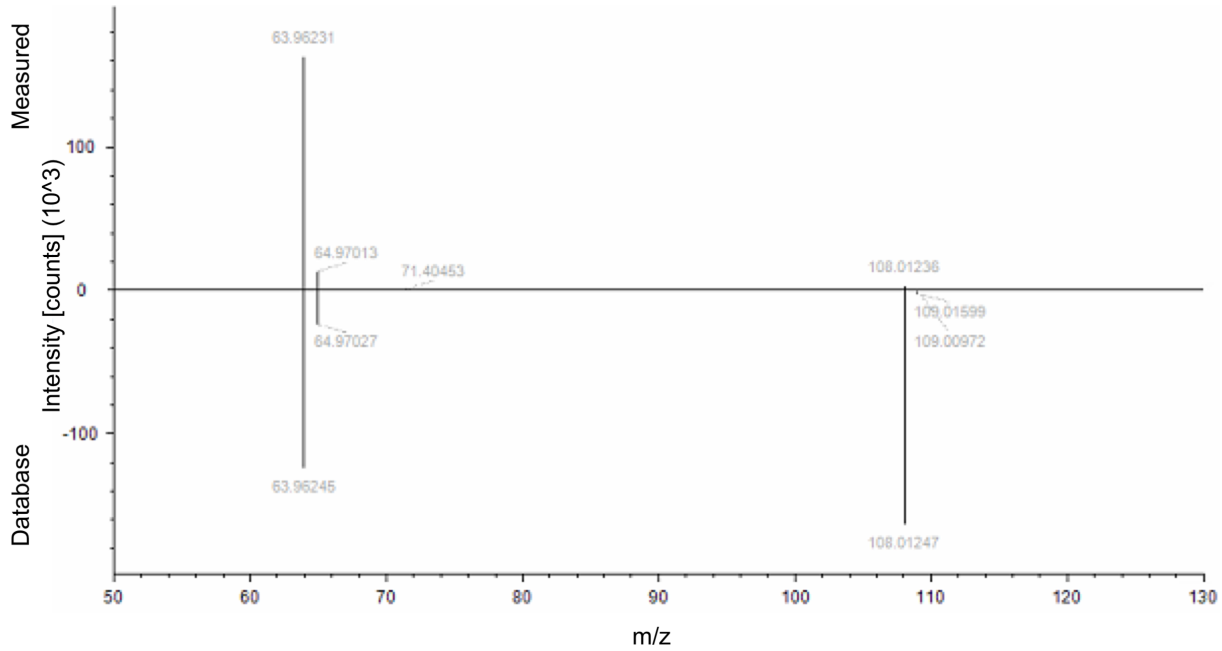

Fig. 62: Experimentally measured (Top): Putative identification: **Hypotaurine**:
Compound Discoverer Fragmentation Score: 82.4
Reference (Bottom): mzCloud library: **Hypotaurine**: C2H7NO2S

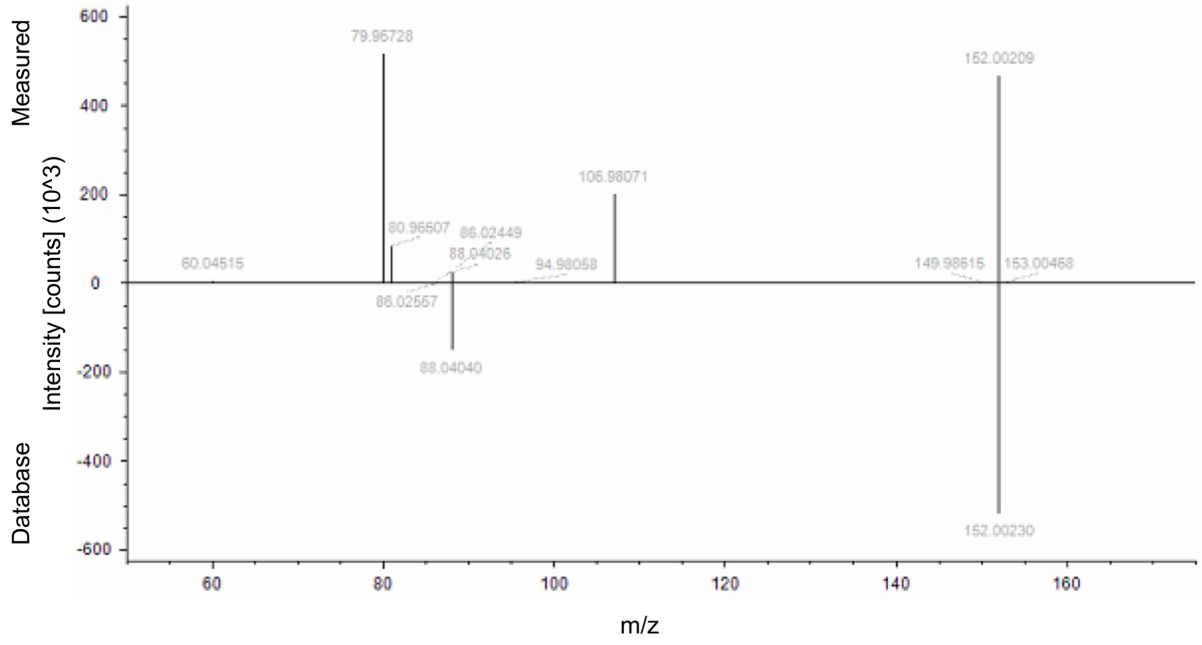

Fig. 63: Experimentally measured (Top): Putative identification: **3-Sulfinoalanine (syn: L-Cysteinesulfinic acid)**:
Compound Discoverer Fragmentation Score: 60.1
Reference (Bottom): mzCloud library: **L-Cysteinesulfinic acid**: C3H7NO4S

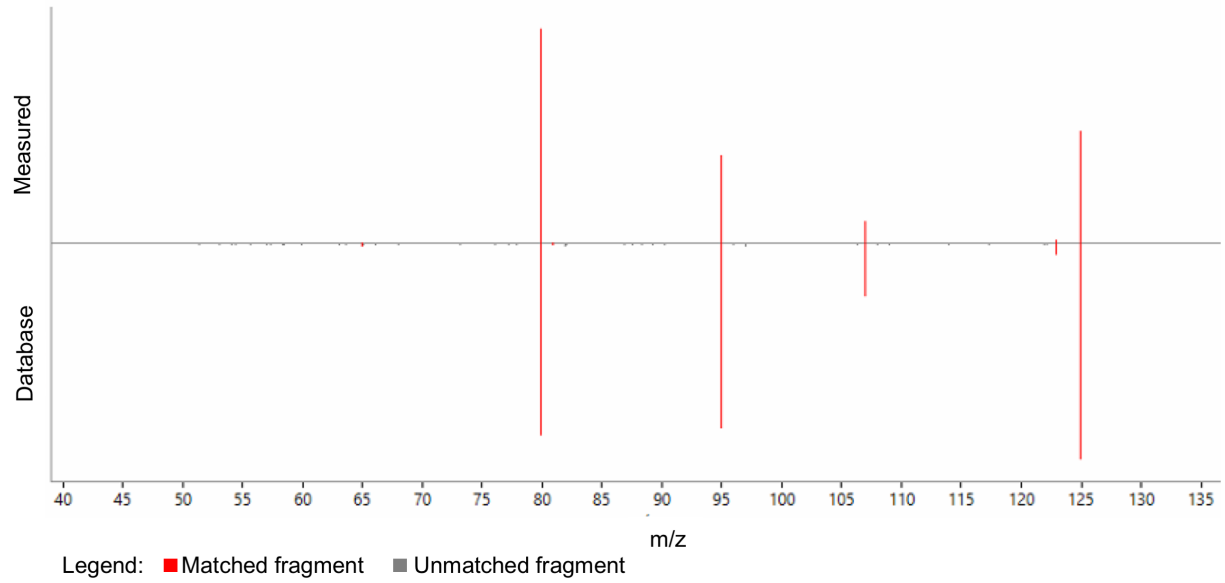

Fig. 64: Experimentally measured (Top): Putative identification: **2-Hydroxyethanesulfonate**:
Progenesis Fragmentation Score: 92.6
Reference (Bottom): In-house library: **2-Hydroxyethanesulfonate**: C2H6O4S

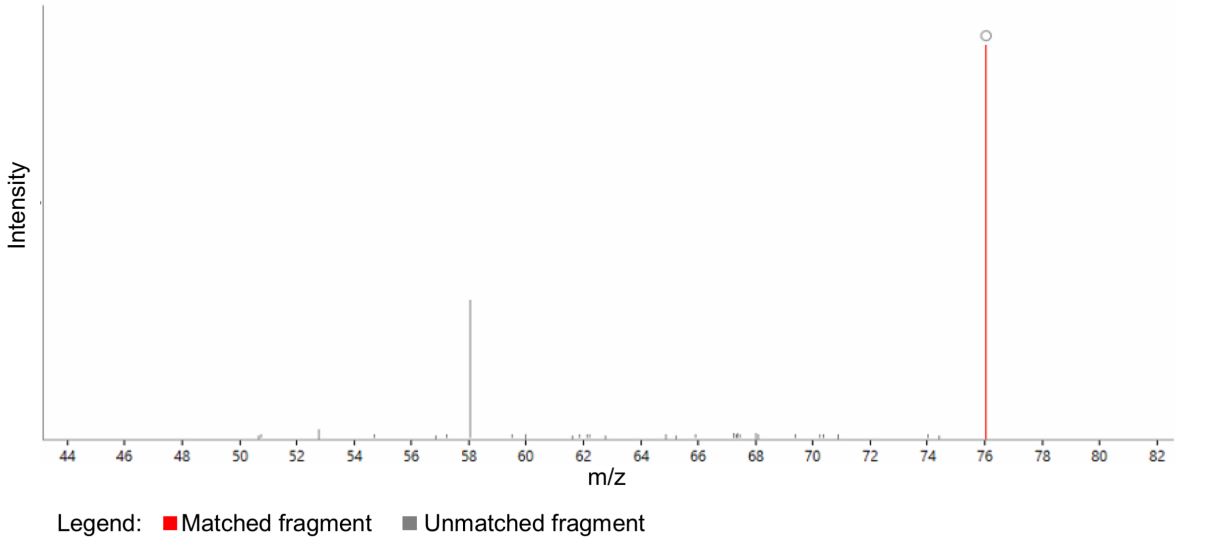

* Instrument method scans low end of mass range at 70 Da, therefore we do not expect ions to be detected below 70 Da.

Fig. 65: Experimentally measured (shown above): Putative identification: **Glycine**
Progenesis Fragmentation Score: 0.0*
Reference (not shown) matched fragments in red: HMDB: **Glycine**: C2H5NO2

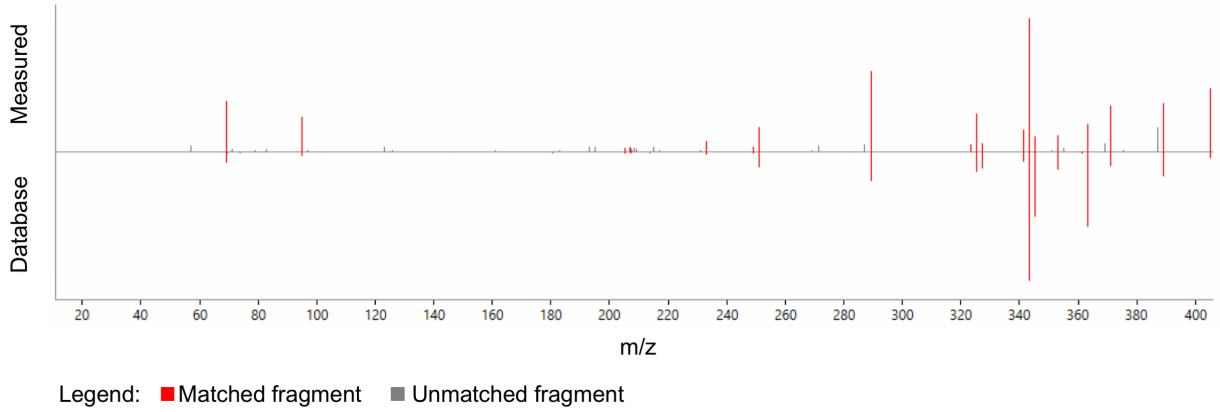

Fig. 66: Experimentally measured (Top): Putative identification: **Cholic Acid**:
Progenesis Fragmentation Score: 82
Reference (Bottom): In-house library: **Cholic Acid**: C24H40O5

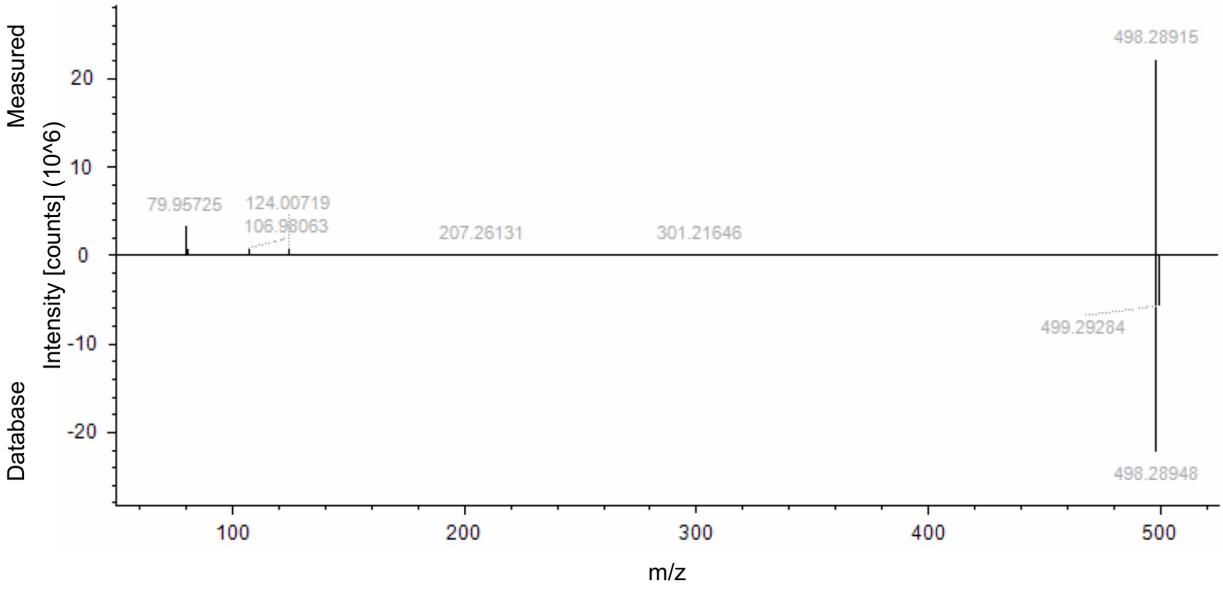

Fig. 67: Experimentally measured (Top): Putative identification: **Taurochenodeoxycholic acid**:
Compound Discoverer Fragmentation Score: 81.3
Reference (Bottom): mzCloud library: **Taurochenodeoxycholic acid**: C26H45NO6S

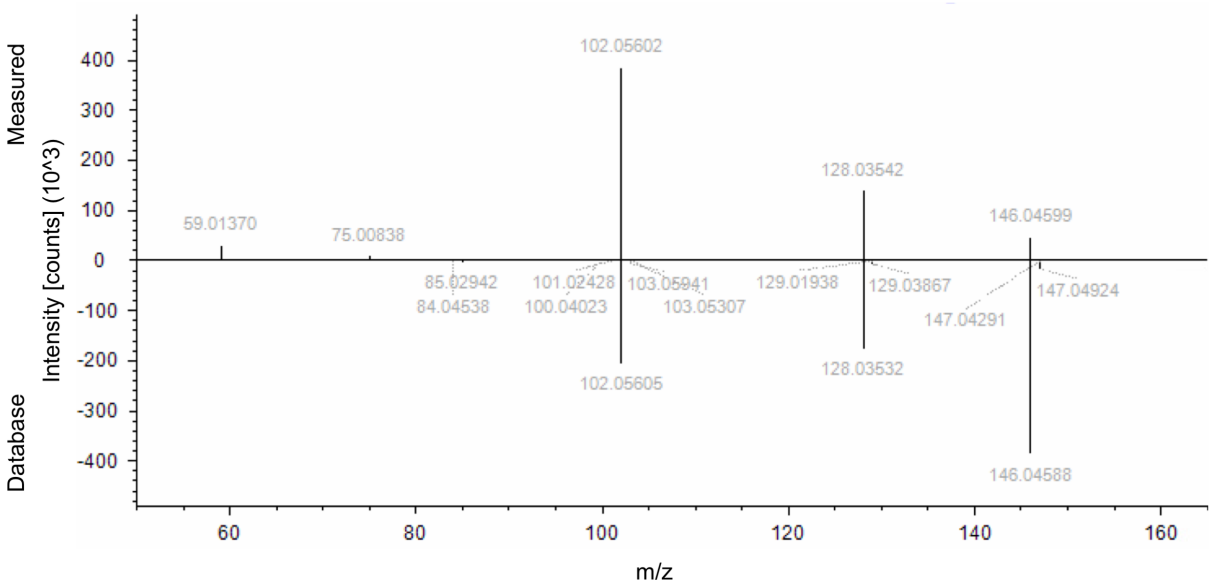

Fig. 68: Experimentally measured (Top): Putative identification: **L-Glutamate**:
Compound Discoverer Fragmentation Score: 89.4
Reference (Bottom): mzCloud library: **L-Glutamic acid**: C5H9NO4

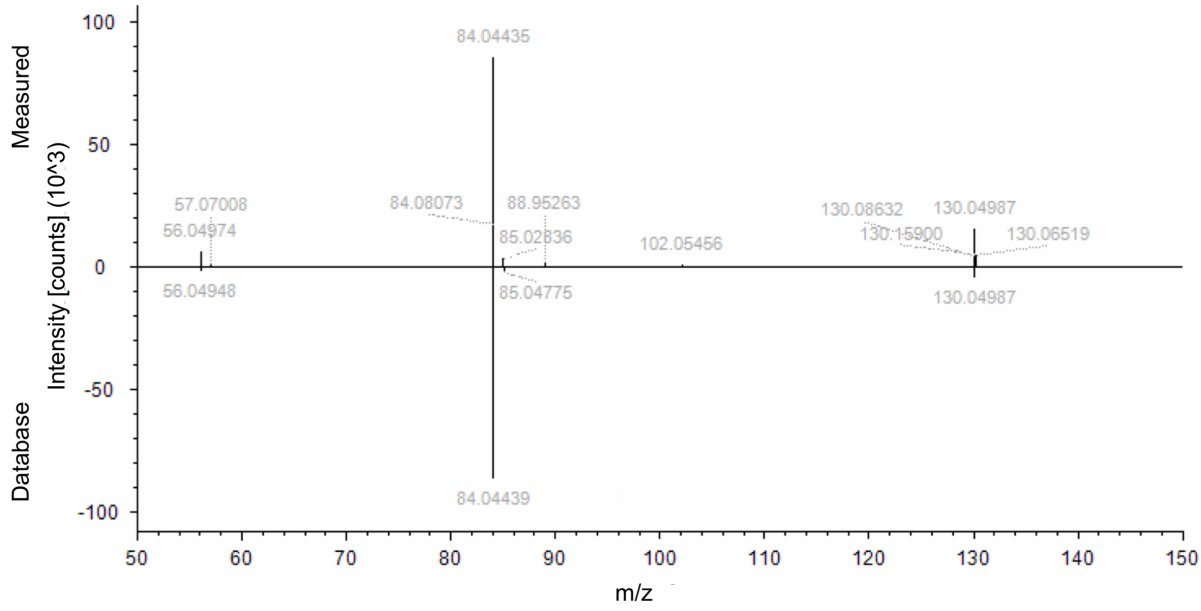

Fig. 69: Experimentally measured (Top): Putative identification: **Pyroglutamic acid**:
Compound Discoverer Fragmentation Score: 83.0
Reference (Bottom): mzCloud library: **Pyroglutamic acid**: C5H7NO3

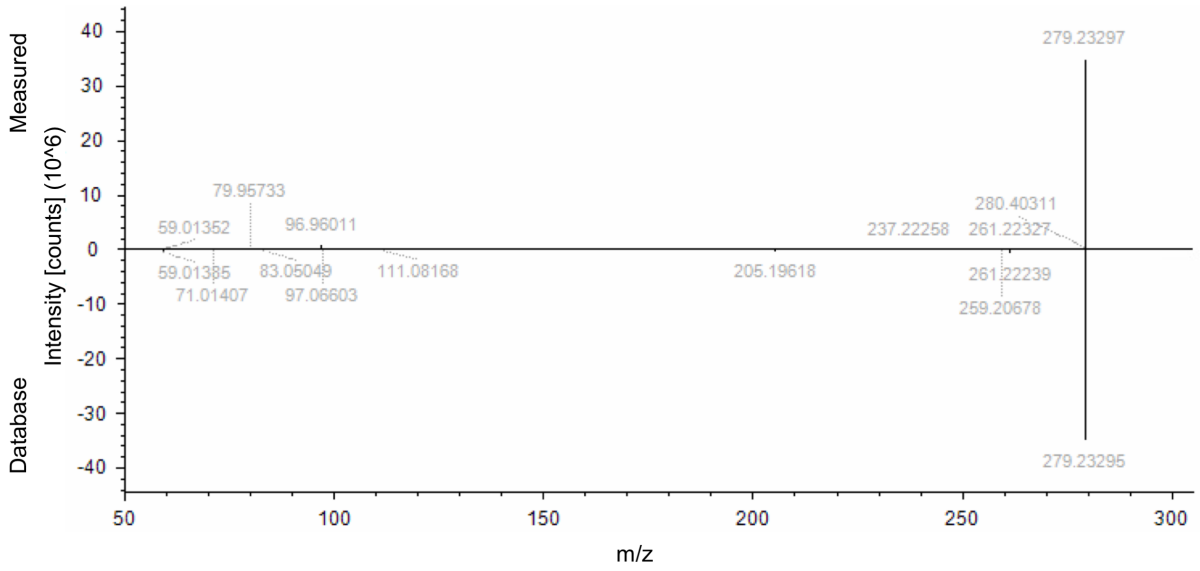

Fig. 70: Experimentally measured (Top): Putative identification: **Linoleic acid**:
Compound Discoverer Fragmentation Score: 87.1
Reference (Bottom): mzCloud library: **Linoleic acid**: C18H32O2

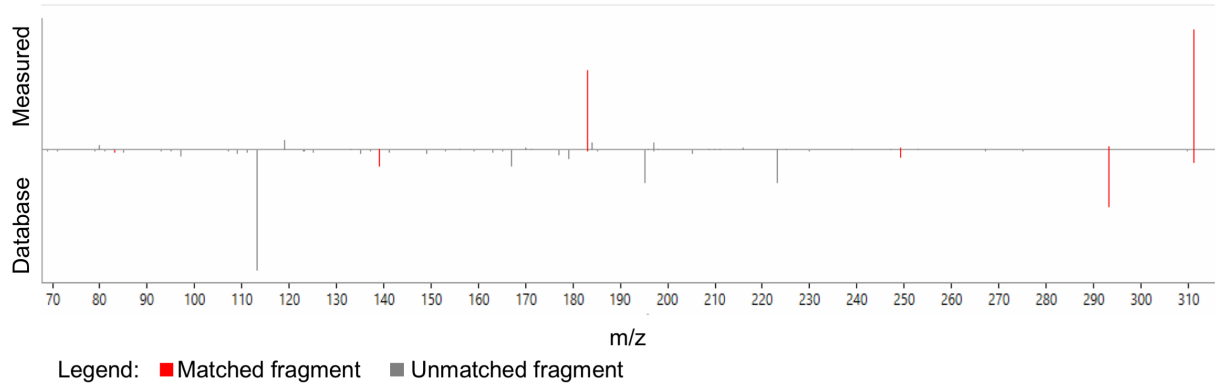

Fig. 71: Experimentally measured (Top): Putative identification: **13(S)-HpODE**:
Progenesis Fragmentation Score: 48.6
Reference (Bottom): Metlin: **13(S)-HpODE**: C18H32O4

Appendix B

A TARGETED/UNTARGETED METABOLOMICS APPROACH TO DETERMINE THE METABOLIC EFFECTS OF CEFTRIAXONE TREATMENT OF MURINE FIBROBLAST CELLS[5]

Introduction

In order to maintain normal brain health, control of excitatory Glu signaling must be tightly regulated. Excess Glu signaling through ionotropic Glu receptors has been shown to lead to Glu-induced excitotoxicity. Many chronic brain disorders such as ALS, PD, and schizophrenia [200, 202, 203] as well as the acute excitotoxicity associated with stroke and glioblastoma, involve dysregulated excitatory signaling ultimately leading to cell death [264, 503]. Regulation of Glu signaling is primarily achieved by glial Glu transporters; the SLC1 (e.g. GLT1) family Glu transporters, responsible for fast Glu clearance at synaptic release sites and the SLC7A11 cystine/Glu exchanger (xCT) that regulates basal extrasynaptic Glu levels [255]. To identify novel therapeutic strategies to regulate Glu signaling, Rothstein and colleagues sought to repurpose FDA-approved medications that altered expression of GLT1 *in vitro* and *in vivo* and alleviated phenotypes of an *in vivo* ALS mouse model [202]. β–lactam antibiotics, including the CNS penetrant Ceftriaxone (Cef), were demonstrated to elevate expression of GLT1. Consequently, many researchers have implemented Cef as a neuroprotective agent in many models of neural diseases, including but not limited to addiction, stroke, PD, epilepsy, etc.

[5] The unpublished study described here was conducted in collaboration with the Michigan Regional Comprehensive Metabolomics Resource Core (MRC2) at the University of Michigan.

While Cef has been shown to derive its neuroprotective effects by elevating expression of GLT1 and xCT to normalize extracellular Glu levels by induction of the NFκB and ARE-1 transcriptional programs respectively [277, 278], a molecular target for this drug, until recently, has remained unidentified. Recently, we have identified that mutations in the *C. elegans* gene, *swip-10*, results in Glu-dependent DA neuron hyper-excitability and degeneration. The protein, SWIP-10, and its putative mammalian ortholog, MBLAC1 contain a conserved metallo β–lactamase domain [146]. Furthermore, we have shown that MBLAC1 is a cytosolic protein expressed in the periphery and CNS, and is an endogenous, and specific binding partner for Cef [182]. To date however, the endogenous substrate for MBLAC1 enzymatic activity remains unknown and the mammalian metabolic alterations due to Cef treatment have not been explored.

In this study, we utilized a targeted/untargeted metabolomic mass spectrometry approach to determine the metabolic changes arising from acute and sustained Cef treatment of the MBLAC-1 expressing mouse fibroblast derived cell line (NIH3T3). We demonstrate that Cef treatment of mammalian cells significantly dysregulates many unidentified features, and these unknowns may represent the endogenous substrate(s) of the Cef interaction partner, MBLAC1.

Materials and Methods

Materials

All biochemical reagents, salts and buffers were obtained from Sigma-Aldrich (St. Louis, MO) unless otherwise specified, and were of the highest quality available.

Sample preparation

The embryonic fibroblast mouse cell line NIH 3T3 was cultured in DMEM containing 20 mmol/l Glucose, 10% fetal bovine serum, 100 U/ml penicillin and 100 µg streptomycin at 37°C in CO_2 cell culture incubators. Cells were seeded onto twelve 10 cm dishes at a density of 1.5 x 10^6/plate. After 24-48 hrs of recovery and adhesion (60-70% cell confluency), fresh culture media was added, and for 4 of the 10cm dishes fresh media supplemented with 50 µM Ceftriaxone (Cef) for 24 hrs. At about 90-100% confluency (23 hrs post media change) 4 x 10 cm dishes were treated with 50 µM Cef or sterile water vehicle for 1 hr. Samples were prepared for metabolite extraction according to previous studies [504]. Briefly, Media was thoroughly aspirated via vacuum aspirator and very rapidly, deionized water rinse buffer was added to the cells and immediately aspirated. Liquid nitrogen was added directly to the cells to quickly quench metabolism and freeze the cells. Cells were stored on dry ice or at -80°C until metabolite extraction.

Metabolite extraction

On dry ice, 1 mL of ice cold extraction buffer (Methanol:Acetonitrile:Acetone, 1:1:1, containing the following internal, exogenous standards; epibrassinolide, Gibberellic acid L-[15N] Anthranilic acid, L-Tryptophan-15N2, and Zeatin) was added to each dish, and the cells were scraped and transferred to a sterile 1.5 mL micro-centrifuge tube on dry ice. Harvested cells were lysed in ice using a probe sonicator and subjugated to a high speed-spin (15,000 rpm) at 4°C for 10 min to precipitate proteins and cellular debris. The metabolite containing supernatant was dried via nitrogen stream and stored at -80°C until analysis.

LC-MS chromatography

For mass spectrometry analysis, dried extracts were reconstituted in 100 µl reconstitution solvent (Methanol:H_2O 2:98) by vortexing for 5 mins. Following a high-speed spin (15,000 rpm for 5 mins), supernatants were transferred to glass inserts within autosampler vials. Quality control samples were prepared by pooling equal volumes from each experimental sample. Extracts (5-10 µl injection volume) were separated on a 1290 Infinity Binary LC System from Agilent with Waters Acquity UPLC HSS T3 1.8 µm 2.1 x 100 mm column in connection with a Waters Acquity UPLC HSS T3 1.8 µm VanGuard pre-column. Liquid chromatography was performed at a 450 µl min^{-1} at 55°C for 34 mins (7 min equilibration time, 27 min data acquisition time) using solvent A (0.1% formic acid in water) and solvent B (0.1% formic acid in methanol) with the following gradient: 98% A : 2% B for 20 min, 25% A : 75% B for 2 min, 2% A : 98% B for 8 min, 98% A : 2% B for 7 min. The same chromatography method was used for both positive and negative ion mode.

Mass spectrometry

Full MS analyses were acquired over a mass range of m/z 50-1000 under an ESI positive profile mode and separately under an ESI negative profile mode using Agilent Technologies 6530 Accurate-Mass Q-TOF with a dual ASJ ESI ion source used as the mass detector. The mass spectrometer settings were as follows; Ion source: 325°C gas temperature, drying gas flow at 10 l/min, nebulizer pressure at 45 psig, 400°C sheath gas temperature, sheath gas flow at 12 l/min, 4000V capillary voltage, 140V gragmentor

voltage, 65V skimmer voltage, 2 spectra/sec acquisition rate. Inline mass calibration was performed using debrisoquine sulfate (m/z 176.1182) and HP-0921 from Agilent (m/z 922.0098) in positive mode and 4-NBA (m/z 166.0146) and HP-0921 from Agilent (m/z 966.0007, formate adduct) in negative mode.

Data analysis

Raw data processing was done using Agilent software (MassHunter Qual and ProFinder, Agilent, Santa Clara, CA). Data analysis was performed with Agilent MassProfiler Pro package using recursive analysis workflow. Custom R and PHP scripts were used to remove redundant data (MRC2 Metabolomics Core at the University of Michigan, Ann Arbor, MI). Quality of analysis was accessed by visual inspection of the chromatographic traces (total ion chromatograms) and relative quantification of the internal standards. Data normalization was performed using feature-by-feature LOESS (Locally Weighted Scatterplot Smoothing) fitting to pooled samples. The normalized data set is limited to the features detected in every pooled sample. Unsupervised Principal Component Analysis (PCA) and subsequent Analysis of Variance (ANOVA) were used to find the statistically significant differences between experimental groups. Feature annotation is based on comparing observed m/z and retention time to the in-house library of ~850 compounds, sampling a wide variety of metabolic pathways (MRC2 Metabolomics core at the University of Michigan). Unidentified/unmatched features are assigned putative molecular formula when possible. Data visualization performed using Venny 2.1 (bioinfogp.cnb.csic.es/tools/venny) and Cytoscape 3.0 (The Cytoscape Consortium, USA). Identification of putative metabolic networks and metabolic pathways

effected by Cef treatment was done using the metabo-informatic tool, *mummichog* 1.0 [419].

Results and Discussion

Generation of an *in vitro* model to assess the effect of ceftriaxone on metabolic pathways

We chose to utilize an *in vitro* model to assess the effect of ceftriaxone on mammalian cell metabolism due to its ease of manipulation and accessibility. Many of the initial studies that demonstrate Cef's ability to regulate transcriptional programs that increase expression of Glu transporters, GLT-1 and xCT, was done utilizing immortalized cell culture lines such as hippocampal neuron derived line and the embryonic murine fibroblast NIH 3T3 cells [277]. Additionally, in our initial efforts to characterize the binding interaction between the mammalian protein, MBLAC1, and Cef, we determined that 3T3 cells endogenously express MBLAC1, detectible via immunoblot [182]. Furthermore, pharmacological manipulation of glutathione production (associated with xCT expression and closely associated with the neuroprotective actions of Cef) via buthionine sulfoximine and N-Acetylcysteine [505, 506] resulted in treatment time course dependent changes in MBLAC1 expression in NIH 3T3 cells (C.L. Retzlaff, unpublished findings). We chose to continue with the NIH 3T3 cell line for our metabolomics study, as other researchers have utilized these cells in other metabolomics studies [507] and to exploit the MBLAC1/Cef binding interaction. We hypothesized that Cef interaction with MBLAC1 would disrupt the enzyme's interaction with its endogenous small molecule substrate and reveal Cef-dependent changes in mammalian cell metabolism. This pilot study is a hypothesis-

generating endeavor designed to identify both known and unknown metabolites altered by acute (1 hr) or semi-chronic (24 hr) Cef in order to further characterize molecular pathways responsible for the neuroprotective actions of Cef (Fig. 72).

Elucidation of ceftriaxone-dependent 3T3 cell metabolome changes

Liquid chromatography coupled to mass spectrometry (LC-MS) approaches are frequently being utilized in metabolomic studies due to their high resolution and sensitivity [508]. In this study, we utilized an established reverse phase liquid chromatography (RPLC) method using both positive (POS) ion mode and negative (NEG) ion mode to increase the breadth of detected metabolites [426].

In order to have confidence in our experimental chromatographic data and feature detection, we utilized vigorous quality control measures including the use of a pooled sample (containing equal volumes of each experimental sample) to determine sample separation and mass spectrometer induced retention time drift. Additionally, each experimental sample was spiked with a mixture of non-endogenous internal standards. To ensure we had achieved high quality and reproducible feature resolution we determined the relative standard deviation of the internal standards across all experimental runs for both RPLC-POS and RPLC-NEG. Table 7 shows that we achieved high quality feature detection as the relative standard deviation of the internal standards across samples was low. We thus have higher confidence in assessing the relative ion abundance differences across our different treatment groups.

We used the Agilent software platforms MassHunter Qual and ProFinder to analyze our raw data and we detected many molecular features with unique mass to chare ratios (m/z) in our dataset, 1834 features in RPLC-POS ion mode and 1836 features

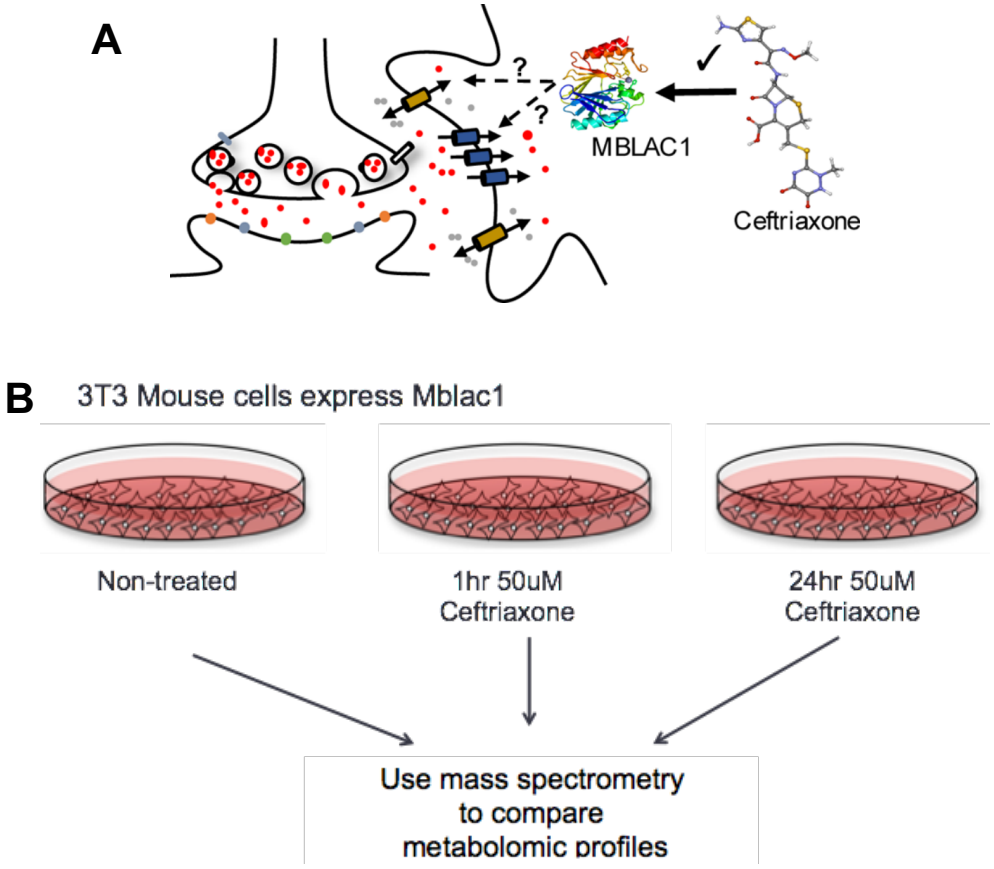

Fig. 72. Experimental design for assessing the effects of ceftriaxone on mammalian cellular metabolism. A. Schematic depicting the hypothesis that ceftriaxone may enact its neuroprotective action (increasing glial Glu transporter expression) via selective and specific interaction with MBLAC1 (Adapted from Retzlaff et al., 2017). B. Experimental design describing the *in vitro* model utilized to study the effects of ceftriaxone on murine cell metabolism.

Internal Standard	Positive Mode – Relative Standard Deviation (%)	Negative Mode – Relative Standard Deviation (%)
Epibrassinolide	9.8	2.7
Gibberellic acid	15.5	2.0
L-[15N] Anthranilic acid		6.5
L-Tryptophan-15N2	4.6	4.7
Zeatin	3.6	11.2

Table 7. Quality of analysis is assessed by the quantification relative standard deviations of the internal standards within experimental samples.

in RPLC-NEG ion mode. Unsupervised principal component analysis (PCA) revealed segregation of untreated and Cef-treated biological replicates (Fig. 73). PCA also reveals segregation of 1 hr and 24 hr Cef treated biological replicates, however this separation is less distinct than the separation from untreated replicates (Fig. 73A-B). Our pooled quality control samples cluster nicely at the center of the PCA plot (Fig. 73A-B). In order to compare ion abundances within treatment groups, we normalized the raw data via feature to feature LOESS fitting to pooled sample data to adjust for instrumental drift during the sample run sequence. Subsequent PCA analysis of the normalized data shows a tight clustering among the pooled samples (Fig. 73C-D) and separation of the experimental groups. After LOESS normalization, the separation between the three experimental conditions (untreated(basal), 1 hr Cef, and 24 hr Cef) becomes more distinct (Fig. 73C-D).

Following normalization, we utilized a one-way ANOVA analysis to nominate features that differ among 0 hr, 1 hr, or 24 hr Cef treatment groups, and a corrected *P*-value < 0.05 was deemed significant. For RPLC-POS, 76 features (4.2%) and for RPLC-NEG, 70 features (3.8%) were revealed to be significantly different across one or both Cef treatment groups. Due to the restricted number of statistically different features due to Cef treatment, we did not impose a fold change threshold on our data for analysis. The ANOVA analysis allowed us to identify features that changed (increased or decreased) across three experimental condition comparisons for both RPLC-POS and RPLC-NEG. We compared the features that changed from 0 hr to 1 hr Cef treatment, 0 hr to 24 hr Cef treatment, and changed from 1 hr to 24 hr Cef. To visualize which features were consistent across these analyses, we utilized Venn diagrams to see which groups shared

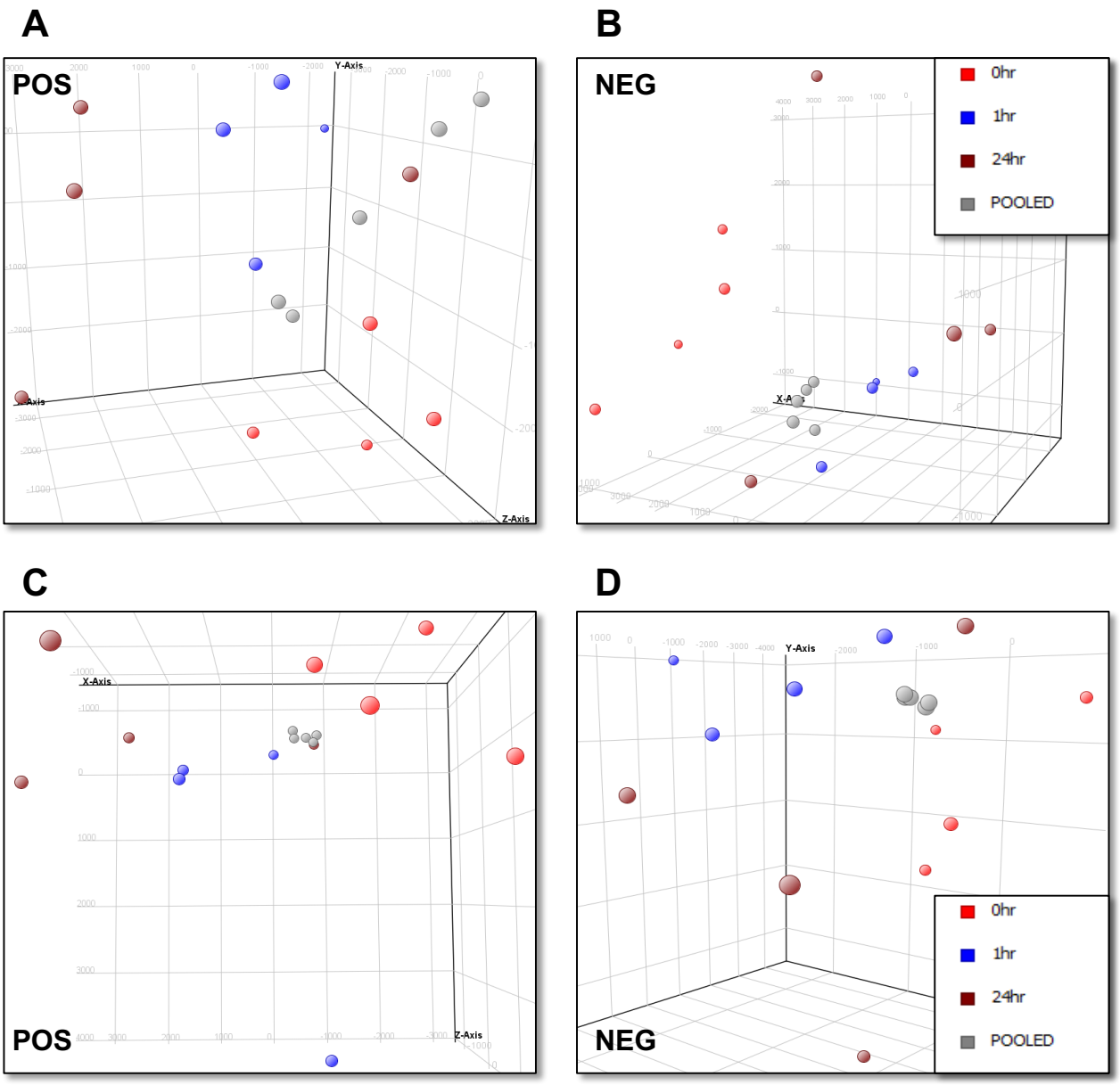

Fig. 73. Global, unsupervised principal component analysis (PCA) illustrates distinct metabolomes across ceftriaxone treatment groups. A. POS and B. NEG raw data unsupervised PCA shows distinct metabolic profiles observed between 3T3 cells treated 0 hr (red) 1 hr (blue) and 24 hr (brown) 50 µM Cef for. The pooled control samples cluster at the center of all the experimental data (grey). C. POS and D. NEG unsupervised PCA on the LOESS normalized data shows more distinct separation across experimental conditions [0 hr (red) 1 hr (blue) and 24 hr (brown) 50 µM Cef], and tighter clustering of the pooled quality control samples (grey).

features with similar directional changes for Cef treatment induced increases and decreases in feature abundances for RPLC-POS and RPLC-NEG (Fig. 74). Tables 8 and 9 summarize the features that significantly differ between Cef treatment groups, and show their relative fold change abundance differences.

Nomination of known/targeted compounds dependent on ceftriaxone

Untargeted metabolomic studies are designed to provide broad coverage of the metabolome and allow researchers to interpret data and generate hypotheses without being limited to pre-conceived ideas. As a caveat to this approach, the analysis conditions cannot be optimized for all types of metabolites that exist in a complex mixture, and thus quantitation is relative to internal standards and ion abundance differences among different groups. Utilization of an in-house metabolite/compound library helps assign feature annotations within experimental samples that match m/z and retention times to known compounds run on the same RPLC-MS platform. We used a library of approximately 850 compounds, by no means comprehensive, that samples metabolites present in most known metabolic pathways. The degree of confidence in this type of identification is high, however it is possible to wrongly annotate compound identifications, especially for structural isomers with similar chromatographic behavior. Tables 8 and 9 show that 6 of the 76 (7.9%) and 4 of the 70 (5.7%), RPLC-POS and RPLC-NEG respectively, significantly different features were assigned compound annotations based on library comparison. Most the features significantly altered by Cef treatment are unknown features requiring further efforts to assign putative annotations to these metabolites.

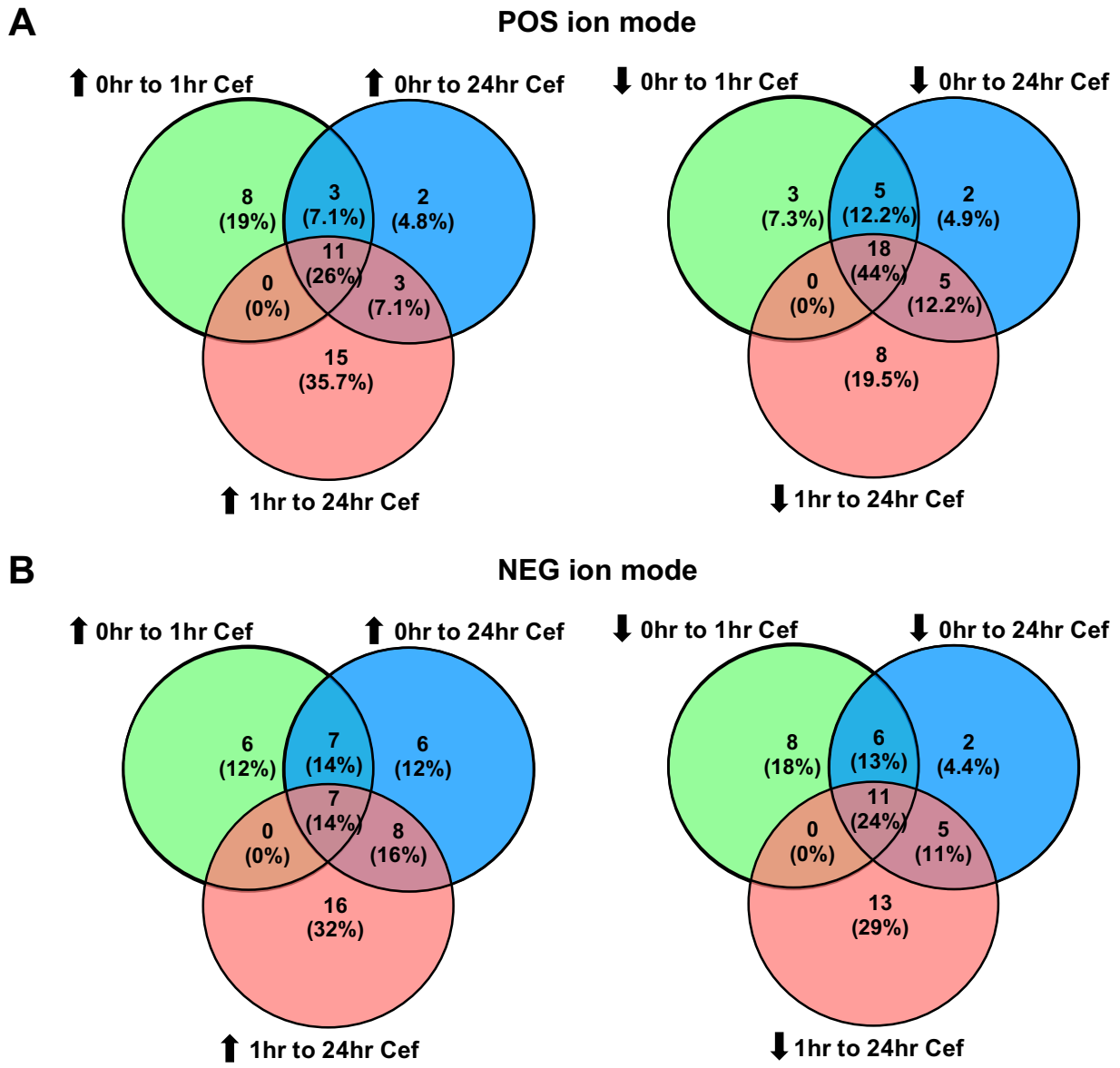

Fig. 74. Venn Diagrams demonstrating the relationship of significantly different compounds in comparison across Cef treatment groups. A. Venn diagrams representing the number of significantly dysregulated compounds (% of total) that are common among treatment conditions (0 hr, 1 hr, 24 hr Cef) either increasing or decreasing in abundance with Cef treatment in POS ion mode. B. Venn diagrams representing the number of significantly dysregulated compounds (% of total) that are common among treatment conditions (0 hr, 1 hr, 24 hr Cef) either increasing or decreasing in abundance with Cef treatment in NEG ion mode.

COMPOUND (Identification or m/z@Retention time)	ANOVA *P*value	ANOVA *P*value(Corr)	Fold Change [0hr] vs [1hr]	Regulation direction due to Cef treatment [0hr] vs [1hr]	Fold Change [0hr] vs [24hr]	Regulation direction due to Cef treatment [0hr] vs [24hr]	Fold Change [1hr] vs [24hr]	Regulation direction due to Cef treatment [1hr] vs [24hr]
INOSINE 5'-PHOSPHATE (M+H)+	0.00E+00	0.00E+00	1.443	↑	1.516	↑	1.051	↑
MANNOSE-6-PHOSPHATE (M+Na)+	0.00E+00	0.00E+00	1.416	↑	1.487	↑	1.051	↑
STEAROYLCARNITINE (*) (M+H)+	0.00E+00	0.00E+00	-1.195	↓	2.413	↑	2.885	↑
GUANOSINE (M+H)+	0.00E+00	0.00E+00	8.594	↑	4.189	↑	-2.052	↓
SERINE (M+H)+	0.00E+00	0.00E+00	-1.356	↓	-1.072	↓	1.265	↑
DECANOATE (2M+Na)+	0.00E+00	0.00E+00	1.739	↑				
367.0735@7.4286165	0.00E+00	0.00E+00					-1.075	↓
866.3625@18.450949	0.00E+00	0.00E+00						
281.1322@15.849048	1.60E-04	4.06E-02	-2.077	↓	-2.047	↓	1.015	↑
624.0129@6.620663	0.00E+00	0.00E+00					1.065	↑
301.2731@15.149294	3.80E-05	2.80E-02	-1.757	↓	-2.592	↓	-1.475	↓
548.007@6.6272955	0.00E+00	0.00E+00					1.072	↑
272.2465@16.167345	3.30E-04	4.12E-02	-1.690	↓	-2.095	↓	-1.239	↓
102.0322@9.968514	0.00E+00	0.00E+00	-3.809	↓	-9.241	↓	-2.426	↓
302.2934@21.512459	0.00E+00	0.00E+00	1.112	↑	-1.494	↓	-1.660	↓
413.2782@17.004766	4.74E-05	2.80E-02	-1.893	↓	-2.475	↓	-1.307	↓
1146.04@6.61318	0.00E+00	0.00E+00					1.144	↑
424.1072@16.48971	0.00E+00	0.00E+00			-185.562	↓		
901.9806@8.293228	0.00E+00	0.00E+00	-1.835	↓	-1.624	↓	1.130	↑
445.2596@19.39078	1.87E-04	4.10E-02	-2.201	↓	-3.126	↓	-1.420	↓
863.5051@14.397863	0.00E+00	0.00E+00						
824.4396@14.097162	0.00E+00	0.00E+00					1.153	↑
337.2275@21.292797	0.00E+00	0.00E+00						
136.0392@1.8396631	0.00E+00	0.00E+00	1.626	↑	1.636	↑	1.007	↑
221.1395@12.586486	1.15E-04	3.39E-02	-1.828	↓	-2.217	↓	-1.213	↓
207.0909@7.7049866	0.00E+00	0.00E+00	1.002	↑	-1.170	↓	-1.172	↓
250.1652@11.600299	3.72E-04	4.12E-02	-2.091	↓	-2.341	↓	-1.119	↓
422.3495@21.358208	0.00E+00	0.00E+00					1.017	↑
323.2084@16.724348	0.00E+00	0.00E+00					1.559	↑
642.2728@21.910091	3.51E-04	4.12E-02	-1.751	↓	-2.108	↓	-1.204	↓
370.355@22.19751	0.00E+00	0.00E+00	-1.226	↓	-1.468	↓	-1.198	↓
726.1914@1.7489973	0.00E+00	0.00E+00					-4.047	↓
736.3847@13.413046	0.00E+00	0.00E+00						
723.4868@23.76065	0.00E+00	0.00E+00	1.134	↑	1.564	↑	1.380	↑
413.0474@4.310522	0.00E+00	0.00E+00					1.029	↑
823.5415@25.355928	0.00E+00	0.00E+00	1.330	↑				
352.1969@12.278598	0.00E+00	0.00E+00	1.400	↑	-1.963	↓	-2.749	↓
294.1727@15.150035	8.66E-05	3.39E-02	-1.709	↓	-2.270	↓	-1.328	↓
1595.0359@24.10364	0.00E+00	0.00E+00	1.132	↑	1.479	↑	1.306	↑
310.2513@22.332325	0.00E+00	0.00E+00	1.018	↑	1.181	↑	1.159	↑
462.3193@11.861967	0.00E+00	0.00E+00						
330.2516@12.347871	0.00E+00	0.00E+00	-1.609	↓	-5.274	↓	-3.277	↓
482.1148@3.2675698	0.00E+00	0.00E+00					1.220	↑
443.1184@7.057534	0.00E+00	0.00E+00					1.758	↑
767.4986@24.062334	0.00E+00	0.00E+00	-1.051	↓	2.128	↑	2.237	↑
572.426@23.118162	0.00E+00	0.00E+00			1.327	↑		
495.2169@11.41645	1.08E-04	3.39E-02	-2.555	↓	-2.902	↓	-1.136	↓
780.4109@13.770803	0.00E+00	0.00E+00						
907.5307@14.675709	0.00E+00	0.00E+00						
448.2321@6.7490387	3.18E-04	4.12E-02	-4.328	↓	-3.334	↓	1.298	↑
276.0619@6.943566	0.00E+00	0.00E+00			2.643	↑		
606.9598@6.6288924	0.00E+00	0.00E+00					1.151	↑
328.2632@22.345112	0.00E+00	0.00E+00	1.648	↑				
234.1066@3.701553	0.00E+00	0.00E+00						
306.0854@6.706207	2.89E-05	2.80E-02	-1.641	↓	-1.729	↓	-1.054	↓

continued from above…

COMPOUND (Identification or m/z@Retention time)	ANOVA *P*value	ANOVA *P*value(Corr)	Fold Change [0hr] vs [1hr]	Regulation direction due to Cef treatment [0hr] vs [1hr]	Fold Change [0hr] vs [24hr]	Regulation direction due to Cef treatment [0hr] vs [24hr]	Fold Change [1hr] vs [24hr]	Regulation direction due to Cef treatment [1hr] vs [24hr]
268.0853@1.8109964	0.00E+00	0.00E+00	1.031	↑	1.343	↑	1.303	↑
821.5259@25.0419	0.00E+00	0.00E+00	1.344	↑	-1.105	↓	-1.485	↓
418.2336@18.634743	2.95E-04	4.12E-02	-1.578	↓	-2.080	↓	-1.318	↓
504.3901@22.6173	0.00E+00	0.00E+00	-1.021	↓	2.435	↑	2.486	↑
527.4653@22.619268	0.00E+00	0.00E+00	1.475	↑	2.467	↑	1.673	↑
250.1779@10.713075	0.00E+00	0.00E+00	-5.601	↓	-6.821	↓	-1.218	↓
720.1482@5.4102445	0.00E+00	0.00E+00					-2.173	↓
1467.7577@15.830882	0.00E+00	0.00E+00	1.553	↑	1.757	↑	1.131	↑
244.063@1.9501071	0.00E+00	0.00E+00					-44.549	↓
214.0082@0.7559997	0.00E+00	0.00E+00	1.829	↑	2.700	↑	1.476	↑
441.2533@20.427996	0.00E+00	0.00E+00	-1.153	↓	-1.461	↓	-1.267	↓
104.0559@16.489931	0.00E+00	0.00E+00			-2.107	↓		
316.1815@12.818161	2.08E-04	4.10E-02	-3.523	↓	-3.211	↓	1.097	↑
366.2128@13.920004	0.00E+00	0.00E+00	2.185	↑	1.254	↑	-1.742	↓
262.0671@4.4064107	3.58E-04	4.12E-02	-1.871	↓	-2.018	↓	-1.079	↓
731.5817@25.344143	0.00E+00	0.00E+00	1.271	↑	1.323	↑	1.041	↑
822.5664@22.942669	0.00E+00	0.00E+00	1.365	↑	1.315	↑	-1.038	↓
429.0287@7.176194	0.00E+00	0.00E+00					-1.192	↓
324.1658@8.666974	0.00E+00	0.00E+00						
444.3304@21.357094	0.00E+00	0.00E+00	1.277	↑	-1.176	↓	-1.501	↓
709.3885@22.861954	2.63E-04	4.12E-02	-2.178	↓	-3.471	↓	-1.593	↓

Table 8. RPLC-POS identified features significantly dysregulated in 3T3 cells due to 1 hr or 24 hr treatment of 50μM ceftriaxone.

COMPOUND (Identification or m/z@Retention time)	ANOVA *P*value	ANOVA *P*value(Corr)	Fold Change [0hr] vs [1hr]	Regulation direction due to Cef treatment [0hr] vs [1hr]	Fold Change [0hr] vs [24hr]	Regulation direction due to Cef treatment [0hr] vs [24hr]	Fold Change [1hr] vs [24hr]	Regulation direction due to Cef treatment [1hr] vs [24hr]
ADENOSINE (M+HCOO)-	0.000	0.000	1.025	↑	1.160	↑	1.132	↑
2-DEOXY-D-GLUCOSE (M+Cl)-	0.000	0.000			1.875	↑		
GLYCEROL 2-PHOSPHATE (M-H)-	0.000	0.000			2.703	↑		
(S)-DIHYDROOROTATE (M-H)-	0.000	0.000	-1.507	↓	-4.304	↓	-2.857	↓
159.0101@6.593837	0.000	0.000					1.084	↑
278.1297@5.311839	0.000	0.000			6.296	↑		
542.465@22.933786	0.000	0.000	-1.780	↓	1.478	↑	2.631	↑
576.0268@6.5964527	0.000	0.000					1.076	↑
404.0233@15.811854	0.000	0.044	-2.215	↓	-2.231	↓	-1.007	↓
970.1923@1.0228755	0.000	0.000			1.820	↑		
446.2058@19.357637	0.000	0.036	-1.979	↓	-2.917	↓	-1.474	↓
292.1915@15.114112	0.000	0.036	-1.710	↓	-2.582	↓	-1.509	↓
368.2192@16.974476	0.000	0.036	-1.791	↓	-2.469	↓	-1.379	↓
284.8834@2.1985018	0.000	0.000					-1.470	↓
425.0533@1.3450001	0.000	0.000					1.036	↑
306.9479@1.2585719	0.000	0.000	2.035	↑	1.020	↑	-1.995	↓
443.1171@7.0362487	0.000	0.000					-1.069	↓
626.4736@23.956873	0.000	0.000	1.897	↑	1.372	↑	-1.383	↓
460.2076@17.569336	0.000	0.000			-1.391	↓		
553.3162@22.38335	0.000	0.000	1.735	↑	2.665	↑	1.536	↑
656.1193@0.70741683	0.000	0.000	-1.149	↓	-1.549	↓	-1.348	↓
559.3392@22.896551	0.000	0.000	1.703	↑	1.187	↑	-1.434	↓
744.4468@22.81848	0.000	0.000	2.123	↑	1.191	↑	-1.783	↓
597.5319@24.62577	0.000	0.000	1.631	↑	-1.520	↓	-2.480	↓
915.5274@24.820147	0.000	0.000	1.272	↑	1.112	↑	-1.144	↓
791.5591@24.818466	0.000	0.000	-1.075	↓	1.252	↑	1.346	↑
946.5132@24.320225	0.000	0.000	1.371	↑	-2.070	↓	-2.838	↓
799.5551@24.617138	0.000	0.000	1.614	↑	-1.710	↓	-2.761	↓
460.2105@19.269295	0.000	0.000			-1.636	↓		
562.3508@22.832893	0.000	0.000	-1.900	↓	1.467	↑	2.786	↑
829.657@25.73587	0.000	0.000	-1.772	↓	2.099	↑	3.719	↑
159.0109@3.6284626	0.000	0.000					1.105	↑
155.0623@0.638125	0.000	0.000	2.754	↑	-1.275	↓	-3.512	↓
222.0889@10.084981	0.000	0.000					-11.664	↓
955.6147@24.605923	0.000	0.000	1.137	↑	1.910	↑	1.679	↑
644.1237@2.332101	0.000	0.000					2.767	↑
472.0136@6.6148376	0.000	0.036	-2.810	↓	-2.644	↓	1.063	↑
476.3125@11.839342	0.000	0.000						
330.256@22.89567	0.000	0.000	2.547	↑	-1.371	↓	-3.493	↓
817.5094@23.655851	0.000	0.000	-1.054	↓	1.921	↑	2.025	↑
636.4966@25.14244	0.000	0.000	1.240	↑	2.047	↑	1.650	↑
324.0331@0.7223639	0.000	0.000					-1.180	↓
302.2248@21.647848	0.000	0.000	1.405	↑	1.511	↑	1.075	↑
835.4988@23.618195	0.000	0.000	1.034	↑				
655.132@0.9965006	0.000	0.000			1.926	↑		
830.0662@0.7553333	0.000	0.036	-2.046	↓	-2.078	↓	-1.016	↓
399.2418@22.625801	0.000	0.000					-2.102	↓
901.5789@24.35239	0.000	0.000	-1.179	↓	1.109	↑	1.307	↑
502.0514@10.025292	0.000	0.000	-1.177	↓	-1.789	↓	-1.520	↓
468.0991@2.070501	0.000	0.000					1.070	↑
939.4553@23.718113	0.000	0.000	-1.064	↓	-1.065	↓	-1.001	↓
270.0952@0.876929	0.000	0.036	-1.715	↓	1.103	↑	1.893	↑
469.1364@1.1947509	0.000	0.000			1.842	↑		
520.0633@3.481776	0.000	0.000					1.322	↑
468.1003@1.3843333	0.000	0.000					1.335	↑
734.1448@7.3576193	0.000	0.000					-1.245	↓
437.2902@22.489838	0.000	0.000	-1.815	↓	-1.341	↓	1.354	↑

continued from above…

COMPOUND (Identification or m/z@Retention time)	ANOVA *P*value	ANOVA *P*value(Corr)	Fold Change [0hr] vs [1hr]	Regulation direction due to Cef treatment [0hr] vs [1hr]	Fold Change [0hr] vs [24hr]	Regulation direction due to Cef treatment [0hr] vs [24hr]	Fold Change [1hr] vs [24hr]	Regulation direction due to Cef treatment [1hr] vs [24hr]
637.356@22.820833	0.000	0.000	2.710	↑	1.634	↑	-1.659	↓
155.0948@3.6401944	0.000	0.036	-7.017	↓	-8.705	↓	-1.241	↓
362.1137@1.5893586	0.000	0.000					1.105	↑
811.483@23.784182	0.000	0.000	1.040	↑	1.388	↑	1.335	↑
578.0533@0.91933364	0.000	0.000	-1.023	↓	2.154	↑	2.204	↑
160.0197@0.7131251	0.000	0.000					1.169	↑
696.3406@22.518839	0	0	-4.03924	↓	-3.1474435	↓	1.2833399	↑
116.0113@1.2591112	0.000179588	0.0356938	1.5743606	↑	1.1658546	↑	-1.350392	↓
438.1991@22.53578	0.000307822	0.045609005	-2.9547791	↓	-2.8971426	↓	1.0198942	↑
117.0388@24.58583	0	0	-1.1377398	↓	-1.937237	↓	-1.7027067	↓
438.9882@10.267615	0.000215355	0.03829017	-1.9021002	↓	-1.6964253	↓	1.1212401	↑
819.5079@24.270622	0	0	1.0555607	↑	1.2885303	↑	1.2207069	↑
555.1298@1.1776925	9.28396E-05	0.0356938	-2.4145498	↓	-1.9539046	↓	1.2357563	↑

Table 9. RPLC-NEG identified features significantly dysregulated in 3T3 cells due to 1 hr or 24 hr treatment of 50μM ceftriaxone.

Unknown metabolites changing in response to acute or semi-chronic ceftriaxone treatment

The process of assigning correct annotations to features detected in LCMS-based metabolomic studies, remains a difficult obstacle in analyzing these datasets. Unlike proteomics, where each protein has a unique amino acid sequence, the m/z ratio of a detected small molecule feature likely matches the m/z ratio attributed to many different metabolites. The experimental m/z ratio of unknown features can be queried against several established metabolite databases (e.g. HMDB (Human metabolome data base), MassBank, and Metlin) to generate a list of candidate annotations. In a communication by A. C. Schrimpe-Rutledge and colleagues, the process and caveats to feature annotation is described in depth. In many cases, feature annotation requires MS_2-dependent (fragmentation) data for comparison with known fragmentation data of standards [418]. As our LCMS dataset primarily consists of MS_1 (parent ion) data, we utilized the program, *mummichog*, an informatics strategy designed to predict biological activity from MS_1 data in order to bypass the typical, labor intensive identification pipelines in order to rapidly generate quality hypotheses to drive future research [418, 419]. *mummichog* is designed more specifically to look at comparisons and differences in ion abundances based on comparisons between two groups, therefore we limited our *mummichog* analysis to two comparisons; 0 hr vs 1 hr Cef treated samples or 0 hr vs 24 hr Cef treated samples, for both RPLC-POS and RPLC-NEG.

The *mummichog* data output provides two complementary ways to biologically understand the significant differences among experimental groups based on 1) MetaFishNet human reference metabolic pathway analysis or 2) undefined networks

(known as modules) [509]. The pathway analysis of *mummichog* is based on predefined human metabolic pathways and determines pathway enrichment after unique m/z are converted to putatively annotated features. Higher pathway enrichment increases confidence in putative feature identification [509, 510]. Table 10 lists the metabolic pathways (defined by MetaFishNet) significantly altered by Cef treatment for either 1 hr or 24 hrs (each compared to 0 hr) for RPLC-POS and RPLC-NEG. Within this table, pathways that are significantly enriched across ion modes and treatment time, serve as a metabolic pathway to target in future studies as important for the actions of Cef. One caveat to the pathway analysis is the unknown directionality of the changes of the metabolites contributing to nominating an enriched pathway, although subsequent versions of *mummichog* address this issue. In both Cef treatment comparisons, and for both RPLC-POS and RPLC-NEG ion mode, the metabolic pathways, pyrimidine metabolism and vitamin B5 CoA biosynthesis, contain significant enrichment of metabolites dysregulated by Cef treatment (Table 10). Subsequent, targeted metabolomic based experiments can be utilized to confirm the effect of Cef on metabolites within these pathways.

Potential significance of Cef-induced alterations in the metabolic pathways, pyrimidine metabolism and vitamin B5 CoA biosynthesis

Interestingly, pyrimidine treatment has been shown to be neuroprotective in several animal models of brain disorders for which Cef is neuroprotective [511]. Researchers demonstrate that injection or ingestion of citicoline, or

POS Ion Mode
0hr vs 1hr Cef

Pathways	Metabolite Overlap (#)	Pathway Size (#)	*P*value (raw)	*P*value
Caffeine metabolism	5	5	0.012	0.000
Vitamin E metabolism	9	16	0.165	0.002
Vitamin B5 - CoA biosythesis	4	6	0.196	0.004
Xenobiotics metabolism	6	11	0.274	0.005
Glutathione metabolism	4	7	0.314	0.009
Pyrimidine metabolism	5	10	0.399	0.012
Pyruvate metabolism	2	2	0.170	0.012
Prostaglandin from dihomo gamma-linoleic acid	3	5	0.340	0.015
Hexose phosphorylation	3	5	0.340	0.015
Starch and sucrose metabolism	4	8	0.436	0.017
N-Glycan biosynthesis	4	8	0.436	0.017
Fatty acid activation	5	1	0.503	0.020
Glycolysis and gluconeogenesis	3	6	0.483	0.030
Pentose phosphate pathway	4	9	0.550	0.031
N-Glycan degradation	2	3	0.370	0.033
Phosphatidylinositol phospate metabolism	2	3	0.370	0.033
CoA Catabolism	2	3	0.370	0.033

NEG Ion Mode
0hr vs 1hr Cef

Pathways	Metabolite Overlap (#)	Pathway Size (#)	*P*value (raw)	*P*value
Alanine and aspartate metabolism	3	8	0.024	0.000
Beta-alanine metabolism	2	4	0.038	0.000
Prostaglandin from dihomo gamma-linoleic acid	2	5	0.060	0.000
Vitamin B5 - CoA biosythesis	2	5	0.060	0.000
Pyrimidine metabolism	3	19	0.215	0.000
Urea cycle/amino group metabolism	3	25	0.361	0.003
Leukotriene metabolism	3	27	0.409	0.005
Aspartate and asparagine metabolism	3	28	0.433	0.007
Bile acid biosynthesis	2	18	0.464	0.033
Arginine and proline metabolism	2	19	0.493	0.043

continued from above…

POS Ion Mode 0hr vs 24hr Cef				
Pathways	**Metabolite Overlap (#)**	**Pathway Size (#)**	***P*value (raw)**	***P*value**
Caffeine metabolism	5	5	0.012	0.002
Vitamin E metabolism	9	16	0.165	0.007
Vitamin B5 - CoA biosyntheis	4	6	0.197	0.018
Xenobiotics metabolism	6	11	0.274	0.020
Glutathione metabolism	4	7	0.314	0.037
Pyrimidine metabolism	5	10	0.399	0.048
Pyruvate metabolism	2	2	0.170	0.050
NEG Ion Mode 0hr vs 24hr Cef				
Pathways	**Metabolite Overlap (#)**	**Pathway Size (#)**	***P*value (raw)**	***P*value**
Alanine and aspartate metabolism	3	8	0.024	0.000
Beta-alanine metabolism	2	4	0.038	0.000
Prostaglandin from dihomo gamma-linoleic acid	2	5	0.605	0.000
Vitamin B5 - CoA biosythesis	2	5	0.060	0.000
Pyrimidine metabolism	3	19	0.215	0.001
Urea cycle/amino group metabolism	3	5	0.361	0.003
Leukotriene metabolsim	3	27	0.409	0.004
Aspartate and asparagine metabolism	3	28	0.433	0.004
Bile acid biosynthesis	2	18	0.464	0.009
Arginine and proline metabolism	2	19	0.493	0.011
Purine metabolism	2	22	0.574	0.017
Prostaglandin formation from arachidonate	3	43	0.730	0.025

Table 10. *Mummichog* pathway analysis reveals putative metabolic pathways significantly enriched for metabolites affected by 1 hr or 24 hr Cef treatment or both. Fisher exact tests computes a contingency table based on fraction of metabolites within a defined pathway identified in the experimental compound list, the more hits on a pathway, the more significant enrichment. Corrected *P*-values are calculated by resampling the data as a Gamma distribution and EASE scores therefore adjusting the raw *P*-value on the cumulative distribution function.

cytidine-5'-diphosphocholine, is neuroprotective in preclinical models of brain ischemia [512], Glu excitotoxicity [513, 514], and neurodegenerative disorders including AD [515]. Also, similar to Cef neuroprotective models, the pharmacological mechanism of citicholine is not well described, however it is known that before crossing the blood brain barrier, citicholine is hydrolyzed and phosphorylated to two intermediate products, cytidine monophosphate and phosphocholine, both of which are pharmacologically active. Other studies provide support that pyrimidines nucleotides may function as pyrimidinergic neurotransmitters, as uridine administration enhanced cholinergic neurotransmission and increased DAG and IP3 levels in the rat brain [516], uridine administration has sleep-promoting and anti-epileptic actions [517], and uridine was shown to activate microglia and stimulate thromboxane A2 release from cultured glial cells [518]. Further investigation to more fully understand the specific Cef-treatment induced changes in pyrimidine metabolism potentially will reveal insight into both Cef and pyrimidine pharmacological mechanisms of action.

Vitamin B5 (pantothenate) is the key precursor for the biosynthesis of coenzyme A (CoA), a cofactor essential for a variety of metabolic reactions [519] and dysregulation of pantothenate and CoA has adverse effects on normal brain functions. The literature clearly describes that disrupting CoA biosynthesis leads to neurodegeneration in humans, and the best characterized example of this is due to genetic mutations disrupting the function of mitochondrial pantothenate kinase (PANK2) resulting in pantothenate kinase-associated neurodegeneration, PKAN, which is associated with pathological iron accumulation and gliosis in the brain [520, 521]. Future studies aimed at elucidating the

effects of Cef treatment on vitamin B5 CoA biosynthesis may implicate key metabolic processes sensitive to the neuroprotective action of Cef.

Modular *mummichog* analysis indicates that Cef treatment influences steroid metabolite abundancies

The modular analysis is less biased by known metabolic pathways, as modules comprise of compounds linked within or between several pathways. Figures 75 and 76 demonstrate the significant modular output from our *mummichog* analysis of the comparisons of 0 hr vs 1 hr Cef and 0 hr vs 24 hr Cef, respectively, for RPLC-POS (no statistically significant, *P*value<0.05, modules were generated from RPLC-NEG data). Metabolites increasing in abundance with Cef treatment are in red, and those decreasing in abundance following Cef treatment are in blue. As these analyses are based on putative feature annotations derived from m/z and biological metabolite connectivity, several putative identifications could be attributed to a single m/z (each node) therefore each node has several metabolite names, with the first listed as the best candidate (Fig. 75 and 76). Findings from both comparisons indicate that perturbations in compounds identified with steroid-associated chemical structures may contribute to the metabolic effects of Cef treatment. According to an expanding set of literature, steroid hormones, both originating from the periphery or synthesized in neurons or glia, clearly play important roles in normal brain function, including developmental neuronal connectivity and differentiation, as well as influencing memory and behavior. Lipophilic steroid hormones readily cross the BBB, and interact with neuronal and glial plasma membranes as well as steroid-receptors expressed throughout the brain to regulate general brain

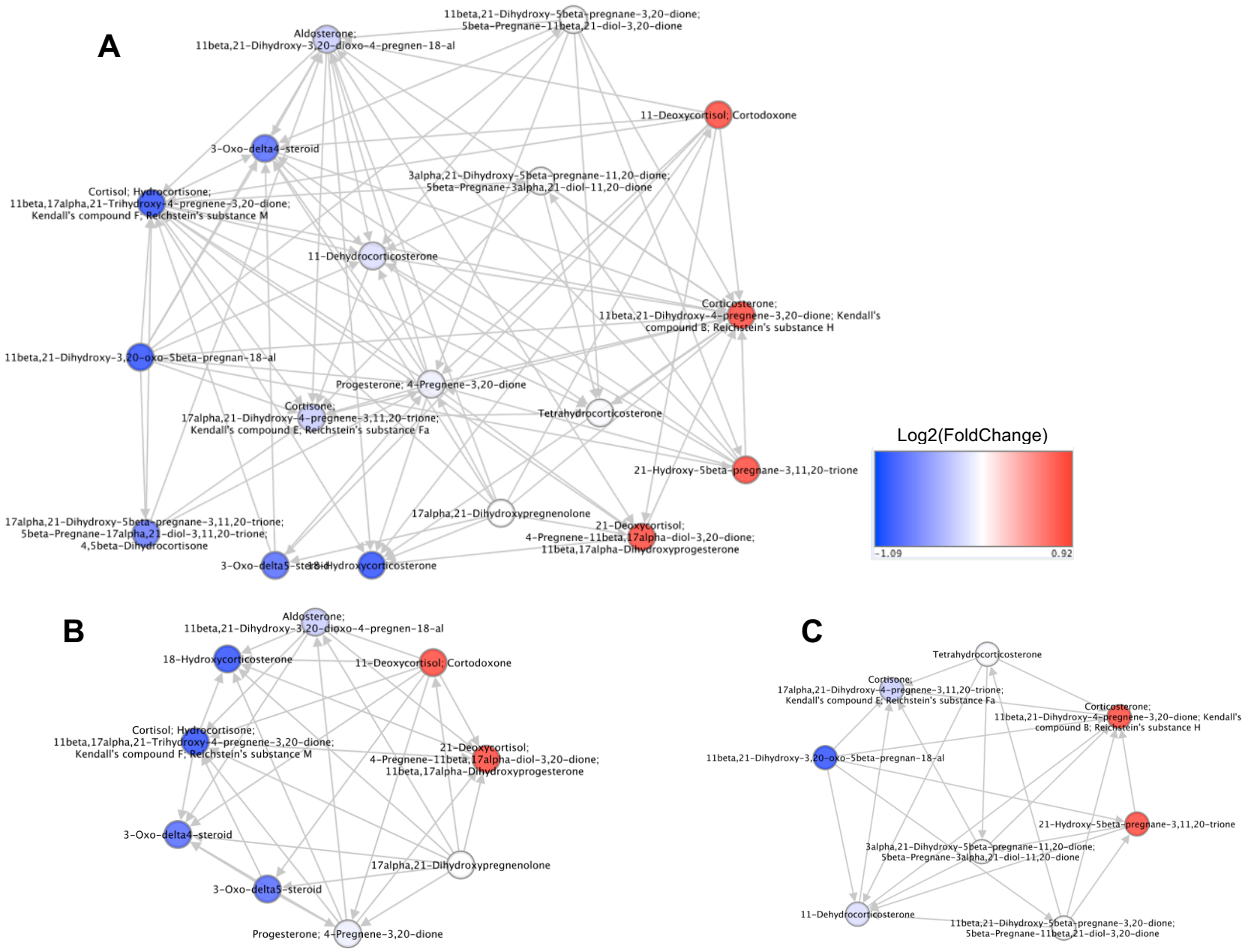
A
11beta,21-Dihydroxy-5beta-pregnane-3,20-dione;
5beta-Pregnane-11beta,21-diol-3,20-dione
Aldosterone;
11beta,21-Dihydroxy-3,20-dioxo-4-pregnen-18-al
11-Deoxycortisol; Cortodoxone
3-Oxo-delta4-steroid
3alpha,21-Dihydroxy-5beta-pregnane-11,20-dione;
5beta-Pregnane-3alpha,21-diol-11,20-dione
Cortisol; Hydrocortisone;
11beta,17alpha,21-Trihydroxy-4-pregnene-3,20-dione;
Kendall's compound F; Reichstein's substance M
11-Dehydrocorticosterone
Corticosterone;
11beta,21-Dihydroxy-4-pregnene-3,20-dione; Kendall's
compound B; Reichstein's substance H
11beta,21-Dihydroxy-3,20-oxo-5beta-pregnan-18-al
Progesterone; 4-Pregnene-3,20-dione
Cortisone;
17alpha,21-Dihydroxy-4-pregnene-3,11,20-trione;
Kendall's compound E; Reichstein's substance Fa
Tetrahydrocorticosterone
21-Hydroxy-5beta-pregnane-3,11,20-trione
17alpha,21-Dihydroxypregnenolone
17alpha,21-Dihydroxy-5beta-pregnane-3,11,20-trione;
5beta-Pregnane-17alpha,21-diol-3,11,20-trione;
4,5beta-Dihydrocortisone
21-Deoxycortisol;
4-Pregnene-11beta,17alpha-diol-3,20-dione;
11beta,17alpha-Dihydroxyprogesterone
3-Oxo-delta5-steroid
18-Hydroxycorticosterone
Log2(FoldChange)
-1.09
0.92
B
Aldosterone;
11beta,21-Dihydroxy-3,20-dioxo-4-pregnen-18-al
18-Hydroxycorticosterone
11-Deoxycortisol; Cortodoxone
Cortisol; Hydrocortisone;
11beta,17alpha,21-Trihydroxy-4-pregnene-3,20-dione;
Kendall's compound F; Reichstein's substance M
21-Deoxycortisol;
4-Pregnene-11beta,17alpha-diol-3,20-dione;
11beta,17alpha-Dihydroxyprogesterone
3-Oxo-delta4-steroid
17alpha,21-Dihydroxypregnenolone
3-Oxo-delta5-steroid
Progesterone; 4-Pregnene-3,20-dione
C
Tetrahydrocorticosterone
Cortisone;
17alpha,21-Dihydroxy-4-pregnene-3,11,20-trione;
Kendall's compound E; Reichstein's substance Fa
Corticosterone;
11beta,21-Dihydroxy-4-pregnene-3,20-dione; Kendall's
compound B; Reichstein's substance H
11beta,21-Dihydroxy-3,20-oxo-5beta-pregnan-18-al
21-Hydroxy-5beta-pregnane-3,11,20-trione
3alpha,21-Dihydroxy-5beta-pregnane-11,20-dione;
5beta-Pregnane-3alpha,21-diol-11,20-dione
11-Dehydrocorticosterone
11beta,21-Dihydroxy-5beta-pregnane-3,20-dione;
5beta-Pregnane-11beta,21-diol-3,20-dione

Fig. 75: Modular network analysis and suggested identification of biologically associated compounds altered by 1 hr 50uM Cef treatment. The *mummichog* modular networks shows putative identifications of compounds affected by 1 hr Cef treatment visualized via Cytoscape 3.4. Metabolites are colored per their FC abundance differences (blue indicated decreased following 1 hr Cef treatement, red indicates increased in 1 hr Cef treated samples). Statistics are based on repeated sampling of randomized m/z from experimental reference list to generate a null distribution, *P*-values are calculated using the random background modeled as a Gamma distribution, with *P*-value <0.05 taken as significant. A. Module populated by the most compounds effected by 1 hr Cef treatment with many connections (enzymatic activity) denoted between nodes, 18 metabolites, *P*value=0.007. B. Significant module network comprised of 9 metabolites, *P*value=0.019. C. Significant module network comprised of 8 metabolites, *P*value =0.028.

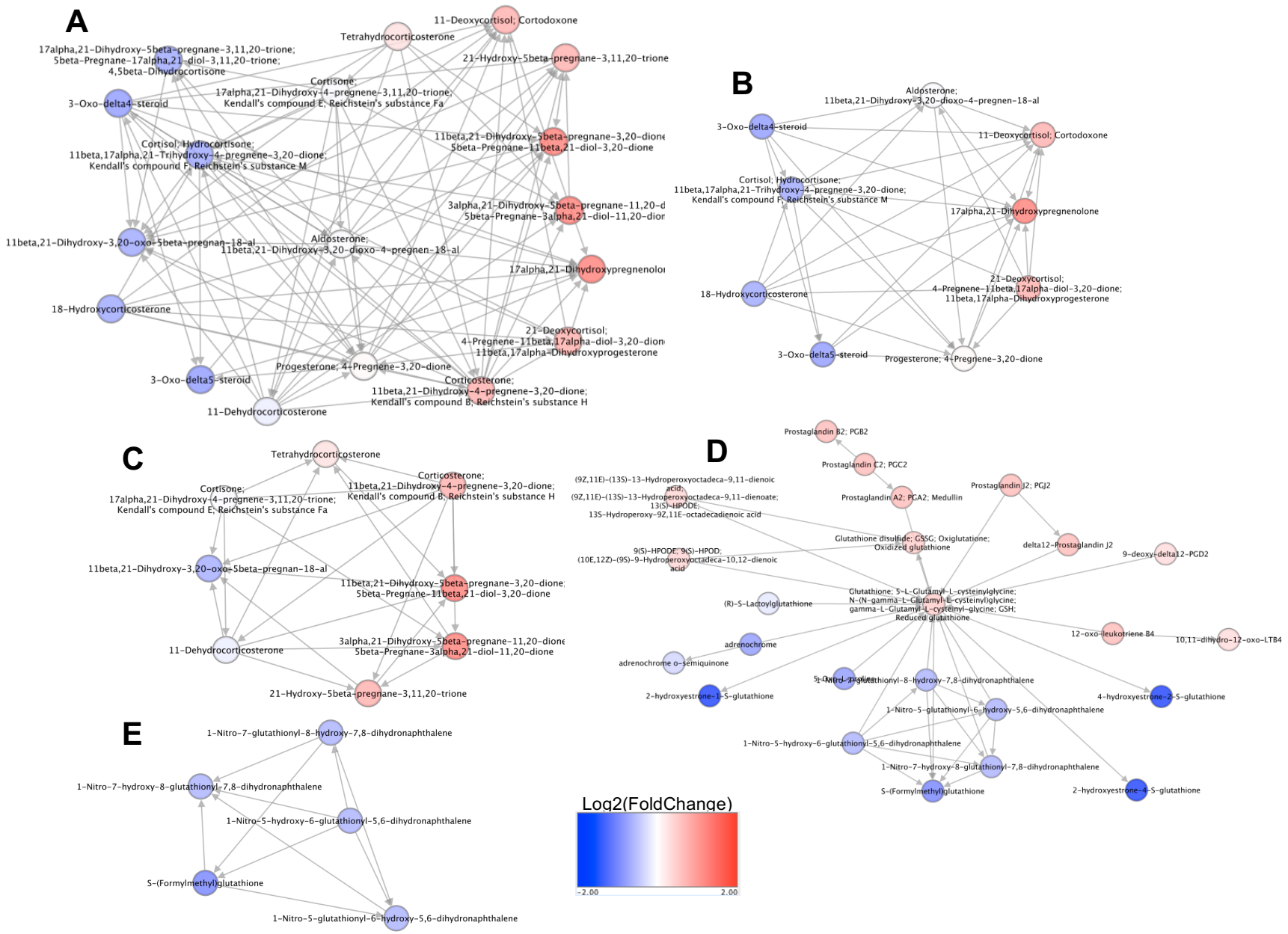
A
11-Deoxycortisol; Cortodoxone
Tetrahydrocorticosterone
17alpha,21-Dihydroxy-5beta-pregnane-3,11,20-trione;
5beta-Pregnane-17alpha,21-diol-3,11,20-trione;
4,5beta-Dihydrocortisone
21-Hydroxy-5beta-pregnane-3,11,20-trione
Cortisone;
17alpha,21-Dihydroxy-4-pregnene-3,11,20-trione;
Kendall's compound E; Reichstein's substance Fa
3-Oxo-delta4-steroid
11beta,21-Dihydroxy-5beta-pregnane-3,20-dione
5beta-Pregnane-11beta,21-diol-3,20-dione
Cortisol; Hydrocortisone;
11beta,17alpha,21-Trihydroxy-4-pregnene-3,20-dione;
Kendall's compound F; Reichstein's substance M
3alpha,21-Dihydroxy-5beta-pregnane-11,20-d
5beta-Pregnane-3alpha,21-diol-11,20-dior
11beta,21-Dihydroxy-3,20-oxo-5beta-pregnan-18-al
Aldosterone;
11beta,21-Dihydroxy-3,20-dioxo-4-pregnen-18-al
17alpha,21-Dihydroxypregnenolor
18-Hydroxycorticosterone
21-Deoxycortisol;
4-Pregnene-11beta,17alpha-diol-3,20-dion
11beta,17alpha-Dihydroxyprogesterone
Progesterone; 4-Pregnene-3,20-dione
3-Oxo-delta5-steroid
Corticosterone;
11beta,21-Dihydroxy-4-pregnene-3,20-dione;
Kendall's compound B; Reichstein's substance H
11-Dehydrocorticosterone
B
Aldosterone;
11beta,21-Dihydroxy-3,20-dioxo-4-pregnen-18-al
3-Oxo-delta4-steroid
11-Deoxycortisol; Cortodoxone
Cortisol; Hydrocortisone;
11beta,17alpha,21-Trihydroxy-4-pregnene-3,20-dione;
Kendall's compound F; Reichstein's substance M
17alpha,21-Dihydroxypregnenolone
18-Hydroxycorticosterone
21-Deoxycortisol;
4-Pregnene-11beta,17alpha-diol-3,20-dione;
11beta,17alpha-Dihydroxyprogesterone
3-Oxo-delta5-steroid
Progesterone; 4-Pregnene-3,20-dione
C
Tetrahydrocorticosterone
Corticosterone;
11beta,21-Dihydroxy-4-pregnene-3,20-dione;
Kendall's compound B; Reichstein's substance H
Cortisone;
17alpha,21-Dihydroxy-4-pregnene-3,11,20-trione;
Kendall's compound E; Reichstein's substance Fa
11beta,21-Dihydroxy-3,20-oxo-5beta-pregnan-18-al
11beta,21-Dihydroxy-5beta-pregnane-3,20-dione;
5beta-Pregnane-11beta,21-diol-3,20-dione
11-Dehydrocorticosterone
3alpha,21-Dihydroxy-5beta-pregnane-11,20-dione
5beta-Pregnane-3alpha,21-diol-11,20-dione
21-Hydroxy-5beta-pregnane-3,11,20-trione
D
Prostaglandin B2; PGB2
Prostaglandin C2; PGC2
(9Z,11E)-(13S)-13-Hydroperoxyoctadeca-9,11-dienoic acid;
(9Z,11E)-(13S)-13-Hydroperoxyoctadeca-9,11-dienoate;
13(S)-HPODE;
13S-Hydroperoxy-9Z,11E-octadecadienoic acid
Prostaglandin J2; PGJ2
Prostaglandin A2; PGA2; Medullin
Glutathione disulfide; GSSG; Oxiglutatione;
Oxidized glutathione
delta12-Prostaglandin J2
9-deoxy-delta12-PGD2
9(S)-HPODE; 9(S)-HPOD;
(10E,12Z)-(9S)-9-Hydroperoxyoctadeca-10,12-dienoic acid
Glutathione; 5-L-Glutamyl-L-cysteinylglycine;
N-(N-gamma-L-Glutamyl-L-cysteinyl)glycine;
gamma-L-Glutamyl-L-cysteinyl-glycine; GSH;
Reduced glutathione
(R)-S-Lactoylglutathione
12-oxo-leukotriene B4
10,11-dihydro-12-oxo-LTB4
adrenochrome
adrenochrome o-semiquinone
1-Nitro-7-glutathionyl-8-hydroxy-7,8-dihydronaphthalene
2-hydroxyestrone-1-S-glutathione
4-hydroxyestrone-2-S-glutathione
1-Nitro-5-glutathionyl-6-hydroxy-5,6-dihydronaphthalene
1-Nitro-5-hydroxy-6-glutathionyl-5,6-dihydronaphthalene
1-Nitro-7-hydroxy-8-glutathionyl-7,8-dihydronaphthalene
S-(Formylmethyl)glutathione
2-hydroxyestrone-4-S-glutathione
E
1-Nitro-7-glutathionyl-8-hydroxy-7,8-dihydronaphthalene
1-Nitro-7-hydroxy-8-glutathionyl-7,8-dihydronaphthalene
1-Nitro-5-hydroxy-6-glutathionyl-5,6-dihydronaphthalene
S-(Formylmethyl)glutathione
1-Nitro-5-glutathionyl-6-hydroxy-5,6-dihydronaphthalene
Log2(FoldChange)
-2.00
2.00

Fig. 76. Modular network analysis and suggested identification of biologically associated compounds altered by 24 hr 50uM Cef treatment. The *mummichog* modular networks shows putative identifications of compounds affected by 24 hr Cef treatment visualized via Cytoscape 3.4. Metabolites are colored per their FC abundance differences (blue indicated decreased following 24 hr Cef treatement, red indicates increased in 24 hr Cef treated samples). Statistics are based on repeated sampling of randomized m/z from experimental reference list to generate a null distribution, *P*-values are calculated using the random background modeled as a Gamma distribution, with *P*-value <0.05 taken as significant. A. Module populated by the most compounds effected by 24 hr Cef treatment with many connections (enzymatic activity) denoted between nodes, 18 metabolites, *P*value=0.004. B. Module network comprised of 9 metabolites, *P*value=0.012. C. Module network comprised of 8 metabolites, *P*value=0.02. D. Module network comprised of 24 metabolites, *P*value=0.04. E. Module network comprised of 5 metabolites, *P*value=0.049.

health [522]. Steroid-based treatments (e.g. progesterone) are shown to be efficacious in models of neurodegenerative diseases (PD, AD, MS) [523, 524] as well as models of stroke, depression, drug dependence and acute brain trauma [525, 526]. As we know the directional change induced by Cef treatment in the modular output from *mummichog,* future studies can validate metabolite alterations and further study how constitutive loss of MBLAC1 either induces changes in similar metabolites or disrupts Cef-induced changes.

Conclusion

Using a targeted/untargeted RPLC-MS metabolomic approach, we assessed the effect of acute and semi-chronic Cef treatment on the metabolome of NIH3T3, MBLAC1 expressing cells. Our analysis provided reliable, reproducible sequence runs as determined by comparing spiked-in exogenous compounds across pooled quality control and experimental samples. Unsupervised PCA analysis revealed distinct separation of our samples, grouped according to Cef treatment (0 hr, 1 hr, or 24 hr), and ANOVA analysis revealed significantly altered features due to Cef treatment. Although the majority of the significantly changed features remained unannotated after comparison with the in-house compound library, we used *mummichog* to nominate the most likely candidate metabolic pathways effected by Cef treatment. Our analysis suggests that Cef treatment induced changes in the metabolic pathways of pyrimidine metabolism and vitamin B5 CoA biosynthesis as well as changes in metabolites with steroid-chemical structures. These pathways should be pursued in future, targeted analyses, and the annotation of *mummichog* nominated metabolites should be validated using mass spectrometry

methods comparing fragmentation data as well as m/z and RT consistencies with available standards. This hypothesis generating study leads us to suspect that Cef has a role in regulating metabolic processes previously indicated as important in maintaining normal brain health.

Future Directions

Global untargeted metabolomic approach to compare the brain metabolomes of WT and MBLAC1 mice treated with saline or ceftriaxone

Together, our previous metabolomic studies, Cef treated cells and assessment of the sera metabolomes of WT and MBLAC1 KO mice, provided us with several metabolic pathways to pursue in future targeted studies, however both studies were conducted as pilot studies, with relatively low sample number. In order to actively follow our hypothesis that Cef mediated changes in the brain are a result of the Cef/MBLAC1 binding interaction, we can couple Cef treatment studies with our newly developed MBLAC1 KO mouse model. We can envision using primary embryonic fibroblast cells derived from MBLAC1 KO and WT mice to monitor the metabolic and/or biochemical effects of Cef treatment *in vitro.* Alternatively, future experiment, we could chronically treat, *in vivo,* MBLAC1 KO and WT littermate controls with Cef, and extract the small molecules from one or more specific brain regions for subsequent metabolomic mass spectrometry-based analysis. Ideally, we will determine 1) specific mass peaks sensitive to constitutive loss of MBLAC1 in the brain, 2) identify specific metabolites within the brain sensitive to Cef treatment, and 3) determine if loss of MBLAC1 disrupts metabolite changes induced by Cef treatment in WT animals.

Appendix C

LIST OF EXPERIMENTS ATTEMPTED OR IN PROGRESS

Swip Related Experiments

1. Swip rescue experiment with N'termSWIP-10::MBLAC1 MBD domain fusion.

    a. BY1155 and BY1156 [*swip-10(tm5915)*; Ex 248 and Ex249 (P_{ptr-10}::swip-10(Pro280)cDNA::(Val21)MBLAC1cDNA::GFP, p_{unc122}::RFP, pBSK)]

    b. BY1157, BY1158, BY1159, and BY1160[*swip-10(tm5915)*;Ex250-Ex253(P_{ptr-10}::swip10(Ser313)cDNA::(Iso80)MBLAC1cDNA::GFP, p_{unc122}::RFP, pBSK)]

    c. Summary: Neither of the fusion expression constructs described above were sufficient to rescue the Swip of *swip-10(tm5915)* mutant animals. This is not entirely suprising, as these fusion constructs were not edited to account for organism specific codon preferences for the encoding of amino acids. Additionally, we chose fusion sites at conserved amino acids however a smaller portion of the Mammalian MBLAC1 fused into the SWIP-10 coding sequence may be better suited to a rescue experiment

2. Swip rescue experiment with N-term signal sequence removed. BY1161-BY1164 [*swip-10(tm5915);* Ex254-Ex257 (P_{ptr-10}::(∆18AA)swip-10cDNA::GFP, p_{unc122}::RFP)

    a. Summary: Interesting, loss of the first 20 amino acids after the Met start codon of the *swip-10* coding sequence resulted in a reduced capacity to rescue the Swip phenotype of *swip-10(tm5915)* animals. The first 20 AAs of the SWIP-10 protein were bioinformatically predicted to encode a secretion signal. As we are unable to see the translational fusion protein however we cannot rule out mosaicism as contributing to this reduction in rescue. This data may suggest that the signal sequence at the N' terminus of the SWIP-10 is essential for the function of the protein. We could also speculate that loss of the N' terminus results in a misfolded protein that is degraded via UPR mechanisms.

3. Basal *aat(s),* and *aat(s);swip-10(tm5915)* Swip assays

    a. Summary: Loss of the amino acid transporters alone do not demonstrate Swip, and loss of *aat-1,* or *aat-3* (the closest to xCT in sequence homology) or combinatorial loss of *aat-1* and *aat-3* did not alter *swip-10(tm5915)* levels of paralysis.

4. Basal Kundra line Swip assays

a. Summary: As described below, we collaborated with the company Kundra employ CRISPR/Cas9 techniques to tag the SWIP-10 with C' terminal MCherry fluorescent protein and a 3X Flag tag with the goal of visualizing the sub-cellular localization of SWIP-10. Three lines genetically positive for the endogenous tags were test for basal Swip. Interestingly we do see a significant level of Swip compared to N2 counterparts, with all three independent lines demonstrating about 75% of animals swimming after 10 mins. We believe that the small level of paralysis observed is due to the tag on the SWIP-10 protein, such that it may slightly but not completely impair SWIP-10 function.

swip-10 DA Neuron Degeneration Related Experiments

1. Another OLL neuron marker. TV12498 [wgIs328 ($p_{ser2prom3}$::myrGFP::unc453'UTR, p_{rab-3}::mCherry, podr-1::RFP)X, and BY1207 [wgIs328;*swip-10(tm5915)*

    a. Summary: The TV12498 OLL neuron marker also allowed us to compare the morphology of the OLL neurons between N2 and *swip-10(tm5915)* mutant animals, and as with the background strain described in Ch. IV, this marker also revealed significant levels of OLL neuron degeneration in *swip-10* mutant animals.

2. Role for the p38 MAPK ortholog, *pmk-1,* in *swip-10* mutant induced DA neuron degeneration. BY1250 [*vtIs7;pmk-1(km25);swip-10(tm5915)*]

    a. Summary: Loss of *pmk-1* significantly reduced the DA neuron degeneration of *swip-10* mutants, the suppression observed was modest and only observed in the measure of shrunken soma, and the total degenerative measure (about 13% reduction in *swip-10* degeneration).

3. Role for *asic-1* in *swip-10* mutant induced DA neuron degeneration. BY1251 [*vtIs7;asic-1(ok415);swip-10(tm5915)*]

    a. Summary: Loss of the acid sensing ion channel expressed in *C. elegans* DA neurons, *asic-1* had no effect on the *swip-10* mutant induced DA neuron degeneration.

4. Chronic pharmacology on DA neuron degeneration

    a. Treatments with:

        i. Methylglyoxal

        ii. N-acetylcysteine (NAC)

        iii. Guanosine

    b. Summary: For all of the above chronic treatments, the drugs were added at various increasing concentrations within the NGM/OP-50 plates on which

synchronized *swip-10* mutants were grown from the L1 stage. None of these drugs had a significant effect on the DA neuron degeneration of GA *swip-10* animals, and N2 controls did not demonstrate altered DA neuron morphology. We test methylglyoxal, a toxic dicarbonyl hydrolyzed by another beta-lactamase, which the Bose lab previously described as resulting in neuronal degeneration. Our hypothesis was that *swip-10* mutants would be more sensitive to methylglyoxal than N2. Our chronic treatment of *swip-10* mutants arose via the literature supporting a neuroprotective role for NAC via its transport through xCT to act as a precursor for GSH, however we do not see any reduction in *swip-10* DA neuron degeneration after chronic NAC treatment. Guanosine was a metabolite found to be increased in 3T3 fibroblast cells following both 1 hr and 24 hr treatment with 50μM Cef, but no effect of Guanosine on N2 or *swip-10* DA neurons was observed.

5. Other archived strains:

    a. BY1178 [*vtIs7;glr-4(tm3239);swip-10(tm5915) glr-6(tm2729)*]

        i. Summary: Combined loss of *glr-4* and *glr-6* did not suppress the DA neuron degeneration of *swip-10* mutant animals.

    b. BY1214 [*vtIs7;eat-4(ky5) vglu-3(tm3390);swip-10(tm5915*)]

        i. Summary: Combined loss of *eat-4* and *vglu-3* did suppress *swip-10* mutant DA neuron degeneration beyond that described for loss of *vglu-3* alone. Generation of the triple VGLUT mutant animal with loss of *swip-10* was attempted but no quadruple mutants were identified.

    c. BY1270 [*vtIs7;glr-1(n2461);crt-1(ok948);swip-10(tm5915)*]

        i. Summary: Combined loss of *glr-1* and *crt-1* does not enhance suppression of *swip-10* mutant DA neuron degeneration, with a similar suppression phenotype to loss of *crt-1* alone. This suggests and is in line with the data described in Ch V. that *glr-1* and *crt-1* act in the same pathway to mediate DA neuron degeneration in the context of loss of *swip-10.*

    d. Stress reporters:

        i. MT17370 [*lin-15(n765)*;*nIs242(*$p_{gcy\text{-}33}$*::*GFP)], and BY1193 [*nIs242;swip-10(tm5915)*]

            1. Summary: nIs242 is an integrated transgene for a transcriptional reporter sensitive to oxidative stress. This strain has been crossed to *swip-10(tm5915)* mutants and archived but has not been characterized.

        ii. SKN-1 localization reporter. LD1 [*ldIs7* (SKN-1b/c::GFP)], and

BY1254 [*IdIs7;swip-10(tm5915)*].

1. Summary: IdIs7 is an integraged transgene for a translational report used to monitor localization of SKN-1. SKN-1 is transcriptional regulator of detoxifying enzymes, and oxidative stress results in nuclear localization of SKN-1. This strain has been crossed to *swip-10(tm5915)* mutants and archived but has not been characterized for basal levels or pharmacologically induced levels of SKN-1 nuclear localization.

Other *swip-10* Related Experiments

1. Created *C. elegans* transgenic strain with DA neuron specific expression of the fluorescent Glu reporter, GluSNFR. [BY1113 [lin-15(n765ts); ex221 (p_{dat-1}::GluSNFR, p_{dat-1}::mcherry, pJM239(lin15+))]

    a. Summary: This line has been generated and archived but not characterized or used in experimentation.

2. Serotonin stimulated pharyngeal pumping

    a. Summary: *swip-10* mutants show significantly increased pump frequency and pump duration and significantly decreased inter-pump interval compared to N2. This work done in collaboration with Peter Rodriguez and Kundra (NemaMatrix).

3. Collaboration with Knudra to use CRISPR/CAS9 to *swip-10* at the endogenous genomic locus. SWIP-10::mCHERRY::3XFLAG

    a. Strains: COP1615 (NV1480.2.4.5), COP1616 (NV1480.3.1.3), COP1617 (NV1480.4.1.3)

        i. Summary: These lines have been imaged using confocal microscopy, however no visible mCherry fluorescence was observed. It is possible that pharmacological or environmental stress may induce expression of SWIP-10, and these lines should be imaged in various stress paradigms.

4. Immunostaining to visualize the endogenously tagged SWIP-10::mCHERRY::3XFLAG (anti-FLAG primary antibody)

    a. Peroxide tube fixation method with β-ME permeablization and formaldehyde fixation

    b. Freeze crack slide fixation method with acetone/methanol fixation

    c. Freeze crack slide fixation method with Paraformaldehyde fixation

d. Summary: These preliminary immunostaining experiments were aimed at determining the most effective protocol to permeablize and fix *C. elegans* for immunostaining detection of C' terminally mCherry and 3XFLAG tagged SWIP-10 protein using anti-FLAG primary antibody. The freeze cracking method with fixation via MeOH/Acetone or 30mins 4%PFA worked for the immunostaining of GFP expressed in BY250 gravid adult and L4 animals. The endogenously tagged SWIP-10 lines generated by Knudra, display less definitive staining, however some specific staining was suggested. Our preliminary efforts indicate that the staining of Knudra lines L4 animals was more successful than L1 or GA animals. It remains undetermined which fixation method is best. These experiments are very preliminary, and there are many variables and protocol options to text in order to find the most effective method for immunostaining these particular strains. As a note, overall morphology of the freeze-cracked animals is extremely distorted, with many animals broken/bent or ripped apart. The vast majority of animals stained (GFP or FLAG) in all protocols attempted did not show any specific staining, indicating inefficient staining methods.

5. Initiated flow-cytometry based sorting of *C. elegans* glia from N2 and *swip-10* mutants, utilizing the *nsIs108* (p_{ptr-10}::myrRFP).

    a. Summary: After multiple attempts to dissociated and flow-sort both glia and DA neurons from *swip-10* mutants and N2 animals, we were able to better troubleshoot our dissociation protocol, however, due to the time and effort needed to conduct these experiments, this line of research is still at a preliminary state, with further method tuning and better controls required.

MBLAC-1 Related Experiments

1. Amino Acid measurements

    a. 3T3 cells +/- 24 hr 50 μM ceftriaxone

        i. Summary: No changes in the measured amino acids (via HPLC) were observed in 3T3 cells due to Cef treatment.

    b. Tissue amino acid levels from hippocampus, cortex, striatum, cerebellum and serum from MBLAC1 KO and WT littermates.

        i. Summary: One cohort of tissue extracted from 4 MBLAC1 KO and 4 littermate WT controls, amino acids measured via mass spectrometry methods at the Vanderbilt Neurochemistry Core. Our preliminary results show no change in amino acid level in different brain regions, however taurine serum levels were significantly reduced in MBLAC1 KO animals, in line with data provided in Ch VI.

2. MBLAC-1 viral-mediated KD in cell culture

a. Summary: Work conducted in collaboration with Dave Poulsen's lab, we generated a plasmid for viral-mediated knock-down (KD) of MBLAC1 in cell culture. We treated glioma cell lines (with high levels of MBLAC1 expression) with various concentrations of the viral KD vector, however we did not see a reduction in MBLAC1 expression assessed by western blot. This was conducted before the generation of the MBLAC1 KO mouse, and our efforts now focus on characterization of the KO animals.

3. Na^+-dependent and Na^+-independent Glu uptake in Mblac1cDNA transiently transfected HEK 293t cells.

    a. Summary: These uptakes were inconsistent in their results but hinted at a potential increase in Na^+-independent Glu uptake. In order to pursue other experiments, these studies were not continued. Cassie Retzlaff continued the investigation of the MBLAC1 effect on Glu uptake in synaptosomes prepared from MBLAC1 KO and WT animals.

4. xCT, GLT-1, and MBLAC1 expression in human derived glioma cell lines.

    a. Summary: Via western blotting, we preliminarily demonstrated that xCT, GLT-1, and MBLAC1 are expressed in several human derived glioma lines, but no further experiments were performed.

5. Monoamine and metabolite measurements in MBLAC1 KO and WT littermates

    a. Summary: These experiments are on-going in the Blakely lab by Paul Gresh and Rania Katamish.

6. MBLAC1 substrate Identification:

    a. HA tagged MBLAC1 expression in HEK 293t cells.

        i. Summary: The HA-MBLAC1_pCDNA plasmid was generated by Andrew Hardaway, and shown to be successfully transfected and expressed in HEK 293t cells via western blot in collaboration with Samara Vilca. Futhermore, HA:MBLAC1 can be conjugated to HA-beads.

    b. Cef interacts with HA:MBLAC1:

        i. Summary: Work done with Cassie Retzlaff and Samara Vilca demonstrates that the HA:MBLAC1 construct retains its ability to bind Cef-conjugated beads.

    c. RPLC-POS and -NEG LCMS/MS analysis of small molecules extracted from MBLAC1 KO cortical lysates incubated with MBLAC1 conjugated or unconjugated HA:beads control.

        i. Two sample sets: High salt buffer vs low salt buffer

ii. HILIC-POS and –NEG samples prepared

1. Summary: Ongoing work in collaboration with the Vanderbilt Center for Innovative Technology (Simona Codreanu and Alex Shrimpe-Rutledge). We have run samples prepared in both low and high salt buffers, for 4 biological replicates, MBLAC1 KO brain lysate incubated with either HA beads conjugated to HA:MBLAC1 or unconjugated beads for 30mins at room temp. Following the removal of conjugated or unconjugated beads, samples were split into two tubes, proteins precipitated and small molecule contain fraction dried down for subsequent mass spectrometry. One set of samples was re-suspended for RPLC-POS and –NEG LCMS/MS. Our results revealed a limited number of features significantly different in samples incubated with MBLAC1 enzyme. These experiments are ongoing, and we have not pursued identification of the unknown features. As described in Ch VII, we expect only a few number of features to appear after acute exposure to MBLAC1, ideally revealing a decrease of the substrate for MBLAC1 or an increase in the product of MBLAC1. We have samples prepared but not run for HILIC-POS and –NEG to provide more comprehensive metabolite coverage.

REFERENCES

1. Carlsson A, Lindqvist M, Magnusson T, Waldeck B. On the presence of 3-hydroxytyramine in brain. Science. 1958;127(3296):471. Epub 1958/02/28. PubMed PMID: 13529006.

2. Carlsson A. Detection and assay of dopamine. Pharmacol Rev. 1959;11(2, Part 2):300-4. Epub 1959/06/01. PubMed PMID: 13667410.

3. Nagatsu T, Levitt M, Udenfriend S. Conversion of L-tyrosine to 3,4-dihydroxyphenylalanine by cell-free preparations of brain and sympathetically innervated tissues. Biochem Biophys Res Commun. 1964;14:543-9. Epub 1964/01/01. PubMed PMID: 5836553.

4. Laatikainen LM, Sharp T, Harrison PJ, Tunbridge EM. Sexually dimorphic effects of catechol-O-methyltransferase (COMT) inhibition on dopamine metabolism in multiple brain regions. PLoS One. 2013;8(4):e61839. Epub 2013/04/25. doi: 10.1371/journal.pone.0061839. PubMed PMID: 23613951; PubMed Central PMCID: PMCPMC3629045.

5. Nagatsu T. Genes for human catecholamine-synthesizing enzymes. Neurosci Res. 1991;12(2):315-45. Epub 1991/10/01. PubMed PMID: 1684650.

6. Kirshner N. Uptake of catecholamines by a particulate fraction of the adrenal medulla. J Biol Chem. 1962;237:2311-7. Epub 1962/07/01. PubMed PMID: 14456353.

7. Erickson JD, Eiden LE, Hoffman BJ. Expression cloning of a reserpine-sensitive vesicular monoamine transporter. Proc Natl Acad Sci U S A. 1992;89(22):10993-7. Epub 1992/11/15. PubMed PMID: 1438304; PubMed Central PMCID: PMCPMC50469.

8. Peter D, Liu Y, Sternini C, de Giorgio R, Brecha N, Edwards RH. Differential expression of two vesicular monoamine transporters. J Neurosci. 1995;15(9):6179-88. Epub 1995/09/01. PubMed PMID: 7666200.

9. Nirenberg MJ, Liu Y, Peter D, Edwards RH, Pickel VM. The vesicular monoamine transporter 2 is present in small synaptic vesicles and preferentially localizes to large dense core vesicles in rat solitary tract nuclei. Proc Natl Acad Sci U S A. 1995;92(19):8773-7. Epub 1995/09/12. PubMed PMID: 7568015; PubMed Central PMCID: PMCPMC41049.

10. Anden NE, Carlsson A, Dahlstroem A, Fuxe K, Hillarp NA, Larsson K. Demonstration and Mapping out of Nigro-Neostriatal Dopamine Neurons. Life Sci (1962). 1964;3:523-30. Epub 1964/06/01. PubMed PMID: 14187491.

11. Carlsson A, Dahlstroem A, Fuxe K, Lindqvist M. Histochemical and Biochemical Detection of Monoamine Release from Brain Neurons. Life Sci (1962). 1965;4:809-16. Epub 1965/04/01. PubMed PMID: 14343933.

12. Ciliax BJ, Heilman C, Demchyshyn LL, Pristupa ZB, Ince E, Hersch SM, et al. The dopamine transporter: immunochemical characterization and localization in brain. J Neurosci. 1995;15(3 Pt 1):1714-23. Epub 1995/03/01. PubMed PMID: 7534339.

13. Kitahama K, Geffard M, Okamura H, Nagatsu I, Mons N, Jouvet M. Dopamine- and dopa-immunoreactive neurons in the cat forebrain with reference to tyrosine hydroxylase-immunohistochemistry. Brain Res. 1990;518(1-2):83-94. Epub 1990/06/04. PubMed PMID: 1975219.

14. Hu Z, Cooper M, Crockett DP, Zhou R. Differentiation of the midbrain dopaminergic pathways during mouse development. J Comp Neurol. 2004;476(3):301-11. Epub 2004/07/23. doi: 10.1002/cne.20230. PubMed PMID: 15269972.

15. Roeper J. Dissecting the diversity of midbrain dopamine neurons. Trends Neurosci. 2013;36(6):336-42. Epub 2013/04/16. doi: 10.1016/j.tins.2013.03.003. PubMed PMID: 23582338.

16. Bunney BS, Aghajanian GK. The precise localization of nigral afferents in the rat as determined by a retrograde tracing technique. Brain Res. 1976;117(3):423-35. Epub 1976/12/03. PubMed PMID: 990939.

17. Watabe-Uchida M, Zhu L, Ogawa SK, Vamanrao A, Uchida N. Whole-brain mapping of direct inputs to midbrain dopamine neurons. Neuron. 2012;74(5):858-73. Epub 2012/06/12. doi: 10.1016/j.neuron.2012.03.017. PubMed PMID: 22681690.

18. Phillipson OT. Afferent projections to the ventral tegmental area of Tsai and interfascicular nucleus: a horseradish peroxidase study in the rat. J Comp Neurol. 1979;187(1):117-43. Epub 1979/09/01. doi: 10.1002/cne.901870108. PubMed PMID: 489776.

19. Portig PJ, Sharman DF, Vogt M. Release by tubocurarine of dopamine and homovanillic acid from the superfused caudate nucleus. J Physiol. 1968;194(2):565-72. Epub 1968/02/01. PubMed PMID: 5639370; PubMed Central PMCID: PMCPMC1365810.

20. Portig PJ, Vogt M. Release to the cerebral ventricles of substances with possible transmitter function in the caudate nucleus. J Physiol. 1969;204(3):687-715. Epub 1969/10/01. PubMed PMID: 4309959; PubMed Central PMCID: PMCPMC1351581.

21. Ng KY, Chase TN, Colburn RW, Kopin IJ. Dopamine: stimulation-induced release from central neurons. Science. 1971;172(3982):487-9. Epub 1971/04/30. PubMed PMID: 5550505.

22. Plotsky PM, Wightman RM, Chey W, Adams RN. Liquid chromatographic analysis of endogenous catecholamine release from brain slices. Science. 1977;197(4306):904-6. Epub 1977/08/26. PubMed PMID: 887928.

23. Wightman RM, Haynes CL. Synaptic vesicles really do kiss and run. Nat Neurosci. 2004;7(4):321-2. Epub 2004/03/30. doi: 10.1038/nn0404-321. PubMed PMID: 15048116.

24. Heien ML, Johnson MA, Wightman RM. Resolving neurotransmitters detected by fast-scan cyclic voltammetry. Anal Chem. 2004;76(19):5697-704. Epub 2004/10/01. doi: 10.1021/ac0491509. PubMed PMID: 15456288.

25. Robinson DL, Venton BJ, Heien ML, Wightman RM. Detecting subsecond dopamine release with fast-scan cyclic voltammetry in vivo. Clin Chem. 2003;49(10):1763-73. Epub 2003/09/23. PubMed PMID: 14500617.

26. Deister CA, Teagarden MA, Wilson CJ, Paladini CA. An intrinsic neuronal oscillator underlies dopaminergic neuron bursting. J Neurosci. 2009;29(50):15888-97. Epub 2009/12/18. doi: 10.1523/JNEUROSCI.4053-09.2009. PubMed PMID: 20016105; PubMed Central PMCID: PMCPMC2824818.

27. Paladini CA, Robinson S, Morikawa H, Williams JT, Palmiter RD. Dopamine controls the firing pattern of dopamine neurons via a network feedback mechanism. Proc Natl Acad Sci U S A. 2003;100(5):2866-71. Epub 2003/02/27. doi: 10.1073/pnas.0138018100. PubMed PMID: 12604788; PubMed Central PMCID: PMCPMC151432.

28. Beckstead MJ, Grandy DK, Wickman K, Williams JT. Vesicular dopamine release elicits an inhibitory postsynaptic current in midbrain dopamine neurons. Neuron. 2004;42(6):939-46. Epub 2004/06/23. doi: 10.1016/j.neuron.2004.05.019. PubMed PMID: 15207238.

29. Burt DR, Enna SJ, Creese I, Snyder SH. Dopamine receptor binding in the corpus striatum of mammalian brain. Proc Natl Acad Sci U S A. 1975;72(11):4655-9. Epub 1975/11/01. PubMed PMID: 1060143; PubMed Central PMCID: PMCPMC388782.

30. Seeman P, Chau-Wong M, Tedesco J, Wong K. Brain receptors for antipsychotic drugs and dopamine: direct binding assays. Proc Natl Acad Sci U S A. 1975;72(11):4376-80. Epub 1975/11/01. PubMed PMID: 1060115; PubMed Central PMCID: PMCPMC388724.

31. Seeman P, Lee T, Chau-Wong M, Wong K. Antipsychotic drug doses and neuroleptic/dopamine receptors. Nature. 1976;261(5562):717-9. Epub 1976/06/24. PubMed PMID: 945467.

32. Giros B, Sokoloff P, Martres MP, Riou JF, Emorine LJ, Schwartz JC. Alternative splicing directs the expression of two D2 dopamine receptor isoforms. Nature. 1989;342(6252):923-6. Epub 1989/12/21. doi: 10.1038/342923a0. PubMed PMID: 2531847.

33. Monsma FJ, Jr., Brassard DL, Sibley DR. Identification and characterization of D1 and D2 dopamine receptors in cultured neuroblastoma and retinoblastoma clonal cell lines. Brain Res. 1989;492(1-2):314-24. Epub 1989/07/17. PubMed PMID: 2665904.

34. Sokoloff P, Giros B, Martres MP, Bouthenet ML, Schwartz JC. Molecular cloning and characterization of a novel dopamine receptor (D3) as a target for neuroleptics. Nature. 1990;347(6289):146-51. Epub 1990/09/13. doi: 10.1038/347146a0. PubMed PMID: 1975644.

35. Sunahara RK, Guan HC, O'Dowd BF, Seeman P, Laurier LG, Ng G, et al. Cloning of the gene for a human dopamine D5 receptor with higher affinity for dopamine than D1. Nature. 1991;350(6319):614-9. Epub 1991/04/18. doi: 10.1038/350614a0. PubMed PMID: 1826762.

36. Zhou QY, Grandy DK, Thambi L, Kushner JA, Van Tol HH, Cone R, et al. Cloning and expression of human and rat D1 dopamine receptors. Nature. 1990;347(6288):76-80. Epub 1990/09/06. doi: 10.1038/347076a0. PubMed PMID: 2168520.

37. Beaulieu JM, Gainetdinov RR. The physiology, signaling, and pharmacology of dopamine receptors. Pharmacol Rev. 2011;63(1):182-217. Epub 2011/02/10. doi: 10.1124/pr.110.002642. PubMed PMID: 21303898.

38. Kilty JE, Lorang D, Amara SG. Cloning and expression of a cocaine-sensitive rat dopamine transporter. Science. 1991;254(5031):578-9. Epub 1991/10/25. PubMed PMID: 1948035.

39. Giros B, Jaber M, Jones SR, Wightman RM, Caron MG. Hyperlocomotion and indifference to cocaine and amphetamine in mice lacking the dopamine transporter. Nature. 1996;379(6566):606-12. Epub 1996/02/15. doi: 10.1038/379606a0. PubMed PMID: 8628395.

40. Gelb DJ, Oliver E, Gilman S. Diagnostic criteria for Parkinson disease. Arch Neurol. 1999;56(1):33-9. Epub 1999/01/29. PubMed PMID: 9923759.

41. Alexander GE. Biology of Parkinson's disease: pathogenesis and pathophysiology of a multisystem neurodegenerative disorder. Dialogues Clin Neurosci. 2004;6(3):259-80. Epub 2004/09/01. PubMed PMID: 22033559; PubMed Central PMCID: PMCPMC3181806.

42. Dexter DT, Jenner P. Parkinson disease: from pathology to molecular disease mechanisms. Free Radic Biol Med. 2013;62:132-44. Epub 2013/02/06. doi: 10.1016/j.freeradbiomed.2013.01.018. PubMed PMID: 23380027.

43. Baba M, Nakajo S, Tu PH, Tomita T, Nakaya K, Lee VM, et al. Aggregation of alpha-synuclein in Lewy bodies of sporadic Parkinson's disease and dementia with Lewy bodies. Am J Pathol. 1998;152(4):879-84. Epub 1998/04/18. PubMed PMID: 9546347; PubMed Central PMCID: PMCPMC1858234.

44. Goedert M. Alpha-synuclein and neurodegenerative diseases. Nat Rev Neurosci. 2001;2(7):492-501. Epub 2001/07/04. doi: 10.1038/35081564. PubMed PMID: 11433374.

45. Caudle WM, Zhang J. Glutamate, excitotoxicity, and programmed cell death in Parkinson disease. Exp Neurol. 2009;220(2):230-3. Epub 2009/10/10. doi: 10.1016/j.expneurol.2009.09.027. PubMed PMID: 19815009.

46. Bose A, Beal MF. Mitochondrial dysfunction in Parkinson's disease. J Neurochem. 2016;139 Suppl 1:216-31. Epub 2016/08/23. doi: 10.1111/jnc.13731. PubMed PMID: 27546335.

47. McNaught KS, Mytilineou C, Jnobaptiste R, Yabut J, Shashidharan P, Jennert P, et al. Impairment of the ubiquitin-proteasome system causes dopaminergic cell death and inclusion body formation in ventral mesencephalic cultures. J Neurochem. 2002;81(2):301-6. Epub 2002/06/18. PubMed PMID: 12064477.

48. Dzamko N, Geczy CL, Halliday GM. Inflammation is genetically implicated in Parkinson's disease. Neuroscience. 2015;302:89-102. Epub 2014/12/03. doi: 10.1016/j.neuroscience.2014.10.028. PubMed PMID: 25450953.

49. Farrer MJ. Genetics of Parkinson disease: paradigm shifts and future prospects. Nat Rev Genet. 2006;7(4):306-18. Epub 2006/03/18. doi: 10.1038/nrg1831. PubMed PMID: 16543934.

50. Ungerstedt U, Ljungberg T, Steg G. Behavioral, physiological, and neurochemical changes after 6-hydroxydopamine-induced degeneration of the nigro-striatal dopamine neurons. Adv Neurol. 1974;5:421-6. Epub 1974/01/01. PubMed PMID: 4531217.

51. Sauer H, Oertel WH. Progressive degeneration of nigrostriatal dopamine neurons following intrastriatal terminal lesions with 6-hydroxydopamine: a combined retrograde tracing and immunocytochemical study in the rat. Neuroscience. 1994;59(2):401-15. Epub 1994/03/01. PubMed PMID: 7516500.

52. Nass R, Hall DH, Miller DM, 3rd, Blakely RD. Neurotoxin-induced degeneration of dopamine neurons in Caenorhabditis elegans. Proc Natl Acad Sci U S A. 2002;99(5):3264-9. doi: 10.1073/pnas.042497999. PubMed PMID: 11867711; PubMed Central PMCID: PMC122507.

53. Alvarez-Fischer D, Guerreiro S, Hunot S, Saurini F, Marien M, Sokoloff P, et al. Modelling Parkinson-like neurodegeneration via osmotic minipump delivery of MPTP and probenecid. J Neurochem. 2008;107(3):701-11. Epub 2008/09/03. doi: 10.1111/j.1471-4159.2008.05651.x. PubMed PMID: 18761710.

54. Vonsattel JP, Myers RH, Stevens TJ, Ferrante RJ, Bird ED, Richardson EP, Jr. Neuropathological classification of Huntington's disease. J Neuropathol Exp Neurol. 1985;44(6):559-77. Epub 1985/11/01. PubMed PMID: 2932539.

55. Spargo E, Everall IP, Lantos PL. Neuronal loss in the hippocampus in Huntington's disease: a comparison with HIV infection. J Neurol Neurosurg Psychiatry. 1993;56(5):487-91. Epub 1993/05/01. PubMed PMID: 8505640; PubMed Central PMCID: PMCPMC1015006.

56. Cepeda C, Murphy KP, Parent M, Levine MS. The role of dopamine in Huntington's disease. Prog Brain Res. 2014;211:235-54. Epub 2014/06/28. doi: 10.1016/B978-0-444-63425-2.00010-6. PubMed PMID: 24968783; PubMed Central PMCID: PMCPMC4409123.

57. Weeks RA, Piccini P, Harding AE, Brooks DJ. Striatal D1 and D2 dopamine receptor loss in asymptomatic mutation carriers of Huntington's disease. Ann Neurol. 1996;40(1):49-54. Epub 1996/07/01. doi: 10.1002/ana.410400110. PubMed PMID: 8687191.

58. van Oostrom JC, Dekker M, Willemsen AT, de Jong BM, Roos RA, Leenders KL. Changes in striatal dopamine D2 receptor binding in pre-clinical Huntington's disease. Eur J Neurol. 2009;16(2):226-31. Epub 2009/01/14. doi: 10.1111/j.1468-1331.2008.02390.x. PubMed PMID: 19138335.

59. Backman L, Farde L. Dopamine and cognitive functioning: brain imaging findings in Huntington's disease and normal aging. Scand J Psychol. 2001;42(3):287-96. Epub 2001/08/15. PubMed PMID: 11501742.

60. Pouladi MA, Stanek LM, Xie Y, Franciosi S, Southwell AL, Deng Y, et al. Marked differences in neurochemistry and aggregates despite similar behavioural and neuropathological features of Huntington disease in the full-length BACHD and YAC128 mice. Hum Mol Genet. 2012;21(10):2219-32. Epub 2012/02/14. doi: 10.1093/hmg/dds037. PubMed PMID: 22328089.

61. Nieoullon A, Cheramy A, Glowinski J. Release of dopamine evoked by electrical stimulation of the motor and visual areas of the cerebral cortex in both caudate nuclei and in the substantia nigra in the cat. Brain Res. 1978;145(1):69-83. Epub 1978/04/21. PubMed PMID: 638784.

62. Meltzer LT, Christoffersen CL, Serpa KA. Modulation of dopamine neuronal activity by glutamate receptor subtypes. Neurosci Biobehav Rev. 1997;21(4):511-8. Epub 1997/07/01. PubMed PMID: 9195610.

63. Paleacu D. Tetrabenazine in the treatment of Huntington's disease. Neuropsychiatr Dis Treat. 2007;3(5):545-51. Epub 2007/10/01. PubMed PMID: 19381278; PubMed Central PMCID: PMCPMC2656291.

64. Assmann BE, Robinson RO, Surtees RA, Brautigam C, Heales SJ, Wevers RA, et al. Infantile Parkinsonism-dystonia and elevated dopamine metabolites in CSF. Neurology. 2004;62(10):1872-4. Epub 2004/05/26. PubMed PMID: 15159499.

65. Kurian MA, Zhen J, Cheng SY, Li Y, Mordekar SR, Jardine P, et al. Homozygous loss-of-function mutations in the gene encoding the dopamine transporter are associated with infantile parkinsonism-dystonia. J Clin Invest. 2009;119(6):1595-603. Epub 2009/05/30. doi: 10.1172/JCI39060. PubMed PMID: 19478460; PubMed Central PMCID: PMCPMC2689114.

66. Kurian MA, Li Y, Zhen J, Meyer E, Hai N, Christen HJ, et al. Clinical and molecular characterisation of hereditary dopamine transporter deficiency syndrome: an observational cohort and experimental study. Lancet Neurol. 2011;10(1):54-62. Epub 2010/11/30. doi: 10.1016/S1474-4422(10)70269-6. PubMed PMID: 21112253; PubMed Central PMCID: PMCPMC3002401.

67. Ng J, Zhen J, Meyer E, Erreger K, Li Y, Kakar N, et al. Dopamine transporter deficiency syndrome: phenotypic spectrum from infancy to adulthood. Brain. 2014;137(Pt 4):1107-19. Epub 2014/03/13. doi: 10.1093/brain/awu022. PubMed PMID: 24613933; PubMed Central PMCID: PMCPMC3959557.

68. Wijemanne S, Jankovic J. Dopa-responsive dystonia--clinical and genetic heterogeneity. Nat Rev Neurol. 2015;11(7):414-24. Epub 2015/06/24. doi: 10.1038/nrneurol.2015.86. PubMed PMID: 26100751.

69. Malek N, Fletcher N, Newman E. Diagnosing dopamine-responsive dystonias. Pract Neurol. 2015;15(5):340-5. Epub 2015/06/06. doi: 10.1136/practneurol-2015-001101. PubMed PMID: 26045581.

70. Cai C, Shi W, Zeng Z, Zhang M, Ling C, Chen L, et al. GTP cyclohydrolase I and tyrosine hydroxylase gene mutations in familial and sporadic dopa-responsive dystonia patients. PLoS One. 2013;8(6):e65215. Epub 2013/06/14. doi: 10.1371/journal.pone.0065215. PubMed PMID: 23762320; PubMed Central PMCID: PMCPMC3675154.

71. Neychev VK, Fan X, Mitev VI, Hess EJ, Jinnah HA. The basal ganglia and cerebellum interact in the expression of dystonic movement. Brain. 2008;131(Pt 9):2499-509. Epub 2008/08/02. doi: 10.1093/brain/awn168. PubMed PMID: 18669484; PubMed Central PMCID: PMCPMC2724906.

72. Carbon M, Argyelan M, Habeck C, Ghilardi MF, Fitzpatrick T, Dhawan V, et al. Increased sensorimotor network activity in DYT1 dystonia: a functional imaging study. Brain. 2010;133(Pt 3):690-700. Epub 2010/03/09. doi: 10.1093/brain/awq017. PubMed PMID: 20207699; PubMed Central PMCID: PMCPMC2842516.

73. Lehericy S, Tijssen MA, Vidailhet M, Kaji R, Meunier S. The anatomical basis of dystonia: current view using neuroimaging. Mov Disord. 2013;28(7):944-57. Epub 2013/07/31. doi: 10.1002/mds.25527. PubMed PMID: 23893451.

74. Rose SJ, Yu XY, Heinzer AK, Harrast P, Fan X, Raike RS, et al. A new knock-in mouse model of l-DOPA-responsive dystonia. Brain. 2015;138(Pt 10):2987-3002. Epub

2015/07/30. doi: 10.1093/brain/awv212. PubMed PMID: 26220941; PubMed Central PMCID: PMCPMC4627353.

75. Polanczyk G, de Lima MS, Horta BL, Biederman J, Rohde LA. The worldwide prevalence of ADHD: a systematic review and metaregression analysis. Am J Psychiatry. 2007;164(6):942-8. Epub 2007/06/02. doi: 10.1176/ajp.2007.164.6.942. PubMed PMID: 17541055.

76. Willcutt EG. The prevalence of DSM-IV attention-deficit/hyperactivity disorder: a meta-analytic review. Neurotherapeutics. 2012;9(3):490-9. Epub 2012/09/15. doi: 10.1007/s13311-012-0135-8. PubMed PMID: 22976615; PubMed Central PMCID: PMCPMC3441936.

77. Sharma A, Couture J. A review of the pathophysiology, etiology, and treatment of attention-deficit hyperactivity disorder (ADHD). Ann Pharmacother. 2014;48(2):209-25. Epub 2013/11/22. doi: 10.1177/1060028013510699. PubMed PMID: 24259638.

78. Brent PJ. Behavioural effects of selective dopamine D-1 and D-2 agonists and antagonists in guinea-pigs. Psychopharmacology (Berl). 1991;104(2):201-7. Epub 1991/01/01. PubMed PMID: 1831560.

79. Dreher JK, Jackson DM. Role of D1 and D2 dopamine receptors in mediating locomotor activity elicited from the nucleus accumbens of rats. Brain Res. 1989;487(2):267-77. Epub 1989/05/22. PubMed PMID: 2525062.

80. Tirelli E, Terry P. Biphasic locomotor effects of the dopamine D1 agonist SKF 38393 and their attenuation in non-habituated mice. Psychopharmacology (Berl). 1993;110(1-2):69-75. Epub 1993/01/01. PubMed PMID: 7870901.

81. Wu J, Xiao H, Sun H, Zou L, Zhu LQ. Role of dopamine receptors in ADHD: a systematic meta-analysis. Mol Neurobiol. 2012;45(3):605-20. Epub 2012/05/23. doi: 10.1007/s12035-012-8278-5. PubMed PMID: 22610946.

82. Swanson JM, Volkow ND. Pharmacokinetic and pharmacodynamic properties of stimulants: implications for the design of new treatments for ADHD. Behav Brain Res. 2002;130(1-2):73-8. Epub 2002/02/28. PubMed PMID: 11864720.

83. Ribases M, Ramos-Quiroga JA, Hervas A, Sanchez-Mora C, Bosch R, Bielsa A, et al. Candidate system analysis in ADHD: evaluation of nine genes involved in dopaminergic neurotransmission identifies association with DRD1. World J Biol Psychiatry. 2012;13(4):281-92. Epub 2012/03/13. doi: 10.3109/15622975.2011.584905. PubMed PMID: 22404661.

84. Cook EH, Jr., Stein MA, Krasowski MD, Cox NJ, Olkon DM, Kieffer JE, et al. Association of attention-deficit disorder and the dopamine transporter gene. Am J Hum Genet. 1995;56(4):993-8. Epub 1995/04/01. PubMed PMID: 7717410; PubMed Central PMCID: PMCPMC1801209.

85. Mazei-Robinson MS, Blakely RD. ADHD and the dopamine transporter: are there reasons to pay attention? Handb Exp Pharmacol. 2006;(175):373-415. Epub 2006/05/26. PubMed PMID: 16722244.

86. Madras BK, Miller GM, Fischman AJ. The dopamine transporter and attention-deficit/hyperactivity disorder. Biol Psychiatry. 2005;57(11):1397-409. Epub 2005/06/14. doi: 10.1016/j.biopsych.2004.10.011. PubMed PMID: 15950014.

87. Yang B, Chan RC, Jing J, Li T, Sham P, Chen RY. A meta-analysis of association studies between the 10-repeat allele of a VNTR polymorphism in the 3'-UTR of dopamine transporter gene and attention deficit hyperactivity disorder. Am J Med Genet B Neuropsychiatr Genet. 2007;144B(4):541-50. Epub 2007/04/19. doi: 10.1002/ajmg.b.30453. PubMed PMID: 17440978.

88. Matthews N, Vance A, Cummins TD, Wagner J, Connolly A, Yamada J, et al. The COMT Val158 allele is associated with impaired delayed-match-to-sample performance in ADHD. Behav Brain Funct. 2012;8:25. Epub 2012/05/30. doi: 10.1186/1744-9081-8-25. PubMed PMID: 22640745; PubMed Central PMCID: PMCPMC3413539.

89. Paloyelis Y, Asherson P, Mehta MA, Faraone SV, Kuntsi J. DAT1 and COMT effects on delay discounting and trait impulsivity in male adolescents with attention deficit/hyperactivity disorder and healthy controls. Neuropsychopharmacology. 2010;35(12):2414-26. Epub 2010/08/26. doi: 10.1038/npp.2010.124. PubMed PMID: 20736997; PubMed Central PMCID: PMCPMC2955909.

90. Mazei-Robison MS, Couch RS, Shelton RC, Stein MA, Blakely RD. Sequence variation in the human dopamine transporter gene in children with attention deficit hyperactivity disorder. Neuropharmacology. 2005;49(6):724-36. Epub 2005/09/21. doi: 10.1016/j.neuropharm.2005.08.003. PubMed PMID: 16171832.

91. Mazei-Robison MS, Bowton E, Holy M, Schmudermaier M, Freissmuth M, Sitte HH, et al. Anomalous dopamine release associated with a human dopamine transporter coding variant. J Neurosci. 2008;28(28):7040-6. Epub 2008/07/11. doi: 10.1523/JNEUROSCI.0473-08.2008. PubMed PMID: 18614672; PubMed Central PMCID: PMCPMC2573963.

92. Mergy MA, Gowrishankar R, Davis GL, Jessen TN, Wright J, Stanwood GD, et al. Genetic targeting of the amphetamine and methylphenidate-sensitive dopamine transporter: on the path to an animal model of attention-deficit hyperactivity disorder. Neurochem Int. 2014;73:56-70. Epub 2013/12/18. doi: 10.1016/j.neuint.2013.11.009. PubMed PMID: 24332984; PubMed Central PMCID: PMCPMC4177817.

93. Mergy MA, Gowrishankar R, Gresch PJ, Gantz SC, Williams J, Davis GL, et al. The rare DAT coding variant Val559 perturbs DA neuron function, changes behavior, and alters in vivo responses to psychostimulants. Proc Natl Acad Sci U S A. 2014;111(44):E4779-88. Epub 2014/10/22. doi: 10.1073/pnas.1417294111. PubMed PMID: 25331903; PubMed Central PMCID: PMCPMC4226116.

94. Davis GL, Stewart A, Stanwood GD, Gowrishankar R, Hahn MK, Blakely RD. Functional coding variation in the presynaptic dopamine transporter associated with neuropsychiatric disorders drives enhanced motivation and context-dependent impulsivity in mice. Behav Brain Res. 2018;337:61-9. Epub 2017/10/02. doi: 10.1016/j.bbr.2017.09.043. PubMed PMID: 28964912; PubMed Central PMCID: PMCPMC5645257.

95. Spencer TJ, Biederman J, Madras BK, Faraone SV, Dougherty DD, Bonab AA, et al. In vivo neuroreceptor imaging in attention-deficit/hyperactivity disorder: a focus on the dopamine transporter. Biol Psychiatry. 2005;57(11):1293-300. Epub 2005/06/14. doi: 10.1016/j.biopsych.2005.03.036. PubMed PMID: 15950001.

96. Volkow ND, Wang GJ, Newcorn J, Fowler JS, Telang F, Solanto MV, et al. Brain dopamine transporter levels in treatment and drug naive adults with ADHD. Neuroimage. 2007;34(3):1182-90. Epub 2006/11/28. doi: 10.1016/j.neuroimage.2006.10.014. PubMed PMID: 17126039.

97. Spencer TJ, Biederman J, Ciccone PE, Madras BK, Dougherty DD, Bonab AA, et al. PET study examining pharmacokinetics, detection and likeability, and dopamine transporter receptor occupancy of short- and long-acting oral methylphenidate. Am J Psychiatry. 2006;163(3):387-95. Epub 2006/03/04. doi: 10.1176/appi.ajp.163.3.387. PubMed PMID: 16513858.

98. Volkow ND, Wang GJ, Kollins SH, Wigal TL, Newcorn JH, Telang F, et al. Evaluating dopamine reward pathway in ADHD: clinical implications. JAMA. 2009;302(10):1084-91. Epub 2009/09/10. doi: 10.1001/jama.2009.1308. PubMed PMID: 19738093; PubMed Central PMCID: PMCPMC2958516.

99. Kandel ER, Schwartz, J.H.1., & Jessell, T.M. . *Principles of neural science* 4th ed. New York.: McGraw-Hill, Health Professions Division; 2000.

100. Wise RA. Dopamine, learning and motivation. Nat Rev Neurosci. 2004;5(6):483-94.

101. Volkow ND, Morales M. The Brain on Drugs: From Reward to Addiction. Cell. 2015;162(4):712-25. Epub 2015/08/16. doi: 10.1016/j.cell.2015.07.046. PubMed PMID: 26276628.

102. Koob GF. Drugs of abuse: anatomy, pharmacology and function of reward pathways. Trends Pharmacol Sci. 1992;13(5):177-84. Epub 1992/05/01. PubMed PMID: 1604710.

103. Kalivas PW. The glutamate homeostasis hypothesis of addiction. Nat Rev Neurosci. 2009;10(8):561-72. Epub 2009/07/03. doi: 10.1038/nrn2515. PubMed PMID: 19571793.

104. Porrino LJ, Daunais JB, Smith HR, Nader MA. The expanding effects of cocaine: studies in a nonhuman primate model of cocaine self-administration. Neurosci Biobehav

Rev. 2004;27(8):813-20. Epub 2004/03/17. doi: 10.1016/j.neubiorev.2003.11.013. PubMed PMID: 15019430.

105. See RE, Elliott JC, Feltenstein MW. The role of dorsal vs ventral striatal pathways in cocaine-seeking behavior after prolonged abstinence in rats. Psychopharmacology (Berl). 2007;194(3):321-31. Epub 2007/06/26. doi: 10.1007/s00213-007-0850-8. PubMed PMID: 17589830.

106. Fuchs RA, Branham RK, See RE. Different neural substrates mediate cocaine seeking after abstinence versus extinction training: a critical role for the dorsolateral caudate-putamen. J Neurosci. 2006;26(13):3584-8. Epub 2006/03/31. doi: 10.1523/JNEUROSCI.5146-05.2006. PubMed PMID: 16571766; PubMed Central PMCID: PMCPMC1643847.

107. Volkow ND, Baler RD. Addiction science: Uncovering neurobiological complexity. Neuropharmacology. 2014;76 Pt B:235-49. Epub 2013/05/22. doi: 10.1016/j.neuropharm.2013.05.007. PubMed PMID: 23688927; PubMed Central PMCID: PMCPMC3818510.

108. Jablensky A. Epidemiology of schizophrenia: the global burden of disease and disability. Eur Arch Psychiatry Clin Neurosci. 2000;250(6):274-85. Epub 2001/01/12. PubMed PMID: 11153962.

109. Saha S, Chant D, Welham J, McGrath J. A systematic review of the prevalence of schizophrenia. PLoS medicine. 2005;2(5):e141. Epub 2005/05/27. doi: 10.1371/journal.pmed.0020141. PubMed PMID: 15916472; PubMed Central PMCID: PMCPMC1140952.

110. Janssen PA, Van De Westeringh C, Jageneau AH, Demoen PJ, Hermans BK, Van Daele GH, et al. Chemistry and pharmacology of CNS depressants related to 4-(4-hydroxy-phenylpiperidino)butyrophenone. I. Synthesis and screening data in mice. J Med Pharm Chem. 1959;1:281-97. Epub 1959/06/01. PubMed PMID: 14406750.

111. Carlsson A. [Theories on the models of action of antipsychotic drugs]. Tidsskr Nor Laegeforen. 1973;93(17):1298-300. Epub 1973/06/20. PubMed PMID: 4356435.

112. Granger B, Albu S. The haloperidol story. Ann Clin Psychiatry. 2005;17(3):137-40. Epub 2006/01/26. PubMed PMID: 16433054.

113. Geddes J, Freemantle N, Harrison P, Bebbington P. Atypical antipsychotics in the treatment of schizophrenia: systematic overview and meta-regression analysis. BMJ. 2000;321(7273):1371-6. Epub 2000/12/01. PubMed PMID: 11099280; PubMed Central PMCID: PMCPMC27538.

114. Carlsson A. Antipsychotic drugs and catecholamine synapses. J Psychiatr Res. 1974;11:57-64. Epub 1974/01/01. PubMed PMID: 4156791.

115. Seeman P, Lee T. Antipsychotic drugs: direct correlation between clinical potency and presynaptic action on dopamine neurons. Science. 1975;188(4194):1217-9. Epub 1975/06/20. PubMed PMID: 1145194.

116. Creese I, Burt DR, Snyder SH. Dopamine receptor binding predicts clinical and pharmacological potencies of antischizophrenic drugs. Science. 1976;192(4238):481-3. Epub 1976/04/30. PubMed PMID: 3854.

117. Mackay AV, Iversen LL, Rossor M, Spokes E, Bird E, Arregui A, et al. Increased brain dopamine and dopamine receptors in schizophrenia. Arch Gen Psychiatry. 1982;39(9):991-7. Epub 1982/09/01. PubMed PMID: 7115016.

118. Howes OD, Williams M, Ibrahim K, Leung G, Egerton A, McGuire PK, et al. Midbrain dopamine function in schizophrenia and depression: a post-mortem and positron emission tomographic imaging study. Brain. 2013;136(Pt 11):3242-51. Epub 2013/10/08. doi: 10.1093/brain/awt264. PubMed PMID: 24097339; PubMed Central PMCID: PMCPMC3808688.

119. Owens DG. Dopamine and schizophrenia. Nurs Mirror. 1978;146(5):23-6. Epub 1978/02/02. PubMed PMID: 244933.

120. Kaalund SS, Newburn EN, Ye T, Tao R, Li C, Deep-Soboslay A, et al. Contrasting changes in DRD1 and DRD2 splice variant expression in schizophrenia and affective disorders, and associations with SNPs in postmortem brain. Mol Psychiatry. 2014;19(12):1258-66. Epub 2013/12/11. doi: 10.1038/mp.2013.165. PubMed PMID: 24322206.

121. Arinami T, Gao M, Hamaguchi H, Toru M. A functional polymorphism in the promoter region of the dopamine D2 receptor gene is associated with schizophrenia. Hum Mol Genet. 1997;6(4):577-82. Epub 1997/04/01. PubMed PMID: 9097961.

122. Bergen SE, O'Dushlaine CT, Lee PH, Fanous AH, Ruderfer DM, Ripke S, et al. Genetic modifiers and subtypes in schizophrenia: investigations of age at onset, severity, sex and family history. Schizophr Res. 2014;154(1-3):48-53. Epub 2014/03/04. doi: 10.1016/j.schres.2014.01.030. PubMed PMID: 24581549; PubMed Central PMCID: PMCPMC4422643.

123. Wang M, Pei L, Fletcher PJ, Kapur S, Seeman P, Liu F. Schizophrenia, amphetamine-induced sensitized state and acute amphetamine exposure all show a common alteration: increased dopamine D2 receptor dimerization. Mol Brain. 2010;3:25. Epub 2010/09/04. doi: 10.1186/1756-6606-3-25. PubMed PMID: 20813060; PubMed Central PMCID: PMCPMC2942879.

124. Howes O, McCutcheon R, Stone J. Glutamate and dopamine in schizophrenia: an update for the 21st century. J Psychopharmacol. 2015;29(2):97-115. Epub 2015/01/15. doi: 10.1177/0269881114563634. PubMed PMID: 25586400; PubMed Central PMCID: PMCPMC4902122.

125. McGowan S, Lawrence AD, Sales T, Quested D, Grasby P. Presynaptic dopaminergic dysfunction in schizophrenia: a positron emission tomographic [18F]fluorodopa study. Arch Gen Psychiatry. 2004;61(2):134-42. Epub 2004/02/06. doi: 10.1001/archpsyc.61.2.134. PubMed PMID: 14757589.

126. Lindstrom LH, Gefvert O, Hagberg G, Lundberg T, Bergstrom M, Hartvig P, et al. Increased dopamine synthesis rate in medial prefrontal cortex and striatum in schizophrenia indicated by L-(beta-11C) DOPA and PET. Biol Psychiatry. 1999;46(5):681-8. Epub 1999/09/03. PubMed PMID: 10472420.

127. Meyer-Lindenberg A, Miletich RS, Kohn PD, Esposito G, Carson RE, Quarantelli M, et al. Reduced prefrontal activity predicts exaggerated striatal dopaminergic function in schizophrenia. Nat Neurosci. 2002;5(3):267-71. Epub 2002/02/28. doi: 10.1038/nn804. PubMed PMID: 11865311.

128. Lavalaye J, Linszen DH, Booij J, Dingemans PM, Reneman L, Habraken JB, et al. Dopamine transporter density in young patients with schizophrenia assessed with [123]FP-CIT SPECT. Schizophr Res. 2001;47(1):59-67. Epub 2001/02/13. PubMed PMID: 11163545.

129. Schmitt GJ, Frodl T, Dresel S, la Fougere C, Bottlender R, Koutsouleris N, et al. Striatal dopamine transporter availability is associated with the productive psychotic state in first episode, drug-naive schizophrenic patients. Eur Arch Psychiatry Clin Neurosci. 2006;256(2):115-21. Epub 2005/11/15. doi: 10.1007/s00406-005-0618-2. PubMed PMID: 16284713.

130. Fusar-Poli P, Meyer-Lindenberg A. Striatal presynaptic dopamine in schizophrenia, Part I: meta-analysis of dopamine active transporter (DAT) density. Schizophr Bull. 2013;39(1):22-32. Epub 2012/01/28. doi: 10.1093/schbul/sbr111. PubMed PMID: 22282456; PubMed Central PMCID: PMCPMC3523907.

131. Brunelin J, Fecteau S, Suaud-Chagny MF. Abnormal striatal dopamine transmission in schizophrenia. Curr Med Chem. 2013;20(3):397-404. Epub 2012/11/20. PubMed PMID: 23157632; PubMed Central PMCID: PMCPMC3866953.

132. Jonsson G, Einarsson P, Fuxe K, Hallman H. Microspectrofluorimetric analysis of the formaldehyde induced fluorescence in midbrain raphe neurons. Med Biol. 1975;53(1):25-39. Epub 1975/02/01. PubMed PMID: 124804.

133. Sulston J, Dew M, Brenner S. Dopaminergic neurons in the nematode Caenorhabditis elegans. J Comp Neurol. 1975;163(2):215-26. Epub 1975/09/15. doi: 10.1002/cne.901630207. PubMed PMID: 240872.

134. McDonald PW, Jessen T, Field JR, Blakely RD. Dopamine Signaling Architecture in Caenorhabditis elegans. Cell Mol Neurobiol. 2006;26(4-6):591-616.

135. Ward S, Thomson N, White JG, Brenner S. Electron microscopical reconstruction of the anterior sensory anatomy of the nematode Caenorhabditis elegans. J Comp Neurol. 1975;160(3):313-37.

136. Gray JM, Hill JJ, Bargmann CI. A circuit for navigation in Caenorhabditis elegans. Proc Natl Acad Sci U S A. 2005;102(9):3184-91. Epub 2005/02/04. doi: 10.1073/pnas.0409009101. PubMed PMID: 15689400; PubMed Central PMCID: PMCPMC546636.

137. Chalfie M, Sulston JE, White JG, Southgate E, Thomson JN, Brenner S. The neural circuit for touch sensitivity in Caenorhabditis elegans. J Neurosci. 1985;5(4):956-64. Epub 1985/04/01. PubMed PMID: 3981252.

138. Jayanthi LD, Apparsundaram S, Malone MD, Ward E, Miller DM, Eppler M, et al. The Caenorhabditis elegans gene T23G5.5 encodes an antidepressant- and cocaine-sensitive dopamine transporter. Mol Pharmacol. 1998;54(4):601-9.

139. Altun ZFH, D.H. Nervous system, neuronal support cells. *WormAtlas*. 2010. doi: 10.3908/wormatlas.1.19.

140. Shaham S. Glial development and function in the nervous system of Caenorhabditis elegans. Cold Spring Harb Perspect Biol. 2015;7(4):a020578. Epub 2015/01/13. doi: 10.1101/cshperspect.a020578. PubMed PMID: 25573712; PubMed Central PMCID: PMCPMC4382739.

141. Bargmann CI, Avery L. Laser killing of cells in Caenorhabditis elegans. Methods Cell Biol. 1995;48:225-50. Epub 1995/01/01. PubMed PMID: 8531727; PubMed Central PMCID: PMCPMC4442485.

142. Yoshimura S, Murray JI, Lu Y, Waterston RH, Shaham S. mls-2 and vab-3 Control glia development, hlh-17/Olig expression and glia-dependent neurite extension in C. elegans. Development. 2008;135(13):2263-75. Epub 2008/05/30. doi: 10.1242/dev.019547. PubMed PMID: 18508862.

143. McMiller TL, Johnson CM. Molecular characterization of HLH-17, a C. elegans bHLH protein required for normal larval development. Gene. 2005;356:1-10. Epub 2005/07/15. doi: 10.1016/j.gene.2005.05.003. PubMed PMID: 16014321; PubMed Central PMCID: PMCPMC2040385.

144. Felton CM, Johnson CM. Modulation of dopamine-dependent behaviors by the Caenorhabditis elegans Olig homolog HLH-17. J Neurosci Res. 2011;89(10):1627-36. Epub 2011/06/21. doi: 10.1002/jnr.22694. PubMed PMID: 21688290.

145. Stout RF, Jr., Verkhratsky A, Parpura V. Caenorhabditis elegans glia modulate neuronal activity and behavior. Front Cell Neurosci. 2014;8:67. Epub 2014/03/29. doi: 10.3389/fncel.2014.00067. PubMed PMID: 24672428; PubMed Central PMCID: PMCPMC3954127.

146. Hardaway JA, Sturgeon SM, Snarrenberg CL, Li Z, Xu XZ, Bermingham DP, et al. Glial Expression of the Caenorhabditis elegans Gene swip-10 Supports Glutamate Dependent Control of Extrasynaptic Dopamine Signaling. J Neurosci. 2015;35(25):9409-23. doi: 10.1523/JNEUROSCI.0800-15.2015. PubMed PMID: 26109664; PubMed Central PMCID: PMC4478255.

147. Wang Y, Apicella A, Jr., Lee SK, Ezcurra M, Slone RD, Goldmit M, et al. A glial DEG/ENaC channel functions with neuronal channel DEG-1 to mediate specific sensory functions in C. elegans. EMBO J. 2008;27(18):2388-99. Epub 2008/08/15. doi: 10.1038/emboj.2008.161. PubMed PMID: 18701922; PubMed Central PMCID: PMCPMC2543049.

148. Wang Y, D'Urso G, Bianchi L. Knockout of glial channel ACD-1 exacerbates sensory deficits in a C. elegans mutant by regulating calcium levels of sensory neurons. J Neurophysiol. 2012;107(1):148-58. Epub 2011/10/14. doi: 10.1152/jn.00299.2011. PubMed PMID: 21994266; PubMed Central PMCID: PMCPMC3349695.

149. Han L, Wang Y, Sangaletti R, D'Urso G, Lu Y, Shaham S, et al. Two novel DEG/ENaC channel subunits expressed in glia are needed for nose-touch sensitivity in Caenorhabditis elegans. J Neurosci. 2013;33(3):936-49. Epub 2013/01/18. doi: 10.1523/JNEUROSCI.2749-12.2013. PubMed PMID: 23325233; PubMed Central PMCID: PMCPMC3711640.

150. Grant J, Matthewman C, Bianchi L. A Novel Mechanism of pH Buffering in C. elegans Glia: Bicarbonate Transport via the Voltage-Gated ClC Cl- Channel CLH-1. J Neurosci. 2015;35(50):16377-97. Epub 2015/12/18. doi: 10.1523/JNEUROSCI.3237-15.2015. PubMed PMID: 26674864; PubMed Central PMCID: PMCPMC4679820.

151. Duerr JS, Frisby DL, Gaskin J, Duke A, Asermely K, Huddleston D, et al. The *cat-1* gene of Caenorhabditis elegans encodes a vesicular monoamine transporter required for specific monoamine-dependent behaviors. J Neurosci. 1999;19(1):72-84.

152. Lints R, Emmons SW. Patterning of dopaminergic neurotransmitter identity among Caenorhabditis elegans ray sensory neurons by a TGFbeta family signaling pathway and a Hox gene. Development. 1999;126(24):5819-31. Epub 1999/11/26. PubMed PMID: 10572056.

153. Hare EE, Loer CM. Function and evolution of the serotonin-synthetic bas-1 gene and other aromatic amino acid decarboxylase genes in Caenorhabditis. BMC Neurosci. 2004;5(1):26.

154. Sawin ER, Ranganathan R, Horvitz HR. *C. elegans* locomotory rate is modulated by the environment through a dopaminergic pathway and by experience through a serotonergic pathway. Neuron. 2000;26(3):619-31.

155. Wintle RF, Van Tol HHM. Dopamine signaling in Caenorhabditis elegans - potential for parkinsonism research. Parkinsonism and Related Disorders. 2001;7:177-83.

156. Nass R, Hahn MK, Jessen T, McDonald PW, Carvelli L, Blakely RD. A genetic screen in Caenorhabditis elegans for dopamine neuron insensitivity to 6-hydroxydopamine identifies dopamine transporter mutants impacting transporter biosynthesis and trafficking. J Neurochem. 2005;94(3):774-85.

157. Cao S, Gelwix CC, Caldwell KA, Caldwell GA. Torsin-mediated protection from cellular stress in the dopaminergic neurons of Caenorhabditis elegans. J Neurosci. 2005;25(15):3801-12.

158. Flames N, Hobert O. Gene regulatory logic of dopamine neuron differentiation. Nature. 2009;458(7240):885-9. Epub 2009/03/17. doi: nature07929 [pii] 10.1038/nature07929. PubMed Central PMCID: PMC2671564.

159. Reckziegel P, Chen P, Caito S, Gubert P, Soares FA, Fachinetto R, et al. Extracellular dopamine and alterations on dopamine transporter are related to reserpine toxicity in Caenorhabditis elegans. Archives of toxicology. 2016;90(3):633-45. Epub 2015/01/13. doi: 10.1007/s00204-015-1451-7. PubMed PMID: 25579234.

160. Nass R, Blakely RD. The Caenorhabditis elegans dopaminergic system: opportunities for insights into dopamine transport and neurodegeneration. Annu Rev Pharmacol & Toxicol. 2003;43:521-44.

161. Suo S, Sasagawa N, Ishiura S. Identification of a dopamine receptor from Caenorhabditis elegans. Neurosci Lett. 2002;319(1):13-6.

162. Chase DL, Pepper JS, Koelle MR. Mechanism of extrasynaptic dopamine signaling in Caenorhabditis elegans. Nat Neurosci. 2004;7(10):1096-103.

163. Sugiura M, Fuke S, Suo S, Sasagawa N, Van Tol HH, Ishiura S. Characterization of a novel D2-like dopamine receptor with a truncated splice variant and a D1-like dopamine receptor unique to invertebrates from Caenorhabditis elegans. J Neurochem. 2005;94(4):1146-57.

164. Smith CJ, Watson JD, Spencer WC, O'Brien T, Cha B, Albeg A, et al. Time-lapse imaging and cell-specific expression profiling reveal dynamic branching and molecular determinants of a multi-dendritic nociceptor in C. elegans. Dev Biol. 2010;345(1):18-33. Epub 2010/06/12. doi: 10.1016/j.ydbio.2010.05.502. PubMed PMID: 20537990; PubMed Central PMCID: PMCPMC2919608.

165. Chase DL, Koelle MR. Biogenic amine neurotransmitters in C. elegans. WormBook. 2007:1-15. Epub 2007/12/01. doi: 10.1895/wormbook.1.132.1.

166. Horvitz HR, Chalfie M, Trent C, Sulston JE, Evans PD. Serotonin and octopamine in the nematode Caenorhabditis elegans. Science. 1982;216(4549):1012-4.

167. Schafer WR, Kenyon CJ. A calcium-channel homologue required for adaptation to dopamine and serotonin in *Caenorhabditis elegans*. Nature. 1995;375:73-8.

168. Calahorro F, Ruiz-Rubio M. Functional phenotypic rescue of Caenorhabditis elegans neuroligin-deficient mutants by the human and rat NLGN1 genes. PLoS One. 2012;7(6):e39277. Epub 2012/06/23. doi: 10.1371/journal.pone.0039277. PubMed PMID: 22723984; PubMed Central PMCID: PMCPMC3377638.

169. Rodriguez-Ramos A, Gamez-Del-Estal MM, Porta-de-la-Riva M, Ceron J, Ruiz-Rubio M. Impaired Dopamine-Dependent Locomotory Behavior of C. elegans Neuroligin Mutants Depends on the Catechol-O-Methyltransferase COMT-4. Behav Genet. 2017;47(6):596-608. Epub 2017/09/08. doi: 10.1007/s10519-017-9868-9. PubMed PMID: 28879499.

170. Hills T, Brockie PJ, Maricq AV. Dopamine and glutamate control area-restricted search behavior in Caenorhabditis elegans. J Neurosci. 2004;24(5):1217-25. Epub 2004/02/06. doi: 10.1523/JNEUROSCI.1569-03.2004
24/5/1217 [pii].

171. Kindt KS, Quast KB, Giles AC, De S, Hendrey D, Nicastro I, et al. Dopamine mediates context-dependent modulation of sensory plasticity in C. elegans. Neuron. 2007;55(4):662-76. Epub 2007/08/19. doi: S0896-6273(07)00544-2 [pii]
10.1016/j.neuron.2007.07.023.

172. Rankin CH, Wicks SR. Mutations of the caenorhabditis elegans brain-specific inorganic phosphate transporter eat-4 affect habituation of the tap-withdrawal response without affecting the response itself. J Neurosci. 2000;20(11):4337-44.

173. Rose JK, Kaun KR, Rankin CH. A new group-training procedure for habituation demonstrates that presynaptic glutamate release contributes to long-term memory in Caenorhabditis elegans. Learn Mem. 2002;9(3):130-7. Epub 2002/06/21. doi: 10.1101/lm.46802. PubMed PMID: 12075001; PubMed Central PMCID: PMCPMC182588.

174. Rose JK, Kaun KR, Chen SH, Rankin CH. GLR-1, a non-NMDA glutamate receptor homolog, is critical for long-term memory in Caenorhabditis elegans. J Neurosci. 2003;23(29):9595-9. Epub 2003/10/24. PubMed PMID: 14573539.

175. Giles AC, Rankin CH. Behavioral and genetic characterization of habituation using Caenorhabditis elegans. Neurobiol Learn Mem. 2009;92(2):139-46. Epub 2008/09/06. doi: 10.1016/j.nlm.2008.08.004. PubMed PMID: 18771741.

176. Matthies DS, Fleming PA, Wilkes DM, Blakely RD. The Caenorhabditis elegans choline transporter CHO-1 sustains acetylcholine synthesis and motor function in an activity-dependent manner. J Neurosci. 2006;26(23):6200-12. Epub 2006/06/10. doi: 10.1523/JNEUROSCI.5036-05.2006. PubMed PMID: 16763028.

177. McDonald PW, Hardie SL, Jessen TN, Carvelli L, Matthies DS, Blakely RD. Vigorous motor activity in Caenorhabditis elegans requires efficient clearance of dopamine mediated by synaptic localization of the dopamine transporter DAT-1. J Neurosci. 2007;27(51):14216-27.

178. Vidal-Gadea A, Topper S, Young L, Crisp A, Kressin L, Elbel E, et al. Caenorhabditis elegans selects distinct crawling and swimming gaits via dopamine and serotonin. Proc Natl Acad Sci U S A. 2011. Epub 2011/10/05. doi: 1108673108 [pii] 10.1073/pnas.1108673108.

179. Brenner S. The genetics of *Caenorhabditis elegans*. Genetics. 1974;77:71-94.

180. Hardaway JA, Hardie SL, Whitaker SM, Baas SR, Zhang B, Bermingham DP, et al. Forward genetic analysis to identify determinants of dopamine signaling in Caenorhabditis elegans using swimming-induced paralysis. . G3 (Bethesda). 2012;2(8):961-75. Epub 2012/08/22. doi: 10.1534/g3.112.003533 GGG_003533 [pii]. PubMed Central PMCID: PMC3411251.

181. Bebrone C. Metallo-beta-lactamases (classification, activity, genetic organization, structure, zinc coordination) and their superfamily. Biochem Pharmacol. 2007;74(12):1686-701. doi: 10.1016/j.bcp.2007.05.021. PubMed PMID: 17597585.

182. Retzlaff CL, Kussrow A, Schorkopf TD, Saetear P, Bornhop DJ, Hardaway JA, et al. Metallo-beta-lactamase Domain-containing Protein 1 (MBLAC1) is a Specific, High-Affinity Target for the Glutamate Transporter Inducer Ceftriaxone. ACS Chem Neurosci. 2017. Epub 2017/08/09. doi: 10.1021/acschemneuro.7b00232. PubMed PMID: 28783953.

183. Brosnan ME, Brosnan JT. Hepatic glutamate metabolism: a tale of 2 hepatocytes. Am J Clin Nutr. 2009;90(3):857S-61S. Epub 2009/07/25. doi: 10.3945/ajcn.2009.27462Z. PubMed PMID: 19625684.

184. Gecz J. Glutamate receptors and learning and memory. Nat Genet. 2010;42(11):925-6. Epub 2010/10/29. doi: 10.1038/ng1110-925. PubMed PMID: 20980986.

185. Brosnan JT, Brosnan ME. Glutamate: a truly functional amino acid. Amino acids. 2013;45(3):413-8. Epub 2012/04/25. doi: 10.1007/s00726-012-1280-4. PubMed PMID: 22526238.

186. Walker MC, van der Donk WA. The many roles of glutamate in metabolism. Journal of industrial microbiology & biotechnology. 2016;43(2-3):419-30. Epub 2015/09/02. doi: 10.1007/s10295-015-1665-y. PubMed PMID: 26323613; PubMed Central PMCID: PMCPMC4753154.

187. Krebs HA. Metabolism of amino-acids: The synthesis of glutamine from glutamic acid and ammonia, and the enzymic hydrolysis of glutamine in animal tissues. Biochem J. 1935;29(8):1951-69. Epub 1935/08/01. PubMed PMID: 16745865; PubMed Central PMCID: PMCPMC1266709.

188. Kew JN, Kemp JA. Ionotropic and metabotropic glutamate receptor structure and pharmacology. Psychopharmacology (Berl). 2005;179(1):4-29. Epub 2005/02/26. doi: 10.1007/s00213-005-2200-z. PubMed PMID: 15731895.

189. Vaidya A, Jain S, Jain AK, Agrawal A, Kashaw SK, Jain SK, et al. Metabotropic glutamate receptors: a review on prospectives and therapeutic aspects. Mini Rev Med Chem. 2013;13(13):1967-81. Epub 2012/04/26. PubMed PMID: 22530579.

190. Rondard P, Pin JP. Dynamics and modulation of metabotropic glutamate receptors. Curr Opin Pharmacol. 2015;20:95-101. Epub 2014/12/23. doi: 10.1016/j.coph.2014.12.001. PubMed PMID: 25529199.

191. Vincent P, Mulle C. Kainate receptors in epilepsy and excitotoxicity. Neuroscience. 2009;158(1):309-23. Epub 2008/04/11. doi: 10.1016/j.neuroscience.2008.02.066. PubMed PMID: 18400404.

192. Chang PK, Verbich D, McKinney RA. AMPA receptors as drug targets in neurological disease--advantages, caveats, and future outlook. Eur J Neurosci. 2012;35(12):1908-16. Epub 2012/06/20. doi: 10.1111/j.1460-9568.2012.08165.x. PubMed PMID: 22708602.

193. Vyklicky V, Korinek M, Smejkalova T, Balik A, Krausova B, Kaniakova M, et al. Structure, function, and pharmacology of NMDA receptor channels. Physiol Res. 2014;63 Suppl 1:S191-203. Epub 2014/02/26. PubMed PMID: 24564659.

194. Bonaccorso C, Micale N, Ettari R, Grasso S, Zappala M. Glutamate binding-site ligands of NMDA receptors. Curr Med Chem. 2011;18(36):5483-506. Epub 2011/12/17. PubMed PMID: 22172060.

195. Gonda X. Basic pharmacology of NMDA receptors. Curr Pharm Des. 2012;18(12):1558-67. Epub 2012/01/28. PubMed PMID: 22280436.

196. Rogawski MA. AMPA receptors as a molecular target in epilepsy therapy. Acta Neurol Scand Suppl. 2013;(197):9-18. Epub 2013/03/27. doi: 10.1111/ane.12099. PubMed PMID: 23480151; PubMed Central PMCID: PMCPMC4506648.

197. Jane DE, Lodge D, Collingridge GL. Kainate receptors: pharmacology, function and therapeutic potential. Neuropharmacology. 2009;56(1):90-113. Epub 2008/09/17. doi: 10.1016/j.neuropharm.2008.08.023. PubMed PMID: 18793656.

198. Lerma J, Marques JM. Kainate receptors in health and disease. Neuron. 2013;80(2):292-311. Epub 2013/10/22. doi: 10.1016/j.neuron.2013.09.045. PubMed PMID: 24139035.

199. Olney JW. Brain lesions, obesity, and other disturbances in mice treated with monosodium glutamate. Science. 1969;164(3880):719-21. Epub 1969/05/09. PubMed PMID: 5778021.

200. Hasan A, Malchow B, Falkai P, Schmitt A. [The glutamate hypothesis of schizophrenia]. Fortschr Neurol Psychiatr. 2014;82(8):447-56. Epub 2014/08/12. doi: 10.1055/s-0034-1366571. PubMed PMID: 25105431.

201. Shen HW, Scofield MD, Boger H, Hensley M, Kalivas PW. Synaptic glutamate spillover due to impaired glutamate uptake mediates heroin relapse. J Neurosci. 2014;34(16):5649-57. Epub 2014/04/18. doi: 10.1523/JNEUROSCI.4564-13.2014 34/16/5649 [pii]. PubMed Central PMCID: PMC3988415.

202. Rothstein JD, Patel S, Regan MR, Haenggeli C, Huang YH, Bergles DE, et al. Beta-lactam antibiotics offer neuroprotection by increasing glutamate transporter expression. Nature. 2005;433:73-7.

203. Lange KW, Kornhuber J, Riederer P. Dopamine/glutamate interactions in Parkinson's disease. Neurosci Biobehav Rev. 1997;21(4):393-400. Epub 1997/07/01. PubMed PMID: 9195597.

204. Lai TW, Zhang S, Wang YT. Excitotoxicity and stroke: identifying novel targets for neuroprotection. Prog Neurobiol. 2014;115:157-88. Epub 2013/12/24. doi: 10.1016/j.pneurobio.2013.11.006. PubMed PMID: 24361499.

205. Noch E, Khalili K. Molecular mechanisms of necrosis in glioblastoma: the role of glutamate excitotoxicity. Cancer biology & therapy. 2009;8(19):1791-7. Epub 2009/09/23. PubMed PMID: 19770591; PubMed Central PMCID: PMCPMC4503249.

206. Olney JW, Sharpe LG. Brain lesions in an infant rhesus monkey treated with monsodium glutamate. Science. 1969;166(3903):386-8. Epub 1969/10/17. PubMed PMID: 5812037.

207. Olney JW. Inciting excitotoxic cytocide among central neurons. Adv Exp Med Biol. 1986;203:631-45. Epub 1986/01/01. PubMed PMID: 3024464.

208. Meldrum B, Garthwaite J. Excitatory amino acid neurotoxicity and neurodegenerative disease. Trends Pharmacol Sci. 1990;11(9):379-87. Epub 1990/09/01. PubMed PMID: 2238094.

209. Choi DW. Excitotoxic cell death. J Neurobiol. 1992;23(9):1261-76. Epub 1992/11/01. doi: 10.1002/neu.480230915. PubMed PMID: 1361523.

210. Kumar A, Singh RL, Babu GN. Cell death mechanisms in the early stages of acute glutamate neurotoxicity. Neurosci Res. 2010;66(3):271-8. Epub 2009/12/01. doi: 10.1016/j.neures.2009.11.009. PubMed PMID: 19944120.

211. Rothstein JD, Jin L, Dykes-Hoberg M, Kuncl RW. Chronic inhibition of glutamate uptake produces a model of slow neurotoxicity. Proc Natl Acad Sci U S A. 1993;90(14):6591-5. Epub 1993/07/15. PubMed PMID: 8393571; PubMed Central PMCID: PMCPMC46978.

212. Bao X, Pal R, Hascup KN, Wang Y, Wang WT, Xu W, et al. Transgenic expression of Glud1 (glutamate dehydrogenase 1) in neurons: in vivo model of enhanced glutamate release, altered synaptic plasticity, and selective neuronal vulnerability. J Neurosci.

2009;29(44):13929-44. Epub 2009/11/06. doi: 10.1523/JNEUROSCI.4413-09.2009. PubMed PMID: 19890003; PubMed Central PMCID: PMCPMC2811066.

213. Ha JS, Lee CS, Maeng JS, Kwon KS, Park SS. Chronic glutamate toxicity in mouse cortical neuron culture. Brain Res. 2009;1273:138-43. Epub 2009/04/07. doi: 10.1016/j.brainres.2009.03.050. PubMed PMID: 19344697.

214. Cao G, Xing J, Xiao X, Liou AK, Gao Y, Yin XM, et al. Critical role of calpain I in mitochondrial release of apoptosis-inducing factor in ischemic neuronal injury. J Neurosci. 2007;27(35):9278-93. Epub 2007/08/31. doi: 10.1523/JNEUROSCI.2826-07.2007. PubMed PMID: 17728442.

215. Bonfoco E, Krainc D, Ankarcrona M, Nicotera P, Lipton SA. Apoptosis and necrosis: two distinct events induced, respectively, by mild and intense insults with N-methyl-D-aspartate or nitric oxide/superoxide in cortical cell cultures. Proc Natl Acad Sci U S A. 1995;92(16):7162-6. Epub 1995/08/01. PubMed PMID: 7638161; PubMed Central PMCID: PMCPMC41299.

216. Portera-Cailliau C, Price DL, Martin LJ. Non-NMDA and NMDA receptor-mediated excitotoxic neuronal deaths in adult brain are morphologically distinct: further evidence for an apoptosis-necrosis continuum. J Comp Neurol. 1997;378(1):88-104. Epub 1997/02/03. PubMed PMID: 9120056.

217. Anilkumar U, Weisova P, Schmid J, Bernas T, Huber HJ, Dussmann H, et al. Defining external factors that determine neuronal survival, apoptosis and necrosis during excitotoxic injury using a high content screening imaging platform. PLoS One. 2017;12(11):e0188343. Epub 2017/11/18. doi: 10.1371/journal.pone.0188343. PubMed PMID: 29145487; PubMed Central PMCID: PMCPMC5690623.

218. Nikoletopoulou V, Markaki M, Palikaras K, Tavernarakis N. Crosstalk between apoptosis, necrosis and autophagy. Biochim Biophys Acta. 2013;1833(12):3448-59. Epub 2013/06/19. doi: 10.1016/j.bbamcr.2013.06.001. PubMed PMID: 23770045.

219. Marini AM, Ueda Y, June CH. Intracellular survival pathways against glutamate receptor agonist excitotoxicity in cultured neurons. Intracellular calcium responses. Ann N Y Acad Sci. 1999;890:421-37. Epub 2000/02/11. PubMed PMID: 10668447.

220. Choi DW. Glutamate neurotoxicity in cortical cell culture is calcium dependent. Neurosci Lett. 1985;58(3):293-7. Epub 1985/08/05. PubMed PMID: 2413399.

221. Choi DW. Ionic dependence of glutamate neurotoxicity. J Neurosci. 1987;7(2):369-79. Epub 1987/02/01. PubMed PMID: 2880938.

222. Matthewman C, Miller-Fleming TW, Miller DMR, Bianchi L. Ca2+ permeability and Na+ conductance in cellular toxicity caused by hyperactive DEG/ENaC channels. Am J Physiol Cell Physiol. 2016;311(6):C920-C30. Epub 2016/10/21. doi: 10.1152/ajpcell.00247.2016. PubMed PMID: 27760755; PubMed Central PMCID: PMCPMC5206307.

223. Wang Y, Matthewman C, Han L, Miller T, Miller DM, 3rd, Bianchi L. Neurotoxic unc-8 mutants encode constitutively active DEG/ENaC channels that are blocked by divalent cations. J Gen Physiol. 2013;142(2):157-69. Epub 2013/07/31. doi: 10.1085/jgp.201310974. PubMed PMID: 23898007; PubMed Central PMCID: PMCPMC3727304.

224. Wang HG, Pathan N, Ethell IM, Krajewski S, Yamaguchi Y, Shibasaki F, et al. Ca2+-induced apoptosis through calcineurin dephosphorylation of BAD. Science. 1999;284(5412):339-43. Epub 1999/04/09. PubMed PMID: 10195903.

225. Brustovetsky T, Bolshakov A, Brustovetsky N. Calpain activation and Na+/Ca2+ exchanger degradation occur downstream of calcium deregulation in hippocampal neurons exposed to excitotoxic glutamate. J Neurosci Res. 2010;88(6):1317-28. Epub 2009/11/26. doi: 10.1002/jnr.22295. PubMed PMID: 19937813; PubMed Central PMCID: PMCPMC2830319.

226. Syntichaki P, Xu K, Driscoll M, Tavernarakis N. Specific aspartyl and calpain proteases are required for neurodegeneration in C. elegans. Nature. 2002;419(6910):939-44. Epub 2002/11/01. doi: 10.1038/nature01108. PubMed PMID: 12410314.

227. Gold M, Koczulla AR, Mengel D, Koepke J, Dodel R, Dontcheva G, et al. Reduction of glutamate-induced excitotoxicity in murine primary neurons involving calpain inhibition. J Neurol Sci. 2015;359(1-2):356-62. Epub 2015/12/17. doi: 10.1016/j.jns.2015.11.016. PubMed PMID: 26671142.

228. Nicholls DG. Mitochondrial dysfunction and glutamate excitotoxicity studied in primary neuronal cultures. Curr Mol Med. 2004;4(2):149-77. Epub 2004/03/23. PubMed PMID: 15032711.

229. Dong XX, Wang Y, Qin ZH. Molecular mechanisms of excitotoxicity and their relevance to pathogenesis of neurodegenerative diseases. Acta Pharmacol Sin. 2009;30(4):379-87. Epub 2009/04/04. doi: 10.1038/aps.2009.24. PubMed PMID: 19343058; PubMed Central PMCID: PMCPMC4002277.

230. Sokka AL, Putkonen N, Mudo G, Pryazhnikov E, Reijonen S, Khiroug L, et al. Endoplasmic reticulum stress inhibition protects against excitotoxic neuronal injury in the rat brain. J Neurosci. 2007;27(4):901-8. Epub 2007/01/26. doi: 10.1523/JNEUROSCI.4289-06.2007. PubMed PMID: 17251432.

231. Dykens JA. Isolated cerebral and cerebellar mitochondria produce free radicals when exposed to elevated CA2+ and Na+: implications for neurodegeneration. J Neurochem. 1994;63(2):584-91. Epub 1994/08/01. PubMed PMID: 8035183.

232. Tenneti L, Lipton SA. Involvement of activated caspase-3-like proteases in N-methyl-D-aspartate-induced apoptosis in cerebrocortical neurons. J Neurochem. 2000;74(1):134-42. Epub 2000/01/05. PubMed PMID: 10617114.

233. Young KW, Pinon LG, Bampton ET, Nicotera P. Different pathways lead to mitochondrial fragmentation during apoptotic and excitotoxic cell death in primary neurons. J Biochem Mol Toxicol. 2010;24(5):335-41. Epub 2010/03/05. doi: 10.1002/jbt.20343. PubMed PMID: 20201108.

234. Vernadakis A. Glia-neuron intercommunications and synaptic plasticity. Prog Neurobiol. 1996;49(3):185-214. Epub 1996/06/01. PubMed PMID: 8878303.

235. Kasischke KA. A new pathway for lactate production in the CNS. J Physiol. 2008;586(5):1207-8. Epub 2008/03/04. doi: 10.1113/jphysiol.2008.151373. PubMed PMID: 18310130; PubMed Central PMCID: PMCPMC2375671.

236. Allaman I, Belanger M, Magistretti PJ. Astrocyte-neuron metabolic relationships: for better and for worse. Trends Neurosci. 2011;34(2):76-87. Epub 2011/01/18. doi: 10.1016/j.tins.2010.12.001. PubMed PMID: 21236501.

237. Machler P, Wyss MT, Elsayed M, Stobart J, Gutierrez R, von Faber-Castell A, et al. In Vivo Evidence for a Lactate Gradient from Astrocytes to Neurons. Cell Metab. 2016;23(1):94-102. Epub 2015/12/25. doi: 10.1016/j.cmet.2015.10.010. PubMed PMID: 26698914.

238. Walz W. Role of astrocytes in the clearance of excess extracellular potassium. Neurochem Int. 2000;36(4-5):291-300. Epub 2000/03/25. PubMed PMID: 10732996.

239. Kofuji P, Newman EA. Potassium buffering in the central nervous system. Neuroscience. 2004;129(4):1045-56. Epub 2004/11/25. doi: 10.1016/j.neuroscience.2004.06.008. PubMed PMID: 15561419; PubMed Central PMCID: PMCPMC2322935.

240. Rothstein JD, Dykes-Hoberg M, Pardo CA, Bristol LA, Jin L, Kuncl RW, et al. Knockout of glutamate transporters reveals a major role for astroglial transport in excitotoxicity and clearance of glutamate. Neuron. 1996;16(3):675-86. Epub 1996/03/01. PubMed PMID: 8785064.

241. Danbolt NC. Glutamate uptake. Prog Neurobiol. 2001;65(1):1-105. Epub 2001/05/23. PubMed PMID: 11369436.

242. Sims KD, Robinson MB. Expression patterns and regulation of glutamate transporters in the developing and adult nervous system. Crit Rev Neurobiol. 1999;13(2):169-97. Epub 1999/10/08. PubMed PMID: 10512489.

243. Danbolt NC, Pines G, Kanner BI. Purification and reconstitution of the sodium- and potassium-coupled glutamate transport glycoprotein from rat brain. Biochemistry. 1990;29(28):6734-40. Epub 1990/07/17. PubMed PMID: 1697765.

244. Danbolt NC, Storm-Mathisen J, Kanner BI. An [Na+ + K+]coupled L-glutamate transporter purified from rat brain is located in glial cell processes. Neuroscience. 1992;51(2):295-310. Epub 1992/11/01. PubMed PMID: 1465194.

245. Levy LM, Lehre KP, Rolstad B, Danbolt NC. A monoclonal antibody raised against an [Na(+)+K+]coupled L-glutamate transporter purified from rat brain confirms glial cell localization. FEBS Lett. 1993;317(1-2):79-84. Epub 1993/02/08. PubMed PMID: 7679083.

246. Pines G, Danbolt NC, Bjoras M, Zhang Y, Bendahan A, Eide L, et al. Cloning and expression of a rat brain L-glutamate transporter. Nature. 1992;360(6403):464-7. Epub 1992/12/03. doi: 10.1038/360464a0. PubMed PMID: 1448170.

247. Storck T, Schulte S, Hofmann K, Stoffel W. Structure, expression, and functional analysis of a Na(+)-dependent glutamate/aspartate transporter from rat brain. Proc Natl Acad Sci U S A. 1992;89(22):10955-9. Epub 1992/11/15. PubMed PMID: 1279699; PubMed Central PMCID: PMCPMC50461.

248. Kanai Y, Hediger MA. Primary structure and functional characterization of a high-affinity glutamate transporter. Nature. 1992;360(6403):467-71. Epub 1992/12/03. doi: 10.1038/360467a0. PubMed PMID: 1280334.

249. Perego C, Vanoni C, Bossi M, Massari S, Basudev H, Longhi R, et al. The GLT-1 and GLAST glutamate transporters are expressed on morphologically distinct astrocytes and regulated by neuronal activity in primary hippocampal cocultures. J Neurochem. 2000;75(3):1076-84. Epub 2000/08/11. PubMed PMID: 10936189.

250. Arriza JL, Fairman WA, Wadiche JI, Murdoch GH, Kavanaugh MP, Amara SG. Functional comparisons of three glutamate transporter subtypes cloned from human motor cortex. J Neurosci. 1994;14(9):5559-69. Epub 1994/09/01. PubMed PMID: 7521911.

251. Kim K, Lee SG, Kegelman TP, Su ZZ, Das SK, Dash R, et al. Role of excitatory amino acid transporter-2 (EAAT2) and glutamate in neurodegeneration: opportunities for developing novel therapeutics. J Cell Physiol. 2011;226(10):2484-93. Epub 2011/07/28. doi: 10.1002/jcp.22609. PubMed PMID: 21792905; PubMed Central PMCID: PMCPMC3130100.

252. Fairman WA, Vandenberg RJ, Arriza JL, Kavanaugh MP, Amara SG. An excitatory amino-acid transporter with properties of a ligand-gated chloride channel. Nature. 1995;375(6532):599-603. Epub 1995/06/15. doi: 10.1038/375599a0. PubMed PMID: 7791878.

253. Hu WH, Walters WM, Xia XM, Karmally SA, Bethea JR. Neuronal glutamate transporter EAAT4 is expressed in astrocytes. Glia. 2003;44(1):13-25. Epub 2003/09/03. doi: 10.1002/glia.10268. PubMed PMID: 12951653.

254. Arriza JL, Eliasof S, Kavanaugh MP, Amara SG. Excitatory amino acid transporter 5, a retinal glutamate transporter coupled to a chloride conductance. Proc Natl Acad Sci U S A. 1997;94(8):4155-60. Epub 1997/04/15. PubMed PMID: 9108121; PubMed Central PMCID: PMCPMC20584.

255. Bridges R, Lutgen V, Lobner D, Baker DA. Thinking outside the cleft to understand synaptic activity: contribution of the cystine-glutamate antiporter (System xc-) to normal and pathological glutamatergic signaling. Pharmacol Rev. 2012;64(3):780-802. Epub 2012/07/05. doi: 10.1124/pr.110.003889
64/3/780 [pii]. PubMed Central PMCID: PMC3400835.

256. Seki Y, Feustel PJ, Keller RW, Jr., Tranmer BI, Kimelberg HK. Inhibition of ischemia-induced glutamate release in rat striatum by dihydrokinate and an anion channel blocker. Stroke. 1999;30(2):433-40. Epub 1999/02/05. PubMed PMID: 9933284.

257. Scofield MD, Kalivas PW. Astrocytic dysfunction and addiction: consequences of impaired glutamate homeostasis. Neuroscientist. 2014;20(6):610-22. doi: 10.1177/1073858413520347. PubMed PMID: 24496610.

258. Rothstein JD, Martin LJ, Kuncl RW. Decreased glutamate transport by the brain and spinal cord in amyotrophic lateral sclerosis. The New England Journal of Medicine. 1992;326:1464-8.

259. Massie A, Goursaud S, Schallier A, Vermoesen K, Meshul CK, Hermans E, et al. Time-dependent changes in GLT-1 functioning in striatum of hemi-Parkinson rats. Neurochem Int. 2010;57(5):572-8. Epub 2010/07/21. doi: 10.1016/j.neuint.2010.07.004. PubMed PMID: 20643175.

260. Bannai S, Kitamura E. Transport interaction of L-cystine and L-glutamate in human diploid fibroblasts in culture. J Biol Chem. 1980;255(6):2372-6. Epub 1980/03/25. PubMed PMID: 7358676.

261. Bannai S. Exchange of cystine and glutamate across plasma membrane of human fibroblasts. J Biol Chem. 1986;261(5):2256-63. Epub 1986/02/15. PubMed PMID: 2868011.

262. Sato H, Tamba M, Ishii T, Bannai S. Cloning and expression of a plasma membrane cystine/glutamate exchange transporter composed of two distinct proteins. J Biol Chem. 1999;274(17):11455-8. Epub 1999/04/17. PubMed PMID: 10206947.

263. Burdo J, Dargusch R, Schubert D. Distribution of the cystine/glutamate antiporter system xc- in the brain, kidney, and duodenum. J Histochem Cytochem. 2006;54(5):549-57. Epub 2006/01/10. doi: 10.1369/jhc.5A6840.2006. PubMed PMID: 16399997.

264. Sontheimer H. Ion channels and amino acid transporters support the growth and invasion of primary brain tumors. Mol Neurobiol. 2004;29(1):61-71. Epub 2004/03/23. doi: 10.1385/MN:29:1:61. PubMed PMID: 15034223; PubMed Central PMCID: PMCPMC2548410.

265. Moran MM, Melendez R, Baker D, Kalivas PW, Seamans JK. Cystine/glutamate antiporter regulation of vesicular glutamate release. Ann N Y Acad Sci. 2003;1003:445-7. Epub 2003/12/20. PubMed PMID: 14684484.

266. Malarkey EB, Parpura V. Mechanisms of glutamate release from astrocytes. Neurochem Int. 2008;52(1-2):142-54. Epub 2007/08/03. doi: 10.1016/j.neuint.2007.06.005. PubMed PMID: 17669556; PubMed Central PMCID: PMCPMC2267911.

267. Bridges RJ, Natale NR, Patel SA. System xc(-) cystine/glutamate antiporter: an update on molecular pharmacology and roles within the CNS. Br J Pharmacol. 2012;165(1):20-34. Epub 2011/05/14. doi: 10.1111/j.1476-5381.2011.01480.x. PubMed PMID: 21564084; PubMed Central PMCID: PMCPMC3252963.

268. Baker DA, Xi ZX, Shen H, Swanson CJ, Kalivas PW. The origin and neuronal function of in vivo nonsynaptic glutamate. J Neurosci. 2002;22(20):9134-41. Epub 2002/10/22. PubMed PMID: 12388621.

269. Melendez RI, Vuthiganon J, Kalivas PW. Regulation of extracellular glutamate in the prefrontal cortex: focus on the cystine glutamate exchanger and group I metabotropic glutamate receptors. J Pharmacol Exp Ther. 2005;314(1):139-47. Epub 2005/03/17. doi: 10.1124/jpet.104.081521. PubMed PMID: 15769865.

270. Piani D, Fontana A. Involvement of the cystine transport system xc- in the macrophage-induced glutamate-dependent cytotoxicity to neurons. J Immunol. 1994;152(7):3578-85. Epub 1994/04/01. PubMed PMID: 8144936.

271. Barger SW, Basile AS. Activation of microglia by secreted amyloid precursor protein evokes release of glutamate by cystine exchange and attenuates synaptic function. J Neurochem. 2001;76(3):846-54. Epub 2001/02/07. PubMed PMID: 11158256.

272. Domercq M, Sanchez-Gomez MV, Sherwin C, Etxebarria E, Fern R, Matute C. System xc- and glutamate transporter inhibition mediates microglial toxicity to oligodendrocytes. J Immunol. 2007;178(10):6549-56. Epub 2007/05/04. PubMed PMID: 17475885.

273. Robinson MB, Jackson JG. Astroglial glutamate transporters coordinate excitatory signaling and brain energetics. Neurochem Int. 2016;98:56-71. Epub 2016/03/26. doi: 10.1016/j.neuint.2016.03.014. PubMed PMID: 27013346; PubMed Central PMCID: PMCPMC4969184.

274. Lipski J, Wan CK, Bai JZ, Pi R, Li D, Donnelly D. Neuroprotective potential of ceftriaxone in in vitro models of stroke. Neuroscience. 2007;146(2):617-29. Epub 2007/03/17. doi: 10.1016/j.neuroscience.2007.02.003. PubMed PMID: 17363173.

275. Knackstedt LA, Melendez RI, Kalivas PW. Ceftriaxone restores glutamate homeostasis and prevents relapse to cocaine seeking. Biol Psychiatry. 2010;67(1):81-4. doi: 10.1016/j.biopsych.2009.07.018. PubMed PMID: 19717140; PubMed Central PMCID: PMC2795043.

276. Leung TC, Lui CN, Chen LW, Yung WH, Chan YS, Yung KK. Ceftriaxone ameliorates motor deficits and protects dopaminergic neurons in 6-hydroxydopamine-

lesioned rats. ACS Chem Neurosci. 2012;3(1):22-30. doi: 10.1021/cn200072h. PubMed PMID: 22860178; PubMed Central PMCID: PMC3369786.

277. Lewerenz J, Albrecht P, Tien ML, Henke N, Karumbayaram S, Kornblum HI, et al. Induction of Nrf2 and xCT are involved in the action of the neuroprotective antibiotic ceftriaxone in vitro. J Neurochem. 2009;111(2):332-43. Epub 2009/08/22. doi: JNC6347 [pii]
10.1111/j.1471-4159.2009.06347.x.

278. Lee SG, Su ZZ, Emdad L, Gupta P, Sarkar D, Borjabad A, et al. Mechanism of ceftriaxone induction of excitatory amino acid transporter-2 expression and glutamate uptake in primary human astrocytes. J Biol Chem. 2008;283(19):13116-23. Epub 2008/03/11. doi: 10.1074/jbc.M707697200. PubMed PMID: 18326497; PubMed Central PMCID: PMCPMC2442320.

279. Kerr JF. A histochemical study of hypertrophy and ischaemic injury of rat liver with special reference to changes in lysosomes. J Pathol Bacteriol. 1965;90(2):419-35. Epub 1965/10/01. PubMed PMID: 5849603.

280. Kerr JF. Shrinkage necrosis: a distinct mode of cellular death. The Journal of pathology. 1971;105(1):13-20. Epub 1971/09/01. doi: 10.1002/path.1711050103. PubMed PMID: 4108566.

281. Kerr JF, Wyllie AH, Currie AR. Apoptosis: a basic biological phenomenon with wide-ranging implications in tissue kinetics. British journal of cancer. 1972;26(4):239-57. Epub 1972/08/01. PubMed PMID: 4561027; PubMed Central PMCID: PMCPMC2008650.

282. Putcha GV, Johnson EM, Jr. Men are but worms: neuronal cell death in C elegans and vertebrates. Cell Death Differ. 2004;11(1):38-48. Epub 2003/12/03. doi: 10.1038/sj.cdd.4401352. PubMed PMID: 14647239.

283. Herman RK, Albertson DG, Brenner S. Chromosome rearrangements in Caenorhabditis elegans. Genetics. 1976;83(1):91-105. Epub 1976/05/01. PubMed PMID: 1269921; PubMed Central PMCID: PMCPMC1213508.

284. Sulston JE. Post-embryonic development in the ventral cord of Caenorhabditis elegans. Philos Trans R Soc Lond B Biol Sci. 1976;275(938):287-97. Epub 1976/08/10. PubMed PMID: 8804.

285. Sulston JE, Horvitz HR. Post-embryonic cell lineages of the nematode, Caenorhabditis elegans. Dev Biol. 1977;56(1):110-56. Epub 1977/03/01. PubMed PMID: 838129.

286. Sulston JE, Schierenberg E, White JG, Thomson JN. The embryonic cell lineage of the nematode Caenorhabditis elegans. Dev Biol. 1983;100(1):64-119. Epub 1983/11/01. PubMed PMID: 6684600.

287. Syntichaki P, Tavernarakis N. Death by necrosis. Uncontrollable catastrophe, or is there order behind the chaos? EMBO reports. 2002;3(7):604-9. Epub 2002/07/09. doi: 10.1093/embo-reports/kvf138. PubMed PMID: 12101090; PubMed Central PMCID: PMCPMC1084192.

288. Horvitz HR, Sulston JE. Isolation and genetic characterization of cell-lineage mutants of the nematode Caenorhabditis elegans. Genetics. 1980;96(2):435-54. Epub 1980/10/01. PubMed PMID: 7262539; PubMed Central PMCID: PMCPMC1214309.

289. Chalfie M, Horvitz HR, Sulston JE. Mutations that lead to reiterations in the cell lineages of C. elegans. Cell. 1981;24(1):59-69. Epub 1981/04/01. PubMed PMID: 7237544.

290. Hedgecock EM, Sulston JE, Thomson JN. Mutations affecting programmed cell deaths in the nematode Caenorhabditis elegans. Science. 1983;220(4603):1277-9. Epub 1983/06/17. PubMed PMID: 6857247.

291. Ellis HM, Horvitz HR. Genetic control of programmed cell death in the nematode C. elegans. Cell. 1986;44(6):817-29. Epub 1986/03/28. PubMed PMID: 3955651.

292. Ellis RE, Horvitz HR. Two C. elegans genes control the programmed deaths of specific cells in the pharynx. Development. 1991;112(2):591-603. Epub 1991/06/01. PubMed PMID: 1794327.

293. Hengartner MO, Ellis RE, Horvitz HR. Caenorhabditis elegans gene ced-9 protects cells from programmed cell death. Nature. 1992;356(6369):494-9. Epub 1992/04/09. doi: 10.1038/356494a0. PubMed PMID: 1560823.

294. Trent C, Tsuing N, Horvitz HR. Egg-laying defective mutants of the nematode Caenorhabditis elegans. Genetics. 1983;104(4):619-47. Epub 1983/08/01. PubMed PMID: 11813735; PubMed Central PMCID: PMCPMC1202130.

295. Conradt B, Horvitz HR. The C. elegans protein EGL-1 is required for programmed cell death and interacts with the Bcl-2-like protein CED-9. Cell. 1998;93(4):519-29. Epub 1998/05/30. PubMed PMID: 9604928.

296. Metzstein MM, Stanfield GM, Horvitz HR. Genetics of programmed cell death in C. elegans: past, present and future. Trends Genet. 1998;14(10):410-6. Epub 1998/11/20. PubMed PMID: 9820030.

297. Strasser A, Cory S, Adams JM. Deciphering the rules of programmed cell death to improve therapy of cancer and other diseases. EMBO J. 2011;30(18):3667-83. Epub 2011/08/25. doi: 10.1038/emboj.2011.307. PubMed PMID: 21863020; PubMed Central PMCID: PMCPMC3173800.

298. Yuan J, Shaham S, Ledoux S, Ellis HM, Horvitz HR. The C. elegans cell death gene ced-3 encodes a protein similar to mammalian interleukin-1 beta-converting enzyme. Cell. 1993;75(4):641-52. Epub 1993/11/19. PubMed PMID: 8242740.

299. Thornberry NA. The caspase family of cysteine proteases. Br Med Bull. 1997;53(3):478-90. Epub 1997/01/01. PubMed PMID: 9374032.

300. Zou H, Henzel WJ, Liu X, Lutschg A, Wang X. Apaf-1, a human protein homologous to C. elegans CED-4, participates in cytochrome c-dependent activation of caspase-3. Cell. 1997;90(3):405-13. Epub 1997/08/08. PubMed PMID: 9267021.

301. Hengartner MO, Horvitz HR. C. elegans cell survival gene ced-9 encodes a functional homolog of the mammalian proto-oncogene bcl-2. Cell. 1994;76(4):665-76. Epub 1994/02/25. PubMed PMID: 7907274.

302. Vaux DL, Cory S, Adams JM. Bcl-2 gene promotes haemopoietic cell survival and cooperates with c-myc to immortalize pre-B cells. Nature. 1988;335(6189):440-2. Epub 1988/09/29. doi: 10.1038/335440a0. PubMed PMID: 3262202.

303. James C, Gschmeissner S, Fraser A, Evan GI. CED-4 induces chromatin condensation in Schizosaccharomyces pombe and is inhibited by direct physical association with CED-9. Curr Biol. 1997;7(4):246-52. Epub 1997/04/01. PubMed PMID: 9094313.

304. Wyllie AH, Kerr JF, Currie AR. Cell death: the significance of apoptosis. Int Rev Cytol. 1980;68:251-306. Epub 1980/01/01. PubMed PMID: 7014501.

305. Hall DH, Gu G, Garcia-Anoveros J, Gong L, Chalfie M, Driscoll M. Neuropathology of degenerative cell death in Caenorhabditis elegans. J Neurosci. 1997;17(3):1033-45. Epub 1997/02/01. PubMed PMID: 8994058.

306. Sulston JE, Albertson DG, Thomson JN. The Caenorhabditis elegans male: postembryonic development of nongonadal structures. Dev Biol. 1980;78(2):542-76. Epub 1980/08/01. PubMed PMID: 7409314.

307. Walker NI, Harmon BV, Gobe GC, Kerr JF. Patterns of cell death. Methods Achiev Exp Pathol. 1988;13:18-54. Epub 1988/01/01. PubMed PMID: 3045494.

308. Nikoletopoulou V, Tavernarakis N. Necrotic cell death in Caenorhabditis elegans. Methods Enzymol. 2014;545:127-55. Epub 2014/07/30. doi: 10.1016/B978-0-12-801430-1.00006-8. PubMed PMID: 25065889.

309. Kourtis N, Nikoletopoulou V, Tavernarakis N. Small heat-shock proteins protect from heat-stroke-associated neurodegeneration. Nature. 2012;490(7419):213-8. Epub 2012/09/14. doi: 10.1038/nature11417. PubMed PMID: 22972192.

310. Scott BA, Avidan MS, Crowder CM. Regulation of hypoxic death in C. elegans by the insulin/IGF receptor homolog DAF-2. Science. 2002;296(5577):2388-91. Epub 2002/06/18. doi: 10.1126/science.1072302. PubMed PMID: 12065745.

311. Yuan A, Santi CM, Wei A, Wang ZW, Pollak K, Nonet M, et al. The sodium-activated potassium channel is encoded by a member of the Slo gene family. Neuron. 2003;37(5):765-73. Epub 2003/03/12. PubMed PMID: 12628167.

312. Chalfie M, Au M. Genetic control of differentiation of the Caenorhabditis elegans touch receptor neurons. Science. 1989;243(4894 Pt 1):1027-33. Epub 1989/02/24. PubMed PMID: 2646709.

313. Chalfie M, Wolinsky E. The identification and suppression of inherited neurodegeneration in Caenorhabditis elegans. Nature. 1990;345(6274):410-6. Epub 1990/05/31. doi: 10.1038/345410a0. PubMed PMID: 2342572.

314. Driscoll M, Chalfie M. The mec-4 gene is a member of a family of Caenorhabditis elegans genes that can mutate to induce neuronal degeneration. Nature. 1991;349(6310):588-93. Epub 1991/02/14. doi: 10.1038/349588a0. PubMed PMID: 1672038.

315. Chalfie M, Driscoll M, Huang M. Degenerin similarities. Nature. 1993;361(6412):504. Epub 1993/02/11. doi: 10.1038/361504a0. PubMed PMID: 8429902.

316. Chatzigeorgiou M, Grundy L, Kindt KS, Lee WH, Driscoll M, Schafer WR. Spatial asymmetry in the mechanosensory phenotypes of the C. elegans DEG/ENaC gene mec-10. J Neurophysiol. 2010;104(6):3334-44. Epub 2010/10/01. doi: 10.1152/jn.00330.2010. PubMed PMID: 20881202; PubMed Central PMCID: PMCPMC3007656.

317. Xu K, Tavernarakis N, Driscoll M. Necrotic cell death in C. elegans requires the function of calreticulin and regulators of Ca(2+) release from the endoplasmic reticulum. Neuron. 2001;31(6):957-71. Epub 2001/10/03. PubMed PMID: 11580896.

318. Bianchi L, Gerstbrein B, Frokjaer-Jensen C, Royal DC, Mukherjee G, Royal MA, et al. The neurotoxic MEC-4(d) DEG/ENaC sodium channel conducts calcium: implications for necrosis initiation. Nat Neurosci. 2004;7(12):1337-44. Epub 2004/11/16. doi: 10.1038/nn1347. PubMed PMID: 15543143.

319. Treinin M, Chalfie M. A mutated acetylcholine receptor subunit causes neuronal degeneration in C. elegans. Neuron. 1995;14(4):871-7. Epub 1995/04/01. PubMed PMID: 7718248.

320. Nagarajan A, Ning Y, Reisner K, Buraei Z, Larsen JP, Hobert O, et al. Progressive degeneration of dopaminergic neurons through TRP channel-induced cell death. J Neurosci. 2014;34(17):5738-46. Epub 2014/04/25. doi: 10.1523/JNEUROSCI.4540-13.2014. PubMed PMID: 24760834; PubMed Central PMCID: PMCPMC3996206.

321. Mano I, Driscoll M. Caenorhabditis elegans glutamate transporter deletion induces AMPA-receptor/adenylyl cyclase 9-dependent excitotoxicity. J Neurochem. 2009;108(6):1373-84. doi: 10.1111/j.1471-4159.2008.05804.x. PubMed PMID: 19054279.

322. Tehrani N, Del Rosario J, Dominguez M, Kalb R, Mano I. The insulin/IGF signaling regulators cytohesin/GRP-1 and PIP5K/PPK-1 modulate susceptibility to excitotoxicity in C. elegans. PLoS One. 2014;9(11):e113060. Epub 2014/11/26. doi: 10.1371/journal.pone.0113060. PubMed PMID: 25422944; PubMed Central PMCID: PMCPMC4244091.

323. Del Rosario JS, Feldmann KG, Ahmed T, Amjad U, Ko B, An J, et al. Death Associated Protein Kinase (DAPK) -mediated neurodegenerative mechanisms in nematode excitotoxicity. BMC Neurosci. 2015;16:25. doi: 10.1186/s12868-015-0158-2. PubMed PMID: 25899010; PubMed Central PMCID: PMC4414438.

324. Hobert O. PCR fusion-based approach to create reporter gene constructs for expression analysis in transgenic C. elegans. Biotechniques. 2002;32(4):728-30. Epub 2002/04/19. PubMed PMID: 11962590.

325. Kenyon C, Chang J, Gensch E, Rudner A, Tabtiang R. A C. elegans mutant that lives twice as long as wild type. Nature. 1993;366(6454):461-4. Epub 1993/12/02. doi: 10.1038/366461a0. PubMed PMID: 8247153.

326. Hall DH. Electron microscopy and three-dimensional image reconstruction. Methods Cell Biol. 1995;48:395-436. Epub 1995/01/01. PubMed PMID: 8531736.

327. Berkowitz LA, Hamamichi S, Knight AL, Harrington AJ, Caldwell GA, Caldwell KA. Application of a C. elegans dopamine neuron degeneration assay for the validation of potential Parkinson's disease genes. J Vis Exp. 2008;(17). Epub 2008/12/11. doi: 10.3791/835. PubMed PMID: 19066512; PubMed Central PMCID: PMCPMC3253614.

328. Ward S, Thomson N, White JG, Brenner S. Electron microscopical reconstruction of the anterior sensory anatomy of the nematode Caenorhabditis elegans.?2UU. J Comp Neurol. 1975;160(3):313-37. Epub 1975/04/01. doi: 10.1002/cne.901600305. PubMed PMID: 1112927.

329. Perkins LA, Hedgecock EM, Thomson JN, Culotti JG. Mutant sensory cilia in the nematode Caenorhabditis elegans. Dev Biol. 1986;117(2):456-87. Epub 1986/10/01. PubMed PMID: 2428682.

330. Doroquez DB, Berciu C, Anderson JR, Sengupta P, Nicastro D. A high-resolution morphological and ultrastructural map of anterior sensory cilia and glia in Caenorhabditis elegans. Elife. 2014;3:e01948. Epub 2014/03/29. doi: 10.7554/eLife.01948. PubMed PMID: 24668170; PubMed Central PMCID: PMCPMC3965213.

331. Graham DG. Oxidative pathways for catecholamines in the genesis of neuromelanin and cytotoxic quinones. Mol Pharmacol. 1978;14(4):633-43. Epub 1978/07/01. PubMed PMID: 98706.

332. Blum D, Torch S, Lambeng N, Nissou M, Benabid AL, Sadoul R, et al. Molecular pathways involved in the neurotoxicity of 6-OHDA, dopamine and MPTP: contribution to the apoptotic theory in Parkinson's disease. Prog Neurobiol. 2001;65(2):135-72.

333. Caudle WM, Richardson JR, Wang MZ, Taylor TN, Guillot TS, McCormack AL, et al. Reduced vesicular storage of dopamine causes progressive nigrostriatal neurodegeneration. J Neurosci. 2007;27(30):8138-48.

334. Simantov R, Blinder E, Ratovitski T, Tauber M, Gabbay M, Porat S. Dopamine-induced apoptosis in human neuronal cells: inhibition by nucleic acids antisense to the dopamine transporter. Neuroscience. 1996;74:39-50.

335. Wang L, Zhai YQ, Xu LL, Qiao C, Sun XL, Ding JH, et al. Metabolic inflammation exacerbates dopaminergic neuronal degeneration in response to acute MPTP challenge in type 2 diabetes mice. Exp Neurol. 2014;251:22-9. Epub 2013/11/14. doi: 10.1016/j.expneurol.2013.11.001. PubMed PMID: 24220636.

336. Mangia S, Giove F, Dinuzzo M. Metabolic pathways and activity-dependent modulation of glutamate concentration in the human brain. Neurochem Res. 2012;37(11):2554-61. Epub 2012/08/01. doi: 10.1007/s11064-012-0848-4. PubMed PMID: 22846967; PubMed Central PMCID: PMCPMC3489977.

337. Sulston J, Dew M, Brenner S. Dopaminergic neurons in the nematode caenorhabditis elegans. Journal of CompNeur. 1975;163:215-26.

338. Sjollema KA, Schnell U, Kuipers J, Kalicharan R, Giepmans BN. Correlated light microscopy and electron microscopy. Methods Cell Biol. 2012;111:157-73. Epub 2012/08/04. doi: 10.1016/B978-0-12-416026-2.00009-1. PubMed PMID: 22857928.

339. Tao J, Wu QY, Ma YC, Chen YL, Zou CG. Antioxidant response is a protective mechanism against nutrient deprivation in C. elegans. Sci Rep. 2017;7:43547. Epub 2017/02/24. doi: 10.1038/srep43547. PubMed PMID: 28230214; PubMed Central PMCID: PMCPMC5322524.

340. Kapulkin WJ, Hiester BG, Link CD. Compensatory regulation among ER chaperones in C. elegans. FEBS Lett. 2005;579(14):3063-8. Epub 2005/05/24. doi: 10.1016/j.febslet.2005.04.062. PubMed PMID: 15907843.

341. Burmeister C, Luersen K, Heinick A, Hussein A, Domagalski M, Walter RD, et al. Oxidative stress in Caenorhabditis elegans: protective effects of the Omega class glutathione transferase (GSTO-1). FASEB J. 2008;22(2):343-54. Epub 2007/09/29. doi: 10.1096/fj.06-7426com. PubMed PMID: 17901115.

342. Ient B, Edwards R, Mould R, Hannah M, Holden-Dye L, O'Connor V. HSP-4 endoplasmic reticulum (ER) stress pathway is not activated in a C. elegans model of ethanol intoxication and withdrawal. Invert Neurosci. 2012;12(2):93-102. Epub 2012/06/05. doi: 10.1007/s10158-012-0136-7. PubMed PMID: 22661239.

343. Henderson ST, Johnson TE. daf-16 integrates developmental and environmental inputs to mediate aging in the nematode Caenorhabditis elegans. Curr Biol. 2001;11(24):1975-80. Epub 2001/12/19. PubMed PMID: 11747825.

344. Driscoll M. Cell death in C. elegans: molecular insights into mechanisms conserved between nematodes and mammals. Brain pathology. 1996;6(4):411-25.

345. Lettre G, Hengartner MO. Developmental apoptosis in C. elegans: a complex CEDnario. Nat Rev Mol Cell Biol. 2006;7(2):97-108.

346. Gonzalez-Zulueta M, Ensz LM, Mukhina G, Lebovitz RM, Zwacka RM, Engelhardt JF, et al. Manganese superoxide dismutase protects nNOS neurons from NMDA and nitric oxide-mediated neurotoxicity. J Neurosci. 1998;18(6):2040-55. Epub 1998/04/18. PubMed PMID: 9482791.

347. Lau A, Tymianski M. Glutamate receptors, neurotoxicity and neurodegeneration. Pflugers Arch. 2010;460(2):525-42. Epub 2010/03/17. doi: 10.1007/s00424-010-0809-1. PubMed PMID: 20229265.

348. Liu Y, Edwards RH. The role of vesicular transport proteins in synaptic transmission and neural degeneration. Annu Rev Neurosci. 1997;20:125-56.

349. Lee RY, Sawin ER, Chalfie M, Horvitz HR, Avery L. EAT-4, a homolog of a mammalian sodium-dependent inorganic phosphate cotransporter, is necessary for glutamatergic neurotransmission in caenorhabditis elegans. J Neurosci. 1999;19(1):159-67.

350. Fremeau RT, Jr., Troyer MD, Pahner I, Nygaard GO, Tran CH, Reimer RJ, et al. The expression of vesicular glutamate transporters defines two classes of excitatory synapse. Neuron. 2001;31(2):247-60.

351. Herzog E, Gilchrist J, Gras C, Muzerelle A, Ravassard P, Giros B, et al. Localization of VGLUT3, the vesicular glutamate transporter type 3, in the rat brain. Neuroscience. 2004;123(4):983-1002. Epub 2004/01/31. PubMed PMID: 14751290.

352. Ni Y, Parpura V. Dual regulation of Ca2+-dependent glutamate release from astrocytes: vesicular glutamate transporters and cytosolic glutamate levels. Glia. 2009;57(12):1296-305. Epub 2009/02/05. doi: 10.1002/glia.20849. PubMed PMID: 19191347; PubMed Central PMCID: PMCPMC2713374.

353. Serrano-Saiz E, Poole RJ, Felton T, Zhang F, De La Cruz ED, Hobert O. Modular control of glutamatergic neuronal identity in C. elegans by distinct homeodomain proteins. Cell. 2013;155(3):659-73. Epub 2013/11/19. doi: 10.1016/j.cell.2013.09.052 S0092-8674(13)01226-9 [pii]. PubMed Central PMCID: PMC3855022.

354. Veljkovic E, Stasiuk S, Skelly PJ, Shoemaker CB, Verrey F. Functional characterization of Caenorhabditis elegans heteromeric amino acid transporters. J Biol Chem. 2004;279(9):7655-62. Epub 2003/12/12. doi: 10.1074/jbc.M309528200 M309528200 [pii].

355. Brockie PJ, Maricq AV. Ionotropic glutamate receptors: genetics, behavior and electrophysiology. WormBook. 2006:1-16. doi: 10.1895/wormbook.1.61.1. PubMed PMID: 18050468.

356. Dillon J, Hopper NA, Holden-Dye L, O'Connor V. Molecular characterization of the metabotropic glutamate receptor family in Caenorhabditis elegans. Biochem Soc Trans. 2006;34(Pt 5):942-8. Epub 2006/10/21. doi: BST0340942 [pii] 10.1042/BST0340942.

357. Mellem JE, Brockie PJ, Zheng Y, Madsen DM, Maricq AV. Decoding of polymodal sensory stimuli by postsynaptic glutamate receptors in C. elegans. Neuron. 2002;36(5):933-44. Epub 2002/12/07. PubMed PMID: 12467596.

358. Strutz-Seebohm N, Werner M, Madsen DM, Seebohm G, Zheng Y, Walker CS, et al. Functional analysis of Caenorhabditis elegans glutamate receptor subunits by domain transplantation. J Biol Chem. 2003;278(45):44691-701. Epub 2003/08/22. doi: 10.1074/jbc.M305497200. PubMed PMID: 12930835.

359. Orrenius S, Zhivotovsky B, Nicotera P. Regulation of cell death: the calcium-apoptosis link. Nat Rev Mol Cell Biol. 2003;4(7):552-65. Epub 2003/07/03. doi: 10.1038/nrm1150. PubMed PMID: 12838338.

360. Gwag BJ, Canzoniero LM, Sensi SL, Demaro JA, Koh JY, Goldberg MP, et al. Calcium ionophores can induce either apoptosis or necrosis in cultured cortical neurons. Neuroscience. 1999;90(4):1339-48. Epub 1999/05/25. PubMed PMID: 10338301.

361. Rami A, Ferger D, Krieglstein J. Blockade of calpain proteolytic activity rescues neurons from glutamate excitotoxicity. Neurosci Res. 1997;27(1):93-7. Epub 1997/01/01. PubMed PMID: 9089703.

362. Samara C, Tavernarakis N. Calcium-dependent and aspartyl proteases in neurodegeneration and ageing in C. elegans. Ageing Res Rev. 2003;2(4):451-71. Epub 2003/10/03. PubMed PMID: 14522246.

363. Liu J, Liu MC, Wang KK. Calpain in the CNS: from synaptic function to neurotoxicity. Sci Signal. 2008;1(14):re1. Epub 2008/04/10. doi: 10.1126/stke.114re1. PubMed PMID: 18398107.

364. Rego AC, Oliveira CR. Mitochondrial dysfunction and reactive oxygen species in excitotoxicity and apoptosis: implications for the pathogenesis of neurodegenerative diseases. Neurochem Res. 2003;28(10):1563-74. Epub 2003/10/23. PubMed PMID: 14570402.

365. Clausen A, McClanahan T, Ji SG, Weiss JH. Mechanisms of rapid reactive oxygen species generation in response to cytosolic Ca2+ or Zn2+ loads in cortical neurons. PLoS One. 2013;8(12):e83347. Epub 2013/12/18. doi: 10.1371/journal.pone.0083347. PubMed PMID: 24340096; PubMed Central PMCID: PMCPMC3858366.

366. Leung CK, Deonarine A, Strange K, Choe KP. High-throughput screening and biosensing with fluorescent C. elegans strains. J Vis Exp. 2011;(51). Epub 2011/06/03. doi: 10.3791/2745
2745 [pii]. PubMed PMID: PDF in file.

367. Salgueiro WG, Goldani BS, Peres TV, Miranda-Vizuete A, Aschner M, da Rocha JBT, et al. Insights into the differential toxicological and antioxidant effects of 4-phenylchalcogenil-7-chloroquinolines in Caenorhabditis elegans. Free Radic Biol Med. 2017;110:133-41. Epub 2017/06/03. doi: 10.1016/j.freeradbiomed.2017.05.020. PubMed PMID: 28571752.

368. Kondo M, Yanase S, Ishii T, Hartman PS, Matsumoto K, Ishii N. The p38 signal transduction pathway participates in the oxidative stress-mediated translocation of DAF-16 to Caenorhabditis elegans nuclei. Mech Ageing Dev. 2005;126(6-7):642-7.

369. Edinger AL, Thompson CB. Death by design: apoptosis, necrosis and autophagy. Curr Opin Cell Biol. 2004;16(6):663-9. Epub 2004/11/09. doi: 10.1016/j.ceb.2004.09.011. PubMed PMID: 15530778.

370. Allen RT, Hunter WJ, 3rd, Agrawal DK. Morphological and biochemical characterization and analysis of apoptosis. J Pharmacol Toxicol Methods. 1997;37(4):215-28. Epub 1997/06/01. PubMed PMID: 9279777.

371. Wang X, Yang C. Programmed cell death and clearance of cell corpses in Caenorhabditis elegans. Cell Mol Life Sci. 2016;73(11-12):2221-36. Epub 2016/04/07. doi: 10.1007/s00018-016-2196-z. PubMed PMID: 27048817.

372. Zhou Z, Hartwieg E, Horvitz HR. CED-1 is a transmembrane receptor that mediates cell corpse engulfment in C. elegans. Cell. 2001;104(1):43-56.

373. Liu QA, Hengartner MO. Candidate adaptor protein CED-6 promotes the engulfment of apoptotic cells in C. elegans. Cell. 1998;93(6):961-72. Epub 1998/07/11. PubMed PMID: 9635426.

374. Reddien PW, Horvitz HR. CED-2/CrkII and CED-10/Rac control phagocytosis and cell migration in Caenorhabditis elegans. Nat Cell Biol. 2000;2(3):131-6. Epub 2000/03/09. doi: 10.1038/35004000. PubMed PMID: 10707082.

375. Offenburger SL, Ho XY, Tachie-Menson T, Coakley S, Hilliard MA, Gartner A. 6-OHDA-induced dopaminergic neurodegeneration in Caenorhabditis elegans is promoted by the engulfment pathway and inhibited by the transthyretin-related protein TTR-33. PLoS Genet. 2018;14(1):e1007125. Epub 2018/01/19. doi: 10.1371/journal.pgen.1007125. PubMed PMID: 29346382.

376. Avery L, Horvitz HR. A cell that dies during wild-type C. elegans development can function as a neuron in a ced-3 mutant. Cell. 1987;51(6):1071-8. Epub 1987/12/24. PubMed PMID: 3690660; PubMed Central PMCID: PMCPMC3773210.

377. Soares FA, Fagundez DA, Avila DS. Neurodegeneration Induced by Metals in Caenorhabditis elegans. Adv Neurobiol. 2017;18:355-83. Epub 2017/09/11. doi: 10.1007/978-3-319-60189-2_18. PubMed PMID: 28889277.

378. Aronoff R, Mellem JE, Maricq AV, Sprengel R, Seeburg PH. Neuronal toxicity in Caenorhabditis elegans from an editing site mutant in glutamate receptor channels. J Neurosci. 2004;24(37):8135-40. Epub 2004/09/17. doi: 10.1523/JNEUROSCI.2587-04.2004. PubMed PMID: 15371514.

379. Offenburger SL, Jongsma E, Gartner A. Mutations in Caenorhabditis elegans neuroligin-like glit-1, the apoptosis pathway and the calcium chaperone crt-1 increase dopaminergic neurodegeneration after 6-OHDA treatment. PLoS Genet. 2018;14(1):e1007106. Epub 2018/01/19. doi: 10.1371/journal.pgen.1007106. PubMed PMID: 29346364.

380. Olney JW, de Gubareff T. Glutamate neurotoxicity and Huntington's chorea. Nature. 1978;271(5645):557-9. Epub 1978/02/09. PubMed PMID: 146165.

381. Olney JW, Price MT, Samson L, Labruyere J. The role of specific ions in glutamate neurotoxicity. Neurosci Lett. 1986;65(1):65-71. Epub 1986/03/28. PubMed PMID: 2871531.

382. Rothman SM, Olney JW. Glutamate and the pathophysiology of hypoxic--ischemic brain damage. Ann Neurol. 1986;19(2):105-11. Epub 1986/02/01. doi: 10.1002/ana.410190202. PubMed PMID: 2421636.

383. Coyle JT. Neurotoxic action of kainic acid. J Neurochem. 1983;41(1):1-11. Epub 1983/07/01. PubMed PMID: 6306166.

384. Simonian NA, Getz RL, Leveque JC, Konradi C, Coyle JT. Kainic acid induces apoptosis in neurons. Neuroscience. 1996;75(4):1047-55. Epub 1996/12/01. PubMed PMID: 8938740.

385. Steiner HX, McBean GJ, Kohler C, Roberts PJ, Schwarcz R. Ibotenate-induced neuronal degeneration in immature rat brain. Brain Res. 1984;307(1-2):117-24. Epub 1984/07/30. PubMed PMID: 6466990.

386. Plaitakis A, Shashidharan P. Glutamate transport and metabolism in dopaminergic neurons of substantia nigra: implications for the pathogenesis of Parkinson's disease. J Neurol. 2000;247 Suppl 2:II25-35. Epub 2000/09/19. PubMed PMID: 10991662.

387. Zorec R, Parpura V, Verkhratsky A. Astroglial Vesicular Trafficking in Neurodegenerative Diseases. Neurochem Res. 2017;42(3):905-17. Epub 2016/09/16. doi: 10.1007/s11064-016-2055-1. PubMed PMID: 27628292.

388. Olsen ML, Khakh BS, Skatchkov SN, Zhou M, Lee CJ, Rouach N. New Insights on Astrocyte Ion Channels: Critical for Homeostasis and Neuron-Glia Signaling. J Neurosci.

2015;35(41):13827-35. Epub 2015/10/16. doi: 10.1523/JNEUROSCI.2603-15.2015. PubMed PMID: 26468182; PubMed Central PMCID: PMCPMC4604221.

389. Mano I, Straud S, Driscoll M. Caenorhabditis elegans glutamate transporters influence synaptic function and behavior at sites distant from the synapse. J Biol Chem. 2007;282(47):34412-9. Epub 2007/08/08. doi: M704134200 [pii] 10.1074/jbc.M704134200.

390. Stennett BA, Frankowski JC, Peris J, Knackstedt LA. Ceftriaxone reduces alcohol intake in outbred rats while upregulating xCT in the nucleus accumbens core. Pharmacol Biochem Behav. 2017;159:18-23. Epub 2017/07/09. doi: 10.1016/j.pbb.2017.07.001. PubMed PMID: 28687200.

391. Sinor JD, Du S, Venneti S, Blitzblau RC, Leszkiewicz DN, Rosenberg PA, et al. NMDA and glutamate evoke excitotoxicity at distinct cellular locations in rat cortical neurons in vitro. J Neurosci. 2000;20(23):8831-7. Epub 2000/01/11. PubMed PMID: 11102491.

392. Gupta K, Hardingham GE, Chandran S. NMDA receptor-dependent glutamate excitotoxicity in human embryonic stem cell-derived neurons. Neurosci Lett. 2013;543:95-100. Epub 2013/03/23. doi: 10.1016/j.neulet.2013.03.010. PubMed PMID: 23518152; PubMed Central PMCID: PMCPMC3725411.

393. Spencer WC, Zeller G, Watson JD, Henz SR, Watkins KL, McWhirter RD, et al. A spatial and temporal map of C. elegans gene expression. Genome Res. 2011;21(2):325-41. Epub 2010/12/24. doi: 10.1101/gr.114595.110. PubMed PMID: 21177967; PubMed Central PMCID: PMCPMC3032935.

394. Nguyen D, Alavi MV, Kim KY, Kang T, Scott RT, Noh YH, et al. A new vicious cycle involving glutamate excitotoxicity, oxidative stress and mitochondrial dynamics. Cell Death Dis. 2011;2:e240. Epub 2011/12/14. doi: 10.1038/cddis.2011.117. PubMed PMID: 22158479; PubMed Central PMCID: PMCPMC3252734.

395. Ikonomidou C, Turski L. Excitotoxicity and neurodegenerative diseases. Curr Opin Neurol. 1995;8(6):487-97. Epub 1995/12/01. PubMed PMID: 8845937.

396. Mehta A, Prabhakar M, Kumar P, Deshmukh R, Sharma PL. Excitotoxicity: bridge to various triggers in neurodegenerative disorders. Eur J Pharmacol. 2013;698(1-3):6-18. Epub 2012/11/06. doi: 10.1016/j.ejphar.2012.10.032. PubMed PMID: 23123057.

397. Djukic B, Casper KB, Philpot BD, Chin LS, McCarthy KD. Conditional knock-out of Kir4.1 leads to glial membrane depolarization, inhibition of potassium and glutamate uptake, and enhanced short-term synaptic potentiation. J Neurosci. 2007;27(42):11354-65. Epub 2007/10/19. doi: 10.1523/JNEUROSCI.0723-07.2007. PubMed PMID: 17942730.

398. McNaught KS, Jenner P. Extracellular accumulation of nitric oxide, hydrogen peroxide, and glutamate in astrocytic cultures following glutathione depletion, complex I

inhibition, and/or lipopolysaccharide-induced activation. Biochem Pharmacol. 2000;60(7):979-88. Epub 2000/09/07. PubMed PMID: 10974207.

399. Mena MA, de Bernardo S, Casarejos MJ, Canals S, Rodriguez-Martin E. The role of astroglia on the survival of dopamine neurons. Mol Neurobiol. 2002;25(3):245-63. Epub 2002/07/12. doi: 10.1385/MN:25:3:245. PubMed PMID: 12109874.

400. Miyazaki I, Murakami S, Torigoe N, Kitamura Y, Asanuma M. Neuroprotective effects of levetiracetam target xCT in astrocytes in parkinsonian mice. J Neurochem. 2016;136(1):194-204. Epub 2015/10/21. doi: 10.1111/jnc.13405. PubMed PMID: 26485447.

401. Kuter K, Olech L, Glowacka U. Prolonged Dysfunction of Astrocytes and Activation of Microglia Accelerate Degeneration of Dopaminergic Neurons in the Rat Substantia Nigra and Block Compensation of Early Motor Dysfunction Induced by 6-OHDA. Mol Neurobiol. 2017. Epub 2017/05/04. doi: 10.1007/s12035-017-0529-z. PubMed PMID: 28466266.

402. Chinta SJ, Woods G, Demaria M, Rane A, Zou Y, McQuade A, et al. Cellular Senescence Is Induced by the Environmental Neurotoxin Paraquat and Contributes to Neuropathology Linked to Parkinson's Disease. Cell Rep. 2018;22(4):930-40. Epub 2018/02/02. doi: 10.1016/j.celrep.2017.12.092. PubMed PMID: 29386135; PubMed Central PMCID: PMCPMC5806534.

403. Hanson AD, Pribat A, Waller JC, de Crecy-Lagard V. 'Unknown' proteins and 'orphan' enzymes: the missing half of the engineering parts list--and how to find it. Biochem J. 2009;425(1):1-11. doi: 10.1042/BJ20091328. PubMed PMID: 20001958; PubMed Central PMCID: PMC3022307.

404. Ramkissoon KR, Miller JK, Ojha S, Watson DS, Bomar MG, Galande AK, et al. Rapid identification of sequences for orphan enzymes to power accurate protein annotation. PLoS One. 2013;8(12):e84508. doi: 10.1371/journal.pone.0084508. PubMed PMID: 24386392; PubMed Central PMCID: PMC3875567.

405. Shearer AG, Altman T, Rhee CD. Finding sequences for over 270 orphan enzymes. PLoS One. 2014;9(5):e97250. doi: 10.1371/journal.pone.0097250. PubMed PMID: 24826896; PubMed Central PMCID: PMC4020792.

406. Pettinati I, Brem J, Lee SY, McHugh PJ, Schofield CJ. The Chemical Biology of Human Metallo-beta-Lactamase Fold Proteins. Trends Biochem Sci. 2016;41(4):338-55. doi: 10.1016/j.tibs.2015.12.007. PubMed PMID: 26805042; PubMed Central PMCID: PMC4819959.

407. Aravind L. An evolutionary classification of the metallo-beta-lactamase fold proteins. In Silico Biol. 1999;1(2):69-91. Epub 2001/07/27. doi: 1998010008 [pii].

408. Daiyasu H, Osaka K, Ishino Y, Toh H. Expansion of the zinc metallo-hydrolase family of the beta-lactamase fold. FEBS Lett. 2001;503(1):1-6. Epub 2001/08/22. PubMed PMID: 11513844.

409. Moshous D, Callebaut I, de Chasseval R, Corneo B, Cavazzana-Calvo M, Le Deist F, et al. Artemis, a novel DNA double-strand break repair/V(D)J recombination protein, is mutated in human severe combined immune deficiency. Cell. 2001;105(2):177-86. PubMed PMID: 11336668.

410. Jinek M, Chylinski K, Fonfara I, Hauer M, Doudna JA, Charpentier E. A programmable dual-RNA-guided DNA endonuclease in adaptive bacterial immunity. Science. 2012;337(6096):816-21. doi: 10.1126/science.1225829. PubMed PMID: 22745249.

411. Sternberg SH, Doudna JA. Expanding the Biologist's Toolkit with CRISPR-Cas9. Mol Cell. 2015;58(4):568-74. doi: 10.1016/j.molcel.2015.02.032. PubMed PMID: 26000842.

412. Cong L, Ran FA, Cox D, Lin S, Barretto R, Habib N, et al. Multiplex Genome Engineering Using CRISPR/Cas Systems. Science. 2013. Epub 2013/01/05. doi: science.1231143 [pii]
10.1126/science.1231143.

413. Wishart DS, Jewison T, Guo AC, Wilson M, Knox C, Liu Y, et al. HMDB 3.0--The Human Metabolome Database in 2013. Nucleic Acids Res. 2013;41(Database issue):D801-7. Epub 2012/11/20. doi: 10.1093/nar/gks1065. PubMed PMID: 23161693; PubMed Central PMCID: PMCPMC3531200.

414. Smith CA, O'Maille G, Want EJ, Qin C, Trauger SA, Brandon TR, et al. METLIN: a metabolite mass spectral database. Ther Drug Monit. 2005;27(6):747-51. Epub 2006/01/13. PubMed PMID: 16404815.

415. Horai H, Arita M, Kanaya S, Nihei Y, Ikeda T, Suwa K, et al. MassBank: a public repository for sharing mass spectral data for life sciences. J Mass Spectrom. 2010;45(7):703-14. Epub 2010/07/14. doi: 10.1002/jms.1777. PubMed PMID: 20623627.

416. A. Jablonski FS, C. J. Powell, and A. Y. Lee. *NIST Electron Elastic-Scattering Cross-Section Database* - Version 4.0. Gaithersburg, MD: National Institute of Standards and Technology; 2016.

417. J. Wang DAP, R. Mistrik and Y. Huang. A Platform to Identify Endogenous Metabolites Using a Novel High Performance Orbitrap MS and the mzCloud Library. San Jose, CA, USA: Thermo Fisher Scientific Inc.; 2013.

418. Schrimpe-Rutledge AC, Codreanu SG, Sherrod SD, McLean JA. Untargeted Metabolomics Strategies-Challenges and Emerging Directions. Journal of the American Society for Mass Spectrometry. 2016;27(12):1897-905. doi: 10.1007/s13361-016-1469-y. PubMed PMID: 27624161; PubMed Central PMCID: PMC5110944.

419. Li S, Park Y, Duraisingham S, Strobel FH, Khan N, Soltow QA, et al. Predicting network activity from high throughput metabolomics. PLoS Comput Biol. 2013;9(7):e1003123. Epub 2013/07/19. doi: 10.1371/journal.pcbi.1003123. PubMed PMID: 23861661; PubMed Central PMCID: PMCPMC3701697.

420. Xia J, Wishart DS. Using MetaboAnalyst 3.0 for Comprehensive Metabolomics Data Analysis. Current protocols in bioinformatics. 2016;55:14 0 1- 0 91. Epub 2016/09/08. doi: 10.1002/cpbi.11. PubMed PMID: 27603023.

421. Hsu PD, Scott DA, Weinstein JA, Ran FA, Konermann S, Agarwala V, et al. DNA targeting specificity of RNA-guided Cas9 nucleases. Nat Biotechnol. 2013;31(9):827-32. doi: 10.1038/nbt.2647. PubMed PMID: 23873081; PubMed Central PMCID: PMC3969858.

422. Shen B, Zhang J, Wu H, Wang J, Ma K, Li Z, et al. Generation of gene-modified mice via Cas9/RNA-mediated gene targeting. Cell Res. 2013;23(5):720-3. doi: 10.1038/cr.2013.46. PubMed PMID: 23545779; PubMed Central PMCID: PMC3641603.

423. Lin L, Huang Z, Gao Y, Yan X, Xing J, Hang W. LC-MS based serum metabonomic analysis for renal cell carcinoma diagnosis, staging, and biomarker discovery. J Proteome Res. 2011;10(3):1396-405. doi: 10.1021/pr101161u. PubMed PMID: 21186845.

424. Spagou K, Wilson ID, Masson P, Theodoridis G, Raikos N, Coen M, et al. HILIC-UPLC-MS for exploratory urinary metabolic profiling in toxicological studies. Anal Chem. 2011;83(1):382-90. doi: 10.1021/ac102523q. PubMed PMID: 21142126.

425. Tan G, Lou Z, Liao W, Dong X, Zhu Z, Li W, et al. Hydrophilic interaction and reversed-phase ultraperformance liquid chromatography TOF-MS for serum metabonomic analysis of myocardial infarction in rats and its applications. Mol Biosyst. 2012;8(2):548-56. doi: 10.1039/c1mb05324h. PubMed PMID: 22037674.

426. D'Alessandro A, Gevi F, Zolla L. A robust high resolution reversed-phase HPLC strategy to investigate various metabolic species in different biological models. Mol Biosyst. 2011;7(4):1024-32. Epub 2011/01/25. doi: 10.1039/c0mb00274g. PubMed PMID: 21258747.

427. Crews B, Wikoff WR, Patti GJ, Woo HK, Kalisiak E, Heideker J, et al. Variability analysis of human plasma and cerebral spinal fluid reveals statistical significance of changes in mass spectrometry-based metabolomics data. Anal Chem. 2009;81(20):8538-44. Epub 2009/09/22. doi: 10.1021/ac9014947. PubMed PMID: 19764780; PubMed Central PMCID: PMCPMC3058611.

428. Chen Z, Xu X, Zhang J, Liu Y, Xu X, Li L, et al. Application of LC-MS-Based Global Metabolomic Profiling Methods to Human Mental Fatigue. Anal Chem. 2016;88(23):11293-6. Epub 2016/12/10. doi: 10.1021/acs.analchem.6b03421. PubMed PMID: 27934122.

429. Feng Q, Liu Z, Zhong S, Li R, Xia H, Jie Z, et al. Integrated metabolomics and metagenomics analysis of plasma and urine identified microbial metabolites associated with coronary heart disease. Sci Rep. 2016;6:22525. doi: 10.1038/srep22525. PubMed PMID: 26932197; PubMed Central PMCID: PMC4773756.

430. Sumner LW, Amberg A, Barrett D, Beale MH, Beger R, Daykin CA, et al. Proposed minimum reporting standards for chemical analysis Chemical Analysis Working Group (CAWG) Metabolomics Standards Initiative (MSI). Metabolomics : Official journal of the Metabolomic Society. 2007;3(3):211-21. Epub 2007/09/01. doi: 10.1007/s11306-007-0082-2. PubMed PMID: 24039616; PubMed Central PMCID: PMCPMC3772505.

431. Members MSIB, Sansone SA, Fan T, Goodacre R, Griffin JL, Hardy NW, et al. The metabolomics standards initiative. Nat Biotechnol. 2007;25(8):846-8. Epub 2007/08/10. doi: 10.1038/nbt0807-846b. PubMed PMID: 17687353.

432. Schymanski EL, Jeon J, Gulde R, Fenner K, Ruff M, Singer HP, et al. Identifying small molecules via high resolution mass spectrometry: communicating confidence. Environmental science & technology. 2014;48(4):2097-8. Epub 2014/01/31. doi: 10.1021/es5002105. PubMed PMID: 24476540.

433. Kanehisa M, Goto S. KEGG: kyoto encyclopedia of genes and genomes. Nucleic Acids Res. 2000;28(1):27-30. PubMed PMID: 10592173; PubMed Central PMCID: PMC102409.

434. Huxtable RJ. Physiological actions of taurine. Physiol Rev. 1992;72(1):101-63. Epub 1992/01/01. doi: 10.1152/physrev.1992.72.1.101. PubMed PMID: 1731369.

435. Tsuji A, Tamai I. Sodium- and chloride-dependent transport of taurine at the blood-brain barrier. Adv Exp Med Biol. 1996;403:385-91. Epub 1996/01/01. PubMed PMID: 8915375.

436. Wu G, Yang J, Sun C, Luan X, Shi J, Hu J. Effect of taurine on alcoholic liver disease in rats. Amino acids. 2009;36(3):457-64. doi: 10.1007/s00726-008-0101-2. PubMed PMID: 18509591.

437. El-Sayed WM, Al-Kahtani MA, Abdel-Moneim AM. Prophylactic and therapeutic effects of taurine against aluminum-induced acute hepatotoxicity in mice. Journal of hazardous materials. 2011;192(2):880-6. doi: 10.1016/j.jhazmat.2011.05.100. PubMed PMID: 21703760.

438. Oveson BC, Iwase T, Hackett SF, Lee SY, Usui S, Sedlak TW, et al. Constituents of bile, bilirubin and TUDCA, protect against oxidative stress-induced retinal degeneration. J Neurochem. 2011;116(1):144-53. doi: 10.1111/j.1471-4159.2010.07092.x. PubMed PMID: 21054389; PubMed Central PMCID: PMC4083853.

439. Froger N, Jammoul F, Gaucher D, Cadetti L, Lorach H, Degardin J, et al. Taurine is a crucial factor to preserve retinal ganglion cell survival. Adv Exp Med Biol. 2013;775:69-83. doi: 10.1007/978-1-4614-6130-2_6. PubMed PMID: 23392925.

440. Gaspar JM, Martins A, Cruz R, Rodrigues CM, Ambrosio AF, Santiago AR. Tauroursodeoxycholic acid protects retinal neural cells from cell death induced by prolonged exposure to elevated glucose. Neuroscience. 2013;253:380-8. doi: 10.1016/j.neuroscience.2013.08.053. PubMed PMID: 24012838.

441. Trantham-Davidson H, Lalumiere RT, Reissner KJ, Kalivas PW, Knackstedt LA. Ceftriaxone normalizes nucleus accumbens synaptic transmission, glutamate transport, and export following cocaine self-administration and extinction training. . J Neurosci. 2012;32(36):12406-10. Epub 2012/09/08. doi: 32/36/12406 [pii] 10.1523/JNEUROSCI.1976-12.2012.

442. LaCrosse AL, O'Donovan SM, Sepulveda-Orengo MT, McCullumsmith RE, Reissner KJ, Schwendt M, et al. Contrasting the Role of xCT and GLT-1 Upregulation in the Ability of Ceftriaxone to Attenuate the Cue-Induced Reinstatement of Cocaine Seeking and Normalize AMPA Receptor Subunit Expression. J Neurosci. 2017;37(24):5809-21. Epub 2017/05/13. doi: 10.1523/JNEUROSCI.3717-16.2017. PubMed PMID: 28495973; PubMed Central PMCID: PMCPMC5473201.

443. Cunnane SC, Anderson MJ. Pure linoleate deficiency in the rat: influence on growth, accumulation of n-6 polyunsaturates, and [1-14C]linoleate oxidation. J Lipid Res. 1997;38(4):805-12. Epub 1997/04/01. PubMed PMID: 9144095.

444. Harris WS, Mozaffarian D, Rimm E, Kris-Etherton P, Rudel LL, Appel LJ, et al. Omega-6 fatty acids and risk for cardiovascular disease: a science advisory from the American Heart Association Nutrition Subcommittee of the Council on Nutrition, Physical Activity, and Metabolism; Council on Cardiovascular Nursing; and Council on Epidemiology and Prevention. Circulation. 2009;119(6):902-7. Epub 2009/01/28. doi: 10.1161/CIRCULATIONAHA.108.191627. PubMed PMID: 19171857.

445. Naughton SS, Mathai ML, Hryciw DH, McAinch AJ. Linoleic acid and the pathogenesis of obesity. Prostaglandins Other Lipid Mediat. 2016;125:90-9. Epub 2016/06/29. doi: 10.1016/j.prostaglandins.2016.06.003. PubMed PMID: 27350414.

446. Moore SA, Yoder E, Spector AA. Role of the blood-brain barrier in the formation of long-chain omega-3 and omega-6 fatty acids from essential fatty acid precursors. J Neurochem. 1990;55(2):391-402. Epub 1990/08/01. PubMed PMID: 2115069.

447. Avellini L, Terracina L, Gaiti A. Linoleic acid passage through the blood-brain barrier and a possible effect of age. Neurochem Res. 1994;19(2):129-33. Epub 1994/02/01. PubMed PMID: 8183422.

448. Bourre JM, Piciotti M, Dumont O, Pascal G, Durand G. Dietary linoleic acid and polyunsaturated fatty acids in rat brain and other organs. Minimal requirements of linoleic acid. Lipids. 1990;25(8):465-72. Epub 1990/08/01. PubMed PMID: 2120529.

449. Su HM, Keswick LA, Brenna JT. Increasing dietary linoleic acid in young rats increases and then decreases docosahexaenoic acid in retina but not in brain. Lipids. 1996;31(12):1289-98. Epub 1996/12/01. PubMed PMID: 8972463.

450. Belin J, Pettet N, Smith AD, Thompson RH, Zilkha KJ. Linoleate metabolism in multiple sclerosis. J Neurol Neurosurg Psychiatry. 1971;34(1):25-9. Epub 1971/02/01. PubMed PMID: 5551691; PubMed Central PMCID: PMCPMC493682.

451. Peet M, Murphy B, Shay J, Horrobin D. Depletion of omega-3 fatty acid levels in red blood cell membranes of depressive patients. Biol Psychiatry. 1998;43(5):315-9. PubMed PMID: 9513745.

452. Snowden SG, Ebshiana AA, Hye A, An Y, Pletnikova O, O'Brien R, et al. Association between fatty acid metabolism in the brain and Alzheimer disease neuropathology and cognitive performance: A nontargeted metabolomic study. PLoS medicine. 2017;14(3):e1002266. doi: 10.1371/journal.pmed.1002266. PubMed PMID: 28323825; PubMed Central PMCID: PMC5360226.

453. Wang D, Wang X, Kong J, Wu J, Lai M. GC-MS-Based metabolomics discovers a shared serum metabolic characteristic among three types of epileptic seizures. Epilepsy Res. 2016;126:83-9. Epub 2016/07/28. doi: 10.1016/j.eplepsyres.2016.07.003. PubMed PMID: 27450370.

454. Cocchi M, Minuto C, Tonello L, Gabrielli F, Bernroider G, Tuszynski JA, et al. Linoleic acid: Is this the key that unlocks the quantum brain? Insights linking broken symmetries in molecular biology, mood disorders and personalistic emergentism. BMC Neurosci. 2017;18(1):38. doi: 10.1186/s12868-017-0356-1. PubMed PMID: 28420346; PubMed Central PMCID: PMC5395787.

455. Mangalam A, Poisson L, Nemutlu E, Datta I, Denic A, Dzeja P, et al. Profile of Circulatory Metabolites in a Relapsing-remitting Animal Model of Multiple Sclerosis using Global Metabolomics. Journal of clinical & cellular immunology. 2013;4. doi: 10.4172/2155-9899.1000150. PubMed PMID: 24273690; PubMed Central PMCID: PMC3837296.

456. Ramautar R, Berger R, van der Greef J, Hankemeier T. Human metabolomics: strategies to understand biology. Current opinion in chemical biology. 2013;17(5):841-6. doi: 10.1016/j.cbpa.2013.06.015. PubMed PMID: 23849548.

457. Caldwell G, Leo GC. Can Untargeted Metabolomics Be Utilized in Drug Discovery/Development? Curr Top Med Chem. 2017. doi: 10.2174/1568026617666170707130032. PubMed PMID: 28685690.

458. Puchades-Carrasco L, Pineda-Lucena A. Metabolomics applications in precision medicine: An oncological perspective. Curr Top Med Chem. 2017. doi: 10.2174/1568026617666170707120034. PubMed PMID: 28685691.

459. Rattray NJW, Charkoftaki G, Rattray Z, Hansen JE, Vasiliou V, Johnson CH. Environmental influences in the etiology of colorectal cancer: the premise of metabolomics. Current pharmacology reports. 2017;3(3):114-25. doi: 10.1007/s40495-017-0088-z. PubMed PMID: 28642837; PubMed Central PMCID: PMC5475285.

460. Guengerich FP, Tang Z, Salamanca-Pinzon SG, Cheng Q. Characterizing proteins of unknown function: orphan cytochrome p450 enzymes as a paradigm. Mol Interv. 2010;10(3):153-63. doi: 10.1124/mi.10.3.6. PubMed PMID: 20539034; PubMed Central PMCID: PMC2895278.

461. Prosser GA, Larrouy-Maumus G, de Carvalho LP. Metabolomic strategies for the identification of new enzyme functions and metabolic pathways. EMBO reports. 2014;15(6):657-69. doi: 10.15252/embr.201338283. PubMed PMID: 24829223; PubMed Central PMCID: PMC4197876.

462. van der Greef J, Stroobant P, van der Heijden R. The role of analytical sciences in medical systems biology. Current opinion in chemical biology. 2004;8(5):559-65. doi: 10.1016/j.cbpa.2004.08.013. PubMed PMID: 15450501.

463. Mir SA, Rajagopalan P, Jain AP, Khan AA, Datta KK, Mohan SV, et al. LC-MS-based serum metabolomic analysis reveals dysregulation of phosphatidylcholines in esophageal squamous cell carcinoma. J Proteomics. 2015;127(Pt A):96-102. doi: 10.1016/j.jprot.2015.05.013. PubMed PMID: 25982385.

464. Rohrer JD, Woollacott IO, Dick KM, Brotherhood E, Gordon E, Fellows A, et al. Serum neurofilament light chain protein is a measure of disease intensity in frontotemporal dementia. Neurology. 2016;87(13):1329-36. doi: 10.1212/WNL.0000000000003154. PubMed PMID: 27581216; PubMed Central PMCID: PMC5047041.

465. Jorgenrud B, Jantti S, Mattila I, Poho P, Ronningen KS, Yki-Jarvinen H, et al. The influence of sample collection methodology and sample preprocessing on the blood metabolic profile. Bioanalysis. 2015;7(8):991-1006. Epub 2015/05/13. doi: 10.4155/bio.15.16. PubMed PMID: 25966010.

466. Beltran A, Samino S, Yanes O. Sample preparation methods for LC-MS-based global aqueous metabolite profiling. Methods Mol Biol. 2014;1198:75-80. Epub 2014/10/02. doi: 10.1007/978-1-4939-1258-2_5. PubMed PMID: 25270923.

467. Tang DQ, Zou L, Yin XX, Ong CN. HILIC-MS for metabolomics: An attractive and complementary approach to RPLC-MS. Mass Spectrom Rev. 2016;35(5):574-600. Epub 2014/10/07. doi: 10.1002/mas.21445. PubMed PMID: 25284160.

468. Banerjee R, Vitvitsky V, Garg SK. The undertow of sulfur metabolism on glutamatergic neurotransmission. Trends Biochem Sci. 2008;33(9):413-9. doi: 10.1016/j.tibs.2008.06.006. PubMed PMID: 18703339.

469. Cui C, Cui Y, Gao J, Sun L, Wang Y, Wang K, et al. Neuroprotective effect of ceftriaxone in a rat model of traumatic brain injury. Neurological sciences : official journal of the Italian Neurological Society and of the Italian Society of Clinical Neurophysiology. 2014;35(5):695-700. doi: 10.1007/s10072-013-1585-4. PubMed PMID: 24277205.

470. Hsu CY, Hung CS, Chang HM, Liao WC, Ho SC, Ho YJ. Ceftriaxone prevents and reverses behavioral and neuronal deficits in an MPTP-induced animal model of Parkinson's disease dementia. Neuropharmacology. 2015;91:43-56. doi: 10.1016/j.neuropharm.2014.11.023. PubMed PMID: 25499022.

471. Blackwell TK, Steinbaugh MJ, Hourihan JM, Ewald CY, Isik M. SKN-1/Nrf, stress responses, and aging in Caenorhabditis elegans. Free Radic Biol Med. 2015;88(Pt B):290-301. Epub 2015/08/02. doi: 10.1016/j.freeradbiomed.2015.06.008. PubMed PMID: 26232625; PubMed Central PMCID: PMCPMC4809198.

472. Nguyen T, Nioi P, Pickett CB. The Nrf2-antioxidant response element signaling pathway and its activation by oxidative stress. J Biol Chem. 2009;284(20):13291-5. Epub 2009/02/03. doi: 10.1074/jbc.R900010200. PubMed PMID: 19182219; PubMed Central PMCID: PMCPMC2679427.

473. Ma Q. Role of nrf2 in oxidative stress and toxicity. Annu Rev Pharmacol Toxicol. 2013;53:401-26. Epub 2013/01/09. doi: 10.1146/annurev-pharmtox-011112-140320. PubMed PMID: 23294312; PubMed Central PMCID: PMCPMC4680839.

474. McCallum KC, Liu B, Fierro-Gonzalez JC, Swoboda P, Arur S, Miranda-Vizuete A, et al. TRX-1 Regulates SKN-1 Nuclear Localization Cell Non-autonomously in Caenorhabditis elegans. Genetics. 2016;203(1):387-402. Epub 2016/02/28. doi: 10.1534/genetics.115.185272. PubMed PMID: 26920757; PubMed Central PMCID: PMCPMC4858787.

475. Guo C, Sun L, Chen X, Zhang D. Oxidative stress, mitochondrial damage and neurodegenerative diseases. Neural Regen Res. 2013;8(21):2003-14. Epub 2013/07/25. doi: 10.3969/j.issn.1673-5374.2013.21.009. PubMed PMID: 25206509; PubMed Central PMCID: PMCPMC4145906.

476. Rolland SG. How to analyze mitochondrial morphology in healthy cells and apoptotic cells in Caenorhabditis elegans. Methods Enzymol. 2014;544:75-98. Epub 2014/06/30. doi: 10.1016/B978-0-12-417158-9.00004-2. PubMed PMID: 24974287.

477. Luz AL, Smith LL, Rooney JP, Meyer JN. Seahorse Xfe 24 Extracellular Flux Analyzer-Based Analysis of Cellular Respiration in Caenorhabditis elegans. Curr Protoc Toxicol. 2015;66:25 7 1-15. Epub 2015/11/03. doi: 10.1002/0471140856.tx2507s66. PubMed PMID: 26523474; PubMed Central PMCID: PMCPMC4632645.

478. Luz AL, Rooney JP, Kubik LL, Gonzalez CP, Song DH, Meyer JN. Correction: Mitochondrial Morphology and Fundamental Parameters of the Mitochondrial Respiratory Chain Are Altered in Caenorhabditis elegans Strains Deficient in Mitochondrial Dynamics and Homeostasis Processes. PLoS One. 2016;11(12):e0168738. Epub 2016/12/16. doi: 10.1371/journal.pone.0168738. PubMed PMID: 27977805; PubMed Central PMCID: PMCPMC5158073.

479. Magistretti PJ, Allaman I. A cellular perspective on brain energy metabolism and functional imaging. Neuron. 2015;86(4):883-901. Epub 2015/05/23. doi: 10.1016/j.neuron.2015.03.035. PubMed PMID: 25996133.

480. Newman LA, Korol DL, Gold PE. Lactate produced by glycogenolysis in astrocytes regulates memory processing. PLoS One. 2011;6(12):e28427. Epub 2011/12/20. doi: 10.1371/journal.pone.0028427. PubMed PMID: 22180782; PubMed Central PMCID: PMCPMC3236748.

481. Steinman MQ, Gao V, Alberini CM. The Role of Lactate-Mediated Metabolic Coupling between Astrocytes and Neurons in Long-Term Memory Formation. Front Integr Neurosci. 2016;10:10. Epub 2016/03/15. doi: 10.3389/fnint.2016.00010. PubMed PMID: 26973477; PubMed Central PMCID: PMCPMC4776217.

482. Hasel P, Dando O, Jiwaji Z, Baxter P, Todd AC, Heron S, et al. Neurons and neuronal activity control gene expression in astrocytes to regulate their development and metabolism. Nat Commun. 2017;8:15132. Epub 2017/05/04. doi: 10.1038/ncomms15132. PubMed PMID: 28462931; PubMed Central PMCID: PMCPMC5418577.

483. Mouchiroud L, Molin L, Kasturi P, Triba MN, Dumas ME, Wilson MC, et al. Pyruvate imbalance mediates metabolic reprogramming and mimics lifespan extension by dietary restriction in Caenorhabditis elegans. Aging Cell. 2011;10(1):39-54. Epub 2010/11/03. doi: 10.1111/j.1474-9726.2010.00640.x. PubMed PMID: 21040400.

484. Fay D, Johnson W. Genetic mapping and manipulation: chapter 10--Suppressor mutations. WormBook. 2006:1-4. Epub 2007/12/01. doi: 10.1895/wormbook.1.99.1. PubMed PMID: 18050454; PubMed Central PMCID: PMCPMC4780890.

485. Fraser AG, Kamath RS, Zipperlen P, Martinez-Campos M, Sohrmann M, Ahringer J. Functional genomic analysis of C. elegans chromosome I by systematic RNA interference. Nature. 2000;408(6810):325-30. Epub 2000/12/01. doi: 10.1038/35042517. PubMed PMID: 11099033.

486. Kamath RS, Martinez-Campos M, Zipperlen P, Fraser AG, Ahringer J. Effectiveness of specific RNA-mediated interference through ingested double-stranded RNA in Caenorhabditis elegans. Genome Biol. 2001;2(1):RESEARCH0002. Epub 2001/02/24. doi: 10.1186/gb-2000-2-1-research0002. PubMed PMID: 11178279; PubMed Central PMCID: PMCPMC17598.

487. Polley SR, Fay DS. A network of genes antagonistic to the LIN-35 retinoblastoma protein of Caenorhabditis elegans. Genetics. 2012;191(4):1367-80. Epub 2012/05/01. doi: 10.1534/genetics.112.140152. PubMed PMID: 22542970; PubMed Central PMCID: PMCPMC3416014.

488. Kage-Nakadai E, Ohta A, Ujisawa T, Sun S, Nishikawa Y, Kuhara A, et al. Caenorhabditis elegans homologue of Prox1/Prospero is expressed in the glia and is

required for sensory behavior and cold tolerance. Genes Cells. 2016;21(9):936-48. Epub 2016/07/13. doi: 10.1111/gtc.12394. PubMed PMID: 27402188.

489. Qadota H, Inoue M, Hikita T, Koppen M, Hardin JD, Amano M, et al. Establishment of a tissue-specific RNAi system in C. elegans. Gene. 2007;400(1-2):166-73. Epub 2007/08/08. doi: 10.1016/j.gene.2007.06.020. PubMed PMID: 17681718; PubMed Central PMCID: PMCPMC3086655.

490. Firnhaber C, Hammarlund M. Neuron-specific feeding RNAi in C. elegans and its use in a screen for essential genes required for GABA neuron function. PLoS Genet. 2013;9(11):e1003921. Epub 2013/11/19. doi: 10.1371/journal.pgen.1003921. PubMed PMID: 24244189; PubMed Central PMCID: PMCPMC3820814.

491. Tong YG, Burglin TR. Conditions for dye-filling of sensory neurons in Caenorhabditis elegans. J Neurosci Methods. 2010;188(1):58-61. Epub 2010/02/13. doi: 10.1016/j.jneumeth.2010.02.003. PubMed PMID: 20149821.

492. Portman DS. Profiling C. elegans gene expression with DNA microarrays. WormBook. 2006:1-11. Epub 2007/12/01. doi: 10.1895/wormbook.1.104.1. PubMed PMID: 18050445; PubMed Central PMCID: PMCPMC4781586.

493. Gaudet J, Mango SE. Regulation of organogenesis by the Caenorhabditis elegans FoxA protein PHA-4. Science. 2002;295(5556):821-5. Epub 2002/02/02. doi: 10.1126/science.1065175. PubMed PMID: 11823633.

494. Portman DS, Emmons SW. Identification of C. elegans sensory ray genes using whole-genome expression profiling. Dev Biol. 2004;270(2):499-512. Epub 2004/06/09. doi: 10.1016/j.ydbio.2004.02.020. PubMed PMID: 15183729.

495. Spencer WC, McWhirter R, Miller T, Strasbourger P, Thompson O, Hillier LW, et al. Isolation of specific neurons from C. elegans larvae for gene expression profiling. PLoS One. 2014;9(11):e112102. Epub 2014/11/06. doi: 10.1371/journal.pone.0112102. PubMed PMID: 25372608; PubMed Central PMCID: PMCPMC4221280.

496. Von Stetina SE, Watson JD, Fox RM, Olszewski KL, Spencer WC, Roy PJ, et al. Cell-specific microarray profiling experiments reveal a comprehensive picture of gene expression in the C. elegans nervous system. Genome Biol. 2007;8(7):R135. Epub 2007/07/07. doi: 10.1186/gb-2007-8-7-r135. PubMed PMID: 17612406; PubMed Central PMCID: PMCPMC2323220.

497. Heiman M, Kulicke R, Fenster RJ, Greengard P, Heintz N. Cell type-specific mRNA purification by translating ribosome affinity purification (TRAP). Nat Protoc. 2014;9(6):1282-91. Epub 2014/05/09. doi: 10.1038/nprot.2014.085. PubMed PMID: 24810037; PubMed Central PMCID: PMCPMC4102313.

498. Gracida X, Calarco JA. Cell type-specific transcriptome profiling in C. elegans using the Translating Ribosome Affinity Purification technique. Methods. 2017;126:130-7. Epub 2017/06/27. doi: 10.1016/j.ymeth.2017.06.023. PubMed PMID: 28648677.

499. Han X, Yang Y, Wu Y, Liu X, Lei X, Guo Y. A bioassay-guided fractionation system to identify endogenous small molecules that activate plasma membrane H+-ATPase activity in Arabidopsis. J Exp Bot. 2017;68(11):2951-62. Epub 2017/06/06. doi: 10.1093/jxb/erx156. PubMed PMID: 28582540.

500. Pollard TD. A guide to simple and informative binding assays. Mol Biol Cell. 2010;21(23):4061-7. Epub 2010/12/01. doi: 10.1091/mbc.E10-08-0683. PubMed PMID: 21115850; PubMed Central PMCID: PMCPMC2993736.

501. Irwin S. Comprehensive observational assessment: Ia. A systematic, quantitative procedure for assessing the behavioral and physiologic state of the mouse. Psychopharmacologia. 1968;13(3):222-57. Epub 1968/09/20. PubMed PMID: 5679627.

502. Sondheimer I, Knackstedt LA. Ceftriaxone prevents the induction of cocaine sensitization and produces enduring attenuation of cue- and cocaine-primed reinstatement of cocaine-seeking. Behav Brain Res. 2011;225(1):252-8. Epub 2011/08/10. doi: S0166-4328(11)00571-7 [pii]
10.1016/j.bbr.2011.07.041.

503. Chamorro A, Dirnagl U, Urra X, Planas AM. Neuroprotection in acute stroke: targeting excitotoxicity, oxidative and nitrosative stress, and inflammation. Lancet Neurol. 2016;15(8):869-81. Epub 2016/05/18. doi: 10.1016/S1474-4422(16)00114-9. PubMed PMID: 27180033.

504. Lorenz MA, Burant CF, Kennedy RT. Reducing time and increasing sensitivity in sample preparation for adherent mammalian cell metabolomics. Anal Chem. 2011;83(9):3406-14. Epub 2011/04/05. doi: 10.1021/ac103313x. PubMed PMID: 21456517; PubMed Central PMCID: PMCPMC3094105.

505. Kolossov VL, Hanafin WP, Beaudoin JN, Bica DE, DiLiberto SJ, Kenis PJ, et al. Inhibition of glutathione synthesis distinctly alters mitochondrial and cytosolic redox poise. Exp Biol Med (Maywood). 2014;239(4):394-403. Epub 2014/03/04. doi: 10.1177/1535370214522179. PubMed PMID: 24586100; PubMed Central PMCID: PMCPMC4120747.

506. Nasca C, Bigio B, Zelli D, de Angelis P, Lau T, Okamoto M, et al. Role of the Astroglial Glutamate Exchanger xCT in Ventral Hippocampus in Resilience to Stress. Neuron. 2017;96(2):402-13 e5. Epub 2017/10/13. doi: 10.1016/j.neuron.2017.09.020. PubMed PMID: 29024663.

507. Vilasi A, Vilasi S, Romano R, Acernese F, Barone F, Balestrieri ML, et al. Unraveling amyloid toxicity pathway in NIH3T3 cells by a combined proteomic and 1 H-NMR metabonomic approach. J Cell Physiol. 2013;228(6):1359-67. Epub 2012/11/30. doi: 10.1002/jcp.24294. PubMed PMID: 23192898.

508. Lin CY, Fuh MR, Huang SD. Application of liquid-liquid-liquid microextraction and high-performance liquid chromatography for the determination of alkylphenols and

bisphenol-A in water. J Sep Sci. 2011;34(4):428-35. Epub 2011/02/08. doi: 10.1002/jssc.201000727. PubMed PMID: 21298782.

509. Li S, Pozhitkov A, Ryan RA, Manning CS, Brown-Peterson N, Brouwer M. Constructing a fish metabolic network model. Genome Biol. 2010;11(11):R115. Epub 2010/12/01. doi: 10.1186/gb-2010-11-11-r115. PubMed PMID: 21114829; PubMed Central PMCID: PMCPMC3156954.

510. Hosack DA, Dennis G, Jr., Sherman BT, Lane HC, Lempicki RA. Identifying biological themes within lists of genes with EASE. Genome Biol. 2003;4(10):R70. Epub 2003/10/02. doi: 10.1186/gb-2003-4-10-r70. PubMed PMID: 14519205; PubMed Central PMCID: PMCPMC328459.

511. Grieb P. Neuroprotective properties of citicoline: facts, doubts and unresolved issues. CNS Drugs. 2014;28(3):185-93. Epub 2014/02/08. doi: 10.1007/s40263-014-0144-8. PubMed PMID: 24504829; PubMed Central PMCID: PMCPMC3933742.

512. Adibhatla RM, Hatcher JF. Cytidine 5'-diphosphocholine (CDP-choline) in stroke and other CNS disorders. Neurochem Res. 2005;30(1):15-23. Epub 2005/03/11. PubMed PMID: 15756928; PubMed Central PMCID: PMCPMC1934404.

513. Matyja E, Taraszewska A, Naganska E, Grieb P, Rafalowska J. CDP-choline protects motor neurons against apoptotic changes in a model of chronic glutamate excitotoxicity in vitro. Folia Neuropathol. 2008;46(2):139-48. Epub 2008/07/01. PubMed PMID: 18587708.

514. Mir C, Clotet J, Aledo R, Durany N, Argemi J, Lozano R, et al. CDP-choline prevents glutamate-mediated cell death in cerebellar granule neurons. J Mol Neurosci. 2003;20(1):53-60. Epub 2003/03/29. doi: 10.1385/JMN:20:1:53. PubMed PMID: 12663935.

515. Alvarez XA, Sampedro C, Lozano R, Cacabelos R. Citicoline protects hippocampal neurons against apoptosis induced by brain beta-amyloid deposits plus cerebral hypoperfusion in rats. Methods Find Exp Clin Pharmacol. 1999;21(8):535-40. Epub 1999/12/22. PubMed PMID: 10599052.

516. Cansev M, Orhan F, Yaylagul EO, Isik E, Turkyilmaz M, Aydin S, et al. Evidence for the existence of pyrimidinergic transmission in rat brain. Neuropharmacology. 2015;91:77-86. Epub 2014/12/30. doi: 10.1016/j.neuropharm.2014.12.019. PubMed PMID: 25541414.

517. Dobolyi A, Juhasz G, Kovacs Z, Kardos J. Uridine function in the central nervous system. Curr Top Med Chem. 2011;11(8):1058-67. Epub 2011/03/16. PubMed PMID: 21401495.

518. Inoue K. Microglial activation by purines and pyrimidines. Glia. 2002;40(2):156-63. Epub 2002/10/16. doi: 10.1002/glia.10150. PubMed PMID: 12379903.

519. Leonardi R, Jackowski S. Biosynthesis of Pantothenic Acid and Coenzyme A. EcoSal Plus. 2007;2(2). Epub 2007/04/01. doi: 10.1128/ecosalplus.3.6.3.4. PubMed PMID: 26443589; PubMed Central PMCID: PMCPMC4950986.

520. Hartig MB, Prokisch H, Meitinger T, Klopstock T. Pantothenate kinase-associated neurodegeneration. Curr Drug Targets. 2012;13(9):1182-9. Epub 2012/04/21. PubMed PMID: 22515741.

521. Venco P, Dusi S, Valletta L, Tiranti V. Alteration of the coenzyme A biosynthetic pathway in neurodegeneration with brain iron accumulation syndromes. Biochem Soc Trans. 2014;42(4):1069-74. Epub 2014/08/12. doi: 10.1042/BST20140106. PubMed PMID: 25110004.

522. Witt KA, Sandoval KE. Steroids and the blood-brain barrier: therapeutic implications. Adv Pharmacol. 2014;71:361-90. Epub 2014/10/14. doi: 10.1016/bs.apha.2014.06.018. PubMed PMID: 25307223.

523. Luchetti S, Huitinga I, Swaab DF. Neurosteroid and GABA-A receptor alterations in Alzheimer's disease, Parkinson's disease and multiple sclerosis. Neuroscience. 2011;191:6-21. Epub 2011/04/26. doi: 10.1016/j.neuroscience.2011.04.010. PubMed PMID: 21514366.

524. Giatti S, Boraso M, Melcangi RC, Viviani B. Neuroactive steroids, their metabolites, and neuroinflammation. Journal of molecular endocrinology. 2012;49(3):R125-34. Epub 2012/09/12. doi: 10.1530/JME-12-0127. PubMed PMID: 22966132.

525. Melcangi RC, Panzica GC. Neuroactive steroids and the nervous system: further observations on an incomplete tricky puzzle. J Neuroendocrinol. 2013;25(11):957-63. Epub 2014/03/04. doi: 10.1111/jne.12110. PubMed PMID: 24580855.

526. Lopez-Rodriguez AB, Acaz-Fonseca E, Spezzano R, Giatti S, Caruso D, Viveros MP, et al. Profiling Neuroactive Steroid Levels After Traumatic Brain Injury in Male Mice. Endocrinology. 2016;157(10):3983-93. Epub 2016/08/23. doi: 10.1210/en.2016-1316. PubMed PMID: 27547849.